Nanomedicine: Development of a Tri-Imageable Nanoparticle for Diagnostics

Ambika Bumb

Oriel College

Supervised by

Professor Peter J. Dobson[1], Professor Lars Fugger[2],
Dr. Martin W. Brechbiel[3], and Dr. Peter L. Choyke[4]

[1] *Begbroke Science Park, Department of Engineering Science, University of Oxford, UK*
[2] *MRC Human Immunology Unit and Department of Clinical Neurology, Weatherall Institute of Molecular Medicine, University of Oxford, UK*
[3] *Radiation Oncology Branch, National Institute of Cancer, NIH, Bethesda, Maryland, USA*
[4] *Molecular Imaging Program, National Institute of Cancer, NIH, Bethesda, Maryland, USA*

Submission: Trinity Term, 2008

This thesis is submitted to the Department of Engineering Science, University of Oxford,
in partial fulfillment of the requirements for the degree of Doctor of Philosophy.

मंज़िलें उन्ही की होती है,
जिनके सपनो में जान होती है |
पंखो से कुछ नहीं होता है दोस्तों,
हौसलों से उड़ान होती है |

(Translation: Destinations are only for those, whose dreams have spirit.
Wings do nothing, friends; morale/determination leads to flight.)

To my parents
and their parents
who are my eternal source of
guidance and inspiration.

Ambika Bumb
Oriel College

Doctor of Philosophy
Trinity Term, 2008

Nanomedicine: Development of a Tri-Imageable Nanoparticle for Diagnostics

Abstract

Targeted, controlled, and noninvasive delivery of therapeutics is a major goal of pharmaceutical development. However, few techniques allow imaging and controlled drug release at the cellular level. Herein, a potential targeted drug delivery platform with three imaging reporters has been developed by coupling the magnetic properties of ultrasmall superparamagnetic iron oxide nanoparticles (USPIOs) with near infrared fluorescence of Cy5.5 and γ-emissions of ^{111}In that is chelated to a conjugated antibody. This silica-coated iron oxide nanoparticle (SCION) allows for verification of localization, characterization of nearby physiology, and quantification.

During each phase of development, the nanoparticles have been characterized for surface charge, structure, optical response, and magnetic properties. Although the size is an advantage for passive delivery, to actively direct SCIONs to a specific location (i.e. epithelial cancers or multiple sclerosis inflammatory foci), various antibodies have been attached to the particle surface. The chelator CHXA"-DTPA was conjugated to antibody for radioisotope labeling. Cell viability, biodistribution, pharmacokinetics, MR, optical, and nuclear imaging studies were conducted.

The results presented demonstrate SCION's potential for application in cell tracking and liver imaging, as well as its promise in the area of sentinel node imaging. *In vivo* optical and magnetic resonance imaging of athymic mice given intracutaneous injection of multimodal SCION in the foot pad reveal visualization of the primary draining lymph nodes. Unlike previous techniques, the particle could first be used to characterize lymph nodes by MR, followed by fluorescence identification during surgery, and further histology using its fluorescence and iron content.

As currently synthesized, the nanoparticles can be used for diagnostics; however, they can also be developed into a method of thermotherapy. Once the delivery construct is traced to its target location, its superparamagnetic properties can be exploited by the application of an AC magnetic field to heat tissue or activate a drug. Thus, with conjugates of this nanoparticle, it should be possible to target specific tissues, verify localization and then non-invasively activate multimodal therapies using extrinsic fields.

Patents

Bumb A, Brechbiel MW, Choyke P, Fugger L, & Dobson PJ. Multifunctional and Multi-Imageable Nanoparticles and Compositions and Methods of Use Thereof. *Pending*. (DHHS E-157-2007/1-US-01; LVM 701850).

Publications

Scientific Journals (published before thesis submission)

Bumb A, Brechbiel MW, Choyke PL, Fugger L, Eggeman A, Prabhakaran D, Hutchinson J, & PJ Dobson. Synthesis and Characterization of Ultra-Small Superparamagnetic Iron Oxide Nanoparticles Thinly Coated with Silica. *Nanotechnology*, **19**(33), 335601-6 (2008).

Boswell AC, Regino CAS, Baidoo KE, Wong KJ, **Bumb A**, Xu H, Milenic DE, Kelley JA, Lai CC, & MW Brechbiel. Synthesis of a Cross-Bridged Cyclam Derivative for Peptide Conjugation and ^{64}Cu Radiolabeling. *Bioconjugate Chemistry*, **19**(7), 1476-84 (2008).

Bumb A, Dobson PJ, Fugger L, Choyke P, & MW Brechbiel. Nanomedicine: Engineering of a Tri-Imageable Nanoparticle for Cancer Diagnostics. *Nanotechnology 2008: Technical Proceedings of the 2008 NSTI Nanotechnology Conference and Trade Show*, **2**, 1-4 (2008).

Bumb A, Brechbiel MW, Choyke P, Fugger L, & PJ Dobson. Nanomedicine: Engineering of a Tri-Imageable Nanoparticle. *Technical Proceedings of the 2007 NSTI Nanotechnology Conference and Trade Show*, **2**, 772-5 (2007).

Book Chapters

Bumb A, Brechbiel MW, & P Choyke. Macromolecular and Dendrimer Based Magnetic Resonance Contrast Agents. In R Arshady, *Molecular Imaging and Therapy*. Kentus Books, London. *In press*.

Acknowledgments

During my graduate days, I have been lucky to meet clever and creative people from diverse backgrounds. Without many of them, this research would not have been conducted, and, although it is not possible to mention them all here, I will be forever grateful.

My greatest gratitude goes to my supervisors extraordinaire: Peter Dobson, Martin Brechbiel, Peter Choyke, and Lars Fugger. Advising a graduate student requires the right mixture of guidance, independence, critique, and praise, and they have perfected the recipe. Their diverse expertise has provided varying insights and has allowed me to explore methods and techniques from different fields - almost different worlds. While for many students, a dissertation project can be taxing and result in a cynical outlook towards research; in my case, my advisors showed me how exciting and fruitful science can be and the last three years have flown by amazingly.

Special mention of the Marshall Commission, NIH Graduate Partnership Program, and Biomedical Research Alliance must be made for allowing me to participate in the collaboration between Oxford and the NIH. Because of them, I was able to setup a doctoral thesis project that spanned four laboratories from two institutes, four disciplines, and two countries. Not many students get that opportunity and I am very grateful.

There are a number of individuals who I greatly respect and admire that took the time out to not just show me a technique, explain its relevance, and answer my infinite number of questions, but in some cases spend hours, even late into the night, with me on my projects: Alex Eggeman and John Hutchinson with TEM, Dharmalingam Prabhakaran with SQUID, Ruth Etzensperger and Kamil Kranc for cell techniques, Andy Boswell for chemistry, Kwamena Baidoo for radio-labeling, Marcelino Bernardo with MRI, and Celeste Regino for pretty much everything.

Though their most endearing quality is sarcasm, a friend circle that I am privileged to have found during graduate school is also one of the most encouraging and inspiring group of individuals I have met. Even with diverse backgrounds and academic interests, intelligent and entertaining discussions with them are often what led my train of thought in directions that turned fruitful. So thank you, Alex, Bhooma, Claire, Jason, Katy, Molly, and Shaz.

I reserve my final acknowledgement for the four people who have been pillars in my life: Shalini Bumb, Nikhil Bumb, Raj Kumari Bumb, and Amar Chand Bumb. Saying thank you to them for their support during only the past three years is meaningless. You know that you have and always will be everything to me.

Table of Contents

List of Figures

List of Tables

Abbreviations

Ab	antibody
AC	ammonia core
AEH	arterial embolization hyperthermia
APTES	3-aminopropyltriethoxysilane
CA	contrast agent
CHX-DTPA	2-(p-isothiocyanatobenzyl)-cyclohexyl-diethylenetriaminepentaacetic acid
CT	computed tomography
DAB	diaminobutane
DAB	diaminobutane
DIH	direct injection hyperthermia
DI	deionized
DLS	dynamic light scattering
DMEM	Dulbecco's Modified Eagle's Medium
DMF	dimethylformamide
DTPA	diethylenetriaminepentaacetic acid
EDA	ethylenediamine
EDTA	ethylenediaminetetraacetic acid
EGFR	epidermal growth factor

FA	flip angle
FDA	Food and Drug Administration
FC	field cool
FLIP	fluorescence loss in photobleaching
FRAP	fluorescence recovery after photobleaching
FRET	Förster or fluorescence resonance energy transfer
FS/FSC	forward scatter
Gd	gadolinium
IA	iodacetamide
IH	intracellular hyperthermia
IND	Investigational New Drug
ITLC	instant thin layer chromatography
LS	lymphoscintigraphy
mAb	monoclonal antibody
MCL	magnetite cationic liposomal
MHC	major histocompatibility complex
MION	monocrystalline iron oxide nanoparticles
MMCM	macromolecular contrast media
MPS	(3-mercaptopropyl)trimethoxysilane
MRA	magnetic resonance angiography
MRI	magnetic resonance imaging
MRL	magnetic resonance lymphography
MWCO	molecular weight cutoff
NDA	New Drug Application
NHS	*N*-hydroxysuccinimide

NIR	near-infrared
PAMAM	polyamidoamine
PBS	phosphate buffered saline
PCS	photon correlation spectroscopy
PE	phycoerythrin
PEG	polyethylene glycol
PET	positron emission tomography
PZC	point of zero charge
QELS	quasi-elastic light scattering
RES	reticuloendothelial system
RIC	radioimmunoconjugates
SCION	silica-coated iron oxide nanoparticle
SE	spin echo
SE-HPLC	size-exclusion high-performance liquid chromatography
SLN	sentinel lymph node
SMCC	succinimidyl-4-(*N*-maleimidomethyl)cyclohexane-1-carboxylate
SPAIR	spectral attenuated inversion recovery
SPECT	single-photon emission computerized tomography
SPGR	spoiled gradient
SPIO	superparamagnetic iron oxide
SQUID	superconducting quantum interference device
SS/SSC	side scatter
s-SMCC	sulfosuccinimidyl-4-(*N*-maleimidomethyl)cyclohexane-1-carboxylate
STIR	short inversion time inversion recovery
TE	echo time

TEA	triethylamine
TEM	transmission electron microscopy
TEOS	tetraethylorthosilicate
TI	inversion recovery time
TLC	thin layer chromatography
TR	repetition time
TSE	turbo spin-echo
USPIO	ultrasmall superparamagnetic iron oxide
ZFC	zero field cool

Chapter 1

Introduction

Magnets in medicine have had a long and interesting history. The Egyptian physician and philosopher Avicenna used magnetite powder for health applications in the 10th century A.D. For the accidental swallowing of rust, he prescribed an antidote of one magnetite grain dissolved in milk with the reasoning that magnetite would render the poisonous iron inert by attracting it and speeding up its excretion through the intestine. In the 15th century, the Swiss physician Paracelsus used natural magnets called 'lodestones' to leach diseases such as epilepsy, diarrhea, and hemorrhage from the body. The belief was that if magnets could attract iron, they could also attract disease from the body. Franz Mesmer set up a popular Parisian salon in the 1700s where he used magnets to cure imbalances in "animal magnetism." Though Louis XVI's Royal Commission invalidated Mesmer's theories, his followers remained 'mesmerized' by magnetic therapy and became the forefathers of hypnotherapy. About 100 years after Mesmer, Daniel David Palmer's School of Magnetic Cure opened in Davenport, Iowa and his philosophy of healing through physical manipulation developed into chiropractic medicine. [1]

Today, the premier example of magnetism used for a medical application is the diagnostic method of magnetic resonance imaging (MRI). MRI takes advantage of the

magnetic properties of hydrogen present in water, membrane lipids, proteins, and other body tissues to non-invasively generate three-dimensional body scans. Early in the development of MRI, it was thought that contrast agents would not be necessary; however it has become increasingly clear that contrast agents can greatly improve the diagnostic value of MRI in many clinical situations.

At the boundary between nanomaterials and medical diagnostics, superparamagnetic iron oxide nanoparticles (SPIOs) are proving to be a class of novel probes useful for *in vitro* and *in vivo* cellular and molecular imaging. Their crystalline structure gives these molecules half-metallic properties that are suitable for MRI [2]. Unlike many nanoprobes, iron-based nanoparticles have a well recognized metabolic fate *in vivo* that has been accepted by regulatory agencies. The work presented here is a novel iron oxide particle that, while also visible through optical and nuclear imaging, has magnetic properties that can be used for MRI, the development of immunochromatographic tests, localized thermotherapy (i.e. hyperthermia), and conversion of a pro-drug to its active form [3].

1.1 Magnetic Resonance Imaging

The advent of MRI has provided scientists and clinicians with a powerful tool to acquire *in vivo* images of anatomy and physiology in whole animals and humans. It is routinely used in the clinic for diagnostic imaging and has the advantage of providing exquisite anatomic resolution, routinely down to 0.5 to 1 mm in plane at clinical field strengths of 1.5 – 3.0 T. The signal to noise ratios in an MR image depend on the density

of protons present in the region of interest and the degree of polarization of the nuclear spin states. When placed in a magnetic field, a slight majority of protons will orient in the direction of the magnetic field and precess at a resonance frequency, known as the Larmor frequency, related to the strength of the magnetic field. Relaxation is measured in two directions, longitudinal and transverse. Longitudinal or spin-lattice relaxation is defined by the time constant T_1 and occurs in the direction of the main magnetic field. Signals related to T_1 relaxation are obtained after excitation by an RF pulse at the Larmor frequency as the proton's dipole moment vector begins to realign or relax back to its ground state of alignment with the main magnetic field. Transverse or spin-spin relaxation corresponds to vector dephasing in the plane perpendicular to the main magnetic field and is characterized by T_2. T_1 represents the time required for the magnetization vector to be restored to 63% of its original magnitude and T_2, a 37% decrease in net signal. T_2 is always equal to or shorter than T_1. Inhomogeneity in the static magnetic field and spin-spin relaxation has an effect on the transverse magnetization and is characterized by:

$$\frac{1}{T_2 *} = \frac{1}{T_2} + \frac{1}{T_2'} \tag{1}$$

where T_2' is a time constant arising from magnetic field inhomogeneity and T_2* is the spin-spin time constant that takes into account these issues. T_2* is always less than T_2. Signals received from spin vectors are used to produce images by the superimposition of magnetic gradients which define the spatial location of the signal. Tissue types vary in their relaxation properties, and thus MRI is used to reconstruct images of structures such as organs and lesions and to evaluate perfusion and flow-related abnormalities.

Despite its complexity, MRI has proven to be extremely successful in the clinical environment. However, all technologies have their limits. In the case of MRI, signal intensity is dependent on several parameters such as proton density, T_1, T_2 and T_2* relaxation rates, magnetic field strength, and pulse sequence. While instrumentation and techniques continue to improve, contrast agents (CAs) can dramatically highlight anatomic and pathologic features of interest. Paramagnetic ions decrease the relaxation time of water protons exchanging with their metal centers. Thus, MR contrast agents are not directly imaged, but rather, indirectly affect the surrounding water molecules that in turn influence signal. Relaxation is also a function of molecular tumbling, the fast exchange between CA-coordinated water molecules and water in the bulk solvent, or the inner and outer shells. If exchange among protons in the shells is rapid, they all exhibit similar relaxation behavior. The overall signal is then a weighted average of relaxation rates from each local proton environment, with the principal contribution from within the hydration sphere of the ion. As a result of their unpaired electrons, paramagnetic ions, including Mn^{2+}, Fe^{3+}, and Gd^{3+}, are a potent class of MRI contrast agents.

Today, contrast media containing paramagnetic or superparamagnetic metal ions are administered in 40–50% of all MR examinations [4]. These image-enhancing contrast agents add significant morphological and functional information to unenhanced MR images. Although theoretical safety concerns exist, MR contrast agents have been shown in clinical use to be safe and well tolerated. Table 1-1 and Table 1-2 list agents used for MR contrast that act predominantly on T_1 relaxation which results in signal enhancement and "positive" contrast, or on T_2 relaxation, which results in signal reduction and "negative" contrast. The following sections will discuss both of these types of MR agents

before describing the concept for the developed particle, tri-imageable silica-coated iron oxide nanoparticle (SCION).

Table 1-1: T_1 contrast agents used for magnetic resonance [5].

T1 AGENTS						
NAME OF COMPOUND	CENTRAL MOIETY	RELAXIVITY*	DISTRIBUTION	INDICATION	DEVELOPMENT STAGE	TRADE MARK
Gadopentate dimeglumine, Gd-DTPA	Gd3+	r1=3.4, r2=3.8, B0=1.0T, Xm=2.7 10-2	intravascular, extracellular	neuro/whole body	for sale	Magnevist
			gastrointestinal	bowel marking	for sale	Magnevist enteral
Gadoterate meglumine, Gd-DOTA	Gd3+	r1=3.4, r2=4.8, B0=1.0T, Xm=2.7 10-2	intravascular, extracellular	neuro/whole body	for sale	Dotarem
Gadodiamide, Gd-DTPA-BMA	Gd3+	r1=3.9, r2=4.3, B0=1.0T, Xm=2.7 10-2	intravascular, extracellular	neuro/whole body	for sale	Omniscan
Gadoteridol, Gd-HP-DO3A	Gd3+	r1=3.7, r2=4.8, B0=1.0T, Xm=2.7 10-2	intravascular, extracellular	neuro/whole body	for sale	Prohance
Gadob gastrointestinal	bowel marking	Phase III, oral suspension	Gadolite 60			
MnCl 2	Mn2+	paramagnetic	gastrointestinal	bowel marking		Lumenhance
Fatty emulsion	fatty liquid	short T1-relaxation time	gastrointestinal	bowel marking		
Vegetable oils	fatty liquid	short T1-relaxation time	gastrointestinal	bowel marking		
Sucrose polyesters	fatty liquid	short T1-relaxation time	gastrointestinal	bowel marking		
Mangafodipir trisodium MN-DPDP, Managnese dipyroxyl diphosphate	Mn2+	r1=2.3, r2=4.0, B0=1.0 T	hepatobiliary, pancreayiv, adrenal	liver lesions	approved	Teslascan
Gadobenate di-meglumine, Gd-BOPTA	Gd3+	r1=4.6, r2=6.2, B0=1.0 T	intravascular, extracellular, hepatobiliary	neuro/whole body, liver lesions	Phase III	Multihance
Gadoxetic acid, Gd-EOB-DTPA	Gd3+	short T1-relaxation time	hepatobiliary	liver lesions	Phase III	Eovist
Fe-HBED	Fe2+		hepatobiliary	liver lesions		
Fe-EHPD	Fe2+		hepatobiliary	liver lesions		
Liposomes, paramagnetic	Gd3+		RES-directed	liver lesions		
Mn-EDTA-PP (liposomes)	Mn2+	r1=37.4, r2=53.2, B0=0.5 T				Memosomes
Polylysine-(Gd-DTPA)x-dextran	Gd3+		lymph nodes	staging of lymph nodes		
Diphenylcyclohexyl phosphodiester-Gd-DTPA, MS 325 EPIX	Gd3+		intravascular, short elimination half life	MR-angiography, vasc. capillary permeability	Phase I	
MP 2269, 4-pentyl-bicyclo [2.2.2] octan-1-carboxyl-di-L-aspartyllysine-DTPA	Gd3+	r1=6.2, B0=1.0 T	intravascular	MR-angiography	preclinical	
(Gd-DTPA)-17, 24 cascade polymer	Gd3+	r1=11.9, B0=1.0 T, (r2=16.5)	intravascular	MR-angiography vascularis	preclinical	Gadomer-17, 24
Gd-DTPA-PEG polymers (polyethylene glycol)	Gd3+	r1=6.0, B0=1.0 T	intravascular	MR-angiography vascularis, capillary permeability	preclinical	
(Gd-DTPA)n-albumin, (Gd-DOTA)n-albumin	Gd3+	r1=14.4, B0=0.23 T	intravascular	MR-angiography vascularis, MR-mammography	preclinical	
(Gd-DTPA)n-polylysine	Gd3+	r1=13.1, B0=0.23T	intravascular	MR-angiography	preclinical	
(Gd-DTPA)n-dextran	Gd3+		intravascular	MR-angiography	preclinical	
Manganese substituted hydroxylapatite PEG-APD (MnHA/PEG-APD)	Mn2+	r1=21.7, r2=26.9, B0=1.0 T	intravascular	MR-angiography	preclinical	
WIN 22181	Gd3+	r1=9.5		MR-urography	preclinical	

*Relaxivities (r1, r2) in mmol-1sec-1 (at varying temperatures); Magnetic susceptibility (Xm) in cgs/mol

Table 1-2: T_2 contrast agents used for magnetic resonance [5].

T2 AGENTS						
NAME OF COMPOUND	CENTRAL MOIETY	RELAXIVITY*	DISTRIBUTION	INDICATION	DEVELOPMENT STAGE	TRADE MARK
Sprodyamide, Dy-DTPA-BMA	Dy2+	T2*enhanced, r1=3.4, r2=3.8, B0=0.47 T, Xm=4.46 102	intravascular	blood flow perfusion	preclinical	
Dy-DTPA	Dy2+	T2*enhanced, Xm=4.8 102	intravascular	blood flow perfusion	preclinical	
Albumin-(Dy-DTPA)x	Dy2+	T2*enhanced	intravascular	blood flow perfusion	preclinical	
Ferrum oxid. (USAN), SPIO, Ami-25, dextran-coated	Fe2+/Fe3+	r1=40.0, r2=160, B0=0.47T, Xm=0.4	RES-directed	liver lesions and control	for sale	Endorem, Feridex
Ferrixan, Carboxy-dextran coated iron oxide nanoparticles, SHU 555A	Fe2+	r1=25.4, r2=151	RES-directed	liver lesions	Phase III	Resovist
USPIO, AMI-227	Fe3+/Fe2+	r1=25, r2=160, B0=0.47T, Xm=0.34, r1=23.3, r2=48.9, B0=0.47T	vascular, lymph v. hepatocyte (AG-USPIO)	MR-angiography vascular staging of RES-directed liver diseases	Phase II/III, lymph nodes	Sinerem, Combidex
Fe O-BPA USPIO	Fe3+/Fe2+		vascular	MR-angiography	preclinical	
MION, Monocrystalline iron oxide nanoparticles	Fe3+/Fe2+	r1=3.7, r2=6.5, B0=0.47T, Xm=0.11	vascular lymph v. (MION-46) tumours, FAB-MION, antimyosin, FAB-MION	MR-angiography, MR-lymphography, tumour detection, infarction	preclinical	
Magnetic starch microspherers		r1=27.6, r2=183.7, B0=1.0T	RES-directed	liver lesions, spleen	preclinical	
PION, polycrystalline iron oxide nanoparticles (larger particles = DDM 128, PION-ASF)	Fe2+/Fe3+	T2*enhanced, r2/r1=4.4, r2/r1=7	RES-directed lymph v. hepatocyte	liver lesions, MR lymphography	preclinical	
Ferromuxsilum (USAN) AMI-121	Fe3+/Fe2+	T2*enhanced, Xm=0.23	gastrointestinal	bowel marking	for sale	Lumirem, Gastromark
Ferristene (USAN) oral magnetic particles (OMP)	Fe2+/Fe3+	T2*enhanced	gastrointestinal	bowel marking	for sale	Abdoscan
Perfluorooctylbromide (PFOB)	water immiscible liquid	proton density reduction, signal void	gastrointestinal	bowel marking	for sale	Perflubron, Imagent R, GI, USA
Barium suspensions and clay mineral particles OMP	Ba3+, Al3+, Si2+	diamagnetic, T2-short	gastrointestinal	bowel marking	no clinical development	various mixtures
Dy-tatraphenyl-porphyrin sulfonate, Dy-TPPS or Ho-TPPS	Dy2+Ho2+	high susceptibility	tumour selective uptake	tumour detection and control	preclinical	

*Relaxivities (r1, r2) in mmol-1sec-1 (at varying temperatures); Magnetic susceptibility (Xm) in cgs/mol

1.2 Gadolinium-Based T_1 Contrast Agents

1.2.1 Small Molecule MR Contrast Agents

The first generation of contrast agents was based on the lanthanide ion gadolinium, a paramagnetic ion with seven unpaired 4*f* electrons. However, its free form is highly toxic. Thus, a number of chelating agents are used to render the ion nontoxic by keeping the metal ion sequestered. These biocompatible complexation cages are

generally highly stable and have a greater affinity for Gd^{3+} than exogenous *in vivo* metal ions such as Zn^{2+}, Ca^{2+}, or Cu^{2+}.

One class of Gd^{3+} complexes is macrocyclic chelates, mostly derivatives of 1,4,7,10-tetraazacyclododecane (cyclen) [6]. The tetraacetic acid derivative complex with gadolinium, Gd-DOTA (gadoterate, Dotarem®) is formulated as its *N*-methylglucamine salt, is highly water soluble, and is thermodynamically stable. Two charge neutral macrocylic derivatives of 1,4,7-tricarboxymethyl-1,4,7,10-tetraazacyclododecane (DO3A) are gadoteridol (ProHance®) and gadobutrol, (Gadovist®). They are characterized by the substitution of one carboxylate with a secondary hydroxyl donor group.

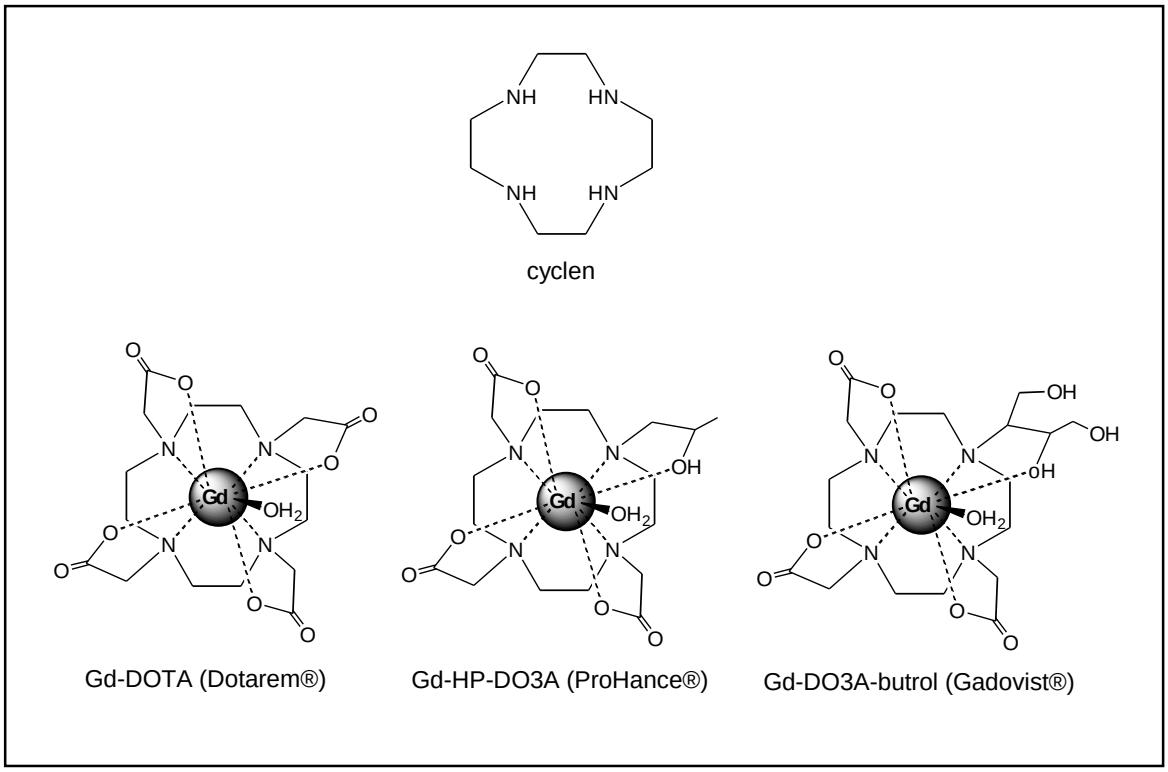

Figure 1-1: Schematic representations of the structures of cyclic chelates that are commercially marketed as MRI contrast agents.

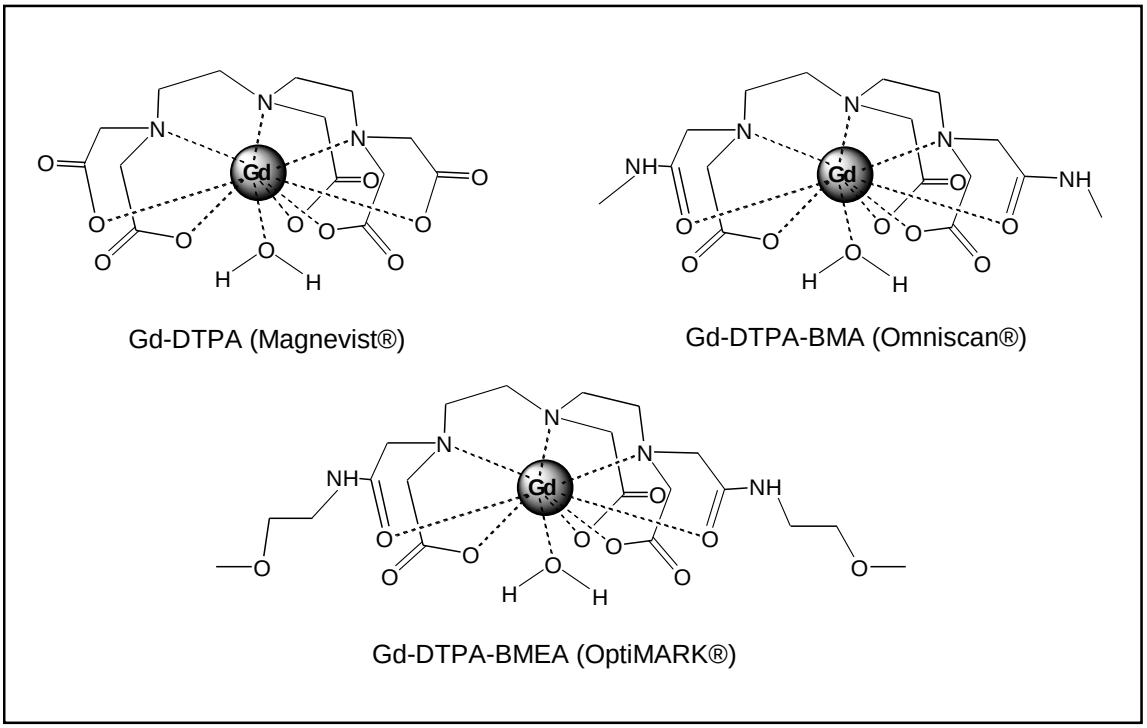

Figure 1-2: Schematic representations of the structures of acyclic chelates that are commercially marketed as MRI contrast agents.

Acyclic chelates (Figure 1-2) are another class of chelates which is comprised of derivatives of aminopolycarboxylic acids such as diethylenetriaminepentaacetic acid (DTPA). Gadolinium diethylenetriaminepentaacetic acid dimeglumine salt (Gd-DPTA), also known as Magnevist®, was approved for clinical use in adult patients in 1988 and has since become the most commonly used MR contrast agent. The chelate has high thermodynamic stability and is water soluble [7]. Two diamide derivatives of DTPA are approved for human use: gadolinium diethylenetriaminepentaacetic acid bismethylamide (Gd-DTPA-BMA, gadodiamide, Omniscan®) and gadolinium diethylenetriaminepentaacetic acid bismethoxyethylamide (Gd-DTPA-BMEA, gadoversetamide, OptiMARK®). By reacting the dianhydride of DTPA with the corresponding amine (methyl amine or methoxyethyl amine, respectively), two carboxylates were converted to two amide oxygen donors, resulting in a neutral charge on

the chelate. These neutral agents remain highly water soluble and were developed in part to lower the osmolality of aqueous solutions [8]. Magnevist, Ominiscan, OptiMARK, MultiHance, and Prohance have been approved for use in the US. In late 2006, however, the FDA issued a warning that exposure to these CAs in patients with severe kidney dysfunction could cause Nephrogenic Systemic Fibrosis, a potentially lethal condition [9, 10].

The number of water molecules coordinated to Gd^{3+} and Gd-DTPA are approximately 8-9 and 1, respectively, and the corresponding relaxivity values are 7.0 and 2.0 at 37°C, 20 MHz, and 0.5 T [11]. While relaxivity is an important property, other factors, namely clearance rate, also determine the efficacy of an agent in obtaining quality images. The amount of time required for a CA to be excreted is dependent on a number of properties such as size, shape, surface charge and chemical makeup of the agent. With a molecular weight of 0.8 kDa, 90% of the injected dose of Gd-DPTA is cleared by renal filtration and vessel leakage in less than an hour [12], necessitating rapid imaging after injection. However, the rapid clearance in patients with normal renal function improves the safety profile.

1.2.2 Macromolecular Gd-Based MR Agents

Macromolecular metal-chelate complexes, also known as blood pool agents or macromolecular contrast media (MMCM), generally have a molecular weight greater than 30kDa and were originally designed for prolonged blood retention. Furthermore, they increase relaxivity due to slower molecular tumbling. The Solomon-Bloembergen-Morgan theory of paramagnetic relaxivity predicts that increasing the rotational correlation time of a paramagnetic ion with a relatively long electronic relaxation time

will increase the ion's relaxivity [13-15]. The molecular dynamics of such paramagnetic ions dominate the dipole-dipole interactions between their unpaired electrons and the water protons in the inner shell [16, 17]. Increased steric hindrance slows the rotation of larger molecules, increasing the rotational correlation time, τ_R, thus increasing relaxivity and resulting in more enhancement per unit dose of the paramagnetic ion. Moreover, using a macromolecular structure potentially allows for the attachment of a large number of chelates and metal ions per agent, further increasing the molar enhancement. This enhancement potentially can result in lower local concentration of the carrier molecule being required for satisfactory image acquisition.

In order to attach paramagnetic ions to macromolecular structures, a family of chelates known as bifunctional chelates (Figure 1-3) were developed, including 2-(4-isothiocyanatobenzyl)-6-methyl-diethylenetriamine pentaacetic acid (1B4M-DTPA), *N*-[2-amino-3-(4-isothiocyanatobenzyl)propyl]-*cis*-cyclohexyl-1,2-diamine-*N*,*N*',*N*',*N*'',*N*'' pentaacetic acid (CHX-A-DTPA), *N*-[2-amino-3-(4-isothiocyanatobenzyl)propyl]-*trans*-cyclohexyl-1,2-diamine-*N*,*N*',*N*',*N*'',*N*''-pentaacetic acid (CHX-B-DTPA), and 2-(4-isothiocyanatobenzyl)-1,4,7,10-tetraazacyclododecane-*N*,*N*',*N*'',*N*'''-tetraacetic acid (p-SCN-Bz-DOTA) [18]. These allow the chelates to sequester a metal ion while also binding that metal complex to a macromolecule.

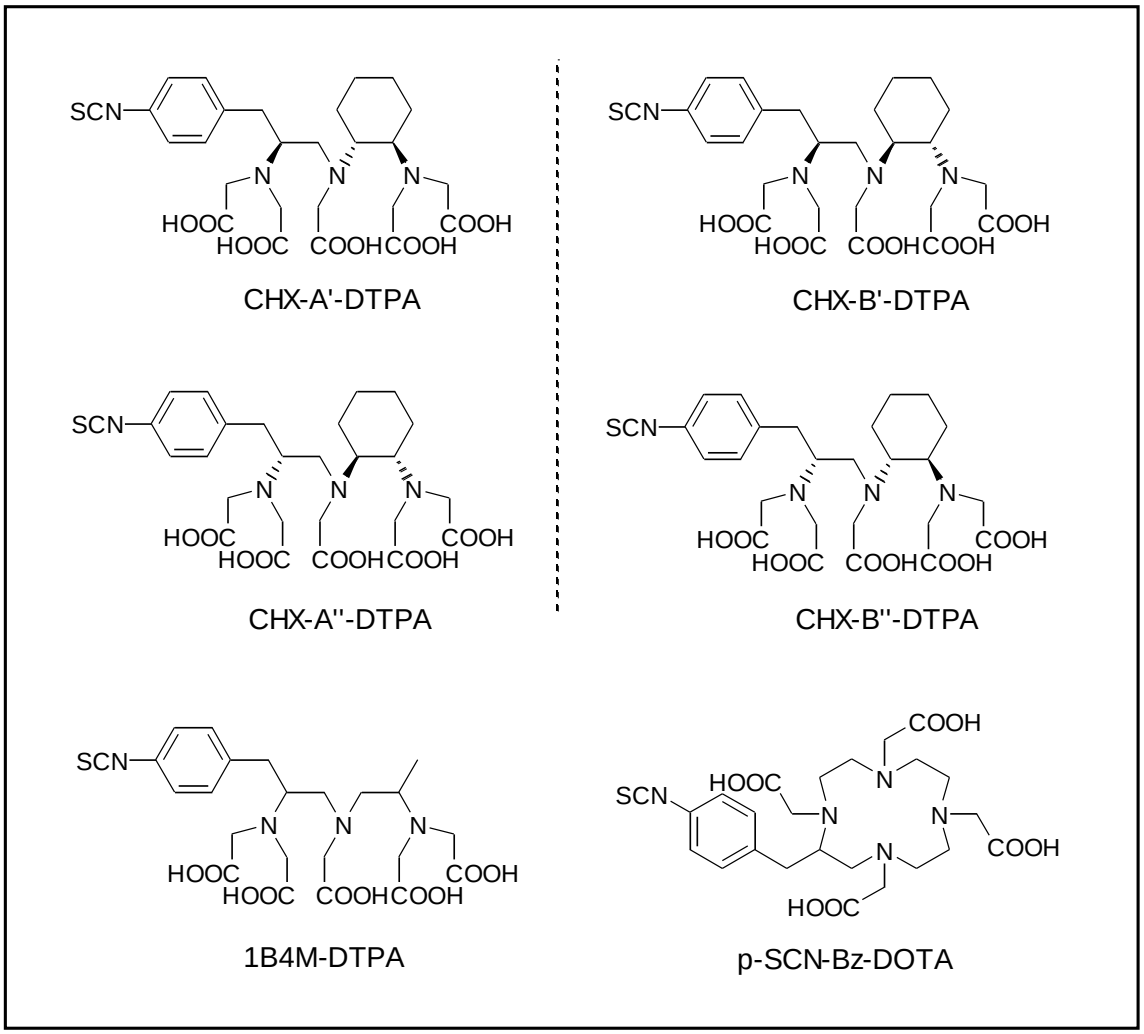

Figure 1-3: Bifunctional chelates synthesized to attach to a ligand while also trapping a metal ion such as Gd^{3+}. Diastereomers of the CHX-DTPA chelates are shown.

In 1987, Ogan and colleagues [19] published groundbreaking work on one of the first macromolecular agents, albumin attached to 19 Gd-DPTA groups. T1 relaxivity of albumin-(Gd-DPTA) at 0.23 T was 273 mM-1s-1 , corresponding to 14.8 mM-1s-1 per gadolinium ion; relaxivity of native albumin is 0.40 mM-1s-1 at similar protein concentration [19]. The relaxivity of Gd-DTPA alone is 4.9 $mM^{-1}s^{-1}$ [20], thus indicating that there was a three-fold increase in relaxation. However, the agent's ability to imitate native circulating albumin also creates a potential problem for its use. Given that only 5% of albumin leaks from blood circulation each hour [21], the albumin complex has

slow clearance from the vessels leading to non-specific pooling in the blood [8]. Elimination is slow and incomplete, with retention times up to several weeks, particularly in the liver and bone, leading to toxicity concerns. To combat this issue, Gd-chelates that would reversibly bind to albumin were developed starting with trisodium 2-(*R*)-[(4,4-diphenylcyclohexyl) phosphonooxymethyl]-diethylenetriaminepentaacetato *aquo* gadolinium (MS-325, Gadofosveset, Figure 1-4) [22, 23]. Others include Gd-EOB-DTPA (Eovist®), Gd-BOPTA(MultiHance®), MP-2269, and B-22956/1.

After injection, these agents bind to serum albumin and other proteins and equilibrium is maintained between free and bound chelate. The primary disadvantage to

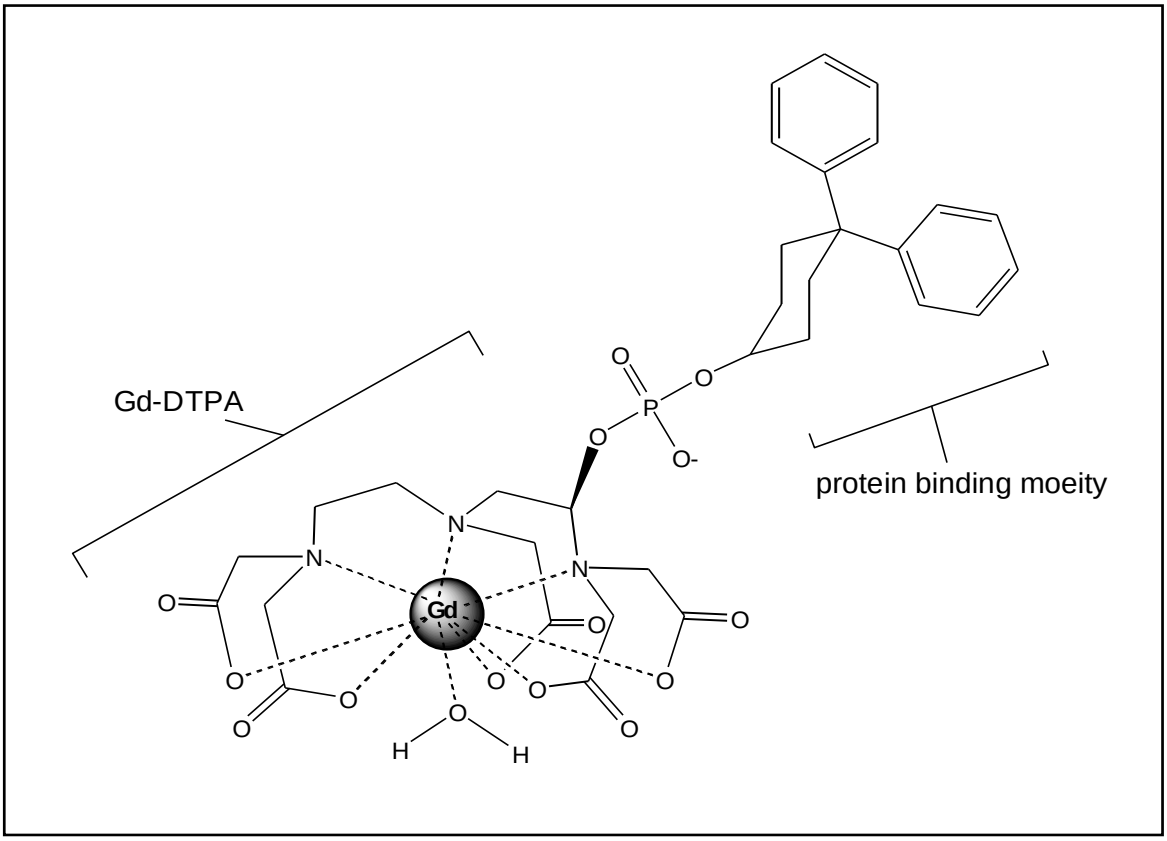

Figure 1-4: Chemical structure of the reversible binding chelate MS-325. It is composed of a Gd-DTPA chelate attached by a phosphodiester linkage to a lipophilic diphenylcyclohexyl group that non-covalently attaches to protein.

these agents is the complex pharmacokinetics of the unpredictable mixture of relatively low molecular weight unbound chelate and the high molecular weight protein-bound chelate. Though albumin-bound agents will have greater relaxivity, imaging instruments cannot differentiate between the enhancement from the free and bound chelate forms, and thus, although the signal from the bound form is higher, the total signal represents the relative proportion of the two states of the contrast agent which changes over time.

A number of polymer based structures have been analyzed for use as platforms for attaching multiple units of chelated Gd^{3+}. Dextran, which has been used as a synthetic plasma expander for 50 years, was one of the initial polysaccharides to be complexed to Gd-chelates [24] and caused it to remain intravascular for at least one hour after injection, showing enhancement of liver, spleen, kidneys, and myocardium. Ladd et al [25] characterized the use of a series of polyethylene glycol (PEG) and Gd-DTPA diamines ranging from 10.8 to 83.4 kDa in a rabbit model. Other polymers that have been loaded with Gd include insulin [26], polylysine [27], and hydroxyethyl starch [28].

Perhaps the most studied polymer structure for MR is the dendrimer which has repeating branched units. Controlled growth of the dendrimer exponentially increases the number of terminal groups from the core. The first dendrimer family to be characterized and commercialized was polyamidoamine (PAMAM) dendrimers. Other dendrimers include diaminobutane (DAB) dendrimers, which unlike PAMAM dendrimers that are comprised of a scaffold of repeating amine and amide units, contain only amines on a propyleneamine scaffold linked through a diaminobutane core. Over fifty other dendrimer families have been characterized, each possessing compositionally different interiors, i.e. carbon, nitrogen, silicon, sulfur, phosphorus or metals [29].

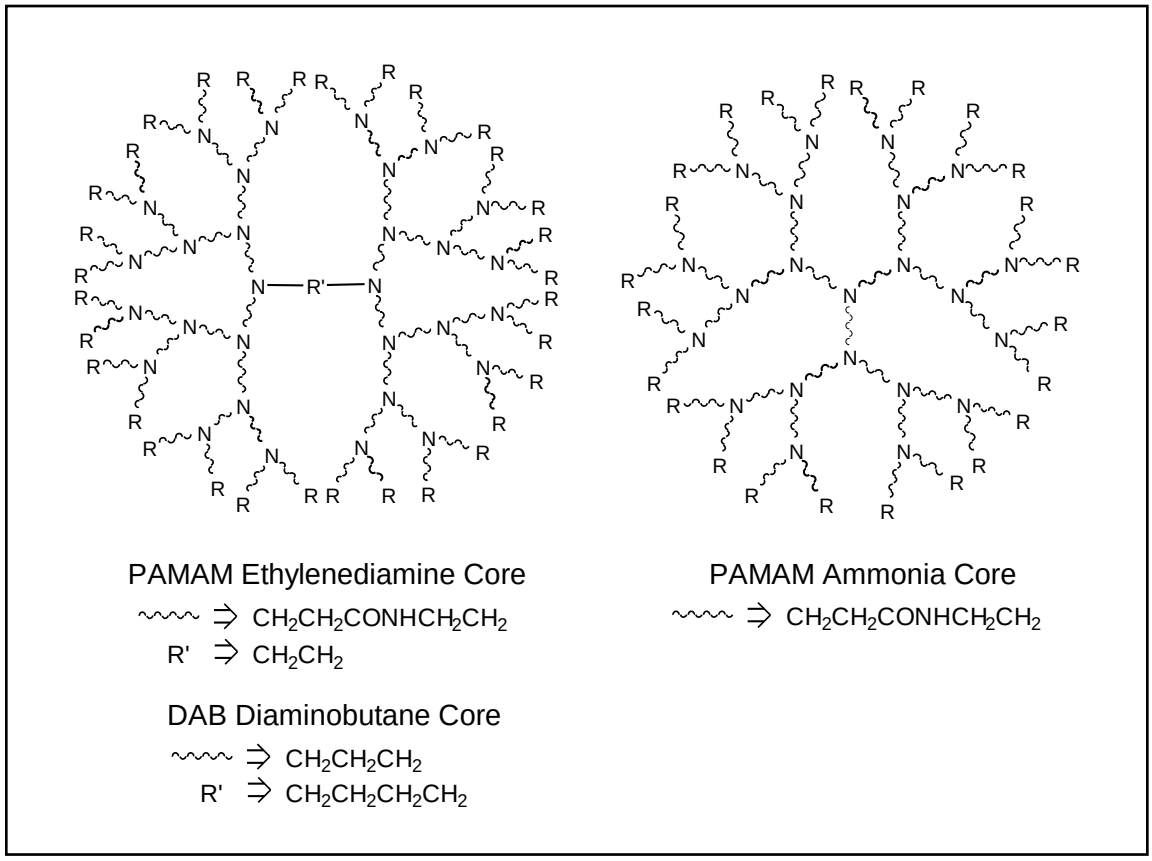

Figure 1-5: Schematic drawing of second generation ammonia core (AC) and ethylenediamine (EDA) PAMAM and diaminobutane (DAB) dendrimers.

Though terminal groups are typically amines or carboxylic acid, they can be functionalized to other end groups, thus allowing them to be tailored for a variety of applications. Larger dendrimers have a greater number of terminal groups and thus more chelates can be attached. G5 and G10 PAMAM-EDA dendrimers can theoretically bind up to 96 and 1860 Gd^{3+} ions, respectively, and demonstrate r_1 relaxivities per gadolinium ion of 30 and 36 $mM^{-1}s^{-1}$ (20 mHz, 0.47 T) [30]. Although such numbers are rarely actually achieved, the net effect of the large numbers of metal ions on a single molecule is to greatly improve MR signal. In addition to Gd conjugation, dendrimers permit the conjugation of targeting ligands. Wu et al [31] and others have demonstrated site-specific

targeting by conjugating antibodies and their fragments to chelated dendrimers with minimal Ab immunoreactivity loss.

A number of gadolinium MR macromolecular contrast agents have developed over the last 30 years, ranging from protein to polymer to dendrimer-based molecules. These agents have diameters greater than 4-5 nm and are therefore generally cleared more slowly by the kidney, if at all. By 8 nm, renal excretion is greatly reduced and the liver begins to predominate as the clearance mechanism and completely dominates by 10-12 nm. Biodistribution of these agents is affected by longer retention times and the limited ability of the agent to extravasate into normal tissue.

1.3 Properties of Superparamagnetic Iron Oxide

While the gadolinium agents described above are T_1 positive contrast agents, superparamagnetic iron oxide nanoparticles (SPIOs) are a class of T_2 MR agents which provide negative contrast for *in vitro* and *in vivo* cellular and molecular imaging. During the first clinical trial in 1988, SPIOs greatly enhanced detection of liver lesions by decreasing the signal from the normal hepatocytes [32]. SPIO particles are crystalline structures with the general formula of $Fe^{3+}{}_2O_3M^{2+}O$, wherein M^{2+} is a divalent metal ion such as iron, manganese, nickel, cobalt, or magnesium. Because of iron's ubiquitous presence in living tissue, the ferrous ion Fe^{2+} is the most common divalent ion used in SPIOs to make magnetite, Fe_3O_4. Indeed, magnetite is particularly suitable for manipulation in MR as it has been isolated from certain birds, fish, and bacteria in which its interaction with the magnetic field of the earth has been found to play a critical role in

navigation [33]. Maghemite/magnetite, γ-Fe_2O_3/Fe_3O_4, particles have face-centered cubic packing of oxygen that allows electrons to jump between iron ions occupying interstitial tetrahedral and octahedral sites. This gives the molecules half-metallic properties that greatly shorten T_2 and T_2* and can increase proton relaxivities ten-fold [34]. The typical SPIO agent has a T_2 relaxivity of 100 $mM^{-1}s^{-1}$ and T_1 relaxivity of 30 $mM^{-1}s^{-1}$, substantially larger than Gd-DTPA's T_2 relaxivity of 6 $mM^{-1}s^{-1}$ and T_1 relaxivity of 4 $mM^{-1}s^{-1}$ [35].

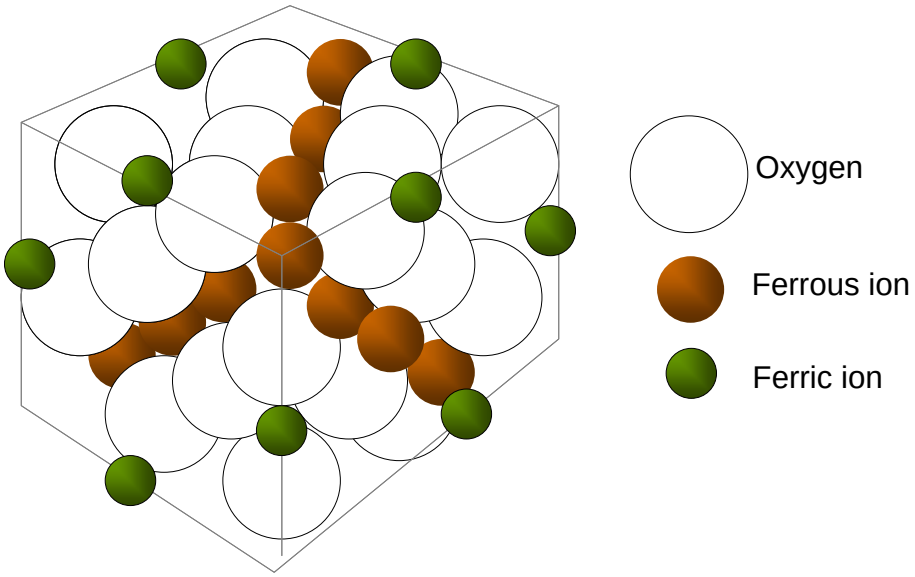

Figure 1-6: Schematic representation of spinal crystal structure for magnetite.

Superparamagnetic materials have physical and chemical properties that are characteristic of neither their atoms nor their ferromagnetic bulk counterparts. Coupling forces in ferromagnetic materials align the magnetic moments of neighboring atoms resulting in large internal magnetic fields and distinguishing them from paramagnetic materials which have random spin orientations with net zero magnetization while in ambient field conditions. Only at temperatures above the Curie temperature for ferromagnetic materials or the Neel temperature for antiferromagnetic materials, is the

thermal energy sufficient to overcome coupling forces, leaving the atomic magnetic moments to fluctuate randomly with paramagnetic behavior.

Superparamagnetic materials, however, display similar behavior even at temperatures below the Curie or Neel temperatures. These materials are composed of small crystallites (1-10nm). Though the thermal energy is not sufficient to overcome the coupling forces between neighboring atoms, it is sufficient to change the direction of magnetization of the entire crystallite. The crystalline magnetic anisotropy energy, which is responsible for keeping magnetic moment oriented in a direction, is less than or comparable to thermal energy. Thus, in the absence of an applied magnetic field, the direction of crystallite magnetization is free to rotate with thermal motion and randomly orient to average a net zero magnetization. The material behaves similarly to a paramagnet, except that instead of each individual atom being independently influenced by an external magnetic field, the magnetic moment of the entire crystallite tends to align with the applied field. Furthermore, the resultant magnetic moment after an external field is applied is much greater for a superparamagnet than for a paramagnet [36, 37]. When removed from the applied field, the magnetic orientation again randomizes with no hysteresis from the previous

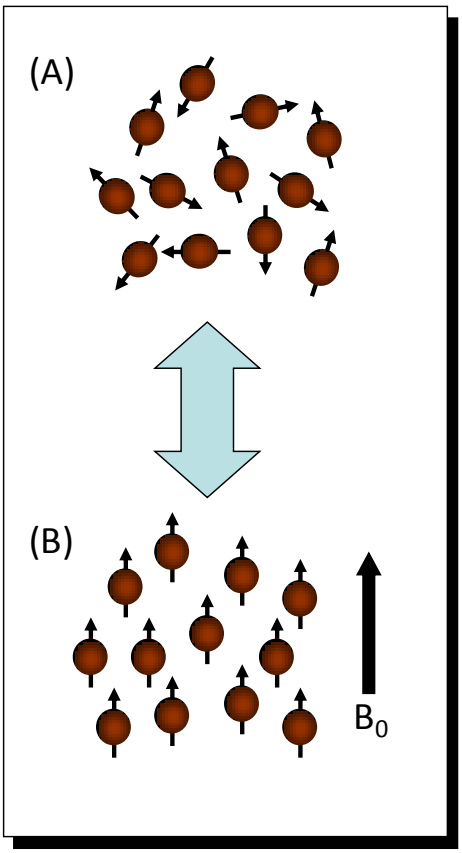

Figure 1-7: Ultrasmall superparamagnetic iron oxide particles in the (A) absence and (B) presence of an external magnetic field.

alignment (Figure 1-7). This behavior applies up to the Neel and Curie temperatures, and above them, the material exhibits normal paramagnetic behavior.

Placing such particles in AC magnetic fields would randomly flip the magnetization direction between parallel and antiparallel orientations, a property that can be manipulated for thermotherapy or hyperthermia in the case of drug delivery or cancer treatment. In past studies, the temperature of tumor cells in F344 rats injected with magnetite cationic liposomal (MCL) nanoparticles was elevated to 43°C after 15 minutes of treatment with an alternating magnetic field. In contrast, the temperature of tumor cells lacking MCLs remained between 35-37°C [38-40]. In Germany, Jordan and co-workers [41] performed a systematic analysis of thermotherapy treatment on experimental glioblastoma multiforme in a rat brain tumor model. Animals received two treatments from an alternating magnetic field applicator system (100 kHz, 0–18 kA/m) following a single intratumoral injection of aminosilane-coated iron-oxide nanoparticles. Thermotherapy with the particles resulted in a 4.5-fold prolongation of survival over controls. The hyperthermic effect of dextran-coated magnetite has also been studied using several human carcinoma cell lines *in vitro* [42].

1.4 Current SPIOs

Superparamagnetic iron oxide contrast agents are loosely categorized into the following groups: large oral SPIOs, standard SPIOs (SSPIO), ultrasmall SPIOs (USPIO) and monocrystalline iron oxide nanoparticles (MION). Oral SPIO preparations typically contain larger particles and are coated with a non-biodegradable and insoluble matrix to

reduce aggregation. They are suspended in viscosity-increasing agents based on ordinary food additives such as starch and cellulose that prevent ingested iron absorption and particle aggregation to allow homogeneous contrast distribution throughout the bowel. Oral SPIO is normally administered over 30-60 minutes, with a volume of 900 mL for contrast enhancement of the whole abdomen, and 400 mL for imaging of the upper abdomen. These suspensions are well-tolerated by the patients where iron is not absorbed and the intestinal mucosal membrane is not irritated [43, 44].

Standard superparamagnetic iron oxide agents are easily sequestered by the reticuloendothelial system (RES) cells in the liver and spleen upon intravenous administration with minimal lymph node uptake. AMI-25 (Endorem or Feridex) consists of iron oxide crystals coated by dextran with a final diameter of 80-150 nm. The T_2 and T_1 relaxivities respectively are 98.3 and 23.9 $mL^{-1}s^{-1}$ [45]. With a blood half-life of 6 min, AMI-25 quickly accumulates in the liver (~80% of the injected dose) and spleen (5-10% of the injected dose) within minutes of injection. Peak concentrations of iron are found in the liver and spleen after 2 hr and 4 hr with half-lives of 3 and 4 days, respectively [45]. The preparation is usually not administered in a bolus injection because of cardiovascular side effects and lumbar pain. The recommended mode of administration is a dose of 15 µmol Fe/kg in 100 mL of 5% glucose with a biphasic infusion (2 mL/min over 10 min and 4 mL/min over 20 min). SHU 555A (Resovist) is a carbodextran SSPIO with 4.2 nm iron crystals and a hydrodynamic diameter of 62 nm. Its T_2 and T_1 relaxivities are 151.0 and 25.4 $mM^{-1}s^{-1}$ respectively. This particle shows no side effects after rapid intravenous injection and a dose of 8 µmol Fe/kg can be scanned within 30 min after administration [46]. Due to smaller size and higher T_1 relaxation,

SHU 555A has also been used for MR angiography (MRA) and dynamic T_1-weighted MR imaging similar to gadolinium chelates [47].

USPIOs typically have iron crystals of 5-12 nm and prolonged blood half-life that affords them the opportunity to eventually cross capillary walls and have more widespread tissue distribution. They can be delivered to the interstitium by non-specific vesicular transport and through transendothelial channels. Once in the interstitium, draining lymphatic vessels transport them to lymph nodes, thus making them suitable agents for MR lymphography (MRL). At low concentrations, these agents can be used for T_1-weighted MRA, though high concentrations will lead to signal loss due to T_2-shortening effects. AMI-227 (Sinerem or Combidex) is a 20-40 nm dextran-coated USPIO with a human bloodpool half-life of more than 24 hr [48]. It can be used as a MRA agent during the early phase of intravenous administration [49-51] and MRL agent during late phase [52, 53]. To avoid hypotensive reactions or acute lumbar pain, AMI-227 is infused slowly over a period of 30 minutes reducing its importance as an MRA agent. NC100150 (Clariscan, Nycomed), a PEGylated USPIO, and HU 555C (Resovist) are bolus-injectable agents developed for MRA and perfusion studies [54, 55]. NC100150 has been tested as a brain T_2*-weight perfusion agent at a dose of 7 µmol Fe/kg [56], but because of some adverse events and improvements in MRI units allowing better MRA with low molecular weight contrast agents, the sponsor (GE Healthcare) discontinued the development of this product.

Monocrystalline iron oxide nanoparticles (MIONs) are a subclass of USPIOs that differ from other SPIOs in their monocrystallinity. Their small diameter, typically 2-9 nm, allows them to pass through capillary endothelium while retaining their superparamagnetism. The size also makes them a potential agent for receptor-directed

and magnetically labeled cell probe MRI. Initial studies used gadolinium chelates as receptor-directed agents, but very high agent concentrations were needed to obtain sufficient signal for imaging, making gadolinium chelates less viable for practical application. MIONs provide high magnetic susceptibility, two to three orders of magnitude greater than gadolinium, so that *in vivo* detection of the agent is feasible with MRI at concentrations as low as 1 µg Fe/g tissue [57, 58]. Targeted imaging with USPIOs has great potential to be a powerful tool for cellular and molecular MRI.

Table 1-3: Superparamagnetic iron oxide (SPIO) particles currently available [59, 60].

Agent	Particle Size	Surface Coating	Target Organs	Dose[a]	Mode of Administration	Classification	Generic Name	Trade Name	Developing Company	Status
OMP	3.5µm	polystyrene	GI lumen	0.5 g/L, 400-600mL	p.o.	Oral SPIO	Ferristene	Abdoscan	Amersham/GE	Approved
AMI-121	300nm	siloxane	GI lumen	52.5mg Fe (=0.94mmol Fe)	p.o.	Oral SPIO	Ferumoxsil	Lumirem	Guerbet	Approved
								Gastromark	Advanced Magnetics/AMAG Pharmaceuticals	Approved
AMI-25	80-150nm	dextran	liver/ spleen, perfusion[b], MRA[b]	15 µmol Fe/kg	slow infusion	SSPIO	Ferumoxide	Endorem	Guerbet	Approved
								Feridex IV	Advanced Magnetics/AMAG Pharmaceuticals	Approved
SHU 555A	62nm	carboxy-dextran	bolus injection	<60kg = 0.45mmol Fe, >60kg = 0.7mmol Fe	bolus injection	SSPIO	Ferrixan	Resovist	Bayer Schering Pharma	Phase 3 completed
AMI-277	20-40nm	dextran	lymph nodes, MRA[c]	14-45µmol Fe/kg	slow infusion	USPIO	Ferumoxtran	Sinerem	Guerbet	Phase 3
								Combidex[d]	Advanced Magnetics/AMAG Pharmaceuticals	Phase 3
NC100150	20nm	PEG	perfusion, MRA	7-100µmol Fe/kg	bolus injection	USPIO	Feruglose	Clariscan	Amersham/GE	Phase 3, discont.

[a] Doses may vary with imaging sequences and target organs
[b] Perfusion imaging and MRA not primary goals of SHU 555A
[c] MRA not primary goal of AMI-277
[d] Also tested as BMS 180549 and Code 7227

1.5 Biodistribution of and Imaging with SPIOs

SPIO agents are endocytosed and metabolized by RES cells and thereafter incorporated into the normal metabolic iron pool (Figure 1-8). Eventually they are

secreted as the body iron stores turn over. Smaller particles degrade faster into paramagnetic forms of iron. When injected at an appropriate rate, the toxicity of SPIO agents is low, and animal toxicity studies have disclosed no acute toxicity or chronic injury at doses >100 times the clinical effective dose [56]. The amount of iron oxide required for clinical MRI is small when compared with actual physiological iron stores [43, 46].

The diameter of superparamagnetic iron oxide particles (SPIOs) greatly affects their localization *in vivo*, even without targeting ligands on the surface. Larger particles

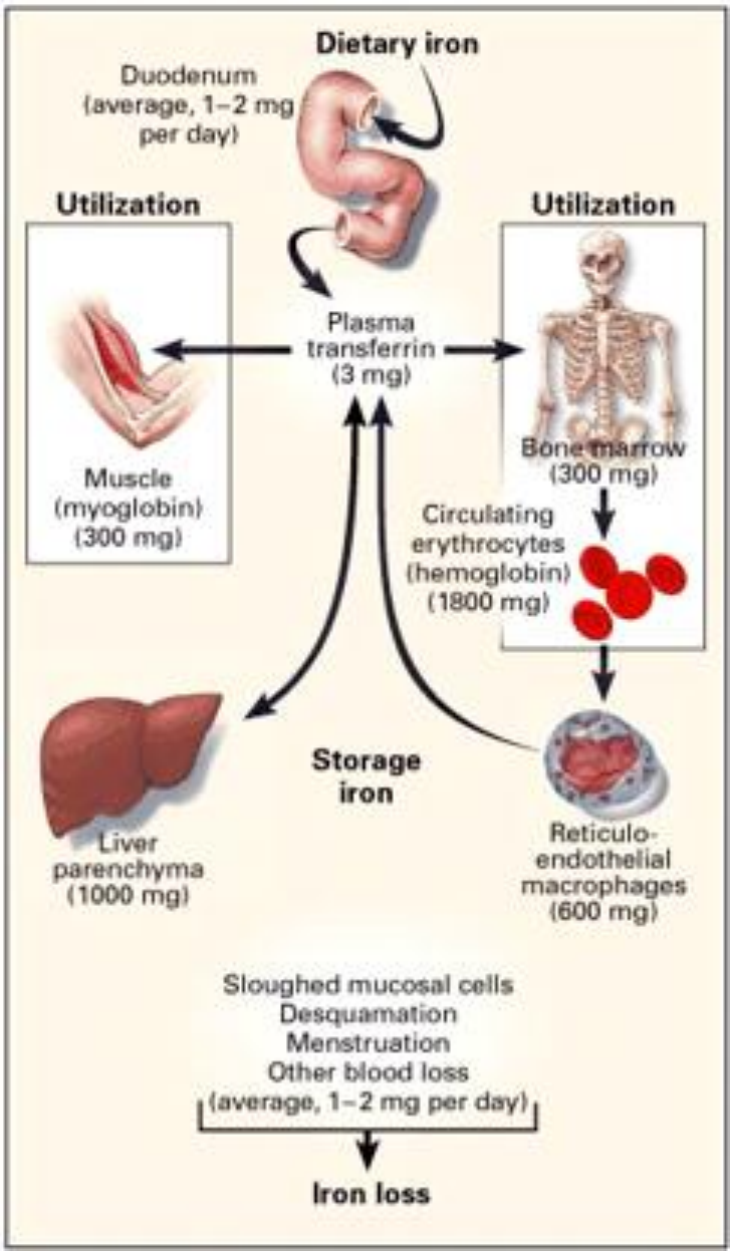

Figure 1-8: Normal iron storage and distribution [61]. Dietary iron is absorbed by duodenal enterocytes and circulates in plasma bound to transferrin. The majority is incorporated into hemoglobin in erythroid precursors and mature red cells, while 10-15% is present in muscle fibers (in myoglobin) and other tissues (in enzymes and cytochromes). Iron is stored in liver parenchymal cells and reticuloendothelial macrophages that provide most of the usable iron by degrading hemoglobin in senescent erythrocytes and reloading ferric iron onto transferrin for delivery to cells.

with diameters ranging from 300 nm to 3.5 μm that are coated with an insoluble layer are used to image the gastrointestinal tract [59]. Particles ranging in size from 60 to 150 nm rapidly appear in the liver and spleen [62]. Particles in the range of 10 to 40 nm, including USPIOs, are optimal for prolonged blood circulation, can cross capillary walls, and are often extensively taken up by lymph nodes and bone marrow [62].

Pharmacokinetic behavior of SPIOs is generally comparable in animals and humans [63, 32, 64, 65, 45]. Hepatic RES Kupffer cells account for 80% of the uptake of the injected dose of AMI-25 (Feridex) [63, 32, 64, 65, 45]. After intravenous injection, the agent has a blood half-life of 10 min and accumulates in the liver and spleen. The first clinical trials with SPIOs were for hepatic imaging [66, 67, 32, 65] where particle uptake by Kupffer cells in healthy liver tissue darkened the normal liver. The cancerous lesions appeared bright against the dark background as they did not take up the SPIOs. Similar studies followed where USPIOs were used to detect cancer metastasis in lymph nodes and bone marrow [53, 68-70]. USPIOs have also been successfully used to visualize inflammation in the brain after stroke (Figure 1-9) [71], surrounding atherosclerotic plaques [72-74], and from transplant rejection [75-78] when macrophages that have phagocytosed particles enter the regions. An application of SPIOs that has not yet reached the clinic is specific cell tracking where nonphagocytotic cells are loaded with particles *in vitro* using cell-permeable peptides [79-81] and transfection agents in combination with the negatively charged surface of magnetic nanoparticles [82-85]. Such a method has allowed the noninvasive tracking of stem cells [79], neural transplants [86], white blood cells [87], T-cells [88-90], and monocytes [91] in animal studies.

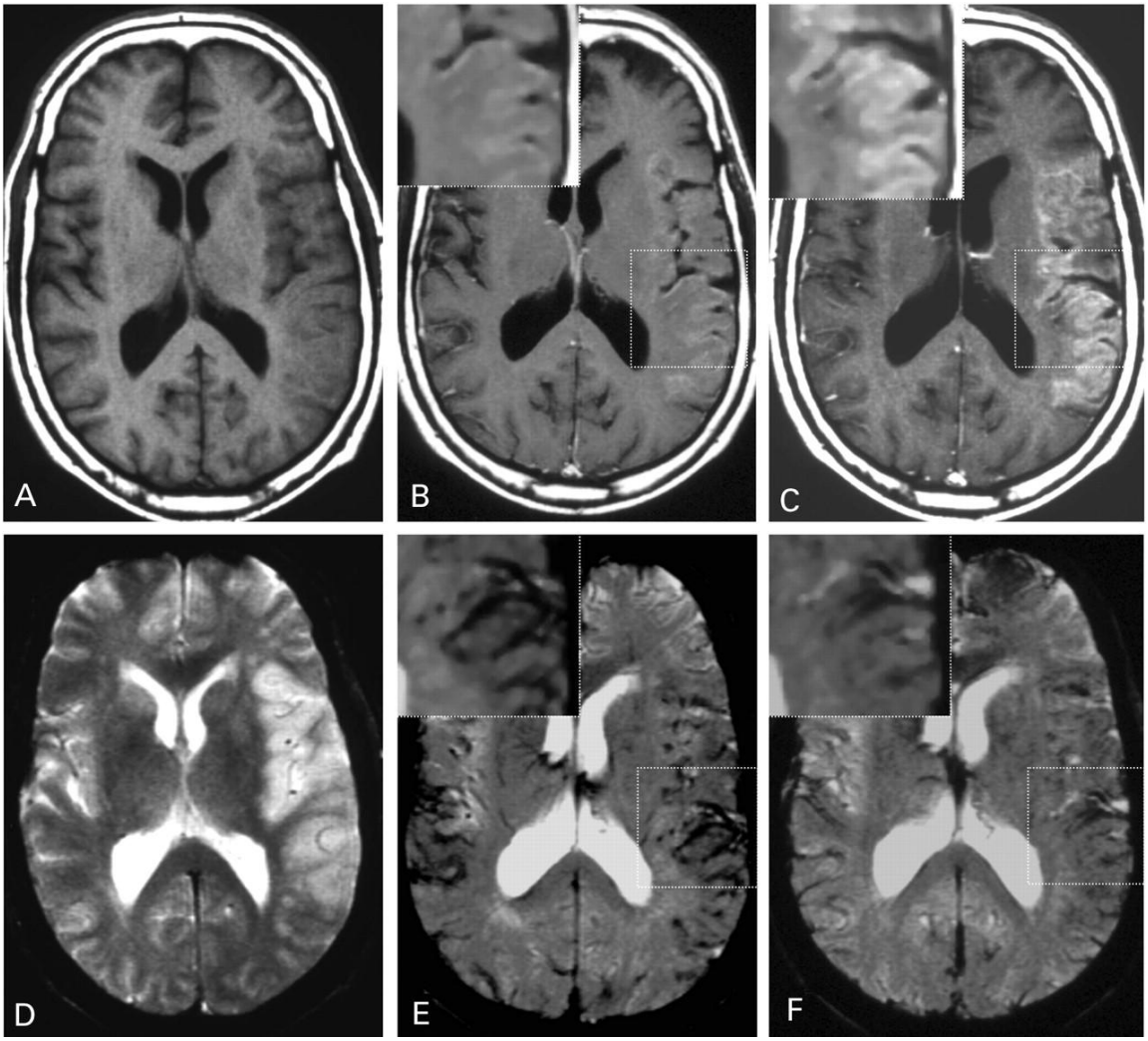

Figure 1-9: Images of a 54-year-old man with infarction of the left middle cerebral artery territory. T_1-weighted images (A) pre (B) 24 h post and (C) 48 h post USPIO infusion show increasing hyperintense signal enhancement in the periphery of the infarcted parenchyma. (D) Non-enhanced T_2*-weighted images 5 days after stroke display hyperintense demarcation of the infarcted area. T_2*-weighted images (E) 24 h and (F) 48 h after infusion show the appearance of the lesion as a hypointense region due to USPIO deposition. [71]

1.6 Fluorescence and Nuclear Imaging

As all technologies have their limitations, the concern with using MRI to image USPIOs is the concentration needed to achieve sufficient contrast [92] and the inability to

easily quantify the number of particles within the target. Furthermore, because of the structure and nature of MR instruments, it is not possible to use this type of scan real-time while performing a procedure. Other technologies such as optical and nuclear imaging have the advantage of sensitivity and ability to quantify, while also having the potential for real-time imaging.

1.6.1 Fluorescence Imaging

Optical imaging is based on the absorption and subsequent re-radiation of light by materials such as organic dyes. This physical phenomenon, known as either fluorescence or phosphorescence, was first described in 1852 by British scientist Sir George G. Stokes who observed that the mineral fluorspar emitted red light when it was illuminated by ultraviolet excitation. Although during the 19th century many minerals, resins, crystals, inorganic compounds, and even butter were found to fluoresce, it was not until the 1930's that fluorescent molecules were used in biological investigations to stain tissue components, bacteria, and other pathogens.

Fluorescence occurs when the molecular absorption of a photon causes electrons to assume an excited state. As they relax back to the ground state, another photon is emitted and fluorescence is observed. Some energy is lost to molecular vibrations or heat, and so the emitted photon will always have a longer wavelength than the one absorbed. This is also known as Stokes' Law or Stokes' shift. The greater the Stokes' shift value, the easier it is to separate excitation from emission light through the use of fluorescence filter combinations. Fluorescence emission is nearly simultaneous with the excitation light absorption and typically lasts less than a microsecond in duration.

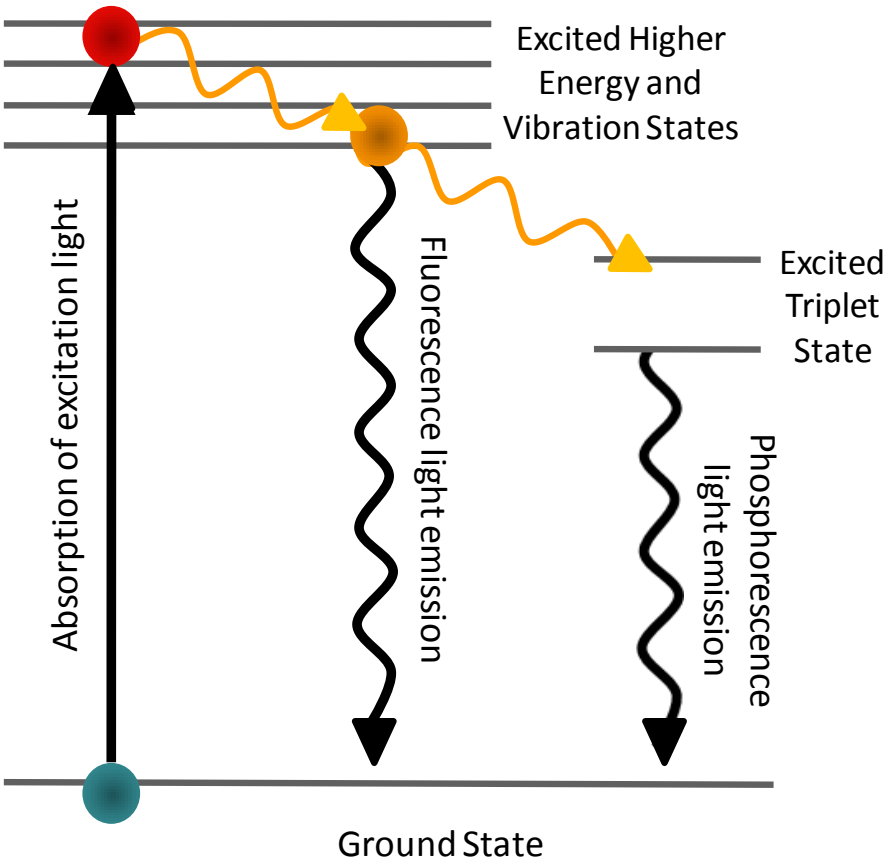

Figure 1-10: Jablonski Diagram: Light of the appropriate wavelength excites a fluorophore's electrons to jump from the ground state to a high energy vibration state. They decay first to the lowest excited state and then back to the ground state by either (1) rapid return and fluorescence emissions or (2) delayed return with phosphorescence. The emitted light wavelength will always be greater than the excitation wavelength because of some energy lost on the way.

Phosphorescence is when emission persists longer after the excitation light has been extinguished. (Figure 1-10)

In biomedical sciences the study of animal tissues and pathogens is often complicated with nonspecific autofluorescence, and so fluorophores or fluorochromes have been developed that are excited by specific wavelengths and emit light of defined wavelength. Quantum yield and extinction coefficients are used to characterize fluorophores. The extinction coefficient describes the efficiency of light absorption as a function of the molecular cross-section and the quantum yield denotes the ratio of the

number of quanta emitted compared to those absorbed. In order to achieve maximum fluorescence intensity, the fluorophore is excited at the peak wavelength of the excitation curve, and the widest possible range of emission wavelengths that include the emission peak are selected for detection.

A number of conditions can reduce fluorescence emission intensity, namely quenching and photobleaching phenomena. Photobleaching is irreversible decomposition of excited state fluorophores caused by interaction with oxygen before emission. It can be exploited in a technique known as fluorescence recovery after photobleaching (FRAP) where a sharply defined specimen region is photobleached by an intense burst of laser light and then monitored for rates and pattern of fluorescence recovery. A related technique known as fluorescence loss in photobleaching (FLIP) observes the decrease of fluorescence in regions lying adjacent to the photobleached area. Both FRAP and FLIP are useful for investigating the diffusion and motion of biological macromolecules in living cells. Quenching of fluorescence intensity occurs through non-radiative energy loss mechanisms, frequently by oxidizing agents, salts, heavy metals or halogen compounds. In some cases, quenching is caused by non-radiative energy transfer between a physically close acceptor molecule and the excited donor fluorophore, a phenomenon known as Förster or fluorescence resonance energy transfer (FRET).

Today, the range of optical microscopy extends from single molecules to whole body animal imaging. With multiple labeling, different probes can simultaneously identify several targets (Figure 1-11). The limitation of this technique is spatial resolution, particularly below the diffraction limit of specific specimen features and depth of penetration which is limited to a few millimeters in most cases. Light scattering by cells is the biggest restriction to spatial resolution.

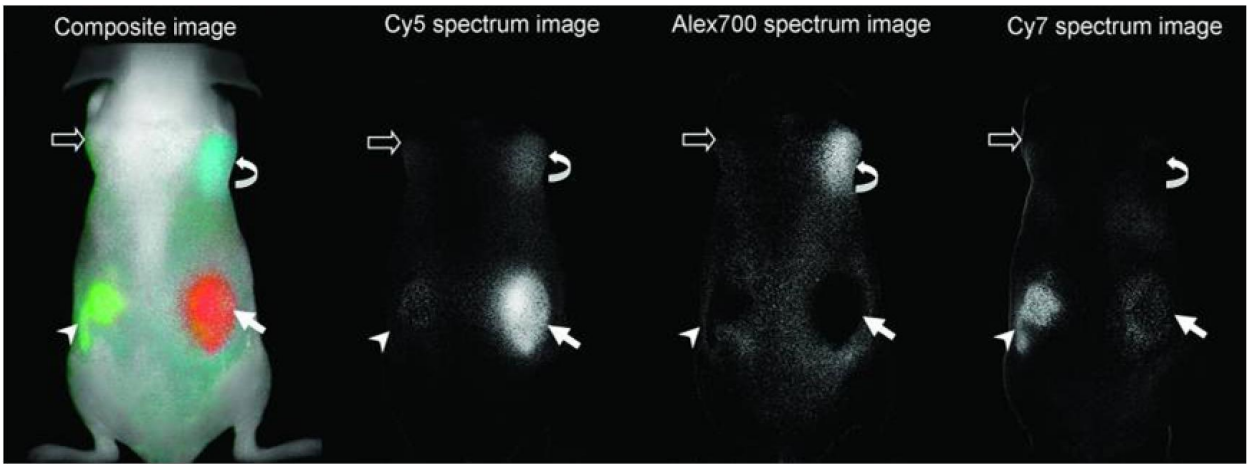

Figure 1-11: Multi-tumor unmixed *in vivo* spectral fluorescence imaging. The composite image (unmixing) allows differentiation of the tumors: red A431, green NIH3T3/HER2+, and blue SP2/Tac (negative control LS-174T). The arrows designate tumor placement: bold arrow=A431, arrowhead=NIH3T3/HER2+, curved arrow=SP2/Tac, and clear arrow=LS-174T tumors. Columns left to right demonstrate composite, Cy5 spectral, AlexaFluor700 spectral, and Cy7 spectral images, respectively. [93]

1.6.2 Nuclear Imaging

Nuclear medicine is based on procedures that utilize pharmaceuticals labeled with radionuclides. A radionuclide, or radioisotope, is an atom with an unstable nucleus that undergoes spontaneous disintegration of the nucleus into a slightly lighter nucleus, accompanied by emission of particles, electromagnetic radiation, or both. The rate at which atoms decay is measured by the half-life ($t_{½}$) of the isotope. As it undergoes radioactive decay, the radioisotope emits charged particles (α, β^-, β^+, Auger) and/or gamma (γ) rays and changes to a different isotope or element, or both. Imaging modalities that utilize radiotracers include γ-camera planar scintigraphy, single-photon emission computerized tomography (SPECT), and positron emission tomography (PET), with PET operating at 10-fold sensitivity superiority to SPECT. Nuclear imaging differs from most other imaging modalities in that it shows physiological function as opposed to

traditional anatomical structure. Some instruments can co-register γ with CT or MR images to highlight locations where the radioisotope has concentrated. Radioimmunoimaging has been traditionally developed in parallel with radioimmunotherapy for evaluating targeting and dosimetry. Monoclonal antibody-based tracers are being used to identify specific molecular targets and visualize tumors at primary and metastatic sites. Drug development is also being revolutionized by molecular imaging probes, especially in the field of oncology.

When selecting the radiotracer (Figure 1-12), inherent nuclear properties such as half-life, decay energy, and range must be considered. When preparing the injection dose, the half-life must be adequate for target accumulation and non-specific clearance. However, if the t½ is unnecessarily long, the emissions could require patient isolation. A radionuclide choice based on its energy is, for therapeutic purposes, a function of clinical parameters such as tumor location and size so that penetration and cumulative radiation dose delivered to the tumor are optimized. Choosing an appropriate radioisotope emission is equally important for imaging applications. For example, a high energy positron (β^+) emission with an isotope such as ^{66}Ga may produce PET images of relatively poor quality and resolution. Lower β^+ and γ energies are associated with higher PET and scintigraphic image quality, respectively. ^{111}In is a popular choice for scintigraphic imaging. Figure 1-13 is a representative image of scintiography with an ^{111}In-labeled antibody.

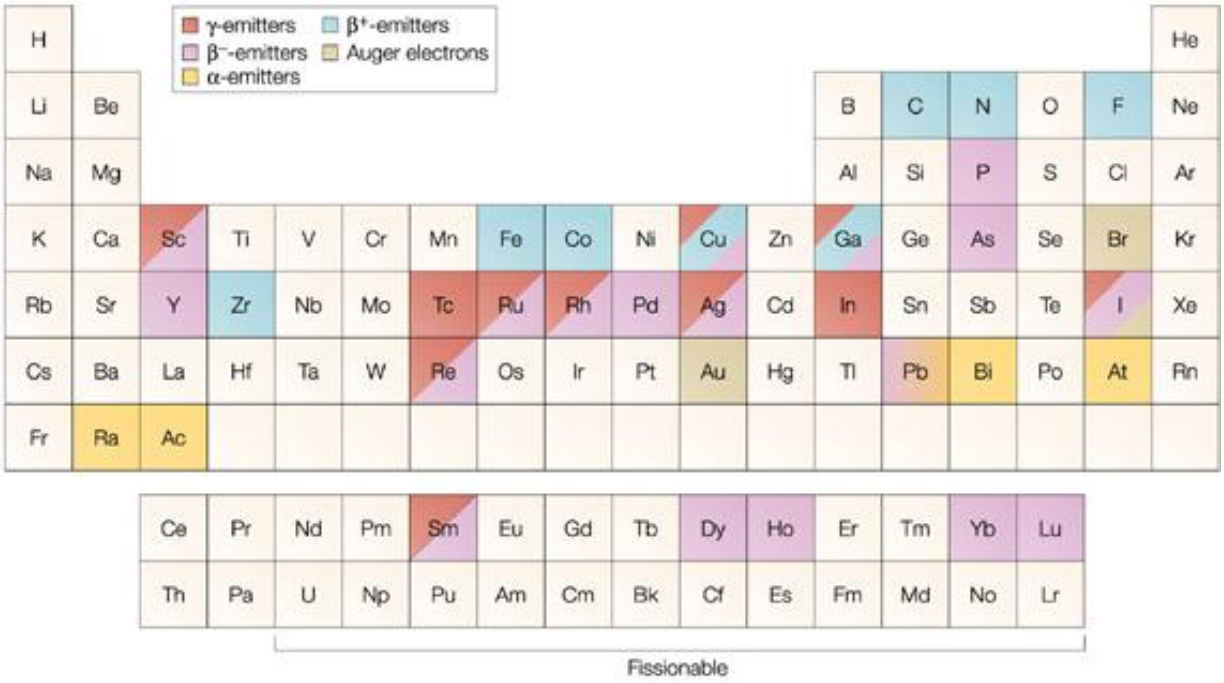

Table 2 | **Therapeutic radionuclides**

Radionuclide	Type	Half-life	E_{max} (MeV)	Mean range (mm)	Imageable
^{90}Y	β	2.7 d	2.3	2.76	No
^{131}I	β, γ	8.0 d	0.81	0.40	Yes
^{177}Lu	β, γ	6.7 d	0.50	0.28	Yes
^{153}Sm	β, γ	2.0 d	0.80	0.53	Yes
^{186}Re	β, γ	3.8 d	1.1	0.92	Yes
^{188}Re	β, γ	17.0 h	2.1	2.43	Yes
^{67}Cu	β, γ	2.6 d	0.57	0.6	Yes
^{225}Ac	α, β	10 d	5.83	0.04–0.1	Yes
^{213}Bi	α	45.7 min	5.87	0.04–0.1	Yes
^{212}Bi	α	1.0 h	6.09	0.04–0.1	Yes
^{211}At	α	7.2 h	5.87	0.04–0.1	Yes
^{212}Pb	β	10.6 h	0.57	0.6	Yes
^{125}I	Auger	60.1 d	0.35	0.001–0.02	Yes
^{123}I	Auger	13.2 h	0.16	0.001–0.02	No
^{67}Ga	Auger, β, γ	3.3 d	0.18	0.001–0.02	Yes
^{195m}Pt	Auger	4.0 d	0.13	0.001–0.02	No

Figure 1-12: Periodic chart and table highlighting therapeutic radionuclides [94].

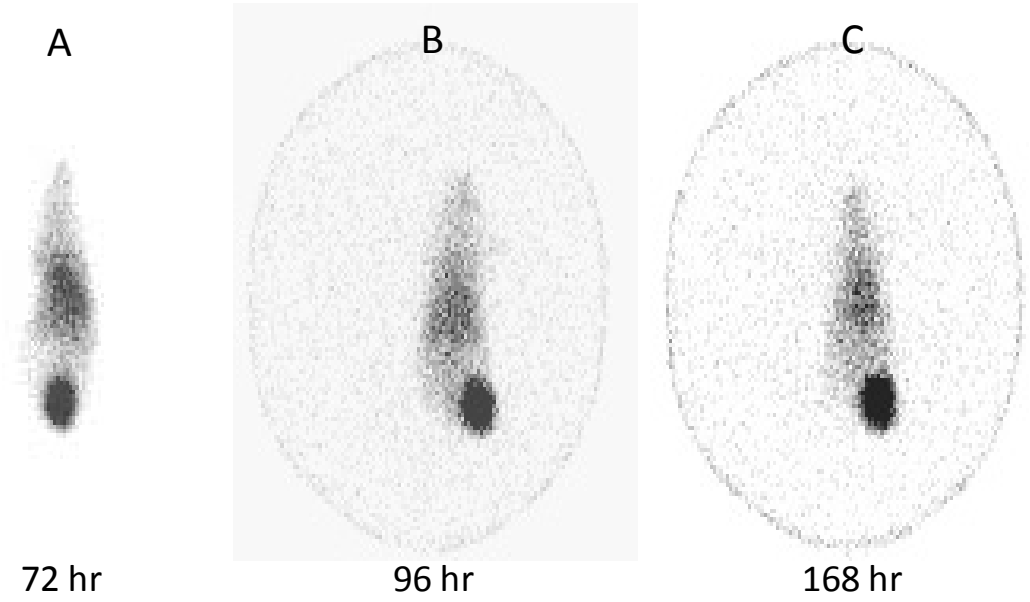

Figure 1-13: Scintigraphic imaging of athymic mice bearing subcutaneous human colon carcinoma xenografts (LS-174T) following a single intravenous administration of ^{111}In-CHX-A"-Herceptin. (courtesy of Martin Brechbiel)

The value in radionuclide imaging lies in its striking sensitivity. In contrast to other modalities, the quantity of naturally occurring background activity in biological organisms is very low. The largest amount of naturally occurring radioactive background is a few thousand Becquerels of potassium-40 and even less carbon-14 [95]. With radiotracers, the activity per unit mass is generally very large. For instance, 10^{-7} moles of freshly eluted ^{99m}Tc will contain approximately one Curie, or 370 Giga Becquerels (GBq) of activity. Most imaging studies administer doses of < 0.7 GBq [95]. In contrast, MRI requires concentrations of paramagnetic substances of about 10^{-6} molar to change relaxivity. Consequently, since radiotracers can be administered in concentrations that have no pharmacologic effect, they are useful to evaluate high affinity, low abundance systems.

1.7 Multi-Imaging with USPIOs

Optical imaging is highly sensitive, but with limited depth penetration, while nuclear imaging allows for quantification, but with limited resolution. Meanwhile, MRI can noninvasively provide exquisite resolution. Combining the three imaging techniques could provide a most effective diagnostic tool. An USPIO that is labeled by both a radioisotope and optical contrast agent would allow for sensitive high resolution imaging and quantification with the ability to verify that the particle has reached its target through three images. For *in vitro* studies, having a fluorescent agent would provide ease for use with typical analysis tools such as confocal microscopy and flow cytometry, whereas the magnetic properties would allow for ease of separation by use of a strong magnet. Nitin et al [96] have reported the development of micelle-encapsulated SPIOs attached to a fluorescent dye and have used the particle for *in vitro* studies (Figure 1-14).

An optical and MR imageable particle is useful for *in vitro* purposes, but attaching a radioisotope as a third mode of imaging would provide great advantages for quantification of the delivered construct and biodistribution studies *in vivo*. Furthermore,

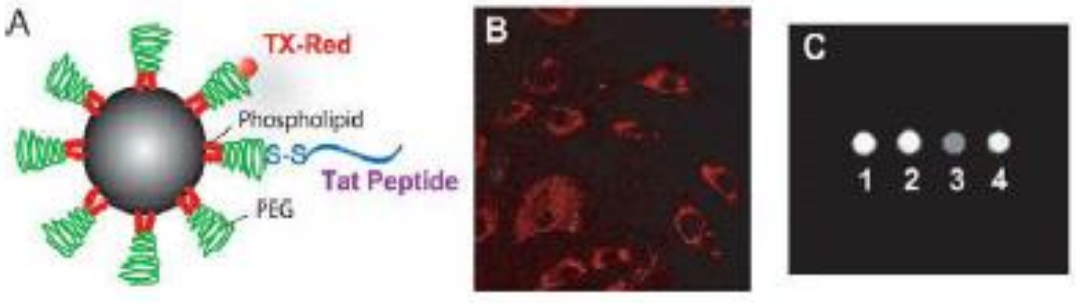

Figure 1-14: (A) Micelle-encapsulated SPIO conjugated with Tat peptide and the fluorescent label Texas Red (TX-Red). (B) Fluorescent images of Tat-linked, TX-Red labeled SPIOs in human dermal fibroblast cells. (C) MRI images of (1) culture media only, (2) cells without SPIOs, (3) cells with SPIOs, (4) culture media only. [96]

targeting these particles would create a noninvasive reporting tool used to monitor a variety of specific biological responses while providing valuable information regarding physiology and pathophysiology. There are a number of SPIO compounds already approved for use in the clinic and others are in clinical trials, but most nonspecifically localize by exploiting the body's natural uptake. Rarely are the particles attached to ligands to target delivery to specific locations. The great potential of superparamagnetic nanoparticles and their bioconjugates as sensitive and versatile probes for *in vivo* cellular and molecular imaging has only just begun to be exploited.

The work presented in the following chapters describes a novel silica-coated iron oxide particle (SCION) that has a near-infrared optical dye embedded within its silica shell and is also coupled to a radiolabeled antibody which functions as the targeting element. The resulting conjugate is capable of being imaged with MRI, optical instruments, and γ-scintigraphy.

Chapter 2

SCION Synthesis

Optimized for biomedical application, 9nm USPIOs have been coated with 2-5nm thin layers of silica embedded with the near infrared optical dye Cy5.5. This chapter describes the synthesis of these silica-coated iron oxide nanoparticles (SCION).

2.1 USPIO Synthesis

Precipitation-based methods, such as co-precipitation of metal salts [97, 98] or reverse micelle synthesis [99, 100] are most commonly used to synthesize SPIOs. Though reverse micelle synthesis can produce very uniform particles, they are soluble only in organic solvents. Therefore, for medical applications, co-precipitation is the more preferred route of synthesis. Developments in co-precipitation synthesis methods have given rise to the ability to produce bulk quantities (~40 g) of magnetic nanoparticles that are highly monodisperse with less than 5% size variation [101]. Herein, USPIOs were synthesized by co-precipitation of ferrous and ferric salts in aqueous solutions.

In 1950, LaMer proposed the mechanism of homogeneous precipitation presented in the LaMer diagram (Figure 2-15) [102]. As concentration increases to past saturation, a point is reached where nucleation occurs. Particle growth most likely transpires by a

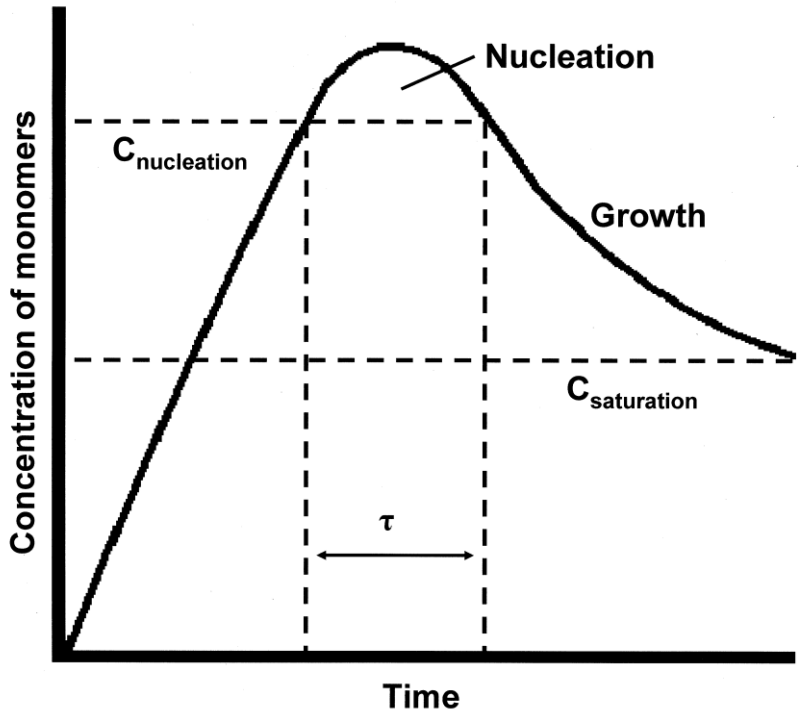

Figure 2-15: LaMer Diagram illustrating the time dependence of monomers to form monodisperse colloids.

combination of diffusion of atoms onto nuclei and irreversible aggregation of nuclei. In order to produce monodisperse particles, the rate of nucleation must be high and τ short, to generate a burst of nuclei. The rate of growth of the nuclei must be fast enough to reduce the concentration below the nucleation concentration to limit the number of particles created. The low surface energy of iron oxide increases the driving force for nucleation, and thus, a large number of nuclei are formed. Temperature, ionic strength, pH, and presence of other ions can be used to manipulate the size of particles produced [103].

Based on a method developed by Massart in 1981 [104], the co-precipitation of ferrous and ferric salts in alkaline and acidic aqueous phase was used to prepare colloids of Fe_3O_4 nanoparticles in the size range of 10-20 nm. With a stoichiometric ratio of

$2Fe^{3+}$:Fe^{2+}, 16 mmol (4.43 g) $FeCl_3 \cdot 6H_2O$ and 8 mmol (1.625 g) of $FeCl_2 \cdot 4H_2O$ were dissolved in 190 mL deionized (DI) water at room temperature by magnetic stirring in a beaker.

$$2Fe^{3+}(aq) + Fe^{2+}(aq) \xrightarrow{OH^-} Fe_3O_4(c) \tag{2}$$

Under conditions of vigorous stirring, 10 mL of 25% v/v NH_3 was poured down the vortex of the iron solution. Immediately, magnetite formed a black precipitate. After stirring for ten minutes, the particles were washed three times with water by magnetic separation. This washing procedure was executed by putting the solution in a strong magnet, such as an electron paramagnetic resonance magnet, allowing the particles to be pulled to the side by the magnetic field. The clear supernatant was then removed by a pipette. In order to stabilize the particles in solution, they were surface-complexed with citrate ions by means of the following process: first, the particle surface was converted from negative to positive by washing twice with 2M HNO_3. These acid washes not only reversed the zeta potential of the magnetite colloid and removed any remaining ammonium ions, but also caused the material to release Fe^{2+}, converting the magnetite to maghemite, with no reduction in particle size [105]:

$$(Fe_8^{3+})_{tet}(Fe_8^{3+}Fe_8^{2+})_{oct}O_{32} \xrightarrow{H^+} \frac{3}{4}(Fe_8^{3+})_{tet}(Fe^{3+}_{\frac{40}{3}}[\ ]_{\frac{8}{3}})_{oct}O_{32} + 8H_2O + 8Fe^{2+} \tag{3}$$

Leaching of Fe^{2+} was noted by the change in supernatant color to a rusty yellow. After the second wash, the particle solution was diluted to 100 mL with water. Samples at this point were evaluated for zeta potential, as will be presented in a later section. In one case, the particles were left in HNO_3 for five days to ensure complete conversion of magnetite to maghemite and then washed and evaluated for zeta potential. Typically, the protocol for stabilization with citrate was continued by raising the pH to 2.5 with NaOH. While

maintaining the pH at ~2.5 with perchloric acid, a volume of 5 mL of 0.5 M $Na_3[C_3H_5O(COO)_3]$ solution was added and the solution stirred for 1.5 hr. The particles were washed with DI water and diluted to 50 mL (~pH 6) for an estimated final concentration of 30 nmol/mL (calculations provided in Section 2.2). The final citrate-complexed USPIOs were quite stable at this pH because the unabsorbed carboxylate groups of the weakly acidic citrate are deprotonated (Figure 2-16) [106].

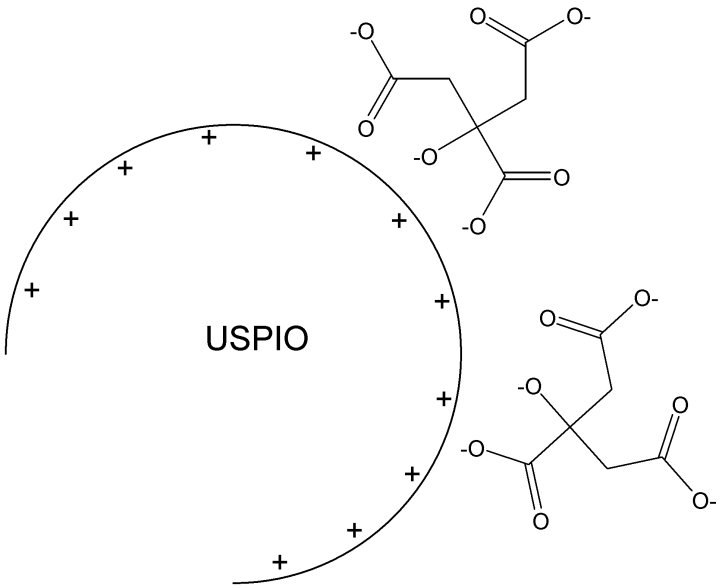

Figure 2-16: Citrate-complexed USPIO.

2.2 USPIO Concentration

Determining the concentration of USPIO prepared by this means was a challenge. Two methods for calculation were generated, both dependent on particle size. To measure particle diameter, the USPIO samples were drop-cast on carbon grids and analyzed with transmission electron microscopy (TEM). Electron microscopy detects the presence of electron-dense material based on the ability of atoms to scatter a beam of electrons [107]. Iron oxide is readily visualized by TEM and size can be measured at known magnifications. However, the technique may potentially underestimate particle size because the edges of these crystals are difficult to define accurately as the boundaries

are thinner than the centers. Densely-packed opaque areas can also hamper analysis by obscuring individual particles. Images, such as Figure 2-17, were collected with a JEOL4000EX microscope, which has a point resolution of 0.16nm and an information limit of below 0.12nm. A particle's diameter was determined as the mean of three cross-sectional measurements evaluated using Gatan DigitalMicrograph 3.6.1 software with images taken at a magnifications of 400000X or 500000X. With the assumption that the particles are spherical, USPIO diameter had a lognormal distribution, as is typical with

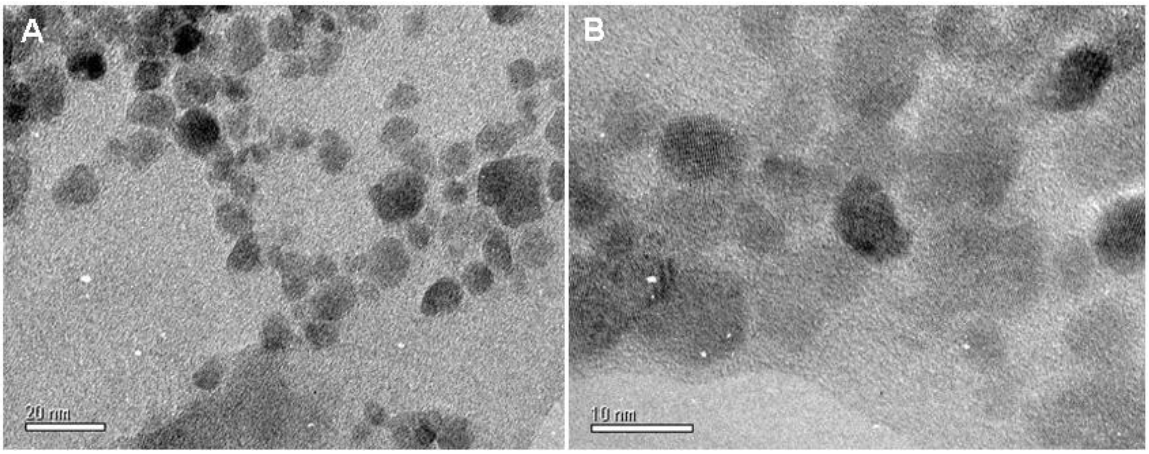

Figure 2-17: TEM using a JEOL 4000EX of synthesized USPIOs. The grayish visible background is from the carbon support film on the electron microscope grid.

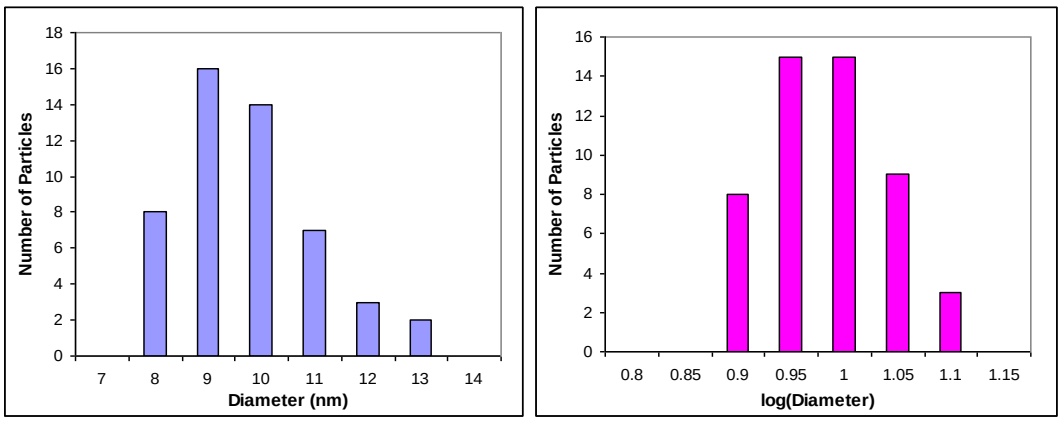

Figure 2-18: Lognormal USPIO diameter distribution (n=50, $\bar{x}$=0.96, s=0.056, $\bar{x}_{geo}$=9.2 nm, s_{geo}=1.1nm) taken from manual measurement of particles from TEM images. Each particle's diameter was determined by the mean of three measurements.

such crystals [108] The geometric mean diameter was 9.2 nm (Figure 2-18). This analysis does have some limitations to be noted. While the image analysis software did allow diameter measurements with a sensitivity of 0.001nm, images from two magnifications were analyzed, as well as the fact that the microscope itself has a lower resolution limit. Thus, all diameters were only recorded at a significance of 0.1nm. However, in all samples, the particles were in the superparamagnetic size range.

To calculate the theoretical estimated concentration of USPIO in final solution, the assumptions made were the complete precipitation of iron chloride, no losses during washing, the particle is composed of only magnetite, and that the particles are spherical.

$$MW_{Fe_3O_4} = 231.54 \frac{g}{mol}$$

$$MW_{FeCl_2.4H_2O} = 198.81 \frac{g}{mol}$$

$$d_{Fe_3O_4} = 5.15 \frac{g}{cm^3}$$

$$r_{USPIO} = 4.6nm$$

$$V_{USPIO} = \frac{4}{3}\pi r_{USPIO}^3 = 407.7nm^3 = 4.077e^{-19}cm^3$$

$$\frac{1.625g\ \ FeCl_2.4H_2O}{MW_{FeCl_2.4H_2O}}\left(\frac{1mol\ \ Fe_3O_4}{1mol\ \ FeCl_2}\right)MW_{Fe_3O_4} = 1.89g\ \ Fe_3O_4$$

$$\frac{\left(1.89g\ \ Fe_3O_4\right)}{V_{USPIO}d_{Fe_3O_4}} = 9.01e^{17}\ \ molecules\ \ USPIO$$

$$\frac{9.01e^{17}\ \ molecules\ \ USPIO}{6.022e^{23}\ molecules/mol}\left(\frac{10^9\ nmol}{mol}\right) \approx 1500\ \ nmol\ \ USPIO$$

$$\frac{1500nmol\ \ USPIO}{50mL} = 30\ nmol/ml\ \ \ USPIO$$

Based on these theoretical calculations, 1500 nmol USPIO were produced per batch. In the final volume of 50 mL H_2O, the concentration of USPIO would be 30 nmol/mL. While these calculations were initially good for estimating approximate concentrations, the assumptions of complete reaction and no losses were not ideal. For later synthesis steps of the full particle, assuming no loss or even a constant amount of 10% loss, would allow for estimations, but not precise concentration. To establish a standard procedure for determination of particle concentration, iron concentration was analyzed. Samples were sent to Desert Analytics (Tucson, Arizona) for iron content analysis. Using the percent mass value of iron and the assumptions that solution density is equal to that of water and the particle iron core is composed of only magnetite, particle concentration could always be calculated by the following method:

$$MW_{Fe_3O_4} = 231.54 \frac{g}{mol}$$

$$d_{Fe_3O_4} = 5.15 \frac{g}{cm^3}$$

$$V_{USPIO} = 4.077e^{-19}\ cm^3/USPIO$$

$$\frac{4.077e^{-19}cm^3}{USPIO}\left(\frac{5.15\ g/cm^3\ Fe_3O_4}{231.54\ g/mol\ Fe_3O_4}\right)\left(\frac{3mol\ Fe}{mol\ Fe_3O_4}\right)\left(\frac{6.022e^{23}USPIO}{mol\ USPIO}\right) = 16400\frac{mol\ Fe}{mol\ USPIO}$$

$$x\%\ Mass\ Fe = \frac{x\ gFe}{100g}$$

$$\frac{x\ gFe}{100g}\left(\frac{1g}{mL}\right)\left(\frac{1000mL}{L}\right)\left(\frac{1000mmol}{mol}\right)\left(\frac{mol\ Fe}{55.85g}\right) = y\ mM\ Fe$$

$$\text{Concentrat ion of USPIO (mM)} = y\ mM\ Fe\left(\frac{mol\ USPIO}{16400mol\ Fe}\right)$$

$$\text{Concentrat ion of USPIO} = \text{Concentrat ion of SCION}$$

Thus, this method of iron content analysis became the standard for evaluation of concentration of SCION for any sample.

2.3 Silica Deposition

A key issue for the application of these particles *in vivo* is the functionalization of the magnetic cores to biomolecules while maintaining a small diameter to prevent clearance. The immobilization of an oxide such as silica on the iron oxide core would allow for tailoring of the particles by straight forward linkage of functional groups. The surface of silica is coated with silanol groups that easily react with alcohols and silane coupling agents [109] to produce dispersions that are stable in non-aqueous solvents and are also ideal for strong covalent bonding with ligands. The silica shell would also play a role in maintaining stability for particle suspensions during changes in pH or electrolyte concentration, due to those same silanol groups making the surface lyophilic [110]. Silica is well known for its optical transparency [111], a useful property when contemplating optical imaging applications, and the advantage it offers for this application is its associated tunable layer thickness.

The Stöber method, developed by Stöber, Fink, and Bohn in 1968 [112], was used to coat these USPIOs with silica. This mechanism involves hydrolysis of an alkoxy silane and condensation of alcohol and water [113]:

$$\equiv Si-OR + H_2O \quad \leftrightarrow \quad \equiv Si-OH + ROH \tag{4}$$

$$\equiv Si-OR + \equiv Si-OH \quad \leftrightarrow \quad \equiv Si-O-Si\equiv + ROH \tag{5}$$

$$\equiv Si-OH + \equiv Si-OH \quad \leftrightarrow \quad \equiv Si-O-Si\equiv + H_2O \tag{6}$$

By using catalysts such as ammonia and carefully controlling reagent ratios, reaction volume, pH, and reaction time, particle synthesis can be controlled ranging from formation of large silica spheres embedded with a number of USPIOs down to single USPIOs coated with very thin layers of silica (Figure 2-19). With observation under TEM, a protocol was optimized for 2 to 3.5 nm thick coatings around single USPIOs. In a typical synthesis, 30 nmol USPIO were sonicated in 2.5 mL DI water for 10 minutes to ensure even distribution and prevent aggregation. A volume of 250 μL tetraethylorthosilicate (TEOS) was injected into 2.25 mL of ethanol and this solution was added to the USPIO solution. To catalyze the reaction, 100 μL of triethylamine

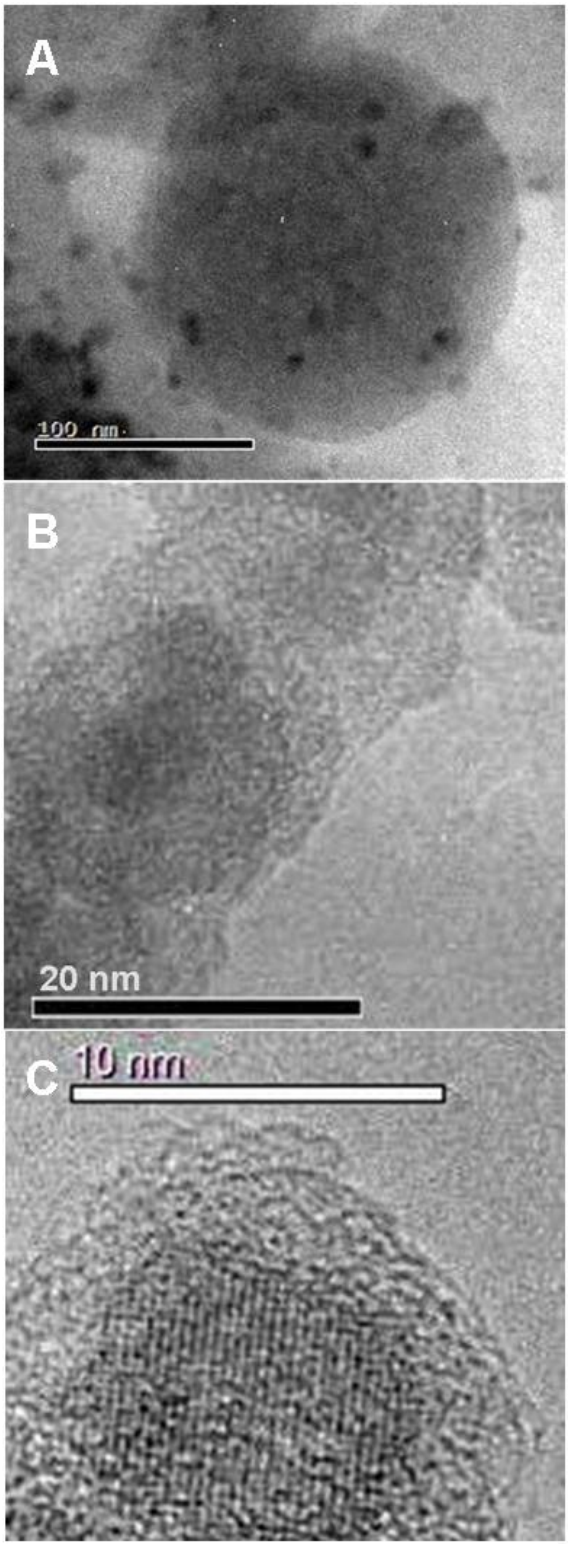

Figure 2-19: TEM using a JEOL 4000EX of synthesized (A) ~175 nm silica beads embedded with USPIOs, (B) USPIOs coated with ~10 nm-thick shells of silica, and (C) USPIOs coated with ~2.5 nm-thick shells of silica.

(TEA) were added. The reaction was run under sonication for 15 min and then washed by magnetic separation with DI water. This procedure is reproducible and can be reasonably scaled as long as solvent and reagent ratios are kept constant.

2.4 Optical Dye Conjugation

Optical fluorescence imaging has been a tool used to monitor specific targets *in vitro* and is becoming increasingly more useful for *in vivo* applications [114-117]. Fluorochromes with emissions below 700 nm only allow for superficial assessment of tissue features because tissue absorption results in small penetration depths of only a few millimeters [118]. The light absorption is due to oxy- and deoxyhemoglobin, melanin, lipid, and other compounds found in living tissue and food [119]. Because the absorption coefficient of tissue is considerably smaller in the near-infrared (NIR) region from 700 to 900 nm, light can penetrate more deeply into tissue to depths of several centimeters (Figure 2-20) [120, 121]. The intrinsic biomolecules of tissue also autofluorescence throughout the visible light spectrum, 350-700 nm, competing with detection of fluorophore emissions in the same wavelength range [122, 123]. Thus, NIR fluorophores provide higher contrast to natural background fluorescence during *in vivo* imaging of small animals. NIR detection is readily accomplished with solid-state optical components, such as diode lasers and CCD detectors.

The NIR fluorophore Cy5.5 was chosen to conjugate to the particles. Commercially available from GE Healthcare, Cy5.5 is a dye evolved from a dye class called cyanines and has excitation and emission peaks at 675 nm and 694 nm,

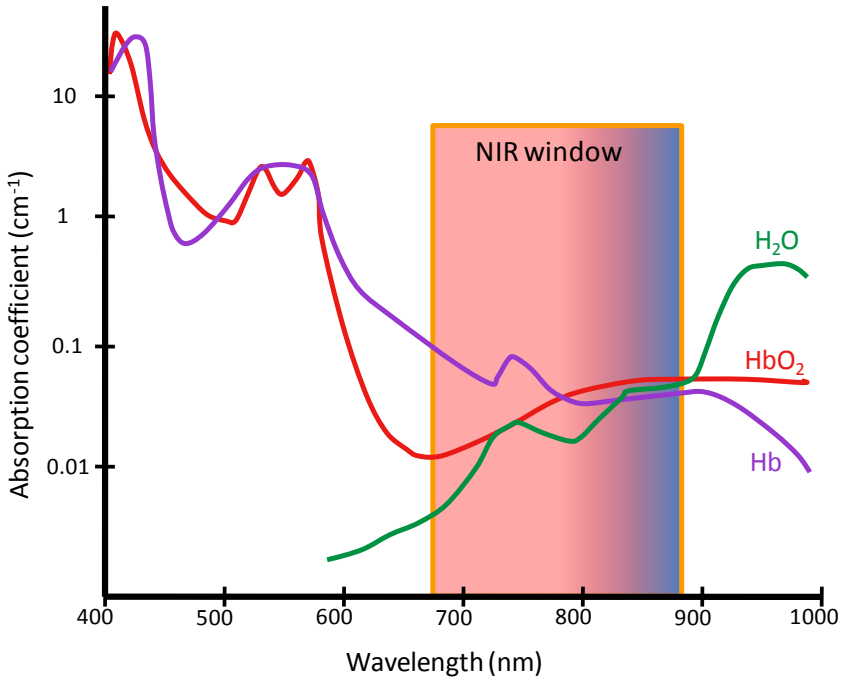

Figure 2-20: Fluorochromes in the NIR window fall in the wavelengths with minimal light absorption by hemoglobin (<650 nm) and water (>900 nm) and thus are good candidates for in vivo imaging of small animals.

respectively. It is a highly sensitive and bright dye with high extinction coefficient and superior photostability compared to more commonly used dyes, such as fluorescein, allowing more time for image detection. Cy5.5 is a good candidate for physiological use because it is stable in the pH range of 3 to 9, soluble in aqueous and organic

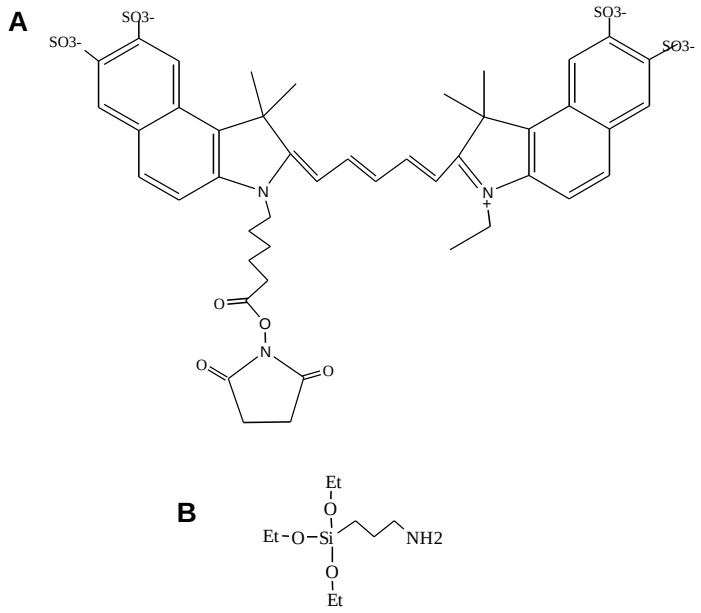

Figure 2-21: Chemical structures of (A) Cy5.5 and (B) APTES.

solvents, and has low non-specific binding. The dye as purchased has an *N*-hydroxysuccinimide (NHS) ester group for reacting with amine groups (Figure 2-21). Thus, the linker 3-aminopropyltriethoxysilane

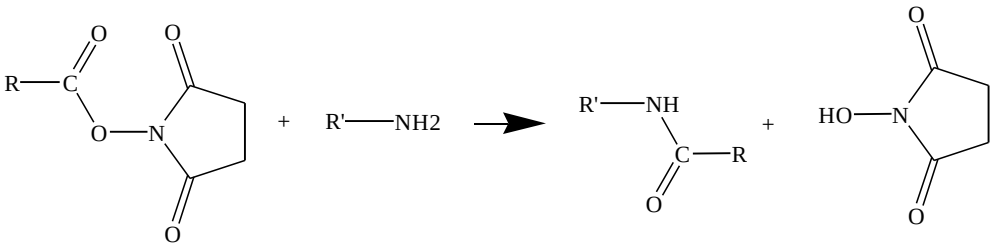

Figure 2-22: Amide bond formation by reaction of NHS ester to amine group.

(APTES) was chosen to conjugate Cy5.5 to particle. The free amine of APTES reacts with the active NHS ester of Cy5.5 (Figure 2-22), while the three alkoxy silane groups follow the previously described Stöber mechanism to attach to the particle surface.

2.4.1 Direct Conjugation to USPIO vs. to Silica Buffer Layer

Initially, Cy5.5 was conjugated directly to the surface of USPIO. While being agitated, 60 nmol of USPIO dissolved in 24 mL ethanol were reacted with 4 mL APTES and 100 μL of TEA as a catalyst. The reaction was run overnight and then washed by magnetic separation three times with ethanol and twice with *N*-dimethylformamide (DMF). The solvent was not changed to water because the Cy5.5 NHS ester would be hydrolyzed before reacting with the amines. A titration study was executed by varying the amounts of Cy5.5 added to samples in the presence of catalytic TEA, allowed to react overnight, and washed into water. The samples were placed in a fluorescence spectrophotometer and studied with an excitation wavelength of 675 nm. Though the

color of the particles to the naked eye had visibly changed with conjugation of the dye, in each case no fluorescence activity was found (Figure 2-23).

It was hypothesized that the USPIO core may be absorbing dye fluorescence. Iron oxide nanocrystals have been shown to possess a broad absorption spectrum from 400 to 600 nm [124]. To test whether Cy5.5 emissions were also being absorbed, USPIOs were first coated with silica and then conjugated to Cy5.5 using the previously described methods. This time, the particles did fluoresce at the expected wavelength (Figure 2-23). Therefore, the thin silica layer provided a "buffer layer" to protect the dye activity. The Cy5.5-silica-USPIO particles were then coated with a final layer of silica to encapsulate the dye and make the outer surface of the particles biocompatible. The same silication protocol as described previously was used with a shortened reaction time.

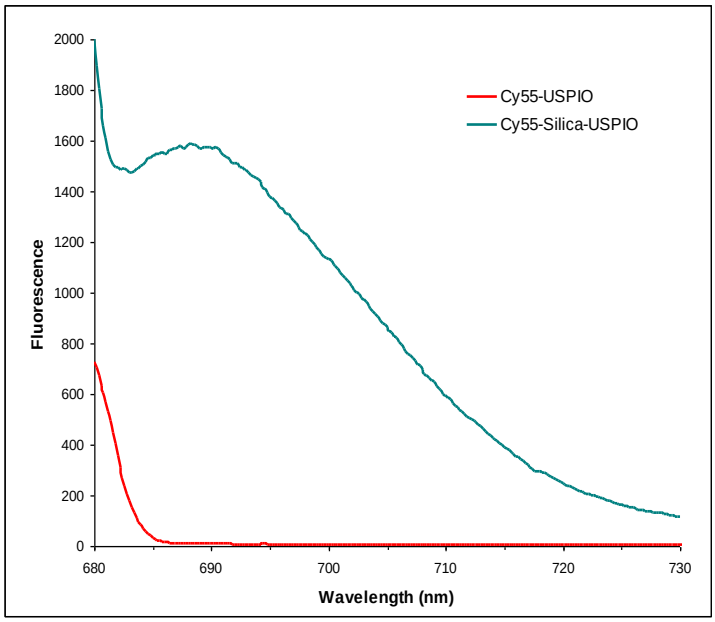

Figure 2-23: Emissions spectrum of Cy5.5 conjugated either directly to USPIO or to silica-coated USPIO.

2.4.2 APTES-Cy5.5 Conjugate

Using these particles, a number of studies were conducted, but observations in the lab and with the fluorescence spectrophotometer later led to the conclusion that the dye was being deactivated. When just the nanoparticle solution itself was placed in the

Maestro optical imaging system (CRi, Inc., Woburn, MA) that would be used for studies with mice, the particles were not found to be bright enough to provide sufficient contrast *in vivo*. Potential reasons for this result could be that: 1) not enough dye was attaching to the particles because it was not reacting to APTES, 2) the concentration of dye per particle was too high leading to self-quenching, or 3) a step in the protocol was changing the structure of the dye and deactivating it. To test the first possibility, APTES and Cy5.5 were reacted in methanol for four hours in room temperature at molar ratios of 1.3:1, 10:1, and 1000:1. For the two latter ratios, the dye solution formed a precipitate and changed from its typical dark blue color to a teal, an indication that the dye was deactivated. The 1.3 APTES:Cy5.5 solution remained the healthy blue color. APTES intrinsically is a base and high concentrations, i.e. high pH, could destabilize Cy5.5. During nanoparticle synthesis, the strategy had been to overpopulate the particle surface with amines from the APTES so that the dye was the limiting agent. Given these results, however, the basic nature of the particle surface may be deactivating the dye. To obviate this condition, instead of functionalizing particles with APTES and then adding Cy5.5, APTES was first attached to Cy5.5. Then, the APTES-Cy5.5 product could react with the silica surface of particles. The final re-silication procedure after dye attachment remained the same.

Thin layer chromatography (TLC), a technique for separating organic compounds, was used to confirm conjugation in the APTES-Cy5.5 sample. A silica plate was spotted with the appropriate samples and the bottom edge was placed in a reservoir of 20% v/v methanol in chloroform. The solvent moved up the plate by capillary action. When the solvent front reached the other edge of the plate, the plate with sample was removed from the reservoir. The separated spots were visualized with ultraviolet light and by placing

the plate in iodine vapor. The different components in the mixture moved up the plate at different rates due to differences in their interaction with the mobile liquid phase and the stationary phase. The components, visible as separated spots, were identified by comparing the distances they traveled with those of the known reference materials.

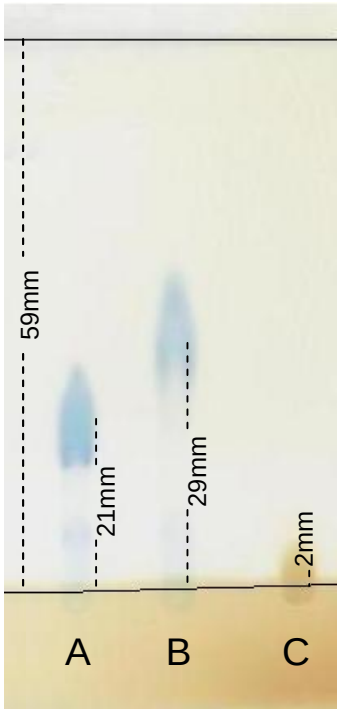

Figure 2-24: Thin layer chromatography of (A) Cy5.5, (B) APTES-Cy5.5 conjugate, and (C) APTES.

Quantitative analysis is done by comparing retardation factors, R_f:

$$R_f = \frac{d_{sample}}{d_{solvent}} \tag{7}$$

where *d* is the distance from the start line to the center of the spot.

As seen in Figure 2-24, the less-polar conjugate moved off the polar silica plate earlier and traveled significantly farther than the more polar Cy5.5 (-NHS ester). R_f values of Cy5.5, APTES-Cy5.5, and APTES were 0.36, 0.49, and 0.03, respectively. The conjugate moved 38% farther than Cy5.5, confirming conjugation.

2.4.3 Quantification of Cy5.5 per SCION

While it is always possible to know the molar equivalence of dye being reacted to particle, precisely quantifying the amount that attached is a true challenge. Typically, dye content is analyzed by fluorescence which is characterized by quantum yield. Fluorescence quantum yield (Φ) is the ratio of photons absorbed to photons emitted

through fluorescence. It represents the probability of the excited state deactivating by fluorescence rather than by other mechanisms such as heat or molecular vibration.

The standard method for measuring quantum yield is a method that compares the test sample to well characterized standard samples with known Φ values [125]. This technique assumes that solutions of the standard and test samples have identical absorbance at the same excitation wavelength. The ratio of two samples' integrated fluorescence intensities recorded under identical conditions will yield the ratio of the quantum yield values. The data is acquired at a number of different absorbances or concentrations and the solvent refractive indices are taken into account within the ratio calculation. Quantum yield is calculated by:

$$\Phi_X = \Phi_{STD}\left(\frac{Grad_X}{Grad_{STD}}\right)\left(\frac{\eta_X^2}{\eta_{STD}^2}\right) \tag{8}$$

where the subscripts STD and X denote standard and test samples respectively, *Grad* is the gradient or slope from the plot of integrated fluorescence intensity versus absorbance, and η is the solvent refractive index.

Taking these measurements, however, is very challenging and difficult for a number of reasons. Concentration effects may result in some self-quenching. The assumption must be made that the solvents of the two samples behave similarly and the standard sample and its Φ value are valid. In the case of SCION particles, neither of these assumptions is reasonable. The ideal standard to use in this case would be Cy5.5 in solution. However, Cy5.5 has a low quantum yield of 0.23 [126] and is not considered a good standard. Regardless of the standard chosen, the solvent properties of the two samples would not be compatible. As mentioned previously, iron oxide particles have an

absorbance spectrum [124] that would greatly alter the already complex measurements. Also, accounting for the refractive index of the particles is difficult.

Given these complications, a different method was used to try to estimate the number of Cy5.5 per particle. Initially, the particles were analyzed directly under a Maestro CRi spectroscopic optical camera. To generate the brightest particle possible, an array of different reacted ratios of Cy5.5:SCION were synthesized and a volume of 10 µL of each final solution was placed under the optical camera. Total fluorescence intensities of the droplets were compared as shown in Figure 2-25. The relationship was linear with a strong correlation coefficient (R=0.995) indicating that in the Cy5.5:SCION reaction range of 1:1 to 20:1, there was no self-quenching effect by overpopulating the particle surface with dye. One might hypothesize that, the silica provides a buffer between the dye molecules as well as from the USPIO core. Reaction equivalence higher than 20 Cy5.5 per SCION may yield an even brighter particle. However, as a practical matter, since the dye is expensive, higher ratios were not evaluated and all SCION syntheses from this point forward were made with a standard reaction equivalence of 20 Cy5.5 per

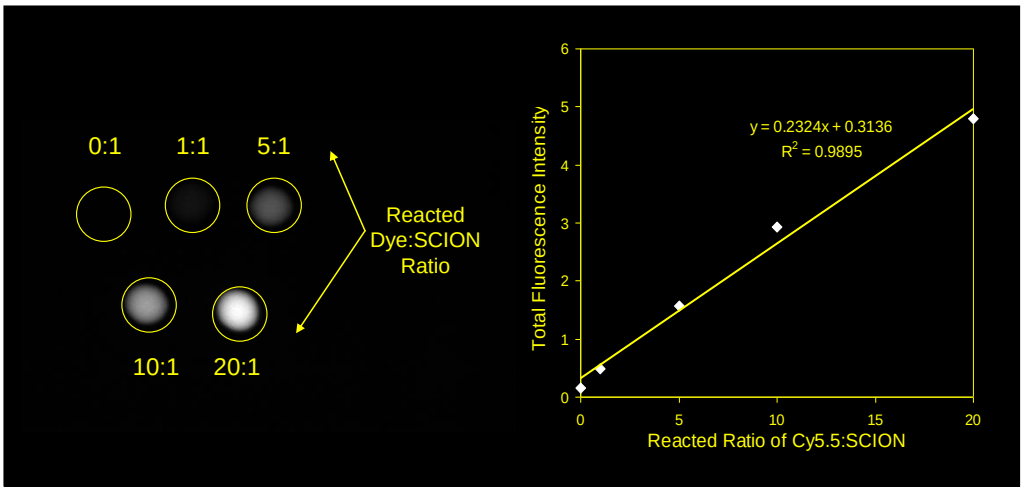

Figure 2-25: Fluorescence in Maestro optical camera of particles made with 0 to 20X reactions with Cy5.5.

SCION. These particles demonstrated strong fluorescence at even low exposure time of 30 ms, indicating that they were bright enough for *in vivo* imaging.

A significant amount of dye is seen in the wash solvent, indicating that not all the APTES-Cy5.5 incorporated into the particle. Because quantum yield measurements are not reliable, a different method was attempted to determine the number of Cy5.5 that attached per SCION particle. Two samples from SCION synthesis were collected (before final silication and final SCION particle) and sent to Desert Analytics for elemental analysis of iron and sulfur content. Given that each dye molecule has 4 sulfurs and assuming that the solution density is equal to water where silica, Cy5.5, etc. are insignificant, calculations were made to determine the number of Cy5.5 per SCION particle:

Table 2-4: Elemental analysis of intermediate and final SCION particles to determine number of Cy5.5 dye molecules per particle.

		g/mol	%Mass	Mean %Mass	mM X	X:Fe	nmol SCION/mL	*Cy5.5/ particle
Cy5.5-Si-USPIO	Fe	55.85	0.399 0.402	0.401	71.71	1.00	4.37	
	S	32.07	0.081 0.083	0.082	25.57	0.357		1460
final SCION particle	Fe	55.85	0.307 0.295	0.301	53.89	1.00	3.29	
	**S	32.07	0.001 0.001	0.001	0.31	5.79E-03		23.7

$$* \ \mathrm{Cy5.5\,per\,SCION} = \frac{molS}{molFe}\left(\frac{16400 molFe}{molSCION}\right)\left(\frac{molCy5.5}{4molS}\right)$$

**below detection limit <0.005

However, as was noted by the received data report, the sulfur content fell below reliable detection limits, and so again these results cannot be relied upon by themselves for characterization. For the sample before the final silication, the sulfur content did not

fall below detection limits, but the calculated ratio of Cy5.5 per SCION exceeds the reacted ratio of 20 Cy5.5 per SCION so it is simply an invalid method for characterization. However, because the particle is bright enough to be visible in the luminescence spectrophotometer, flow cytometry, and the Maestro *in vivo* imaging system, work was continued. It is in fact typical for laboratories to work with dyes conjugated to various ligands without always quantifying how many are attached in the final or intermediate products.

2.5 Silica Layer Thickness

As described in Section 2.4, after APTES-Cy5.5 conjugation to silica-coated USPIOs, an additional layer of silica was applied to encapsulate the dye and complete the

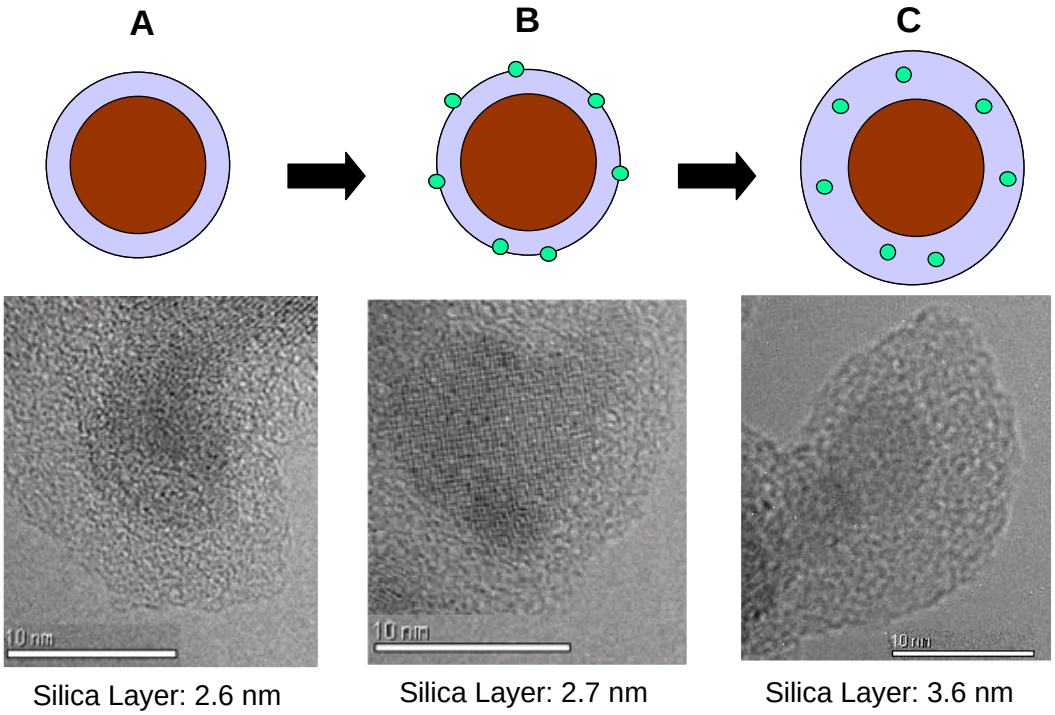

Figure 2-26: TEM characterization of mean silica layer thickness during each step of functionalization: (A) initial silication (stdev=0.56nm), (B) conjugation to Cy5.5 (stdev=0.35nm), and (C) final encapsulation with silica (stdev=0.47nm).

SCION particle. Samples from each point during nanoparticle synthesis were observed using TEM, confirming that the Cy5.5 conjugation process did not degrade the silica layer (Figure 2-26). The p-value of a one-tail t-test comparing silica thickness pre- and post-dye conjugation (steps A and B) was statistically insignificant with a p-value of 0.289. The same t-test comparing final particle silica layer thickness (C) to synthesis steps A and B was significant at p=3.27e-6 and p=5.88e-7, respectively.

The layer thickness was also evaluated using elemental analysis of Si content, similar to how USPIO concentration is calculated. Assumptions were made that solution density is equal to water and silica was deposited evenly to form spherical particles.

Table 2-5: Silica layer thickness calculations based on elemental analysis.

		g/mol	%Mass	Mean %Mass	mM X	X:Fe	nmol SCION/mL	Volume SiO_2 (nm^3/SCION)	Particle Diameter (nm)	SiO_2 Layer Thickness (nm)
Si-USPIO	Fe	55.85	0.756	0.778	139.21	1.00	8.49	1464	10.41	1.21
			0.799							
	Si	28.09	0.780	0.770	274.12	1.97				
			0.760							
Cy5.5-Si-USPIO	Fe	55.85	0.399	0.401	71.71	1.00	4.37	1421	10.38	1.18
			0.402							
	Si	28.09	0.380	0.385	137.06	1.91				
			0.390							
SCION	Fe	55.85	0.307	0.301	53.89	1.00	3.29	1424	10.38	1.18
			0.295							
	Si	28.09	0.290	0.290	103.24	1.92				
			0.290							

$$MW_{SiO2} = 60.07\frac{g}{mol}$$

$$d_{SiO_2} = 2.2\frac{g}{cm^3}$$

$$\text{Volume } SiO_2 \text{ per SCION} = V_{SiO_2} = \frac{\frac{mol\ Si}{mol\ Fe}\left(\frac{16400 mol\ Fe}{mol\ SCION}\right)\left(\frac{60.07 g\ SiO_2}{mol}\right)\left(\frac{10^7 nm}{cm}\right)^3}{\left(6.022e23 SCION/mol\right)\left(2.2 g/cm^3\ SiO_2\right)}$$

$$V_{SiO_2} = \frac{4}{3}\pi\left(r_{SCION}^3 - r_{USPIO}^3\right)$$

$$\text{Silica Layer Thickness} = r_{SCION} - r_{USPIO}$$

Calculations through elemental analysis revealed a silica layer of ~1.2 nm, a value slightly less than what was observed by TEM. This difference exists for number of reasons. The density values used for the above calculations are based on dry density. However, silica is well known for water absorbing properties and is a commonly used desiccant, and the hydrated and dry silica do have different properties, including density. Furthermore, in TEM when the electron beam hits an area such as silica, the sample actually can be affected. Many groups have demonstrated deformation processes of silicon oxide nanostructures induced by an electron beams [127, 128]. Bombardment of high purity silica with electron and ion beams often results in the reduction of surface stoichiometry and release of O_2 [128].

While the sample diameters measured cannot be directly compared across techniques, silica was found to be deposited in both cases in the desired range of less than 5 nm, where it is sufficient to encapsulate and protect the fluorophore and modify the iron oxide surface to enhance biocompatibility.

2.6 Final SCION Particle

A schematic of the complete particle synthesis protocol is displayed in Figure 2-27. Table 2-6 lists values that characterize the final SCION particle, where mass and iron content are estimated with the assumptions that the iron core is composed of only magnetite and there are 5 dye molecules per particle.

The procedure has been optimized for synthesis of a unique dual-modality particle with properties that make it ideal for medical diagnostics. These properties include not

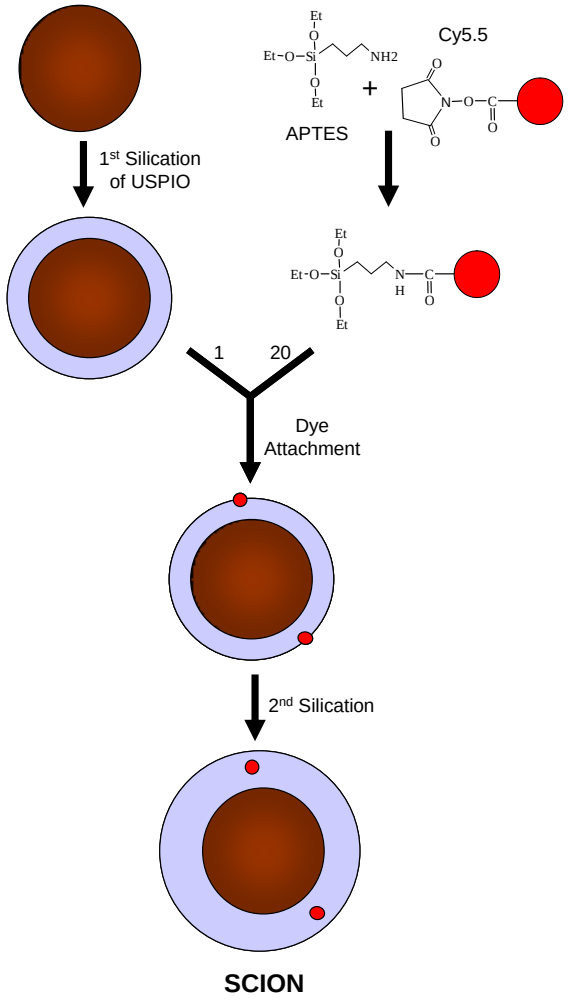

Figure 2-27: SCION particle synthesis.

Table 2-6: Properties of the SCION particle.

Particle Diameter	~16 nm
Iron Oxide Diameter	9.2 nm
Silica Layer Thickness	~3.5 nm
Mass*	6.11e-18 g/SCION
	3.68e6 g/mol SCION
Fe Content*	4.46 mmol Fe/g SCION
*assumes 5 Cy5.5/SCION and iron core is magnetite	

only imaging capability but also size, surface charge, and superparamagnetic properties that are analyzed in the following chapter.

Chapter 3

Particle Characterization

3.1 Diffraction Pattern

The techniques of electron, X-ray, and neutron diffraction are based on the phenomenon of wave-particle duality. In the 1920s, Louise de Broglie earned a Nobel Prize for Physics on his PhD thesis work where he determined that particles also behave as waves. His work described that their wavelength is inversely proportional to the momentum of a particle and that the frequency is directly proportional to the particle's kinetic energy [129]. The formula was confirmed for electrons a few years later with the independent observation of electron diffraction by Clinton Joseph Davisson and Lester Halbert Germer who guided their beam through a crystalline grid [130] and by George Paget Thomson who passed a beam of electrons through a thin metal film and observed the predicted interference patterns [131]. The great advantage of the transmission electron microscopy (TEM) is the ability to observe both real space images and reciprocal space diffraction patterns for the same region to characterize not only physical attributes such as size and morphology, but also crystalline structure. In the 1940s, Vainshtein and his colleagues in the Soviet Union focused electron beams with an elektronograf to obtain diffraction structures of organic and inorganic materials with scattering angles up to 3-5°

[132]. Their pioneering work to use electron diffraction to solve crystallographic problems is the basis for modern TEM diffraction.

TEM captures electron scatter from beams directed at sample materials, as shown in Figure 3-28. A perpendicular beam of electrons enters the specimen and is scattered in

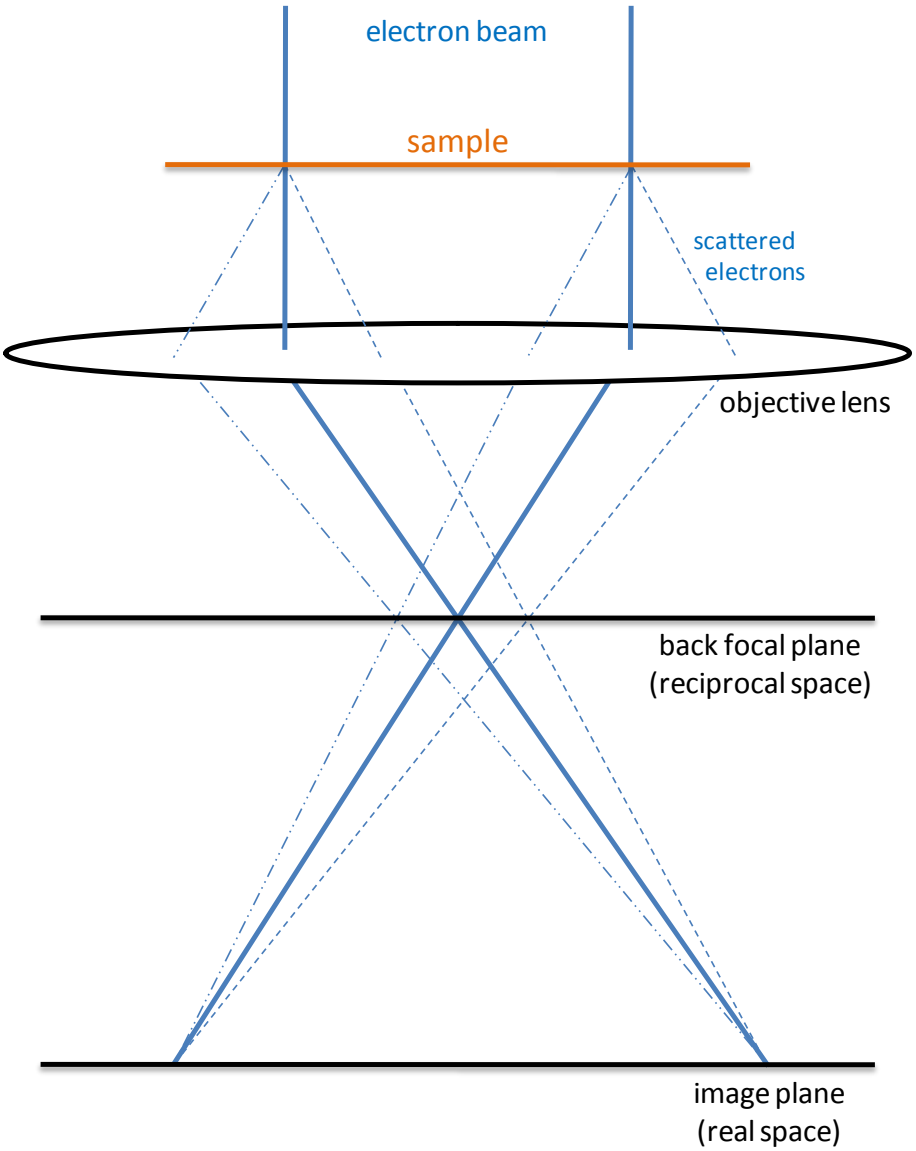

Figure 3-28: TEM electron beam enters the specimen and is scattered in various directions. The objective lens is used to collect all scattered beams (dotted lines) originating from one point on the sample in one point in the image plane. In the back focal plane electrons originating at different points on the sample but scattered in the same direction, are collected and observed as the diffraction pattern.

various directions. Electron waves scattered by the sample's crystalline structure are focused by electromagnetic objective lens to project an arrangement of diffraction patterns on the reciprocal space back focal plane. Diffracted waves are then recombined to form an image on the real space plane. A magnified sample image is generated if the transmitted and diffracted beams interfere on the image plane. The transformation between reciprocal to real space is mathematically related by the Fourier transform. Notice that electrons originating from different areas from the sample are scattered in the same direction and collected in specific groups or patterns on the back focal plane. This periodic scattering distribution of the electrons is characteristic to the sample structure. Working back from the observed diffraction pattern, it is often possible to deduce the specimen crystalline structure.

Selected area diffraction patterns can be recorded from almost every grain in a polycrystalline material. The scattering cross section of matter for electrons is 10^3 to 10^4 times larger than for x rays and neutrons and typical wavelengths (~2 pm) are one hundredth of those for x rays and neutrons, allowing the electron beam to be focused to extremely fine probe sizes (~1 nm) [133]. Thus, single crystal structural information can be obtained for materials such as fine precipitates and nanoparticles for which single crystals of the sizes suitable for x-ray or neutron diffraction are unavailable. While Vainshtein's elektronograf worked with 50 keV to 100 keV beams to generate low resolution images [132], modern electron microscopes have resolutions of around 0.2 Å at 300 kV beam energy [133, 134].

Diffraction pattern ring diameters can be correlated to the lattice plane spacings of a crystal by the following formula:

$$rd = \lambda L \tag{9}$$

where r is the diffraction ring diameter, d is the lattice spacing, L is the microscope effective camera length, and λ is the accelerating voltage wavelength. Measuring the precise values of L or λ is difficult, but even without knowing them, an unknown lattice spacing can be analyzed by measuring r. Known lattice spacings of many polycrystalline materials have been characterized and cataloged and can be used as a standard for comparison. A completely isotropic fine-grained polycrystalline sample will give a diffraction pattern of concentric rings, as the many small crystals at random orientations produce a continuous angular distribution of spots at distance $1/d_{hkl}$ from the straight-through beam's 000 index spot. This method was followed to compare the diffraction patterns of SCION particles to known standards of various forms of iron and silicon oxides.

Both "bare" USPIO and silica-coated USPIOs were analyzed using a JEOL 4000EX TEM. The samples were drop-cast onto carbon grids. The electron microscope was operated in the selected area diffraction mode and the diffraction patterns from the core shell particles were used to analyze the crystalline structure of these materials. Table 3-7 provides the data generated from the measured radii from Figure 3-29. The mean radius was determined by averaging five measurements per ring. As would be expected by the fcc packing of iron oxide crystals, the diffraction rings h,k,l are either all even or all odd, where zero is considered even. Based on the diffraction rings, the core structure was confirmed to be magnetite or maghemite and that TEOS was condensed on the USPIO surface as silicon (IV) oxide.

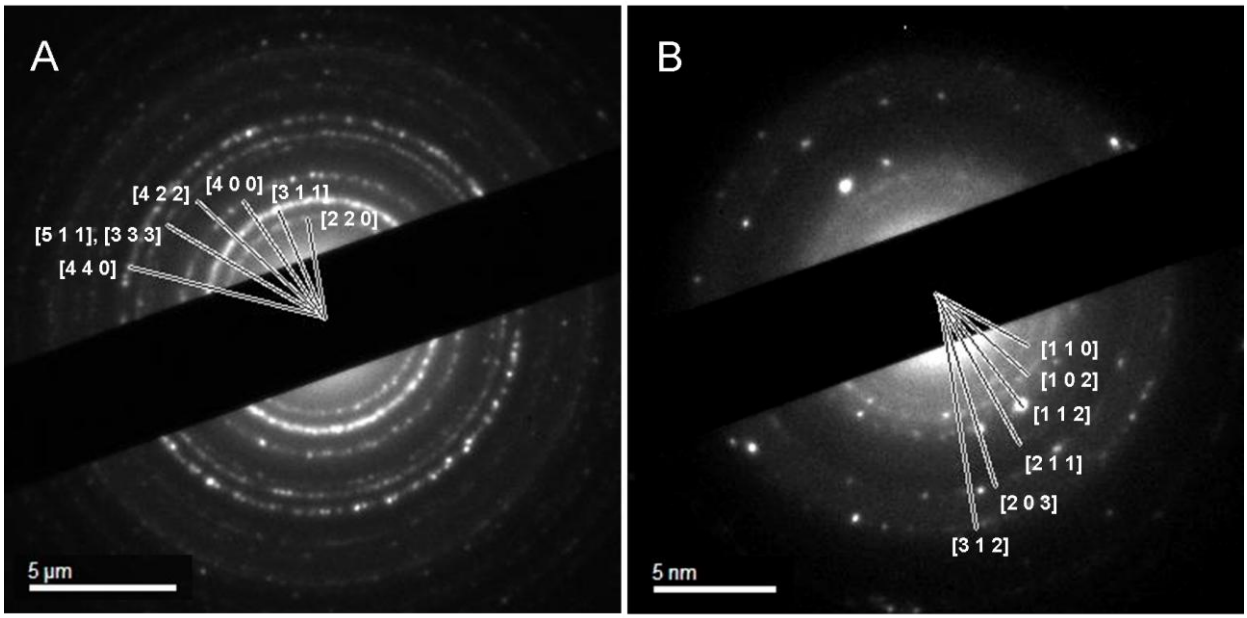

Figure 3-29: Diffraction patterns using JEOL 4000EX of silica-coated USPIOs: (A) magnetite/maghemite core, and (B) silicon(IV) oxide outer shell.

Table 3-7: D spacing characterization of diffraction patterns of SCION particle.

IRON OXIDE CORE DIFFRACTION					
Standardized Diffraction Values [135, 136]				TEM Diffraction	
Magnetite	Maghemite			Presence of Corresponding Ring	Mean Radius (µm)
d (A)	d (A)	hkl	Relative Intensity (I/I_1)		
2.97	2.95	220	34	yes	3.3
2.53	2.52	311	100	yes	3.8
2.10	2.08	400	24	yes	4.6
1.71	1.70	422	12	yes	5.6
1.61	1.61	511,333	33	yes	6.0
1.48	1.48	440	53	yes	6.6
SILICA SHELL DIFFRACTION					
Standardized Diffraction Values [135]				TEM Diffraction	
Silicon(IV) Dioxide				Presence of Corresponding Ring	Mean Radius (nm)
d (A)	hkl	Relative Intensity (I/I_1)			
2.46	110	12		yes	4.1
2.28	102	12		yes	4.8
1.82	112	17		yes	5.6
1.54	211	15		yes	6.9
1.37	203	11		yes	7.9
1.08	312	4		yes	9.3

3.2 Zeta Potential

When a fundamental state of matter (solid, liquid, or gas) is finely dispersed in another, it is known as a colloidal system. Examples of colloidal systems include aerosols, emulsions, and SCION particle suspensions. Under certain circumstances, particles may adhere to one another where the initially formed aggregate is called a floc and the process of its formation is flocculation. If the aggregate changes to a denser form, it is said to undergo coagulation. Both flocculation and coagulation, terms that are often used interchangeably, can result in sedimentation and phase separation.

In the 1940s, Derjaguin, Verwey, Landau and Overbeek developed a theory suggesting that the stability of a colloidal system is determined by the sum of van der Waals attractive and electrical double layer repulsive forces. The particles move in the fluid under Brownian motion and an energy barrier prevents two particles approaching one another from adhering together. However, if the particles collide with sufficient energy to overcome the energy barrier, the van der Waals attractive force will pull them together to adhere strongly, resulting in flocculation. Thus, colloidal stability is maintained when repulsive forces, such as steric or electrostatic, dominate.

Typically, particles in an aqueous dispersion acquire a surface charge, either by ionization of surface groups or adsorption of charged species. Particles with a net surface charge interact with and affect the distribution of surrounding ions, which in turn affects colloidal stability. The liquid layer that forms around the particle exists as an inner Stern layer where the ions are strongly bound and an outer diffuse region where they are less firmly associated. A notional boundary, known as the slipping plane or hydrodynamic plane of shear, exists in the diffuse layer inside which the ions and particle form a stable

entity that move as a unit. Ions outside the boundary stay with the bulk dispersant. Zeta potential, sometimes thought of as a 'charge' measurement, is the potential at this slipping plane or surface of hydrodynamic shear. Zeta potential may or may not be related to the surface charge, but it, and not the charge at the particle surface, is what controls charge interactions.

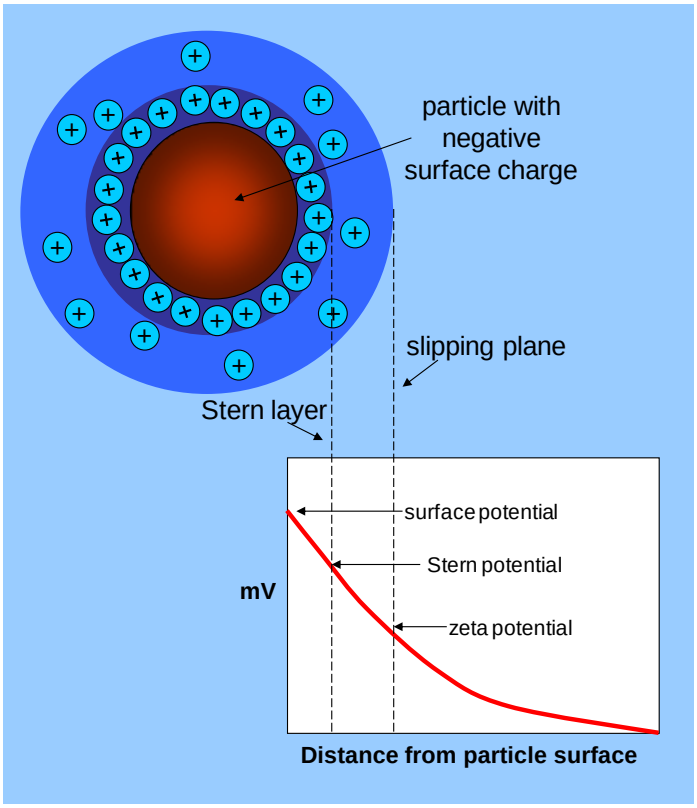

Figure 3-30: Schematic of double layer formation around a particle in aqueous suspension and its measurement of zeta potential.

The magnitude of zeta potential provides an indication of colloidal stability. A large zeta potential, typically > +30 mV or < -30 mV, causes particles to repel each other and promotes the suspension to remain stable. At a low zeta potential, there is not enough electrostatic repulsion to prevent flocculation. The zeta potential of a sample varies with solution pH. The isoelectric point, also referred to as point of zero charge (PZC), is the pH at which the particles in suspension have a net charge of zero, no mobility in an electric field, and the least amount of colloidal stability.

Zeta potential is measured by applying an electric field across the dispersion, after which charged particles are attracted towards the electrode of opposite charge. Viscous forces acting on the particles tend to oppose this movement. The particles move with a

constant velocity that can be detected when equilibrium is reached between these two opposing forces. The velocity of a particle in a unit electric field is referred to as its electrophoretic mobility and is related to zeta potential:

$$U_E = \frac{2\varepsilon\zeta \quad f(\kappa a)}{3\eta} \tag{10}$$

where U_E is the electrophoretic mobility, ζ is zeta potential, ε equals the dielectric constant, η is solution viscosity, and $f(\kappa a)$ is Henry's function. The reciprocal of the Debye length, κ, is often taken as a measure of the "thickness" of the electrical double layer and *a* refers to the radius of the particle. Electrophoretic mobility is measured using laser Doppler anemometry, where moving particles result in a frequency or phase shift of an incident laser beam. The electrophoretic mobility is then used to calculate zeta potential.

Characterizing the particle surface properties of the SCION particles is necessary to understand and predict their properties under physiological conditions and also to optimize conjugation chemistry. Samples were analyzed for zeta potential with a Malvern Zetasizer Nano ZS and the results are presented in Figure 3-31. Although it is sample dependent, the Zetasizer detects the zeta potential of particles in the hydrodynamic diameter range of 5nm to 10μm with a maximum sample conductivity of 200mS/cm. All sample readings fell within these limits. Adjustments in pH were made with potassium hydroxide and hydrochloric acid. USPIOs that were only washed with nitric acid showed partial conversion to maghemite as is evident by the dip in zeta potential near pH 5. By re-characterizing surface charge after allowing the particles to sit in nitric acid for five days for full conversion of magnetite to maghemite, the PZC of maghemite was confirmed to be lower than magnetite. The PZCs obtained were

comparable to literature values of pH 5.1 [137] and pH 7 [138] for maghemite and magnetite respectively. Both citrate complexation and coating with silica made the sol anionic across the working pH range. The stable negative charge in the pH range of 6-7 is desirable because it imitates the negative charge of most biomolecules in physiological conditions [139].

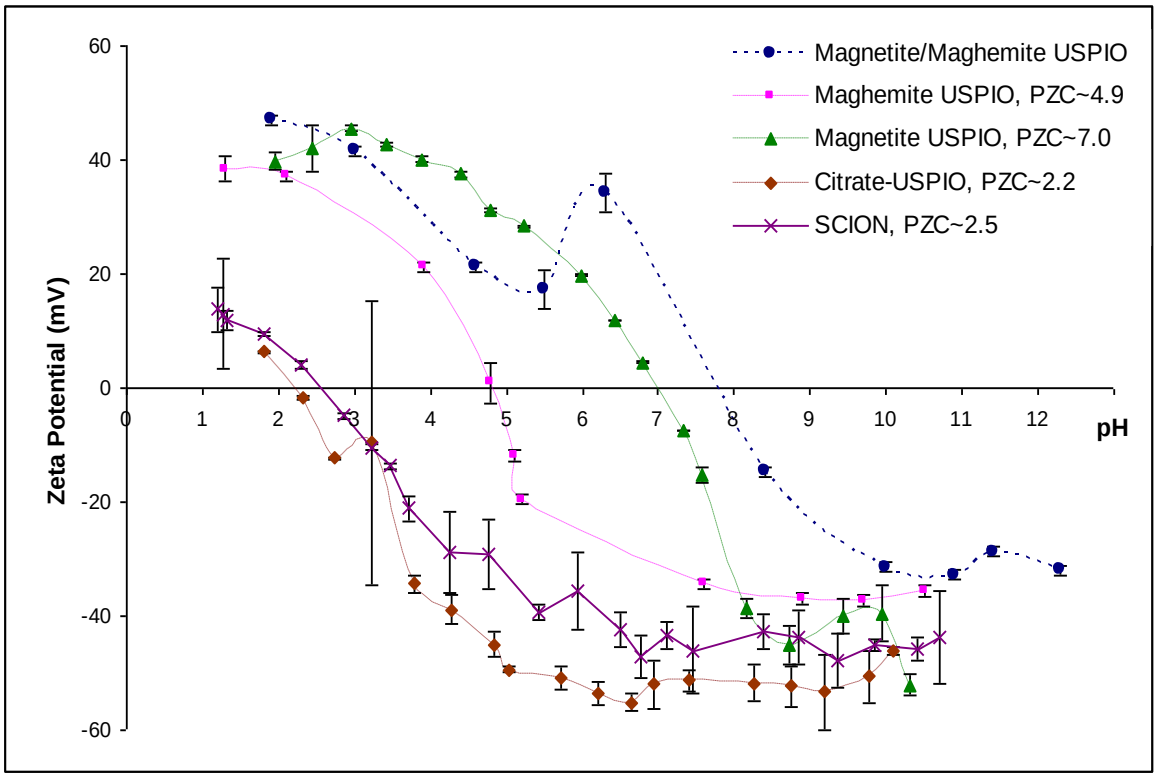

Figure 3-31: Surface charge characterization of particles in water.

3.3 Hydrodynamic Diameter

Dynamic light scattering (DLS), also known as photon correlation spectroscopy (PCS) or quasi-elastic light scattering (QELS), is a method used to measure the

hydrodynamic diameter of particles or emulsions dissolved in liquids. The technique relates particle size to measured Brownian motion, the random movement of particles due to thermal energy and the bombardment of surrounding solvent molecules. Larger particles have slower Brownian motion, while smaller particles are "kicked" further by solvent molecules.

When a laser is directed through a suspension, particles scatter light in all directions. For large particles equivalent to the illuminating light wavelength, the intensity of scattered light follows Mie Theory and is angle dependent. When particles are small compared to the light wavelength (typically less than 60nm for a He-Ne laser), Rayleigh scattering occurs where the light scatter is essentially isotropic, or uniform in all directions. When the particles in solution undergo Brownian motion, fluctuations in the scattering intensity are observed. Time-dependent recording of constructive and destructive interference of light scattered gives rise to a diffusion coefficient. The translational diffusion coefficient, *D*, is related to the hydrodynamic diameter by the Stokes-Einstein equation:

$$d(H) = \frac{kT}{3\pi\eta_0 D} \tag{11}$$

where *d(H)* is the hydrodynamic diameter, k_B is the Boltzmann constant, *T* is temperature, and η_0 is solvent viscosity. The hydrodynamic diameter obtained by this technique is the diameter of a sphere which has the same average diffusion speed as the particle being measured. It will be affected by various factors such as the ionic strength which influences the thickness of the electrical double layer (i.e. Debye length), adsorbed layers on the particle surface, and particle shape.

The size obtained from DLS will almost always be larger than that from electron microscopy because of an influence of the Debye length on the diffusion coefficient and because the intensity of light scattered is dependent upon the size of particles present. The Rayleigh approximation tells us that the intensity of light scattered (I) is proportional to d^6, where d = particle diameter. Hence, a 20 nm particle will scatter one million times as much light as a 2 nm particle. If a sample is polydisperse, larger particles which may be present in low numbers will dominate the scattering and the result will be biased towards the larger end of diameter in the intensity distribution. Hydrodynamic diameter can also be analyzed by volume and number distributions, where the number distribution is most similar to electron microscopy because it is a representation of the number of particles of each size present. However, care must be taken when evaluating these distributions as they are calculated based on an intensity data conversion which has some errors associated with it.

Hydrodynamic diameter does not directly correspond with the hydrodynamic shear boundary where zeta potential is measured. The slipping plane exists at some point within the electrical double layer and is not necessarily at the edge of the electrical double layer. Particle size does not influence zeta potential because the number of charges on the particle surface driving the particle forward as it undergoes electrophoresis and the viscous drag on the particle preventing it from moving, are both proportional to surface area. As the average particle size decreases, the viscous drag reduces proportionally. These changes cancel out any size dependence of the measurement. How hydrodynamic diameter and zeta potential are related has to do with flocculation. When zeta potential is low ($-30\text{mV} < \zeta < 30\text{mV}$), electrostatic repulsion is no longer strong enough to prevent

the particles from aggregating and the recorded hydrodynamic diameter reading also increases.

Using a Malvern Zetasizer Nano ZS, the hydrodynamic diameter (Figure 3-32A) and zeta potential (Figure 3-32B) of the SCION particles were analyzed. Though it is sample dependent, the Zetasizer detection limits for the hydrodymanic diameter of most samples are 1nm to 6µm. Adjustments in pH were made with potassium hydroxide and hydrochloric acid. In cases where the zeta potential was low, the hydrodynamic diameter was higher, with its peak near the PZC. In the range above pH 5, a strong negative zeta potential allowed the particles to remain in colloidal suspension with a diameter of ~18 nm. This hydrodynamic diameter was measured in number distributions and was relatively close to the TEM measurements of ~15 nm. Ideal for biomedical applications, the nanoparticles remain stable as a colloid without flocculation in the physiological pH range.

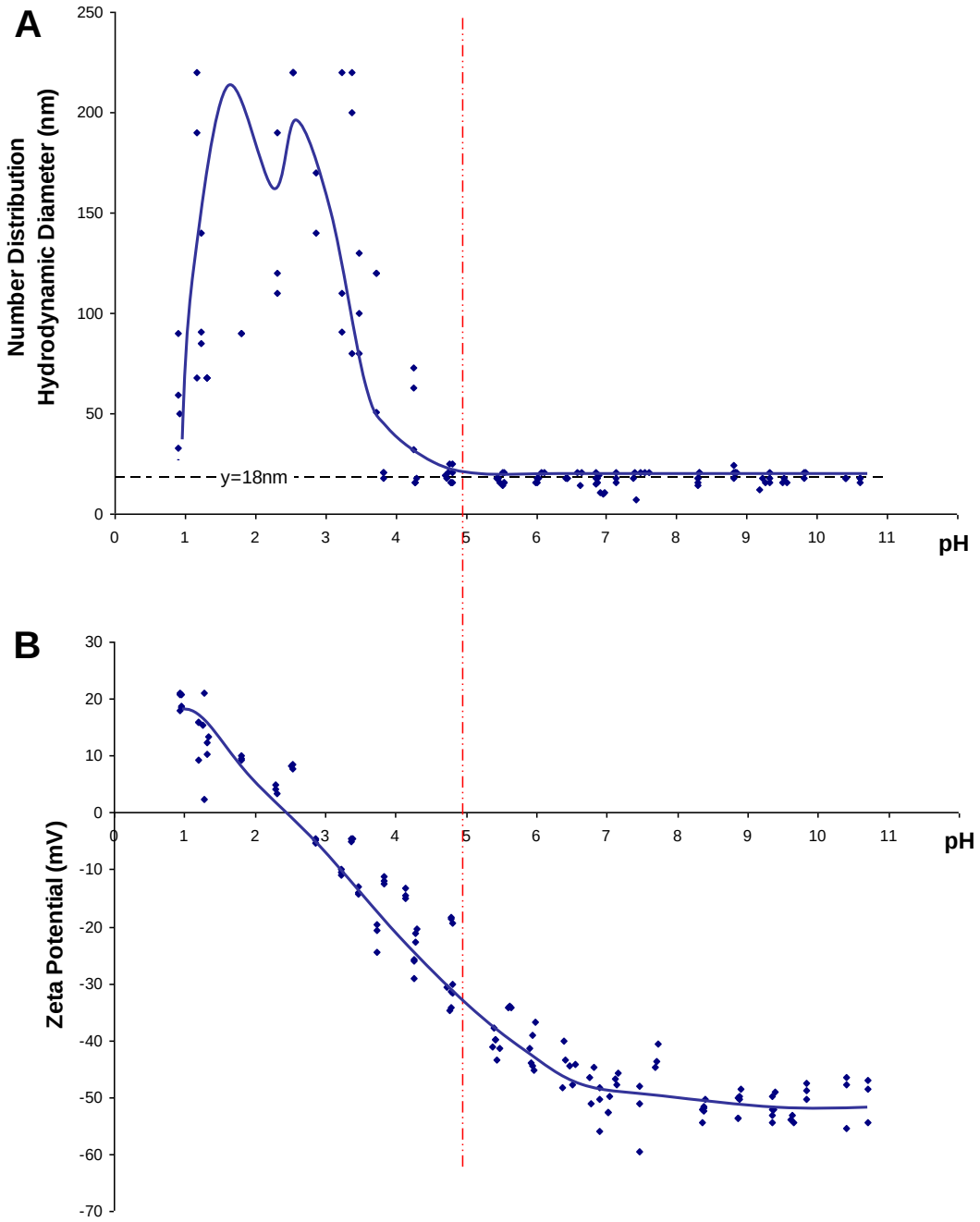

Figure 3-32: SCION particles characterized across pH range for (A) number distribution hydrodynamic diameter and (B) zeta potential. Left of the red line, the absolute value of the zeta potential is less than 30 mV and flocculation is observed. Right of the red line, zeta potential is strong and the observed hydrodynamic diameter is ~18 nm.

3.4 Blocking Temperature

Solutions of USPIOs and SCIONs were lyophilized to their solid form and each sample was collected for analysis using a superconducting quantum interference device (SQUID) (Quantum Design MPMS XL). The company manual gives the minimum sensitivity of the setup used as $5x10^{-9}$ emu; however, the university SQUID's acceptable limit without noise is on the scale of 10^{-6} emu. The measurements in both Sections 3.4 and 3.5 were performed on sample masses of a minimum of 45mg, where all readings were well above the lower limits of the instrument. Field cool (FC) and zero field cool (ZFC) curves were used to determine the blocking temperature (T_B), the temperature at which material begins to demonstrate superparamagnetic behavior.

In 1949, Neel explained that at temperatures above T_B the stable bulk magnetization cannot be established due to thermal fluctuations acting on small particles, while at temperatures below T_B, thermal fluctuations do not dominate and the magnetic moments 'freeze' in random orientation and cannot rotate freely [140]. In the absence of an external magnetic field, the effective magnetic anisotropy energy E_α serves as an energy barrier for blocking the flips of magnetic moments and can be approximated by:

$$E_\alpha = K_{eff} V \tag{12}$$

where K_{eff} is the effective magnetic anisotropy energy constant per unit volume, and V is the volume of magnetic nanocrystal. Thermal activation can overcome the anisotropy energy barrier when E_α becomes comparable with the thermal activation energy [141, 142]:

$$K_{eff} V = \beta k_B T_B \tag{13}$$

where k_B is the Boltzmann constant, T_B is the critical blocking temperature, and the constant β, which typically varies between 25 and 34 [142], represents the ratio between anisotropy and thermal energy when the relaxation time of a given particle is similar to the characteristic measuring time of the experiment. At this point, the magnetization direction flips randomly and the material becomes superparamagnetic.

For ZFC, the sample was cooled down to 2K before applying a 0.01 T field and measuring magnetization (M). The field remained constant as the temperature was increased to 370 K. For FC, the temperature was first brought to 370 K. The 0.01 T field was then applied and held constant as susceptibility was recorded as a function of decreasing temperature (Figure 3-33). A characteristic of superparamagnetic systems is the bi-furcation of ZFC and FC curves at temperature T_{diff}. When a particle size distribution exists, a broad maximum for the ZFC curve occurs at a temperature T_{max} that is lower than T_{diff}. Particles are blocked at various temperatures between the two, where a fraction of the largest particles freeze at T_{diff}, while the majority of sample's particles are blocked at T_{max} [143]. Figure 3-33 displays the ZFC and FC curves and blocking temperature ranges for uncoated USPIO and SCION.

Both T_{max} and T_{diff} were significantly lower for SCION particles (T_{max} = 72 K and T_{diff} = 163 K) as compared to USPIO (T_{max} = 118 K and T_{diff} = 244 K), indicating silica layer deposition around individual USPIOs, which is consistent with TEM results. Interparticle separation increases for SCION particles, thus reducing magnetic dipole–dipole interaction and decreasing T_B. This result is typical for coated nanoparticles where the buffer layer reduces magnetic interactions between the particles. Kim et al [144] showed similar effects for iron oxide particles covered with an oleate layer and Tartaj et

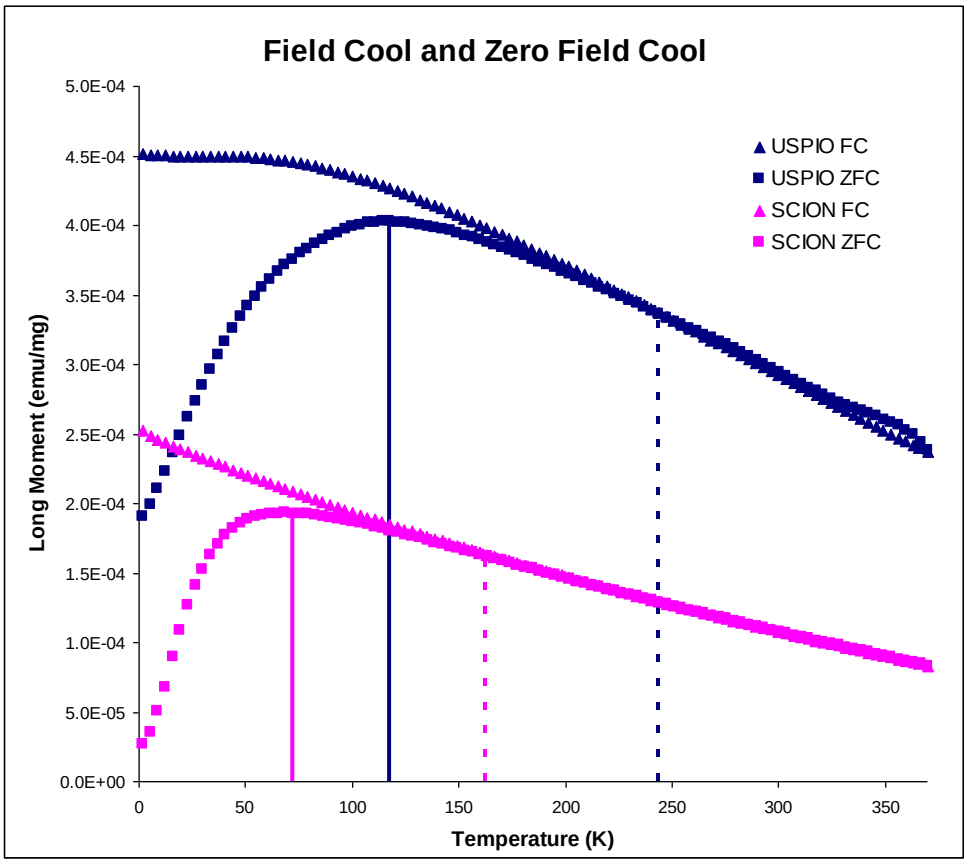

Figure 3-33: Temperature dependence of the magnetization (ZFC & FC) of USPIO and SCION at H=0.01T. T_{max} and T_{diff} for USPIO were measured at 118 K and 244 K, and 72 K and 163 K for SCION.

al [145] demonstrated the same for γ-Fe_2O_3 particles dispersed in silica. The ZFC curves show a broad maximum as a result of inhomogeneous agglomeration. The different aggregates were blocked at varied temperatures, creating the distribution of blocking temperatures. The silica-coated sample had a steeper curve indicating reduced iron core aggregation. The difference in magnitudes for the two samples can be explained by the additional mass of non-magnetic coating surrounding the magnetic core for SCION particles.

3.5 Magnetic Hysteresis

To further characterize particle behavior by confirming that the particles were in fact superparamagnetic, hysteresis curves were analyzed. Magnetic domains of ferromagnetic materials have a magnetic memory where once aligned in an applied field, they do not return to their original state without expenditure of energy. This dependency on recent history traces a hysteresis loop and energy loss is measured by the area of the loop. Superparamagnetic materials have no permanent magnetic moment and, hence, no hysteresis loop. To test the magnetic behavior of the two samples, the temperature was held constant at 2 K, 100 K, and 310 K (body temperature) for hysteresis measurements in two applied field ranges: ±7 T and ±0.01 T (Figure 3-34). At 2K (Figure 3-34A&D), both samples showed some hysteresis as would be expected because the temperature was held constant below their blocking temperatures. At 100K (Figure 3-34B&E), minimal hysteresis was found for the SCION sample while there was still more for USPIO. This phenomenon is most likely because the temperature was above T_{max} for SCION so the majority of particles were already superparamagnetic, while for USPIO T_{max} had not yet been reached and most particles were below the blocking temperature. By 310K (Figure 3-34F), the shape of the hysteresis curves for both samples with the lower applied field were tight with no hysteresis losses as is typical behavior for a superparamagnet.

Under high applied field at 310K (Figure 3-34C), SCION behaved as expected but USPIO did show hysteresis losses, suggesting that some aggregation occurred as the sample was dried or an error occurred (contamination, instrument, etc) during the measurement. The measurement was repeated on a different sample of USPIO as is

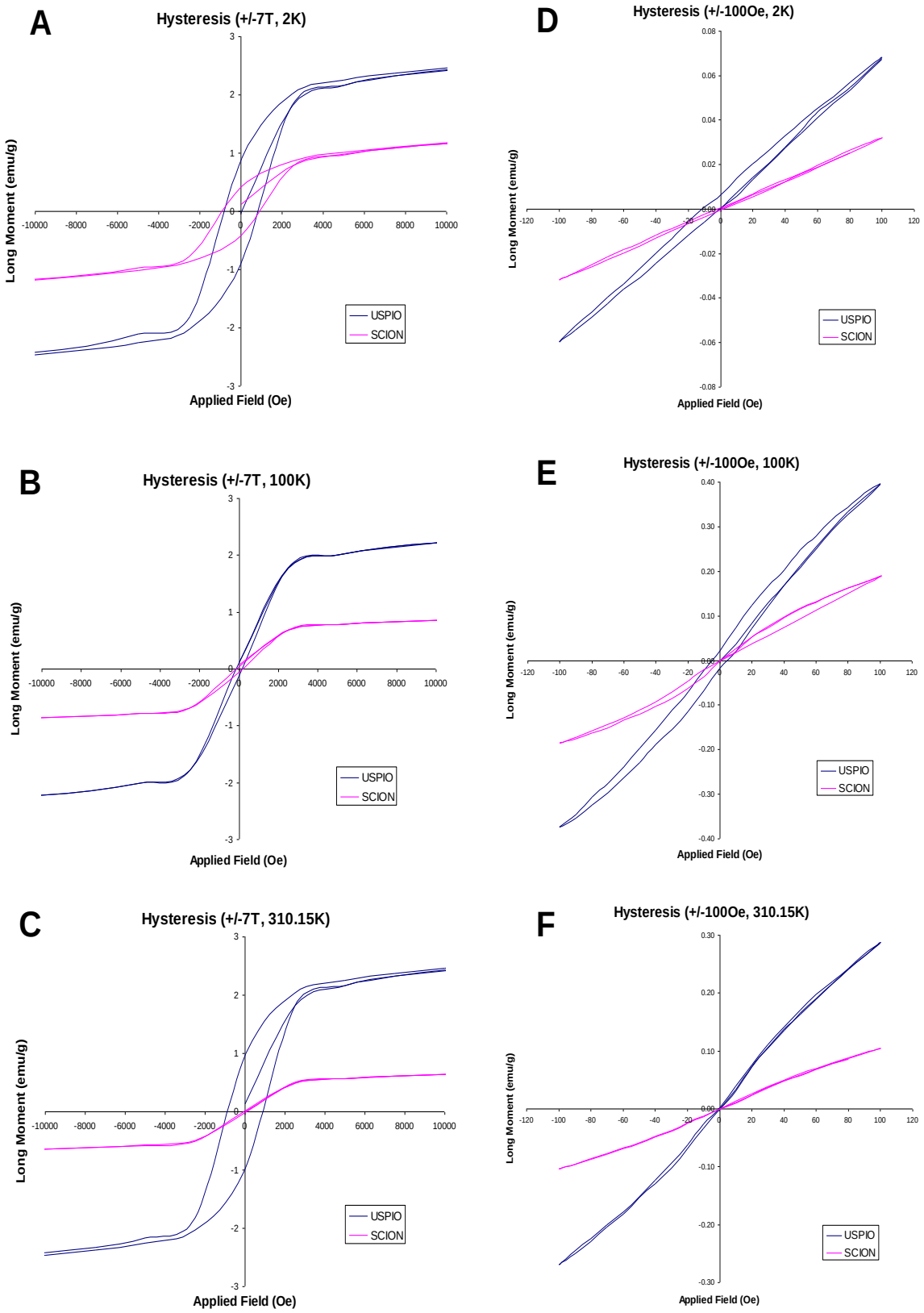

Figure 3-34: Hysteresis analysis of USPIO and SCION at (A) T=2K (±7 T), (B) T=100K (±7 T), (C) T=310K (±7 T), (D) T=2K (±0.1 T), (E) T=100K (±0.1 T), and (E) T=310K (±0.1 T).

shown in Figure 3-35, where no hysteresis was observed. Assuming zero susceptibility of silica, the differences in saturation magnetization of the samples can partially be attributed to the percent mass composition of silica.

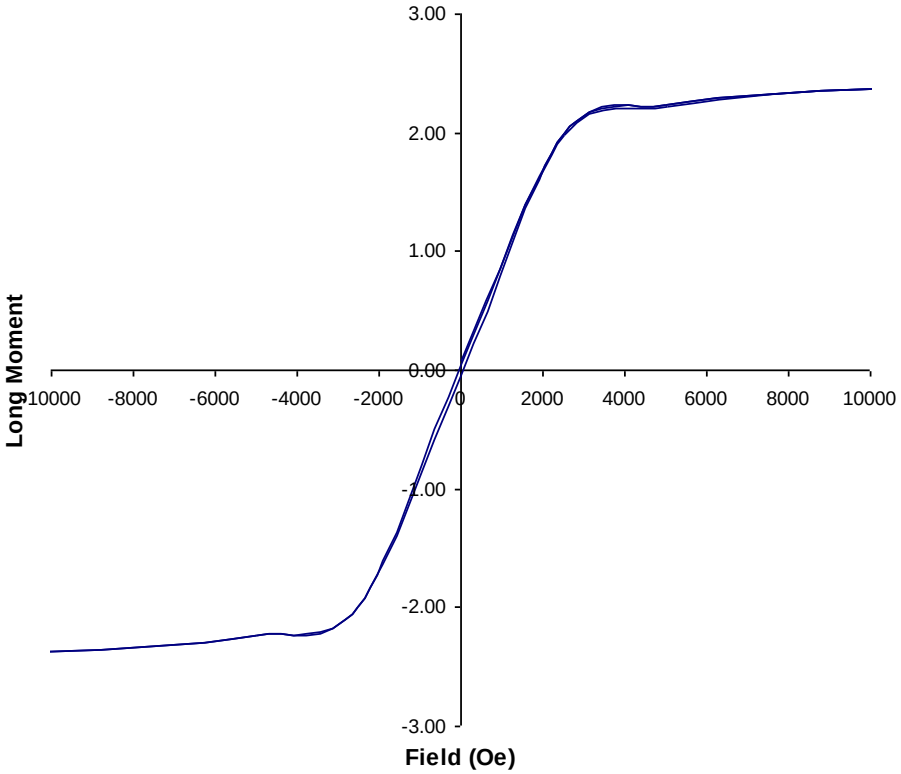

Figure 3-35: Hysteresis analysis of a different sample of USPIO at T=310K and ±7 T.

3.6 Relaxivity

The relaxivity of SCION particles was compared to that of Gd-DTPA and Feridex. While Gd-DTPA solutions (0-1.0 mM Gd) were made in water, SCION and Feridex preparations (0 –1.0mM Fe) were in 0.25% agarose water gels to ensure even dispersion and to prevent particles from collecting on the sides of the tubes while in the

MR magnet. Relaxivity measurements (performed by Celeste Regino, National Cancer Institute) on duplicate samples were obtained at room temperature (~22°C) using a 3T clinical scanner (Signa Excite, General Electric Medical System, Waukesha, WI, USA) equipped with a rectangular single loop receiver coil (84 x 126 x 6 mm). For T_1 calculations, images of the solutions using a 2D-spin echo (2D-SE) sequence were acquired with repetition times (TR) of 100, 350, 750, 1250, 2500 and 5000 ms at echo time (TE) of 11 ms. For T_2 analysis, the sequence was an 8-echo spin-echo with TR = 5000 ms and TE = ~9ms. T_1 and T_2 maps were calculated using ImageJ MRI Analysis plug-in (www.rsb.info.nih.gov/ij/plugins/mri-analysis.html). Relaxivities, r_1 and r_2, were

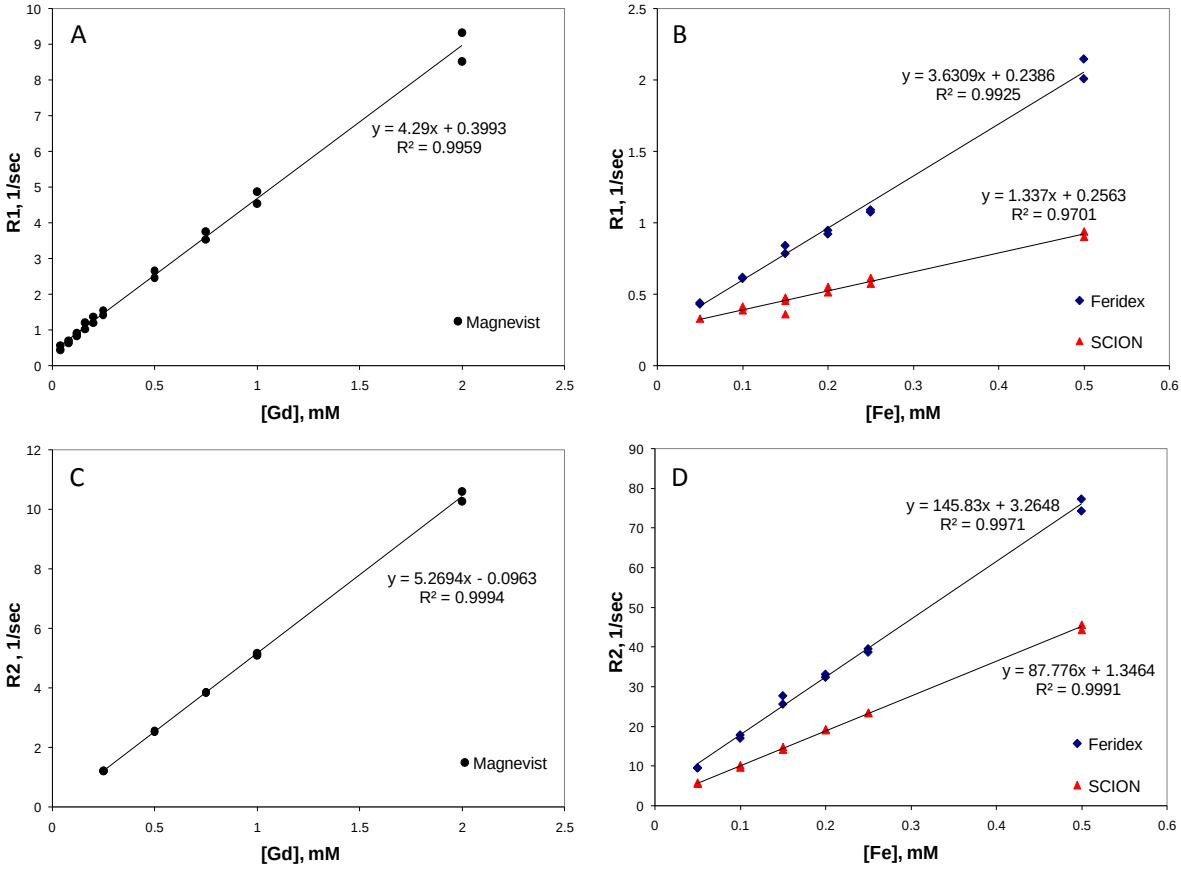

Figure 3-36: Relaxivity measurements ($mM^{-1}s^{-1}$) in a 3T magnet of SCION (r_1=1.34, r_2=87.78) compared to Feridex (r_1=3.63, r_2=145.83) and Magnevist (r_1= 4.29, r_2=5.27): (A) and (B) r_1 analysis and (C) and (D) r_2 analysis.

determined from the slopes of the plot of relaxation rates, $R_1=1/T_1$ and $R_2=1/T_2$,vs [Fe or Gd] (Figure 3-36). Both T_2 agents, Feridex (r_1 = 3.36 $mM^{-1}s^{-1}$) and SCION (r_1 = 1.34 $mM^{-1}s^{-1}$), have lower r_1 than the standard T_1 (r_1 = 4.29 $mM^{-1}s^{-1}$) agent Magnevist. Feridex and SCION have more than 16x's enhanced r_2, respectively 145.83 and 87.78 $mM^{-1}s^{-1}$, compared to Magnevist's 5.27 $mM^{-1}s^{-1}$. SCION does have lower r_1 and r_2 than Feridex. This reduction may be a result of particle size, ease of water exchange through coating pores, or differences in crystalline structure. We have continued using this SCION particle in our studies, but it is possible to enhance relaxivity by dosing the magnetite core with ions such as zinc [146] and manganese [147].

3.7 Effect on Cell Viability

Flow cytometry is a particularly effective biological tool that is used to count, examine, and even sort large numbers of microscopic particles suspended in a fluid. As its name suggests, the method is an optically based technique for the measurement (meter) of various characteristics of single cells (cyto) as they flow by in a saline fluid. A number of detectors are aimed at the point where the stream of individual cells passes through the directed illuminating laser light beam, one in line with the light beam for forward scatter (FS or FSC), several perpendicular to it for side scatter (SS or SSC), and one or more fluorescent detectors (Figure 3-37) [148-150]. FS characterizes cell size and refractive index, whereas SS is correlated with nuclear shape or cellular granularity. Surface ligands or intracellular molecules, can also be quantified if the marker of interest is labeled with a fluorescent dye, for example optical dyes that are sensitive to local

chemistry such as pH or Ca^{2+} concentration or that bind to structures such as mitochondria and DNA. An entire industry has arisen around fluorescently-labeled antibodies to target specific receptors that are used to characterize the activity and phentotype of various cell types. To observe specific fluorophores, the excitation laser beam and the collected emissions must be filtered for specific wavelengths. Flow cytometers have the ability to detect multiple fluorophores, or colors, simultaneously, ranging from 3- to 18-color instruments. If different dyes' emission spectra overlap, signals at the detectors can be compensated electronically as well as computationally.

Today's cytometers can analyze several thousand particles per second in real time, and can actively separate and isolate particles based on the recorded properties. Though

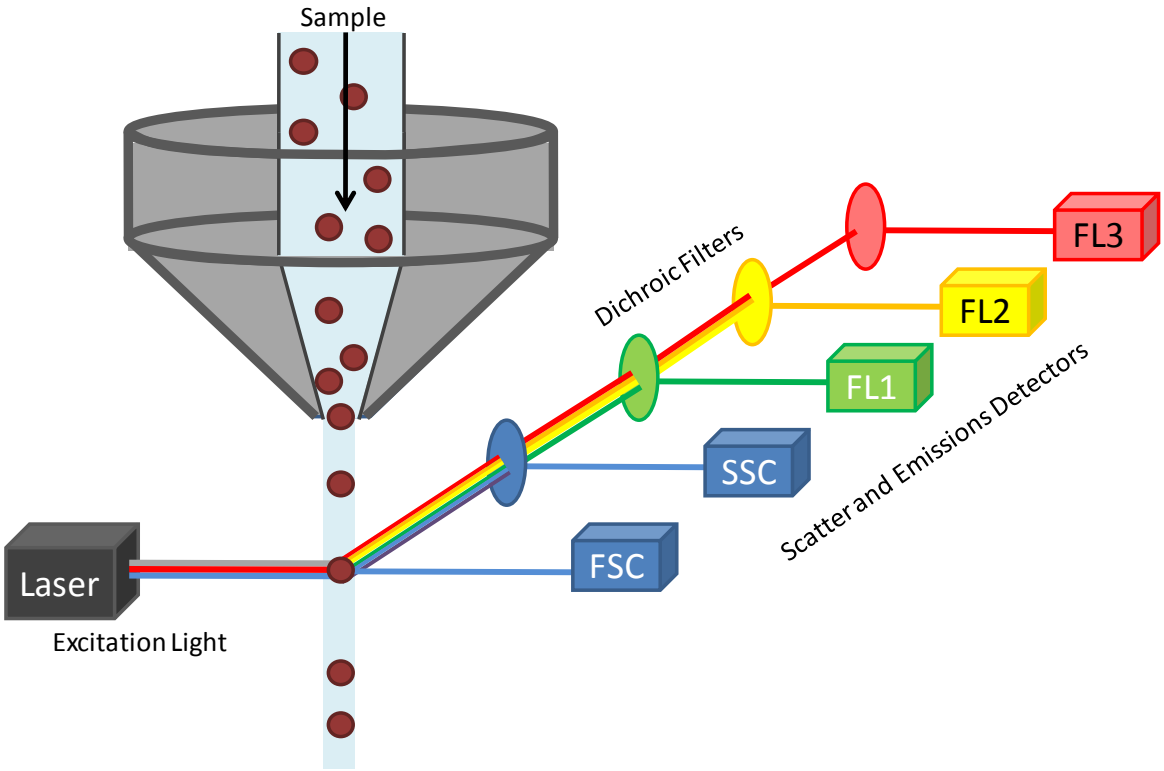

Figure 3-37: Schematic of a flow cytometer. Excitation light from a laser is directed at a hydrodynamically focused stream of particles, and the scattered light is collected and analyzed with a set of dichroic filters and optical detectors.

some instruments can take digital images of individual cells so that fluorescent localization can be analyzed, typically the data generated is plotted in single dimension histograms or two or three dimensional dot plots. Most samples when run through a flow cytometer have cellular debris or sets of particulates which can be excluded from analysis by setting gates around desired regions of interest. Using Boolean logic, these regions selected for morphology or fluorescence can be included or excluded in further analysis [149, 150]. Figure 3-38 demonstrates the application of this technique. The first dot plot represents a sample of only cells and the second with only SCION particle. Not surprisingly, SCION particles when compared to cells tend to be smaller in size and higher in granularity, because of aggregation. Using this understanding of the morphological differences between the two, in samples with both, the area with only cells can be gated with region 1 (R1), as shown in Figure 3-38C, and then analyzed on other plots for their fluorescent characteristics.

Flow cytometry was used to analyze the optimal concentration of SCION particles to stain human B lymphocytes and for their effect on cell viability. A number of cell lines were evaluated for particle uptake and short-term viability, including SKOV3, A431,

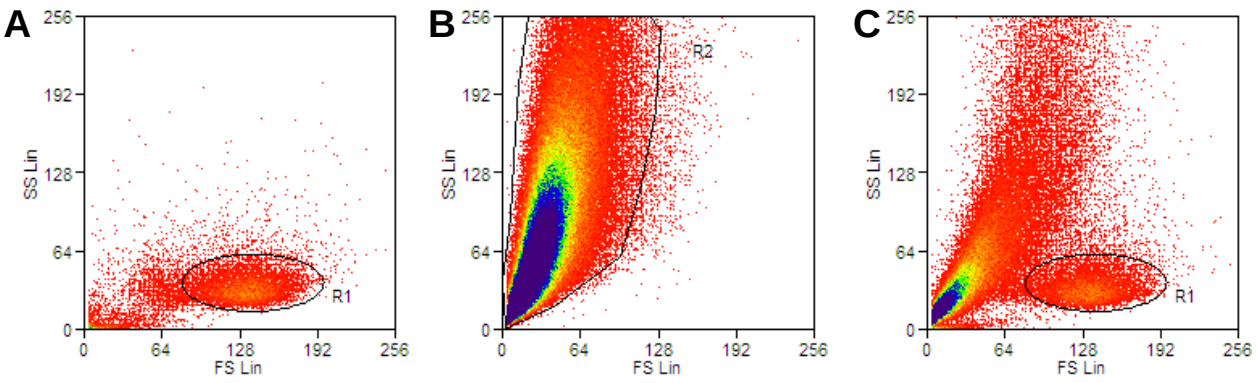

Figure 3-38: Dot plot of forward versus side scatter of (A) L cells only, (B) SCION particles only, and (C) L cells stained with high concentration of SCION.

MGAR, and L cells. However, in those cases, the particles were conjugated to antibody for targeted uptake and their results will be discussed in a later chapter. Non-targeted uptake with unconjugated SCION was low. Human B lymphocytes were chosen to analyze particle affect on viability over a longer time course for two reasons. First, a large percentage of these cells showed uptake of untargeted SCION, and thus the confounding factor of antibody effect could be eliminated. Secondly, whereas the other cells were immortal cell lines and had been split many times, these cells were primary lymphocytes extracted directly from patients and should be representative of a more natural behavior. B lymphocytes are white blood cells that play a crucial role in the adaptive immune response producing and secreting antibodies in response to antigens. They develop in the bone marrow and then migrate through the bloodstream, representing 5-15% of the circulating lymphoid pool.

Samples of B cells were incubated for one hour at 37°C with a titration (0, 0.0001, 0.005, 0.001, 0.005, 0.01, 0.1 nmol SCION per million cells) at a concentration of 10 million cells/mL of RPMI-1640 media. The cells were then washed twice with media by centrifuging at 500g/4°C for two minutes and decanting the media. The cells were maintained for a period of 65 hours, where at different time points some cells were evaluated for viability with the dye Hoechst 33528 (excitation 352nm, emission 461 nm), a dead cell stain used to detect morphological changes in the nuclear chromatin of cells undergoing apoptosis. After staining 0.5 million cell samples for 20 min on ice and washing, the samples were diluted to 1 mL 4% FBS/PBS and analyzed with flow cytometry using excitation lasers at 405 and 635 nm and emissions filters of 645-685 nm and 400-500 nm. FSC and SSC are studied with light collected at 488 nm. The histograph in Figure 3-39 demonstrates the effectiveness of staining B cells with SCION.

Higher concentrations yielded higher percentage uptake. Concentrations of 0.005 and 0.01 nmol SCION per million cells are sufficient to stain 90% of the cell population, however the latter yields more than 70% higher mean fluorescence intensity, or greater uptake of particle per cell. Each time a new cell line was stained with SCION particle, the titration of concentrations for optimal staining was re-evaluated.

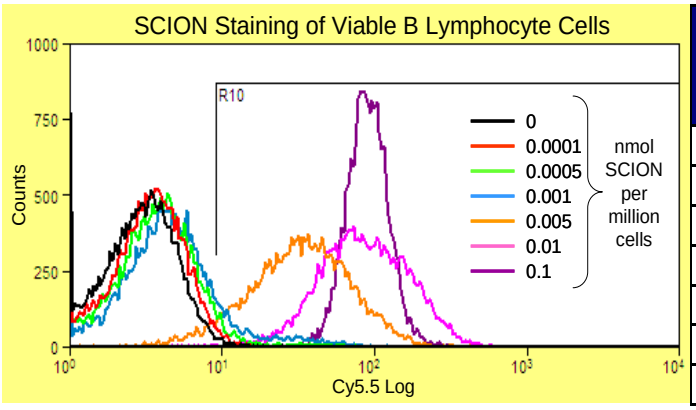

Staining Concentration of SCION (nmol/10^6cells)	%Stained Cells at 0.5hr	Mean Intensity of Stained Cells at 0.5hr
0	1.31	16.31
0.0001	2.14	14.47
0.0005	5.70	16.02
0.0010	13.59	20.37
0.0050	93.58	40.76
0.0100	99.56	70.12
0.1000	99.97	73.98

Figure 3-39: Percent of viable B lymphocytes stained with SCION and their mean fluorescence intensity 0.5hr after incubation with titration of concentrations of SCION.

B cell viability was observed by analyzing dot plots such as the ones in Figure 3-40. Cells that are undergoing apoptosis show high uptake of Hoechst 33528, near 10^3 on

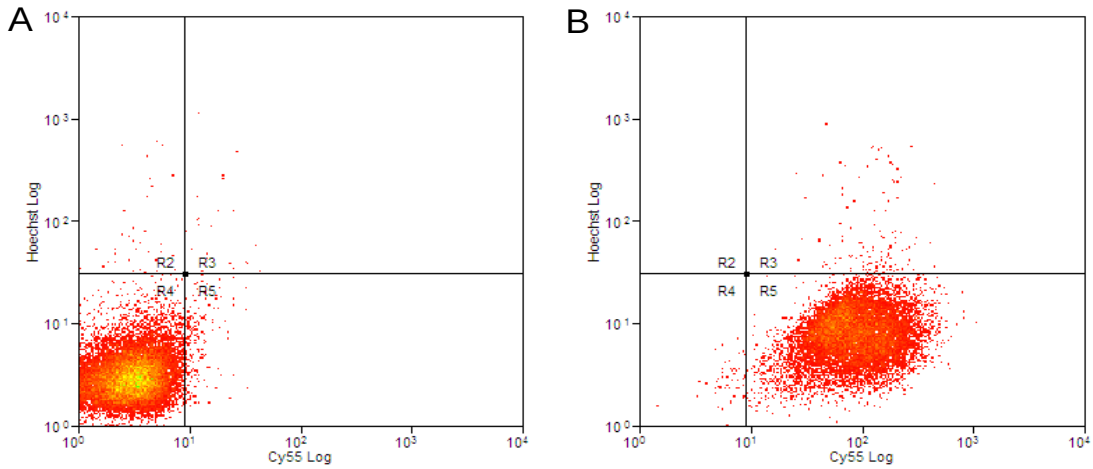

Figure 3-40: Flow cytometry dot plot analyzing viability (y-axis) and SCION uptake (x-axis) of (A) unstained and (B) stained B lymphocytes.

the log scale for this sample's settings, and appear in R2 or R3 on the dot plot. Cells that have absorbed SCION appear in R3 and R5. Over a time period of 65 hr, the percentage of cells with SCION particle decreased, most likely because of digestion of the particles. The majority (85%) of peripheral B cells display first-order exponential kinetics defined

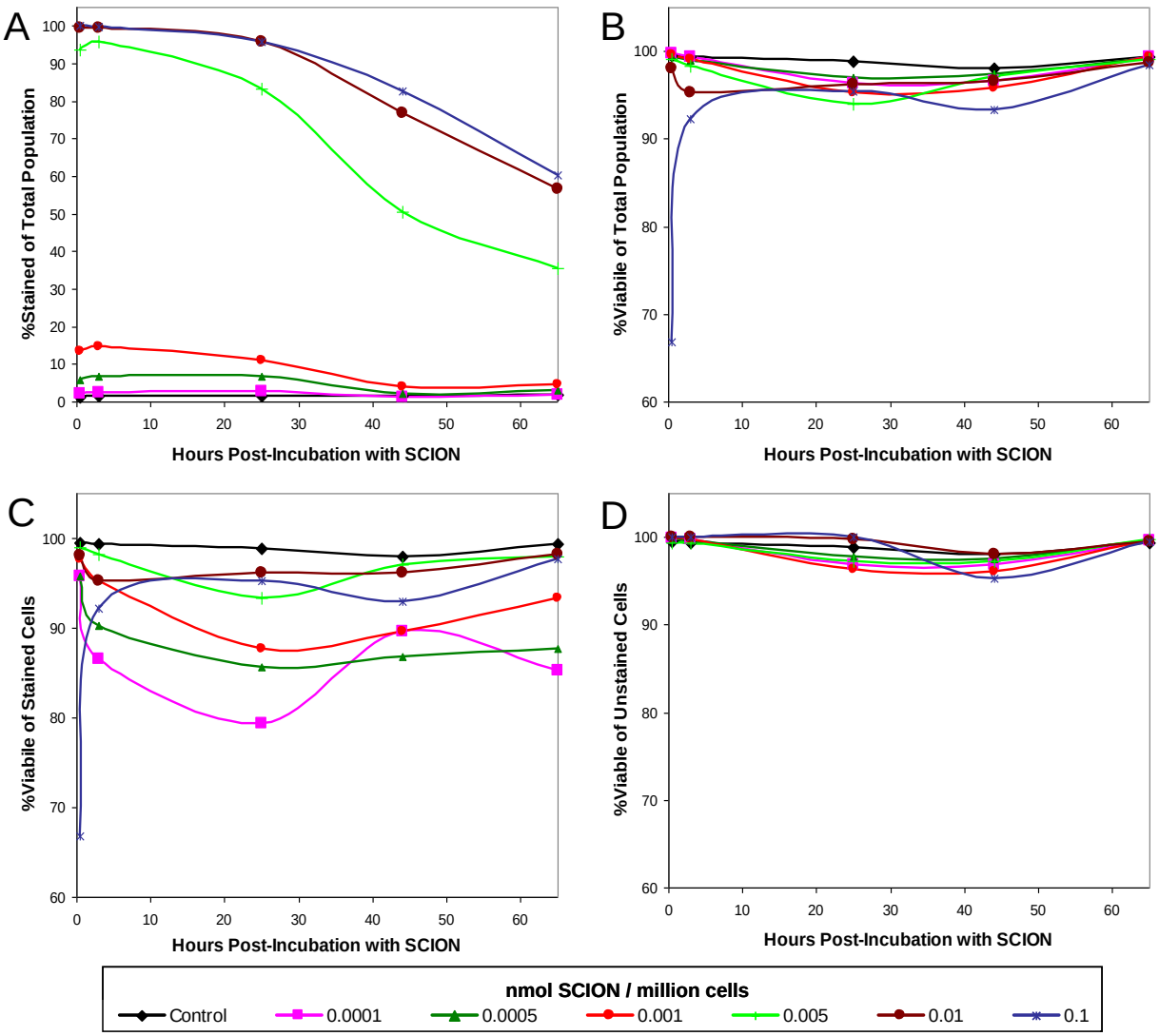

Figure 3-41: Percentage (A) of B cells displaying fluorescence associated with SCION uptake (R3+R5), (B) of total cell population that are viable (R4+R5), (C) of stained cells that are viable (100*R5/[R3+R5]), and (D) of unstained cells that are viable (100*R4/[R2+R4]) observed over a time period of 65hrs.

by a half-life of 5-6 weeks, whilst the remainder are short-lived with a life span of several days [151], so the decrease in percentage of cells with SCION probably was not because of cell division, or mitosis. The lower concentration of stained cells reached background or control level percentages by 48 hr, whereas the three higher concentrations decreased 40-60% by the end of the 65 hr. The study also revealed that cell viability of both the cells that picked up particles and those that did not remained viable. The SCION particle did not directly affect cells that ingested it and did not cause them to release cytokines that would indirectly kill other cells in the population. The one anomaly in the graphs is the starting point of 0.1 nmol/million cells sample, with ~66% viability in both Figure 3-41B and C. Because viability for the later time points remains high, it is possible that the cells were contaminated or affected in some way during staining with Hoechst dye, rather than during incubation with the high concentration of SCION. Either way, such high concentrations of SCION actually are not needed for staining of these cells.

The results obtained, along with studies performed by others groups, suggest that *in vivo* injections of SCION will not significantly affect B lymphocyte viability. Tsouchnikas and co-workers evaluated the effect of iron load on peripheral blood lymphocytes and on circulating cytokine levels in iron-depleted hemodialysis patients receiving recombinant erythropoietin. They determined no change in major lymphocyte subsets, including B cells [152]. Though initial studies in a controlled environment and previous work on similar products look promising for *in vivo* application of SCION, full toxicology studies would need to be conducted to obtain conclusive results.

Chapter 4

Antibody Conjugation to SCION

The clinician's dream is to have an agent that will accumulate efficiently and specifically in target locations, allowing for accurate diagnosis at a stage when disease is still treatable. As in radioisotope imaging, antibodies conjugated to Gd-chelates have been designed to be MR agents particularly for tumor diagnosis [153, 154]. Initial studies of simple adsorption of antibodies to magnetic nanoparticles were successful in maintaining the immunoreactivity of the antibody as well as full relaxation of the particle [155]. Later, IgG antibody was attached to MION by means of electrostatic adsorption or covalent binding for targeting sites of acute inflammation [58]. After *i.v.* administration to normal rats, most MION–IgG localized in the liver, spleen, and bone marrow. In an animal model of myositis, the agent reduced T_2-signal intensity at the site of inflammation. Meanwhile, there was no change in signal intensity after an injection of unlabelled MION. More sophisticated conjugation to magnetic cores have since been reported with different ligands, i.e. human polyclonal IgG [58], mouse monoclonal IgG [156], Fab strands [57], etc. Small animal investigations revealed that it is possible to achieve a high concentration of a magnetic label at the target. This chapter describes a strategy of conjugation used to attach a number of antibodies to a SCION particle.

4.1 Antibody Conjugation to SCION

From silicated quantum dots to silicon wafers, attaching antibody to silica surfaces has become a common practice. A number of techniques exist to achieve this conjugation [157-163]. Because maleimide-thiol reactions are highly selective and strong, the approach used here to conjugate SCION with antibody involved functionalizing the two components with maleimide and thiol groups, similar to the protocol described by Wolcott et al [157].

The first method followed the schematic shown in Figure 4-42, where the antibody was functionalized with maleimide groups and the SCION particle with thiols. The strategy was to over-functionalize the particle surface with thiols and use the antibody as the limiting reagent in the reaction. Sulfosuccinimidyl-4-(*N*-maleimidomethyl)cyclohexane-1-carboxylate (s-SMCC) is a water-soluble and non-cleavable crosslinker that contains an amine-reactive NHS ester and a sulfhydryl- reactive maleimide group. Amines on the antibody form strong amide bonds with the NHS ester of s-SMCC. The SCION surface can be functionalized with thiols using (3-mercaptopropyl)trimethoxysilane (MPS), once again by the Stöber mechanism (Chapter 2). The double bond of s-SMCC's maleimide undergoes an alkylation reaction with free SCION thiol groups to form stable thioether bonds [164]. Maleimide reactions are specific for sulfhydryl groups in the pH range of 6.5-7.5. At higher pH values, some cross-reactivity with amino groups takes place, but at pH 7, the reaction of maleimide with sulfhydryl occurs at a rate 1000 times greater than its reaction with amines [164].

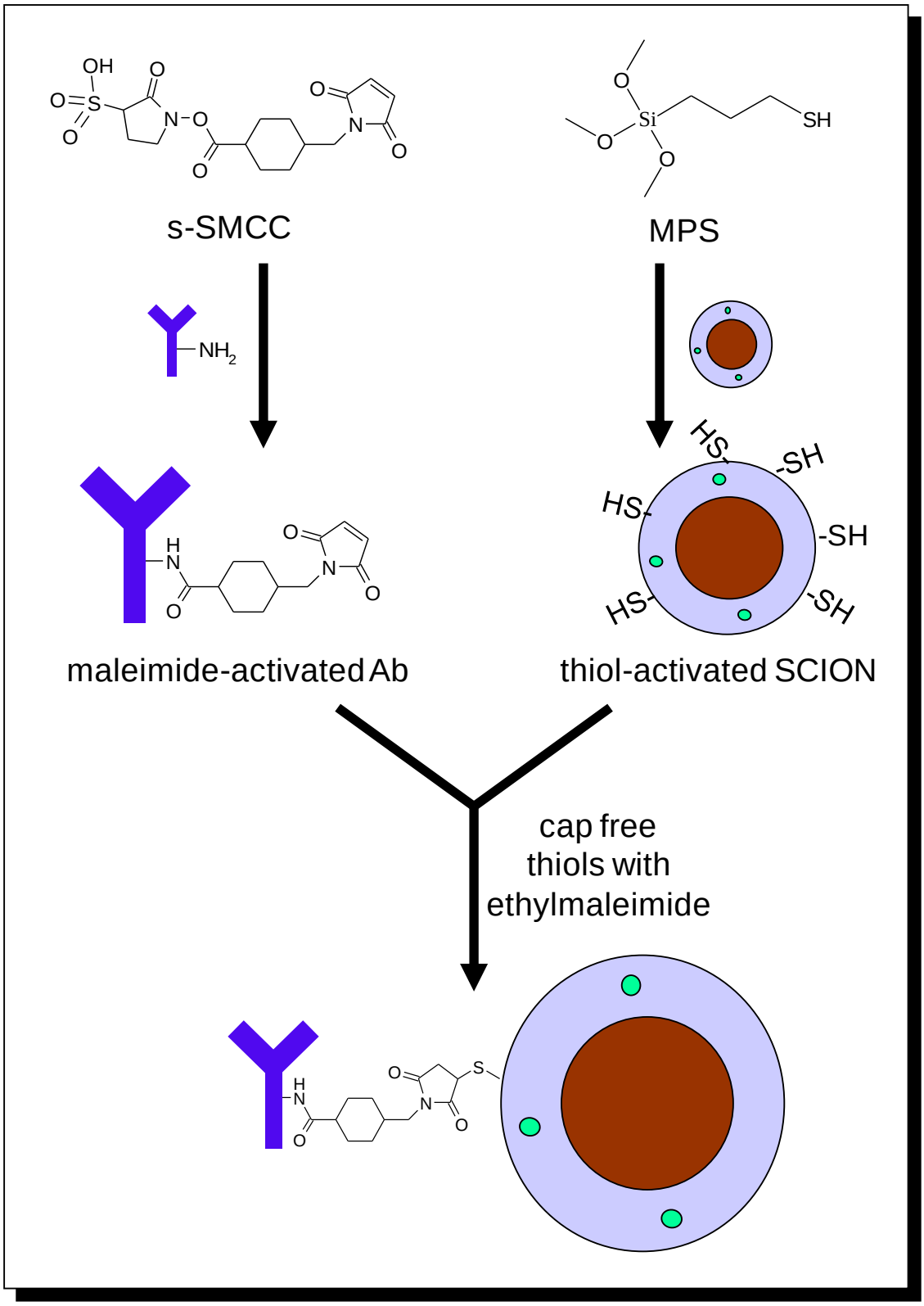

Figure 4-42: Method 1 for antibody-SCION conjugation. Antibody was maleimide- and SCION thiol-functionalized before the two were reacted.

In the standard protocol, antibody was prepared by incubating in 1X phosphate buffered saline (PBS) at room temperature with s-SMCC at a molar ratio of 10:1 s-SMCC:Ab for 1.5 hr with gentle stirring. The activated Ab was separated from excess linker by centrifugation at 3000rpm/10°C in a Centriprep filter with a molecular weight cutoff (MWCO) of 10,000. Meanwhile, SCION particles were functionalized with thiols. For a typical conjugation, 5 nmol SCION were dispersed in 5 mL ethanol and incubated in room temperature with 250 μL of MPS for forty min. The particles were then washed by magnetic separation into a solution of PBS. The maleimide-activated Ab and thiol-activated SCION were then allowed to react overnight in 4°C. For the final step, *N*-ethyl maleimide was added to cap any free thiols. The Ab-SCION sample was washed by magnetic separation with PBS and stored at 4°C.

While this procedure was successful in producing antibody-conjugated particles, it did present some problems. Washing the free MPS off from the thiol-functionalized SCION was problematic especially in high concentration reactions where in the solution would become opaque and gel-like. In such cases, the particles would not separate by magnetic separation, despite sitting in the magnet for days. Another concern was that while handling and storing thiol-functionalized SCION, the sulfhydryls may be oxidized and/or form both intra- and inter-particle disulfide bonds, as shown in Figure 4-43. Since it is necessary to reduce particle aggregation in order to have prolonged blood circulation, the strategy of over-functionalizing particle surface with sulfhydryls was not ideal.

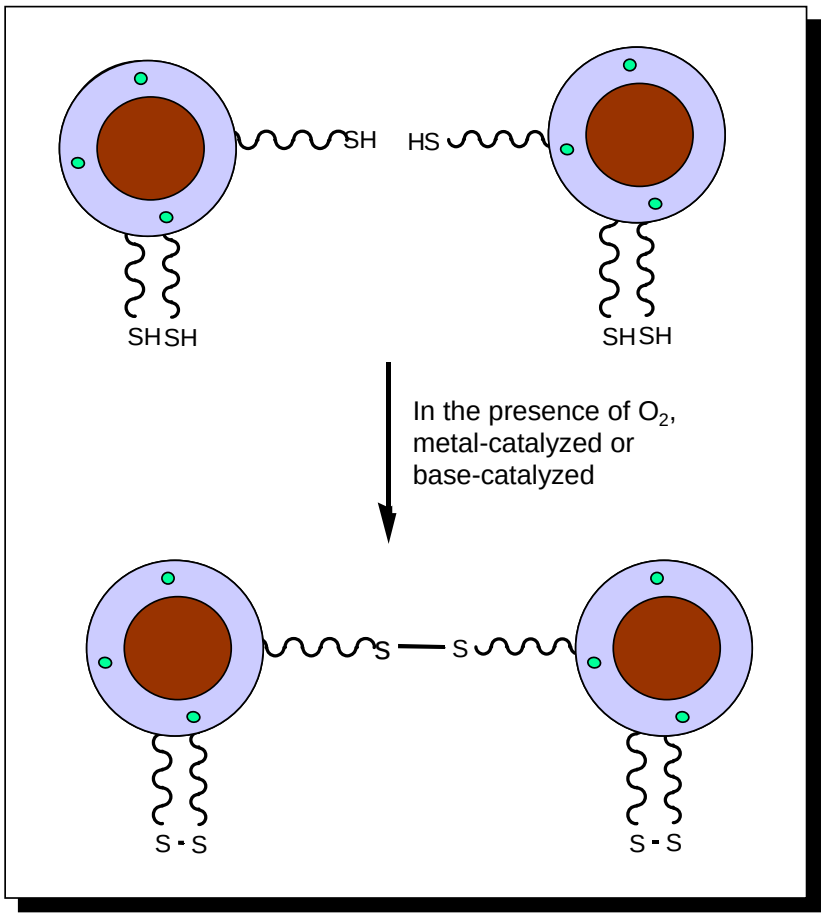

Figure 4-43: Oxidation of sulfhydryls on SCION particles.

In order to address the issues with this method, a modification was made to the conjugation procedure. Rather than functionalizing SCION particles with many thiol groups and then capping free ones after antibody attachment, MPS was reacted to Ab-SMCC conjugate and then the Ab-SMCC-MPS complex was attached to SCION (Figure 4-44). This protocol change prevented potential particle-particle bonds forming between sulfhydryls, as described in Figure 4-43. Maleimide-activated Ab was reacted with MPS at an equivalence of 50 MPS:Ab in PBS at 4°C overnight. SCION particles were then added to the reaction mixture and was once again left at 4°C overnight. The final Ab-SCION sample was washed by magnetic separation with PBS and stored at 4°C.

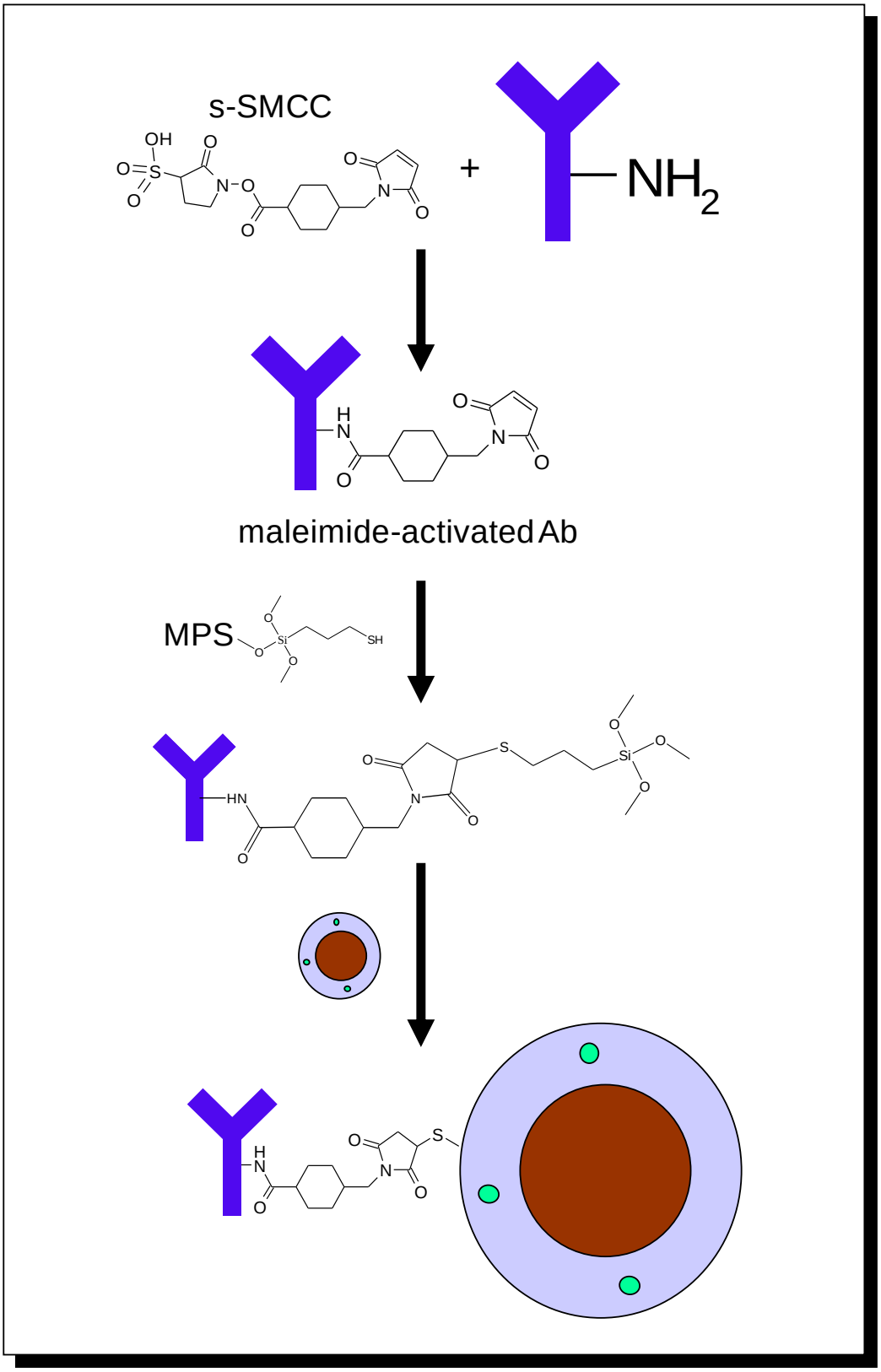

Figure 4-44: Method 2 for antibody-SCION conjugation. Silanized antibody was formed as a Ab-SMCC-MPS reagent before reacting with SCION.

4.2 Flow Cytometry Analysis with Targeted SCION

4.2.1 Fibroblasts Stained with Antibody-Conjugated SCION

The first antibody attached to SCION was L243, an anti–HLA-DR monoclonal antibody (mAb) [165, 166], with the intention of future applications for directing the particles to inflammatory foci in the brain and for evaluation in an available DR2 expressing humanized mouse model for multiple sclerosis [167, 168]. L243 was conjugated to SCION with the first conjugation method from Section 4.1, but for this specific study, free thiols were not capped with ethylmaleimide. Samples of one million fibroblast L cells that express HLA-DR antigens were incubated for 30 minutes in room temperature with a titration (0.0001, 0.001, 0.01, 0.1 nmol SCION) of L243-conjugated or only thiol-functionalized SCION. L243 labeled with the fluorophore phycoerythrin (PE, excitation 488 nm, emission 578 nm) was used as a positive control stain. The cells were then washed three times with 4%FBS/PBS by centrifuging at 500g/4°C for two min and decanting the media. The samples were diluted to 1 mL with 4%FBS/PBS and analyzed with flow cytometry (Cyan ADP Dako cytometer) using an APC laser which excites at 630 nm and collects emissions at 660 ± 20 nm. The cells were gated and 10,000 counts were collected from each sample (refer to Section 3.7 and Figure 3-38). The percentage of cells that displayed fluorescence was recorded (Summit v4.3 software) and signal-to-noise ratio calculated by dividing percent fluorescent of L243-SCION-stained cells by untargeted SCION-stained cells (Figure 4-45).

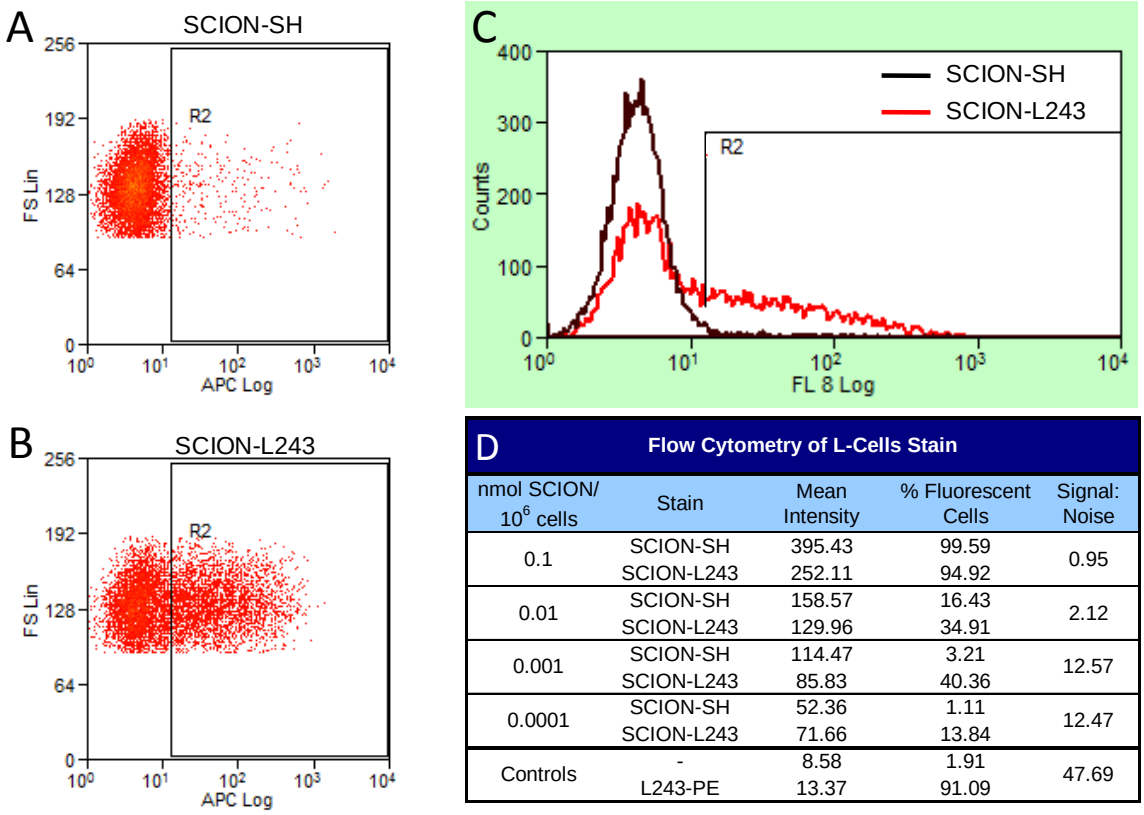

D

Flow Cytometry of L-Cells Stain

nmol SCION/ 10^6 cells	Stain	Mean Intensity	% Fluorescent Cells	Signal: Noise
0.1	SCION-SH	395.43	99.59	0.95
	SCION-L243	252.11	94.92	
0.01	SCION-SH	158.57	16.43	2.12
	SCION-L243	129.96	34.91	
0.001	SCION-SH	114.47	3.21	12.57
	SCION-L243	85.83	40.36	
0.0001	SCION-SH	52.36	1.11	12.47
	SCION-L243	71.66	13.84	
Controls	-	8.58	1.91	47.69
	L243-PE	13.37	91.09	

Figure 4-45: Fluorescence analysis using flow cytometry of L cells stained with (A) unconjugated but thiol-functionalized SCION and (B) L243-conjugated SCION. With APC filter (excitation at 630 nm, emission at 670 nm), cells in gate R2 were considered stained. (C) A histogram representation of the dot plot in (A) and (B). (D) Table summarizing the fluorescence of L cells stained with a range of concentrations of SCION.

The results show that the antibody-conjugated SCION was successful in staining cells *in vitro* with a signal-to-noise ratio of 12.6. This ratio is not as high as the control ratio of 47.7. The antigen-receptor kinetics may be hindered by the attached particle or the antibody may have lost some of its immunoreactivity during conjugation. Note that the filter being used is not optimal for Cy5.5 emissions, whereas for the positive control a PE filter, specific to the fluorophore, was used. Also, the particles in this study were from an initial SCION synthesis batch where fluorescence of the particles had not been optimized. Thus, they would have low detection, even if present. This titration has,

along with a number of similar studies, led to the conclusion that optimal SCION staining occurs at near 0.001 nmol SCION/million cells.

4.2.2 B Cells Stained with Antibody-Conjugated SCION

The same anti–HLA-DR mAb L243 and mAb OX35 were conjugated to SCION with the first conjugation method from Section 4.1. OX35 is a murine anti-rat-CD4 antibody that was used as a negative control antibody for this study. To reduce oxidation, reactions with thiols were conducted under an argon atmosphere. Argon is inert and a heavier molecule than oxygen, so it displaces any oxygen in the solution. Samples of one million DR-expressing MGAR cells (B lymphocytes) were incubated for 1 hr on ice with a titration (0.0005, 0.001, 0.005, 0.01, 0.25 nmol SCION) of L243- or OX35- conjugated SCION. L243 and OX35 labeled with the fluorophore PE were used for control staining. The cells were then washed three times with cold 4%FBS/PBS by centrifuging at 1500rpm/10°C for five min and decanting the media. The samples were diluted to 1 mL 4%FBS/PBS and analyzed with flow cytometry using an APC laser which excites at 630 nm and collects emissions at 660 ± 20 nm. The PE-controls were excited with 488 nm laser and filtered emissions were collected at 575 ± 25 nm. Cells were gated and 10,000 counts were collected from each sample. The percentage of cells that displayed fluorescence was recorded and signal-to-noise ratios calculated by dividing percentage fluorescent of L243-SCION-stained cells by OX35-SCION-stained cells (Figure 4-46).

Once again, the highest signal-to-noise ratio was at the staining concentration of 0.001 nmol SCION per million cells. However, this ratio was not particularly high at 3.15. While the percent binding of L243-SCION (28.44%) was about half that of the

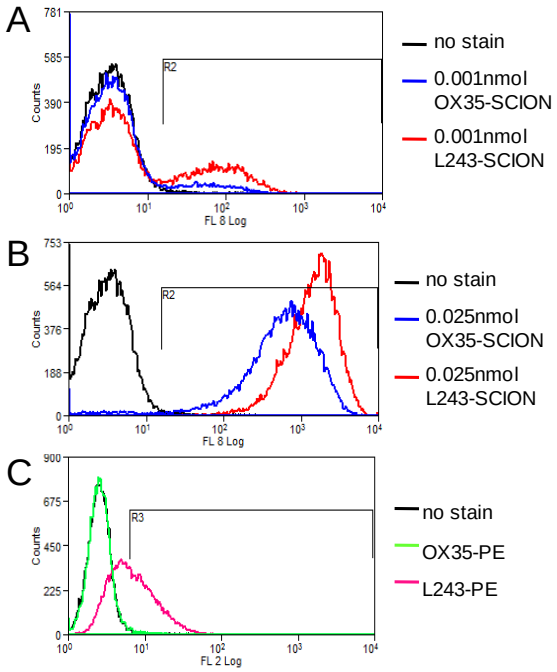

D **Flow Cytometry of MGAR Stain**

nmol SCION/ 10^6 cells	Antibody (-SCION)	Mean Intensity	% Fluorescent	Signal: Noise
0.0005	L243 OX35	133.35 35.23	39.81 29.09	1.37
0.001	L243 OX35	110.63 82.58	28.44 9.02	3.15
0.005	L243 OX35	138.24 159.63	78.14 54.06	1.45
0.01	L243 OX35	486.97 294.27	99.33 74.37	1.34
0.025	L243 OX35	1843.42 749.89	99.85 96.77	1.03
APC Background	-	46.10	1.34	
Controls	L243-PE OX35-PE	10.37 8.66	50.19 2.11	23.79
PE Background	-	8.06	1.48	

Figure 4-46: Flow cytometry of MGAR cells stained with (A) 0.001 nmol SCION per million cells and (B) 0.025 nmol SCION per million cells of OX35 (negative mAb) and L243 (positive mAb) conjugated SCION. (C) Histogram of control staining with PE-labeled OX35 and L243. (D) Table summarizing the fluorescence of MGAR cells stained with a range of concentrations of SCION.

control L243-PE antibody (50.19%), the mean signal intensity was significantly higher with a clear separation of peaks of stained versus unstained cells. In the case of the control antibodies, the mean signal intensity was low for cells labeled with L243-PE (10.37), indicating low expression of the receptor. Thus, the high intensity of low expressing cells stained with targeted-SCION suggests that either when SCION binds it does so in large quantities or that the particles are bright. Figure 4-46B demonstrates that at high SCION concentrations, MGAR cells will uptake the particle regardless of the directing antibody. However, there is a separation of the curves showing a similar difference in intensity between OX35- and L243-SCION when compared to staining by OX35- and L243-PE.

4.2.3 T Cells Stained with Tetramer-Conjugated SCION

A tetramer is a polymer consisting of four identical monomers (Figure 4-47). More specifically, in immunology, major histocompatibility complex (MHC) tetramers can be used to characterize and quantify antigen-specific T cells. MHC tetramers are based on recombinant class I molecules that have been biotinylated. These molecules are folded with the peptide of interest and tetramerized by a fluorescently-labeled streptavidin which binds four biotins per molecule. The tetramer reagent labels T cells that express T cell receptors specific for the given peptide-MHC complex. Tetrahedral tetramers can bind to three TCRs at once, allowing specific binding in spite of low (10^{-6} molar) affinity of the typical class I-peptide-TCR interaction. They demonstrate significantly greater affinity than single labeled MHC class I molecules. The specific and sensitive tetramer allows for detailed evaluation of surface and intracellular phenotype with even very small samples.

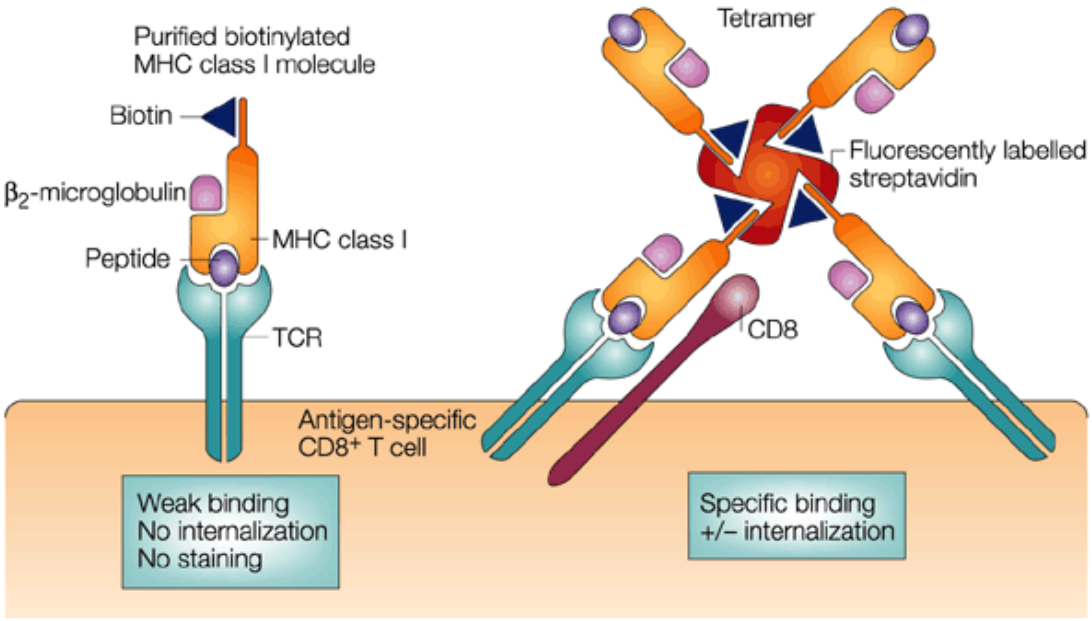

Figure 4-47: Monomer and tetramer binding of T cell receptors [169].

Anti–HLA-A2/Tax biotin tetramer (provided by Lone Friis, Human Immunology Unit, University of Oxford) was conjugated to SCION with the second conjugation method from Section 4.1. The cell lines used for this staining were two T cell lines provided by Manuel Friese (Human Immunology Unit, University of Oxford), BW58 (murine T hybridoma line that lacks endogenous TCR chains [170]) and B7-transfected BW58 cells. B7 is a TCR that recognizes Tax peptide, a protein from HTLV-1 virus presented by HLA-A2 [171]. Samples of one million cells were incubated for 1.5 hr on ice with a 0.001 nmol tetramer-SCION. Free tetramer, which is labeled with PE, was used for control staining on both cell lines as well. The cells were then washed three times with cold 4%FBS/PBS by centrifuging at 1500rpm/4°C for two minutes and decanting the media. The samples were further stained for viability with Hoechst33258 (excitation 352 nm, emission 461 nm). During flow cytometry, the samples were illuminated with excitation lasers with wavelengths of 405, 488, and 635nm. Emissions were collected with filters for FS/SS (488 ± 10 nm), APC (660 ± 20 nm), PE (575 ± 25 nm), and Hoechst33258 (450 ± 50 nm). 10,000 counts were gathered from each sample and viable cells gated. Signal-to-noise ratios were calculated by dividing the percentage stained BW58-B7 cells by the percentage stained BW58 cells (Figure 4-48).

Tetramer-conjugated SCION showed mediocre attachment to B7 on T cells at 28.8% staining. The signal to noise ratio was noticeable at 4.7, but not as high as the free tetramer's 12.4 with staining at 80.5%. There is minimal non-specific uptake by these cells of either SCION or tetramer.

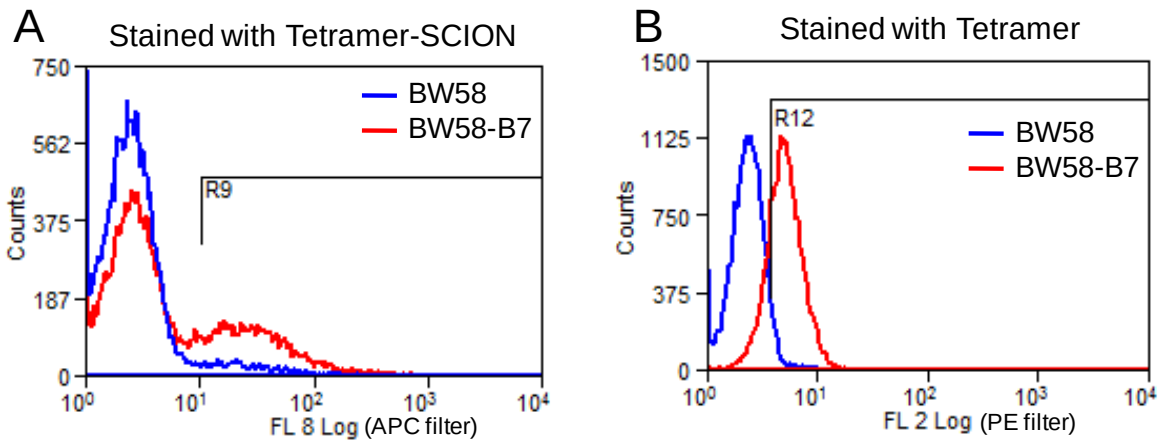

	B7 Expressor	Mean Intensity	% Fluorescent	Signal: Noise
tetramer-SCION	+	55.81	28.76	4.71
	-	41.39	6.11	
tetramer	+	5.89	80.05	12.35
	-	4.81	6.48	

Figure 4-48: Flow cytometry histographs of gated viable B7 positive and negative BW58 cells stained with (A) tetramer-conjugated SCION and (B) free tetramer. (A) Table summarizing staining.

All three of these flow analyses, show that while there is staining with targeted-SCION, it is not very high. A number of issues may be affecting these results. The first is that there is not enough ligand or that the reactivity of the ligand has been reduced. There was, however, a more practical problem observed. The targeted particles all had difficulties associated with solubility in PBS after conjugation to the ligand. In all cases, the agent would precipitate after ~1 hr. During the cell staining protocol, there was always a concern that the particles would not stay dispersed affecting receptor-binding kinetics, and in samples of higher concentrations, this was visibly noted. The same behavior was true during washing steps that involved centrifugation. Particles would accumulate with the cells due to the centrifugal force, and would have to be redispersed by pipetting. False positive results were not a concern because the cells could easily be gated and separated with flow. Perhaps, a longer staining time period or agitation during

the staining period would have enhanced staining. The best solution would of course be to address solubility issues. An antibody-SCION sample was analyzed with DLS, and the point of zero charge, as determined from zeta potential measurements, was found to have increased to ~pH5 with significant aggregation in the range of pH 4-7. At a higher a pH, Ab-SCION remained in solution. However, this is not a practical solution, because cells are not healthy or viable in basic conditions. Strategies to reduce surface charge and keep the conjugated particles in solution are still being explored.

4.3 Chelated Antibody Conjugation to SCION

Thus far, the SCION particle that has been synthesized is a targeted dual-modality particle which provides contrast for MR and optical imaging. To also be able to use it for nuclear imaging techniques, a chelate must be attached, preferably to the antibody. When the radio-labeled antibody that targets delivery is co-registered at the same location as the MRI and optical signal, the stability of the entire compound can be confirmed. Given that both a chelate and a linker to conjugate to SCION are attached to the antibody, the goal is to minimize these groups to reduce an effect on immunoreactivity. Because there were problems with generating repeatable results on the number of silane (or maleimide) groups per antibody, a different method was used to conjugate antibody to particle, outlined in Figure 4-49. Particles were functionalized with maleimides and the antibody then was functionalized with thiols.

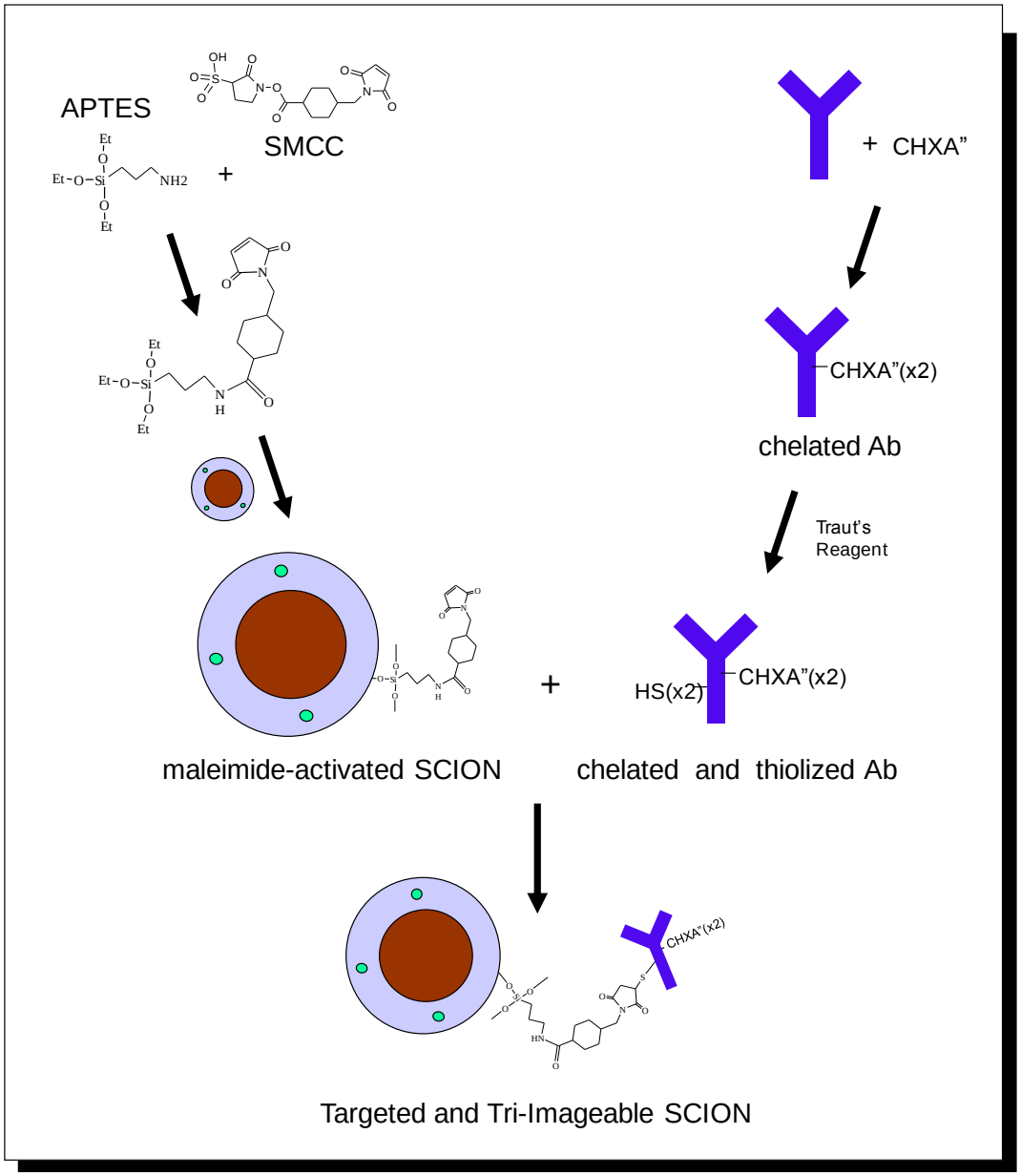

Figure 4-49: Method for conjugating chelated antibody to SCION by thiolizing the antibody and maleimide-activating the particle.

4.3.1 Maleimide-Activation of SCION

First, succinimidyl-4-(*N*-maleimidomethyl)cyclohexane-1-carboxylate (SMCC) and 3-aminopropyltriethoxysilane (APTES or APS) were reacted at an equivalence of 1.3 APTES:SMCC and concentration of 50mM APTES in DMSO. The reaction was run for

1 hr with agitation at room temperature. The conjugation was always confirmed using thin layer chromatography with silica plate and 50% methanol in chloroform, i.e. Figure 4-50.

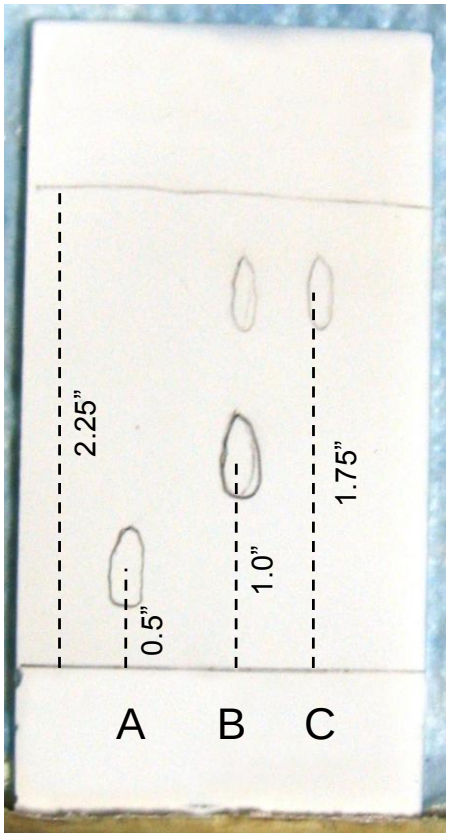

Figure 4-50: Thin layer chromatography of (A) APTES (r.f. = 0.222), (B) APTES-sSMCC conjugate (r.f. = 0.778), and (C) sSMCC (r.f. = 0.444).

The SMCC-APTES conjugate solution was then reacted with SCION overnight in room temperature at an equivalence of ~150 SMCC-APTES:SCION. Typically the solution was at a concentration of 1-2 nmol SCION/mL in water. The particles were then dialyzed with tubing or float-a-lyzer of 100,000 MWCO in four washes of a minimum of 1 L water for 4 hrs to remove unreacted SMCC-APTES. Ellman’s Reagent was used to quantify the number of maleimides per particle. When 5,5'-dithio-bis-(2-nitrobenzoic acid), more commonly known as DTNB or Ellman’s reagent, is reduced by free thiols, it releases 2-nitro-5-thiobenzoic acid (TNB) as a product that can be detected by absorbance at 412 nm [172].

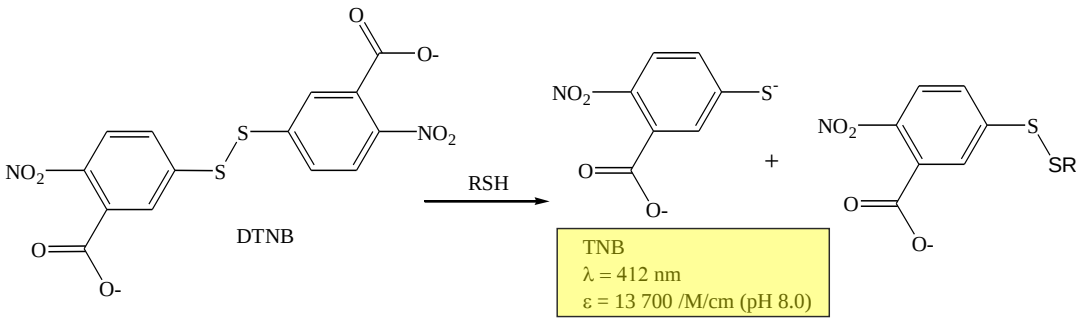

Figure 4-51: Reaction of Ellman’s reagent with free sulfhydryls

SCION's maleimides were measured by first reacting duplicates of the un-functionalized and functionalized particles with different amounts of cysteine for 20 min and then with Ellman's reagent for 15 min. After these steps, the particles were separated from the solution by centrifugation with 50 kDa filter to prevent differences in absorption due to particle scattering and absorption. The difference in cysteine of corresponding particle samples was calculated and compared to a standard curve of cysteine absorption and a control sample with particle and no cysteine that followed the same washing and analysis

Table 4-8: Quantification of maleimides on SCION particle using Ellman's reagent and a standard curve with cysteine.

Standard Curve	
uM Cysteine	Abs 412
0	-0.00013
4	0.02883
8	0.08882
16	0.17625
30	0.35100
40	0.46959
50	0.59816
75	0.87461

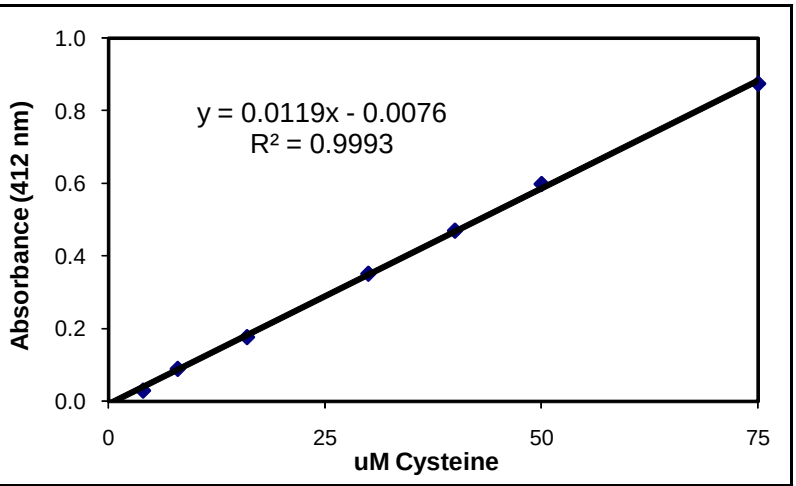

Samples						
uM Cysteine added	Sample	Abs 412	Mean A412	Difference in A412	Maleimide per SCION	Mean Maleimide per SCION
30	SCION	0.38439	0.37377	0.104	88.5	83.4
		0.36315				
	SCION-mal	0.25853	0.27020			
		0.28186				
40	SCION	0.47533	0.49179	0.093	79.1	
		0.50825				
	SCION-mal	0.41366	0.39926			
		0.38486				
50	SCION	0.58403	0.59110	0.097	82.5	
		0.59816				
	SCION-mal	0.51277	0.49457			
		0.47636				
0	SCION-mal	0.00214	0.00744			
		0.01275				

(Table 4-8). The particles on average had ~80 maleimides per SCION. Because maleimides are stable groups at pHs below 8.0, these functionalized particles could be made and stored for long time periods.

4.3.2 Chelation of Antibody

A number of chelating agents that are dependent on the coordination chemistry of the chosen radionuclide have been developed. One such family of chelates, 2-(p-isothiocyanatobenzyl)-cyclohexyl-diethylenetriaminepentaacetic acid (CHX-DTPA), shown in Figure 4-52, provides efficient labeling with ^{111}In and demonstrates maintenance of integrity and immunoreactivity of its radioimmunoconjugates [173, 174]. Its aromatic isothiocyanate arm can be used for attaching to amines on antibodies.

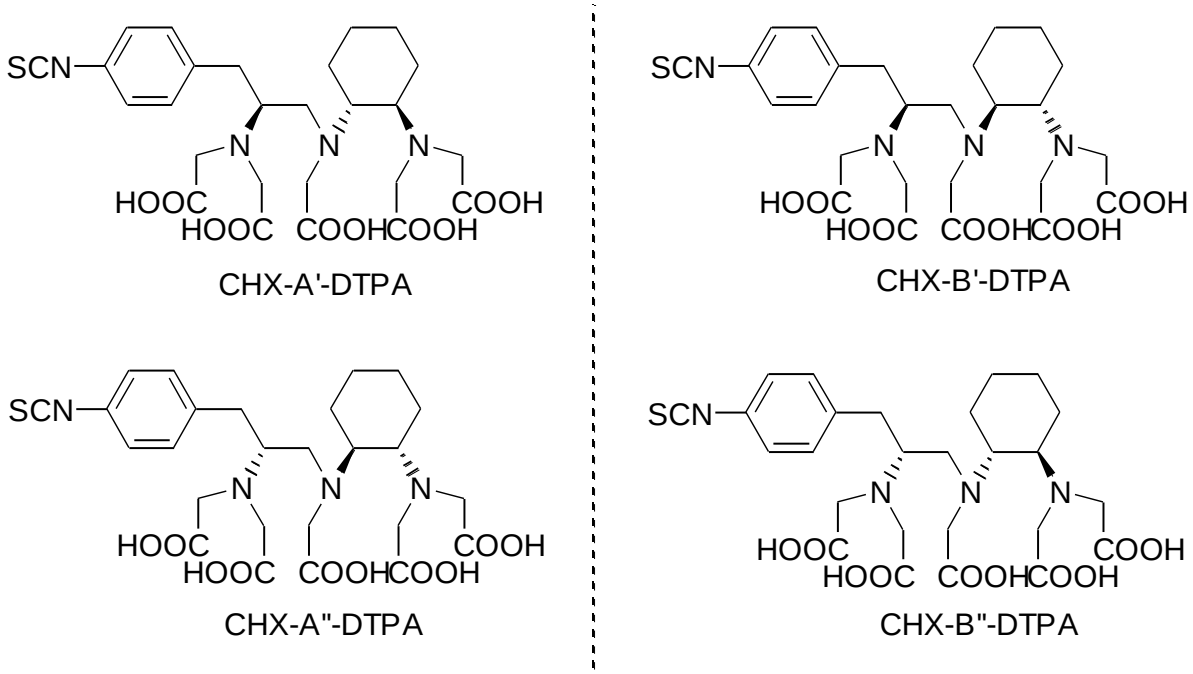

Figure 4-52: Structures of stereoisomers of the CHX-DTPA chelating agents.

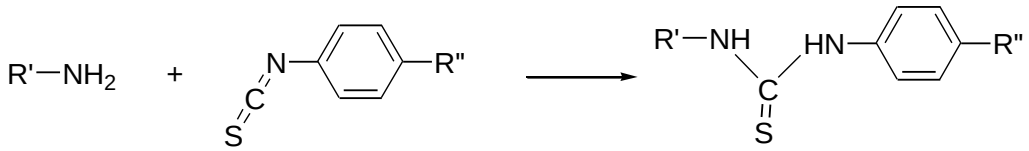

Figure 4-53: Reaction of CHX-DTPA isothiocyanate with Ab amine.

When compared in athymic mice bearing human colon carcinoma LS-174T tumors, CHX-A radioimmunoconjugates demonstrated greater *in vivo* stability with lower blood clearance rates and more efficient and stable tumor localization than conjugates with its isomer CHX-B [175]. In another study, a small but significant ($p<0.05$) difference was recorded between CHX-A" and CHX-A', wherein CHX-A" was found to be slightly more stable [176].

The most crucial requirement for the antibody chelation is that it is conducted under stringent *metal-free* conditions. All vessels and reagents must be prepared to meet this constraint. For demetallation of all buffers, a Chelex-100 (BioRad Na^+ form 200-400 mesh resin) column was used. Two buffers were prepared and passed through the chelex column to remove any metal.

1) 10X Conjugation Buffer: 80.44g $NaHCO_3$, 4.50g Na_2CO_3, and 175.32g NaCl in 2L deionized water
2) 10X Ammonium Acetate Buffer: 1.5M NH_4OAc solution

Glass containers were avoided and only metal free pipette tips were used. Extreme care was taken to keep all steps metal-free. Antibody was reacted to CHX-A" at a molar equivalence of 10 chelate:Ab in 1X conjugation buffer with 0.05 M ethylenediaminetetraacetic acid (EDTA) at ~pH 8. The reaction was run 3.5 hr at 37°C and, subsequently, dialyzed (SPECTRUM cellulose dialysis kit, MWCO 10,000) five times against 1 L metal-free 1X ammonia acetate buffer for a minimum of 4 hrs each at

4°C while stirring gently. The number of chelates (~2 chelates per Ab) was always evaluated by the Lowry assay and a spectrophotometric assay using yttrium–arsenazo III complex [177]. First described in 1951 [178], the Lowry protocol is one of the most widely-used protein determination assays. Under alkaline conditions, copper complexes with protein. When folin phenol reagent is added, it binds to the protein and is slowly reduced, changing color from yellow to blue. Absorbance at 750 nm can then be correlated to protein concentration. The spectrophotometric method used for quantifying chelate is based on the reaction between chelate and a yttrium(III) complex of arsenazo III, a highly sensitive colorimetric reagent [177].

$$Y(AAIII)_2 + CHXA'' \rightarrow Y(CHXA'') + 2AAIII \quad (14)$$

The absorbance of $Y(AAIII)_2$ (λ_{max} = 662 nm) decreases upon the addition of CHX-A" while the corresponding absorbance of AAIII (λ_{max} = 538 nm) increases.

Further analysis was performed to examine the ability to radiolabel the chelated antibody. Antibodies that were chelated were EGFR1 mAb Cetuximab (Erbitux; ImClone Systems, New York, NY) [179] and its negative control of humanized mAb HuM195 that targets CD33 [180] absent in mice. Typically, to radiolabel CHX-A"-Cetuximab , 350 µCi of ^{111}In would be incubated with 50 µg mAb at 37°C and pH 7 in a volume of 20 µL for 1 hr. A volume of 4 µL of 0.1 M EDTA would be added to remove free ^{111}In and then the solution could be collected in fractions as it was passed through a PD10 desalting column with PBS solvent. The first peak of radioactive material would be collected as the labeled antibody, typically with ~90% labeling efficiency. The labeled conjugate was analyzed by size-exclusion high-performance liquid chromatography (SE-HPLC) and instant thin layer chromatography (ITLC). HPLC is a form of column chromatography used to separate and identify compounds, and size exclusion

chromatography (SEC), also known as gel permeation or filtration chromatography, separates based on size. A TSK Gel G3000SW column (Tosoh Bioscience, Montgomeryville, PA) once loaded with sample, was pumped with PBS at a flow rate of 0.5 mL/min while a detector recorded the retention times of molecules as they came off the column. Retention times vary depending on interactions between the column packing material, the molecules of interest, and the solvent. Both the absorbance at 280 nm and the radioactivity of the labeled antibody were recorded as material came off the column (Figure 4-54A). The signals for antibody and radioactivity co-registered indicating that the antibody did in fact label.

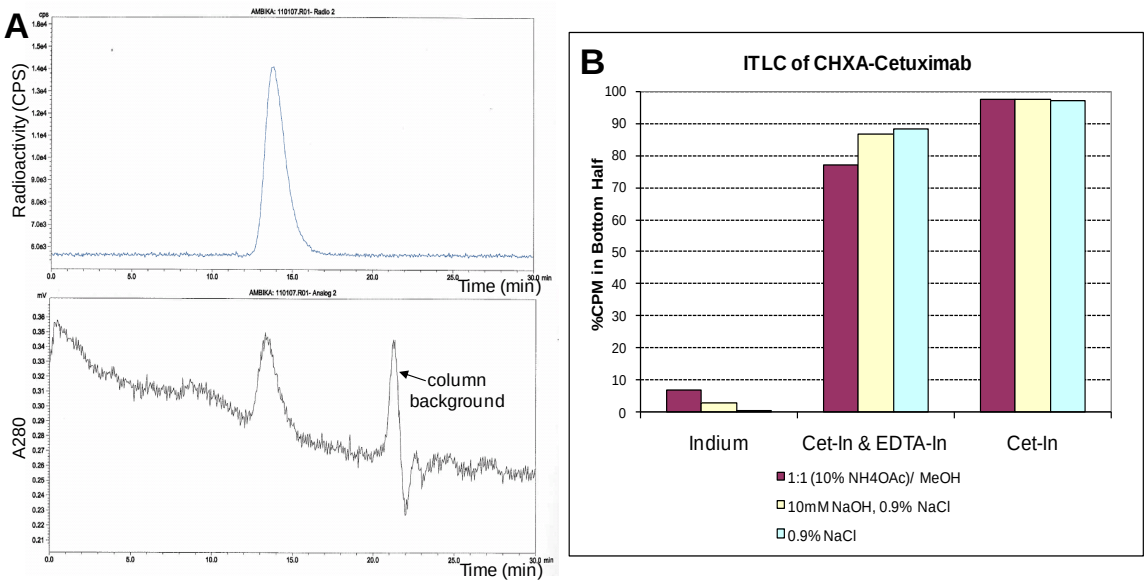

Figure 4-54: Analysis of ^{111}In-labeled Cetuximab. (A) Size exclusion HPLC demonstrating radioactive peak at same retention time as A280 antibody peak. (B) Percent radioactivity in bottom half of strips from ITLC of ^{111}In, labeling reaction mixture, and separated ^{111}In-labeled Cetuximab in three different solvents.

ITLC is similar to TLC but rather than using a silica plate and visually identifying separation, strips of absorbent glass microfiber sheets were dotted with free ^{111}In, the reaction mixture of ^{111}In-labeled EDTA and ^{111}In-labeled Cetuximab, or the separated

fraction of ^{111}In-labeled Cetuximab. Three solvents were used: 1:1 10%EDTA/0.1M NH_4OAc, 10 mM NaOH in 0.9% NaCl, and 0.9% NaCl. After the solvent reached near the top through capillary action, the strips were cut into a bottom and top half and both were individually counted in a γ-scintillation counter with a three inch crystal (Wizard, 1480 Autogamma counter, EG&G WALLAC, Turku, Finland). The percentage of the total cpm per strip found in the bottom half of the strips are presented in Figure 4-54B. Free ^{111}In and labeled EDTA moved to the top half of the strip while the labeled-Ab remained at the bottom. There was high labeling efficiency, based on results of the reaction mixture, and a clean collection of labeled-Ab was demonstrated by the mean 97.5% reactivity in the bottom half of the filtered final sample.

4.3.3 Thiol-Functionalization of Chelated Antibody

To functionalize the Ab, the solvent was first changed to 5 mM EDTA in PBS by filtered centrifugation and the antibody concentrated to 10 mg/mL. Traut's reagent (2-iminothiolane•HCl) was added at a molar equivalence of 15 Traut's:Ab. Traut's reagent is a water soluble molecule that reacts with primary amines at pH 7-10 to introduce sulfhydryl groups [181].

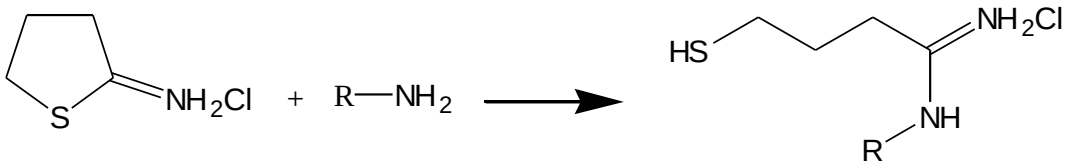

Figure 4-55: Traut's reagent reaction with amine group.

The reaction mixture was always kept under argon. Thiols can form disulfide bonds in the presence of O_2, metal, or when in basic conditions. Thus, the presence of

EDTA to pick up free metals and argon to displace oxygen reduced disulfide formation that could cause antibody aggregation. After reaction for 1 hr at room temperature, the modified antibody was separated from free Traut's reagent by PD-10 column elution with PBS, degassed, and the vial capped under argon. The number of thiols (2-3 thiols/Ab) were determined by first the Lowry assay to measure protein concentration, followed by thiol quantification using Ellman's reagent and a cysteine standard curve.

4.3.4 Final Tri-Imageable SCION

For the final conjugation of chelated and thiol-functionalized antibody to maleimide-activated SCION, the two components were reacted overnight at 4°C at a molar equivalence in the range of 20-35 Ab:SCION. Free antibody was washed away by centrifugation with 6-8 spins of 4 min at 1500rpm and removal of supernatant. To cap free particle maleimides, iodacetamide (IA) was added at an equivalence of 100 IA:SCION and reacted for 40 min at room temperature. Free IA was removed by dialysis against PBS, and the final product was stored in PBS. Quantifying the number of antibodies per particle was a challenge that was not adequately completed. When using the Lowry protein determination assay, the absorbance at 750nm would not stabilize and continuously increased to a peak value off the linear region of the standard curve regardless of the concentration of particle in the sample. A second strategy of quantifying the number of chelates per particle was tried; however, again the controls and absorbance readings were not satisfactory. Though the number of Ab was not quantified, their presence was established. The particles were successfully radiolabeled.

To radiolabel the particle, 0.175 nmol of SCION was incubated with 900 μCi of ^{111}In in a volume of 60 μL of 5M NH_4OAc (pH 7) at 37°C for 45 min. A volume of 4 μL

of 0.1 M EDTA would be added to quench the reaction and remove free ^{111}In. To collect the labeled particles, the solution was spin filtered with an Amicon 50 kDa filter and the collected sample showed a radiolabeling efficiency of ~70%.

4.4 Radioimmunoassays

To understand the effect of SCION conjugation on the antibody, a series of binding assays was conducted. The immunoreactivity of the ^{111}In-Cetuximab-SCION conjugate was assessed in comparison to ^{111}In-labeled Cetuximab and ^{125}I-labeled Cetuximab (labeling by Kwamena Baidoo, NCI Radiation Oncology Branch) by a solid-phase radioimmunoassay. 100 ng (100 μL) of antigen EGFR (Sigma-Aldrich) was adsorbed overnight onto the wells of microtiter 96-well plates at 4°C. Prior to use, the wells were washed thrice with 150 μL 1% BSA in PBS. The solvent wash was removed by flicking the plate onto an absorbant pad. Serial dilutions of the radioimmunoconjugates (RICs) in 1% BSA in PBS (50 μL) were added in duplicate to the antigen-coated microtiter wells starting at ~200,000 cpm. As a control to confirm the specific reactivity of the RICs, wells were also incubated with ~200,000 cpm of the RIC along with an excess (10 μg) of unlabeled Cetuximab. Following 4 hr of incubation at 37°C, the wells were again emptied and washed three times with 1% BSA in PBS. The radioactivity was then transferred to tubes using 0.2 M NaOH and evaluated in a γ-scintillation counter. The percentage of radioactivity remaining was calculated for each dilution of RIC and the percentage of binding reported was the average value of the serial dilutions.

Table 4-9: Immunoreactivity assessment of SCION-conjugated Cetuximab from an antigen binding assay.

	% Binding	% Binding with excess unlabeled Cetuximab
^{111}In-Cetuximab-SCION	8.8%	1.5%
^{111}In-Cetuximab	56.8%	0.1%
^{125}I-Cetuximab	52.8%	0.1%

The observed percentage of binding was low, not just for the SCION-conjugated Ab, but also free Ab. Given that the positive controls were not as high as they typically are and that antigen binding assays with EGFR are a bit problematic, a cell binding assay was performed to confirm if immunoreactivity has truly been compromised.

This time, the ^{111}In-Cetuximab-SCION conjugate was compared only to ^{111}In-labeled Cetuximab and rather than plating wells with EGFR antigen, human squamous carcinoma A431 cells that have high *in vitro* levels of EGFR expression were used for binding assessment. A431 cells were harvested, pelleted at 1000g (Allegra 6KR; Beckman Coulter, Palo Alto, CA), re-suspended in PBS (pH 7.2) containing 1% BSA and added to polypropylene tubes (1×10^6 cells in 100 μL). Again, serial dilutions of the RICs in 1% BSA in PBS (50 μL) were added in duplicate to the cells starting at ~200,000 cpm. As a control to confirm the specific reactivity of the RICs, cells were also incubated with ~200,000 cpm of the RIC along with an excess (10 μg) of unlabeled Cetuximab. Following an overnight incubation at 4°C, the cells were washed once with 4 mL of 1% BSA in PBS, pelleted at 1000 g for 5 min and the supernatant decanted. The pelleted cells were then counted in a γ-scintillation counter and the percentage of binding was calculated.

Table 4-10: Immunoreactivity assessment of SCION-conjugated Cetuximab from a cell binding assay.

	% Binding	% Binding with excess unlabeled Cetuximab
^{111}In-Cetuximab-SCION	69.1%	61.1%
^{111}In-Cetuximab	61.4%	9.0%

The percentage binding of SCION-conjugated Cetuximab (69.1%) was slightly higher than even the positive control of unconjugated Cetuximab (61.4%). However, the negative control with excess unlabeled Cetuximab also showed high binding. It is possible that during washing centrifugation steps, the particles, bound or unbound, pelleted out with the cells. A second reason may be that cell uptake is partially facilitated by the SCION particle and thus this assay is not assessing Ab reactivity.

To rule out the second option, the same cell binding assay was performed with A431 cells that were fixed in 70% ethanol and then washed into 1% BSA in PBS. Four RICs were evaluated in the assay: ^{111}In-Cetuximab-SCION, ^{111}In-Cetuximab, ^{111}In-HuM195-SCION, and ^{111}In-HuM195. The results are presented in Table 4-11.

Table 4-11: Immunoreactivity assessment of SCION-conjugated Cetuximab from a fixed cell binding assay.

	% Binding	% Binding with excess unlabeled Cetuximab
^{111}In-Cetuximab-SCION	96.42%	99.68%
^{111}In-Cetuximab	65.02%	4.79%
^{111}In-HuM195-SCION	61.94%	65.97%
^{111}In-HuM195	4.19%	3.99%

Again, binding was high, particularly with SCION-conjugated Cetuximab (96.42%). The control antibodies were correct with background binding levels at ~4% for labeled HuM195 and quenching with excess Cetuximab with both labeled Cetuximab and HuM195. However, the particle negative control of HuM195-SCION (61.94%) displayed binding as high as positive control labeled-Cetuximab (65.02%). Excess cold Cetuximab made no difference in either SCION sample, indicating that there is a protocol problem with washing by centrifugation and that this assay was not correctly assessing Ab immunoreactivity. The difference in binding of Cetuximab-SCION and HuM195-SCION might indicate some binding, but again, this was not a reliable analysis. Ensuring complete washing of unbound SCION is a challenge for most binding assays. Because the NCI Radiation Oncology Branch lab is well equipped for tumor-bearing small animal studies, it was decided that work would proceed by studying the biodistribution of Cetuximab-SCION compared to that of HuM195-SCION to understand the targeting ability of these particles. The results are presented in Chapter 5.

Chapter 5

SCION *In Vivo* Studies

5.1 *In Vivo* Tri-Imaging with SCION Injection

Interest in the development of multi-modal nanoprobes for *in vivo* disease diagnosis and therapy has increased significantly. Existing non-invasive diagnostic techniques such as MRI and CT are very valuable for diagnosis. However, they do not allow direct and gross visualization of tumor tissue with the naked eye during surgery. It would be ideal to have an agent that enhances contrast in pre-operative diagnosis imaging techniques and then also optically enhances tumors in real-time during surgery. Therefore, we have developed a tri-imageable ^{111}In-Cy5.5-USPIO particle.

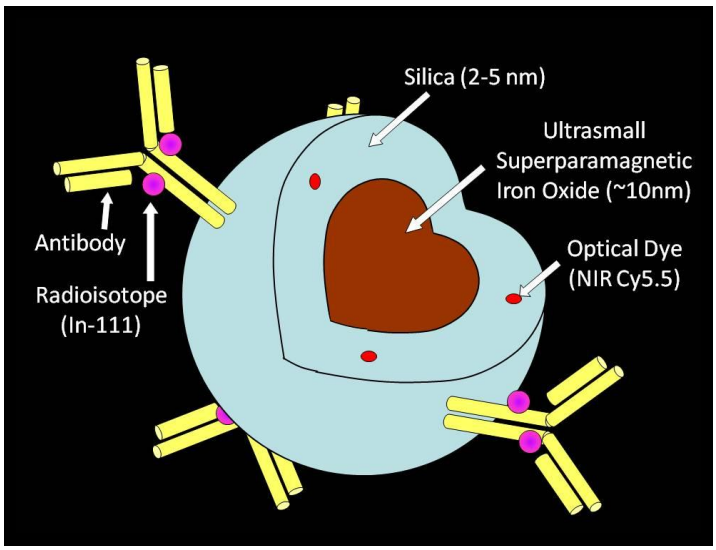

Figure 5-56: Tri-imageable SCION particle schematic.

As a proof-of-principle study to determine if the agent could be imaged *in vivo*, mice bearing subcutaneous human colon carcinoma LS-174T tumors were given

intratumoral injections of ^{111}In-Cet-SCION and examined with MR, optical, and γ-imaging. For all studies, female athymic (*nu/nu*) mice were purchased from Charles River Laboratories at 4–6 weeks of age and housed in a specific pathogen-free American Association for Laboratory Animal Care approved facility. Animals were used between 6 and 8 weeks of age and all experiments were approved by the National Cancer Institute's Animal Care and Use Committee. LS-174T tumor cells were obtained from the NIH and cultured in Dulbecco's Modified Eagle's Medium (DMEM) supplemented with 10% Fetalplex and 1 mM L-glutamine, in a 5% CO_2 environment. Cells were harvested by mild trypsinization at mid-log growth phase, washed in complete growth medium and re-suspended after centrifugation in DMEM with 20% Matrigel at $5x10^6$ cells per mL. Subcutaneous injections of 200 µL into the mouse right hind leg were given within 30 min of harvest. After approximately two weeks of growth, animals bearing tumors of 0.1 to 0.5 g were selected. Because of radioactive safety requirements and the inability to transfer to or scan radioactive animals in the MRI facility, the study was divided into two groups (n=2-3 each) with one set for MR/optical imaging and another for γ-/optical imaging.

The first group was given cold (not labeled with ^{111}In) intratumoral injections of Cet-SCION (40 µL of 11.5mM Fe SCION in conjugation buffer). MR images were obtained using a 3T clinical scanner (Signa Excite, General Electric Medical System, Waukesha, WI, USA) equipped with a solenoidal coil with an inner diameter of 40 mm and a coil length of 40 mm (Philips Research, Hamburg, Germany) (Figure 5-57). MRI was performed with assistance by Celeste Regino (NCI). The coronal images were positioned based on axial scout images. Mice were anesthetized using gas mixtures of 1.5-2.5% isofluorane in O_2 to maintain a respiration rate of ~30 bpm during the entire

MRI. Respiratory triggered, fat suppressed, short inversion time inversion recovery (STIR) images (repetition time of 5000 ms, echo time of 32.44 ms, 90° flip angle, voxel size of 0.16 x 0.16 x 1.00 mm, resolution of 6.398 pixels per mm) were obtained prior to injection of the imaging agent and post-injection at 2 hr.

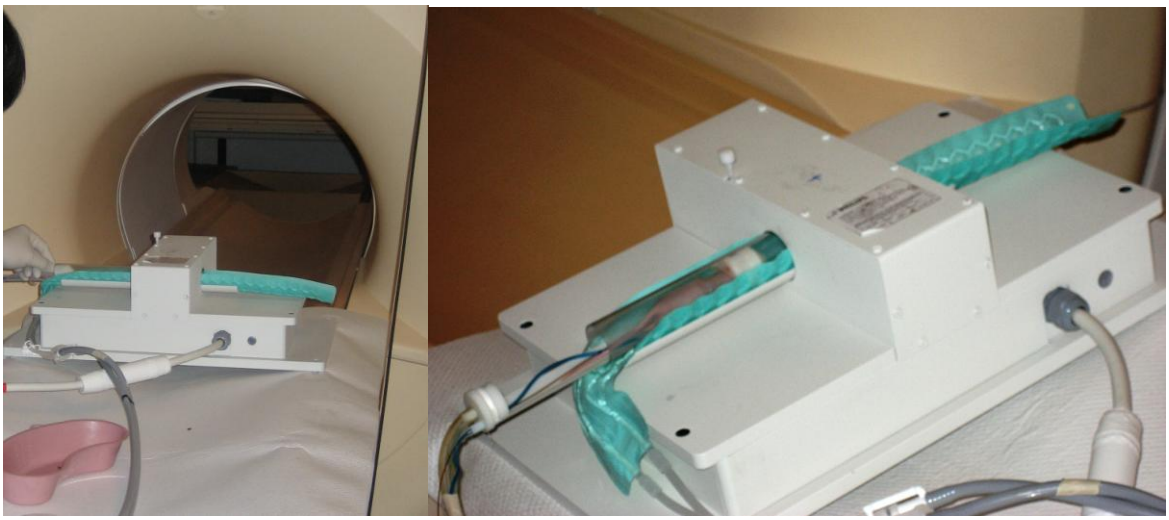

Figure 5-57: Solenoidal coil (inner diameter = 40 mm, coil length = 40 mm) used for single animal MRI. The animal was positioned in the center of the coil. The holding tube had continuous oxygen and anesthesia flow and was and was kept warm with a heating pad.

After the final MR image acquisition for each mouse, it was sacrificed by CO_2 inhalation. Whole body spectral fluorescence images using the Maestro *In Vivo* Imaging System (CRi, Inc., Woburn, MA) were obtained with a 575 to 605 nm band pass excitation filter and a 645 nm long pass emission filter. The tunable filter was automatically stepped in 10 nm increments from 650 to 850 nm while the camera captured images at each wavelength interval with constant exposure. Spectral unmixing was performed using the Maestro software (CRi, Inc., Woburn, MA) to create unmixed and composite images of SCION and autofluorescence spectra.

The second group of animals was given intratumoral injections of ^{111}In-Cet-SCION (40μL of 100 μCi ^{111}In in conjugation buffer). Both γ and optical images were taken post-injection at t=0, 4, and 29 hr. Gamma scintigraphy was performed using a γ-camera that was built by an in-house group of engineers led by Mike Green, Wenze Xi, and Jurgen Seidel (NCI's Molecular Imaging Program). The system is a comparatively simple and inexpensive portable dual γ-camera projection imaging system for visualizing and roughly quantifying the biodistribution of putative diagnostic and therapeutic single photon emitting radiotracers in animals the size of mice. Two identical miniature pixelated NaI(Tl) gamma cameras (Figure 5-58A) look up through the tabletop of a portable cart where animals are placed directly on each camera's custom-made parallel hole collimator. In each camera, every 1-inch deep collimator hole (2 mm diameter round) matches a single crystal (2 mm square x 10 mm deep) in the 19 x 42 (2.2 mm pitch) pixelated array to yield a mouse-size field-of-view of 42 mm x 92 mm. Full functional capability, e.g. dynamic, ECG-gated acquisitions, image analysis and display, etc., was achieved by marrying these custom cameras to an onboard, clinical commercial data acquisition/image processing package (NucLear Mac, Scientific Imaging, Crested Butte, CO). The user operates the system through a wireless Macintosh laptop link to the commercial system. The initial phantom test results (Figure 5-58B) indicated that the system should perform well in the mouse whole-body imaging regime (2.2 mm resolution, 5.8 cps/μCurie sensitivity at 140 keV+15%), and so its first trial with mice was with ^{111}In-labeled SCION.

The SCION study results demonstrated clear signals from MR, optical, and gamma scintigraphy (Figure 5-59). As far as we know, this particle is unique in its ability

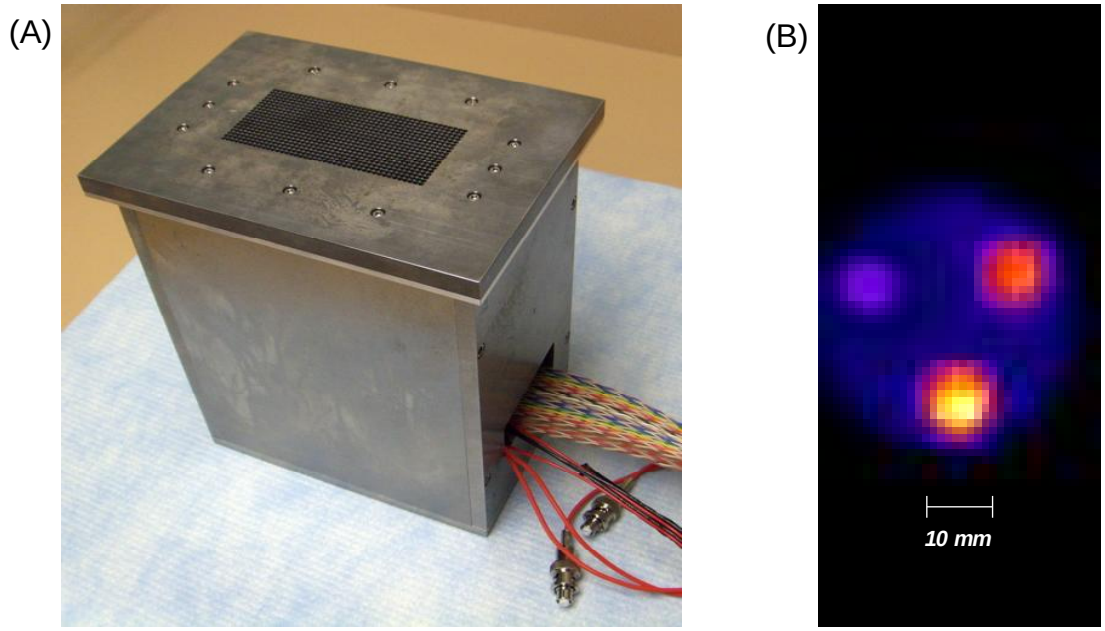

Figure 5-58: NIH Molecular Imaging Program's new portable γ-camera. (A) One of two γ-cameras inset flush with the tabletop of the portable cart. (B) Early four compartment ^{99m}Tc phantom image obtained with operational γ-camera.

to be imaged by MR, optical and radionuclide imaging techniques. Much work has been done to develop a number of dual-modality probes, such as optical/MR [182, 96, 183], optical/SPECT [184], MR/PET [185], and ultrasound/MR [186]. The only other published work on tri-imageable nanoparticles we are aware of to date is a Ru(bpy):Gd^{3+}/SiO_2 particle synthesized to provide contrast in CT, MR, and optical imaging [187].

In this particular study, the targeting aspect of the particle was not put to test. Direct intratumoral injection was used, firstly, to simplify the study to examine whether the particle could in fact be imaged as well as to simultaneously assess and validate the new γ-camera. However, even this administration route has both considerable research and clinical value, particularly for hyperthermia treatment. Jordan et al [188] have shown

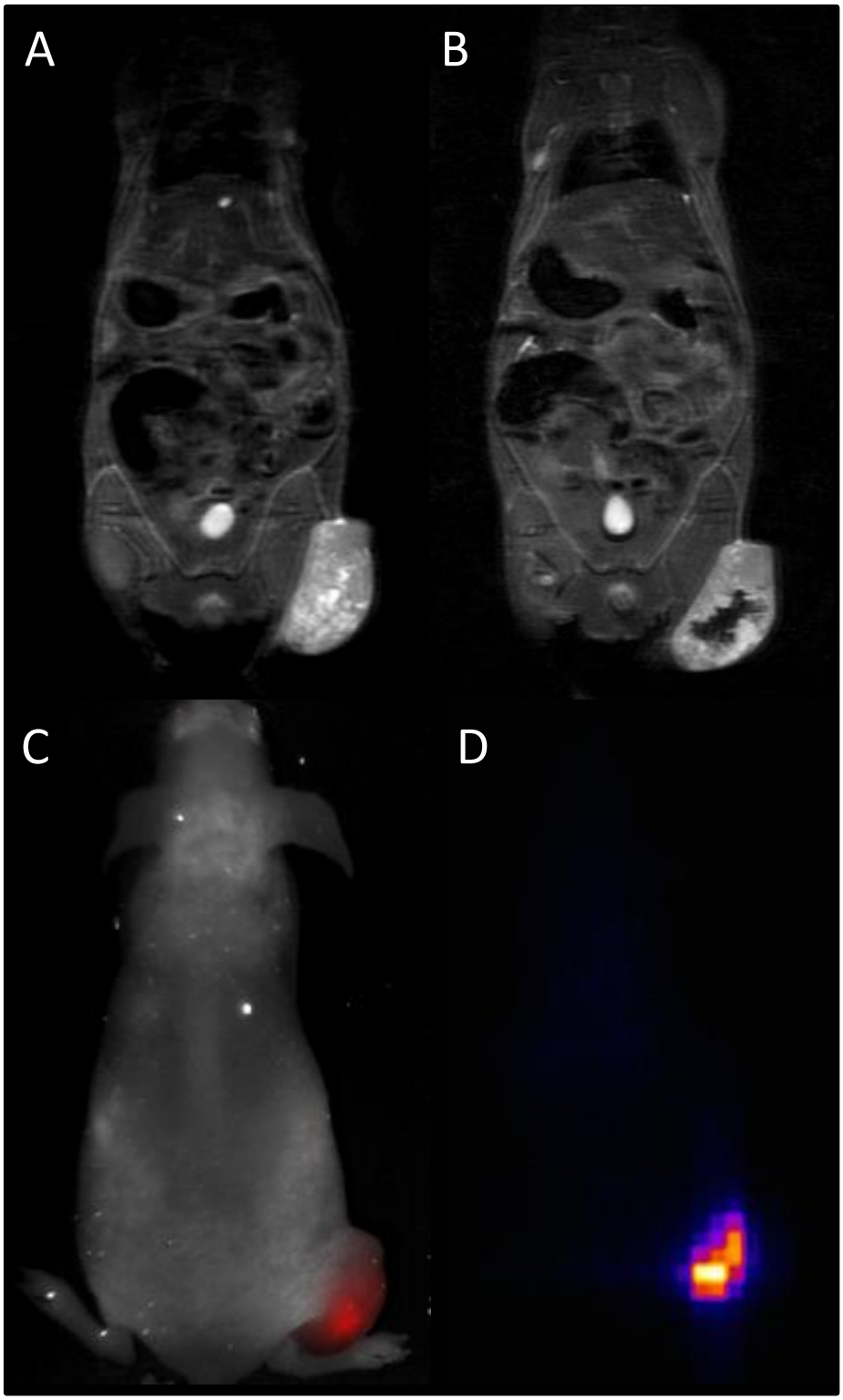

Figure 5-59: Tri-imageable SCION intratumoral injection into subcutaneous LS-174T colon carcinoma mouse model. MR T_2-weighted images (A) pre-injection and (B) 2 hr post-injection demonstrate clear and significant signal loss. (C) Optical image (composite of spectrally unmixed white light and NIR light) at 2 hr post-SCION injection. (D) γ-scintigraphy image at 4 hr post-SCION injection.

local tumor control after an intratumoral injection of USPIO and AC magnetic field application in a mouse C3H mammary carcinoma model. The German company MagForce is also implementing the strategy of intratumoral injections of a silica-coated USPIO to treat brain tumors. From their initial studies in rat experimental glioblastoma tumor models [41] to Phase I [189] and currently open Phase II clinical trials, they have demonstrated the clinical feasibility of the procedure, its tolerability, and local effectiveness. A further discussion of using USPIOs for hyperthermia is provided in Chapter 6.

5.2 Hepatic Imaging with Untargeted SCION

Detection of hepatic metastases has a critical impact on the diagnosis, treatment planning, and follow-up care for cancer patients. The liver is second only to regional lymph nodes as the site of metastases for tumors, where 25% to 50% of terminal patients have hepatic metastases. Hepatic resection of segments containing cancer has been shown to prolong survival, particularly for those with metastatic Wilm's tumor and colorectal cancers. Characterizing not only the presence or absence of hepatic lesions, but also their number, location, and size can influence therapy and survival.

Current imaging modalities used for assessment of hepatic metastases include ultrasound, computed tomography (CT), F-18 fluorodeoxyglucose (^{18}FDG) positron emission tomography (PET), and MRI. While CT has been found to be more sensitive than ultrasound or scintigraphy [190, 191] for this purpose, CT has limited specificity and is not sensitive enough to detect very early lesions. A number of studies have concluded

that non-enhanced MR imaging can equal or exceed the accuracy of contrast-enhanced CT [192-194]; however, contrast-enhanced dynamic MRI provides even more sensitivity for detecting focal hepatic metastasis.

5.2.1 SPIO-Enhanced MRI

Iron oxides such as AMI-25, or Feridex, have proven to be powerful MR contrast agents capable of enhanced detection of tumors in the liver and spleen. Extensive pre-clinical studies began with dextran-coated iron oxide Feridex in 1985 at Massachusetts General Hospital [64, 63, 45] with the first clinical trial in 1988 elucidating the biological and pharmaceutical principles for MRI with SPIOs and the enhanced detection of liver lesions [32]. The injection formulation was 0.2 mM Fe with T_2 relaxivity (R_2) of 1×10^5 $(\text{sec mol})^{-1}$ and T_1 relaxivity (R_1) of 3×10^5 $(\text{sec mol})^{-1}$. These studies were followed by additional trials in France, Belgium, and Japan.

Pharmacokinetic behavior of SPIO is generally comparable in animals and humans where they are promptly sequestered by the reticuloendothelial system (RES). Immediately after injection of AMI-25, T_2 shortening is observed in the blood, liver, and spleen, but the blood signal quickly (blood clearance half-life of 10 minutes) returns to normal as the ~100 nm dextran-coated SPIO are cleared by hepatic RES Kupffer cells ultimately accounting for 80% of the injected dose [63, 64, 195, 45]. The powerful effect on proton relaxation is observed at doses as low as 8 μmol/kg. Localized in approximately 2% of the hepatic cellular volume, this dosage demonstrates essentially complete signal loss from the entire liver. Neoplastic tumor nodules are devoid of phagocytic Kupffer cells (Figure 5-60). Thus, they do not sequester SPIO and appear bright in T_2-weight images.

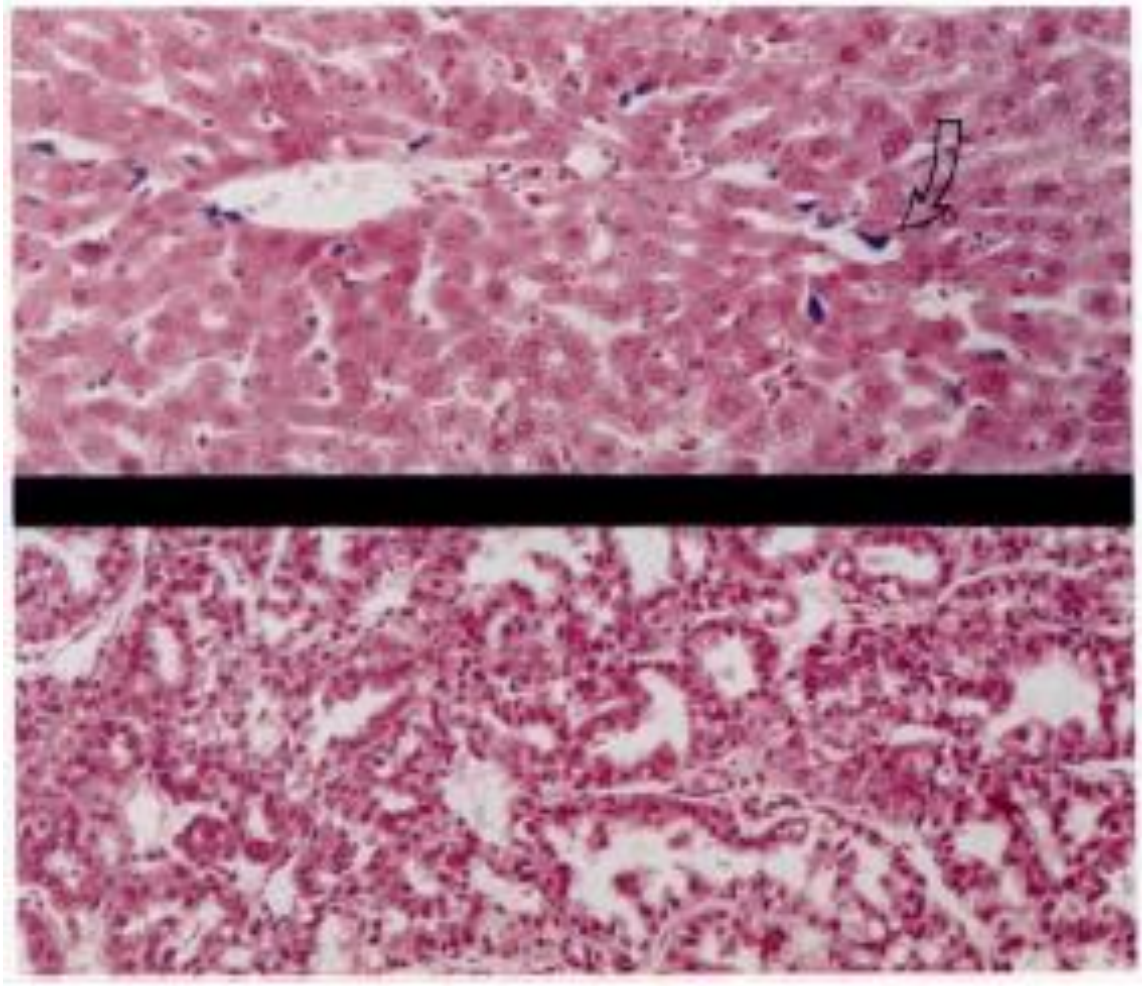

Figure 5-60: Light microscopy images of Prussian blue iron stained sections of normal rat liver (top, x320) and tumor tissue (bottom, x200). Intravenously administered SPIOs were sequestered in hepatic reticuloendothelial cells (arrow) but not in hepatocytes or tumor tissue [196].

With administration of a SPIO agent, there is increased lesion conspicuity because the signal ratio between normal RES tissue and tumor is greatly enhanced. In *ex vivo* studies of a rat liver tumor model, this signal ratio increased from 49% to 280% after administration of SPIO [196]. The enhanced contrast also leads to a lower threshold size for lesion detection. Tsang and co-workers [197] were one of the first groups to correlate MR images after SPIO injection with pathologic analysis of tumors. Mammary tumors were implanted in rat livers, and 39 separate tumor nodules ranging from 1-10 mm in

diameter were imaged with a widely available SE 500/32ms pulse sequence on a 0.6-T clinical MR system before and after SPIO administration. With contrast enhancement, the mean threshold size for lesion detectability decreased from 1 cm to <3 mm in diameter. When compared to actual pathologic measurements, even small millimeter-sized nodules were found not to be obscured by imaging or underestimated in size. In a similar study, Kawamura et al [198] implanted 89 rat tumors, including some less than 2 mm in diameter. Tumor detection increased from 9 (10%) before SPIO injection to 58 (65%) after.

In 1988, Stark and co-workers [32] published the analyses of 15 human patients with liver tumors in patients who received intravenous AMI-25 at doses ranging from 10 to 50 μmol/kg at a rate of 1 mL (11.2 mg Fe)/min. Using 0.3 and 0.6 T scanners, they were imaged 1 hr after injection, though it was noted that satisfactory clinical imaging results could be achieved as late as 48 hr. Both liver and spleen signal intensity decreased in all patients, as early as 5 min after agent administration. As seen in Figure 5-61, the agent profoundly enhanced the detection of tumor from metastatic carcinomas.

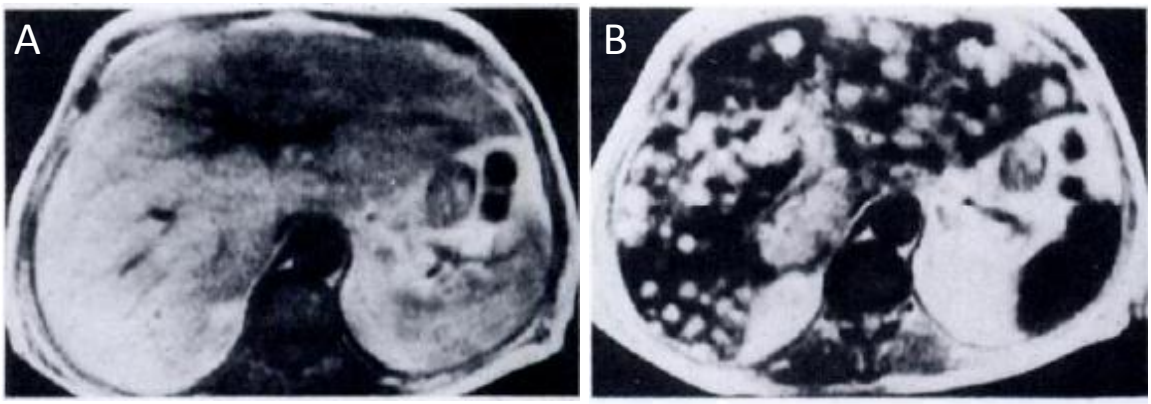

Figure 5-61: Improvement in lesion detection in a patient with metastatic renal cell carcinoma. T_2-weighted images of upper abdominal cavity (A) before SPIO administration showing normal anatomy with and (B) 15 minutes after SPIO administration clearly identifying diffuse hepatic metastases, many smaller than 0.5cm in diameter [32].

The number of lesions detected after contrast administration increased from 89 to 349 out of a total of 370 identified lesions and the size threshold for lesion detectability decreased at a statistically significant ($p < 0.05$) value from 1.5 to 0.3 cm.

To directly compare SPIO-enhanced MRI with contrast-enhanced CT for detection of liver cancer, Fretz et al [199] used receiver-operating-characteristic (ROC) analysis for quantitative comparisons of diagnostic accuracy on 731 individual images. SPIO-enhanced images obtained with a SE 1500/40 sequence yielded statistically significant ($p < 0.005$) greater accuracy than contrast-enhanced CT. 19% and 36% more lesions than the best un-enhanced MR sequence and contrast-enhanced CT, respectively were detected.

5.2.2 Intravenous Injection of Untargeted SCION

To test if SCION particles would be cleared by the body in the same manner as larger SPIOs such as Feridex, and to determine if they could be used to image the liver, a study was conducted with 11 female athymic mice given tail intravenous injections of untargeted (no antibody, peptide or small molecule vector) SCION. The dose of 50 μL of 50 mM Fe in saline solution was administered along with 100 μL of saline at 150 μL/sec. For MRI (assisted by Marcelino Bernardo), the same setup as described in Section 5.1**Error! Reference source not found.** was used but with a Philips Medical Systems 3T clinical scanner (Intera). Respiratory triggered T_2-weighted multi-slice turbo spin-echo (TSE) images (repetition time of 3000 ms, echo time of 30 ms, 90° flip angle, voxel size of 0.15 x 0.15 x 0.6 mm, resolution of 6.6 pixels per mm) were obtained prior to injection of the imaging agent (t = 0 hr) and post-injection at 1 hr, 24 hr, and 48 hr. After the final MR image was acquired for each mouse, it was sacrificed by CO_2 inhalation. The

abdominal wall was then incised and the abdominal cavity was exposed for spectral fluorescence imaging.

Within the first hour, T_2 signal was lost from the liver as the SCION particle was cleared from circulation. Figure 5-62 displays the clear signals obtained by both MR and optical imaging after i.v. administration of SCION.

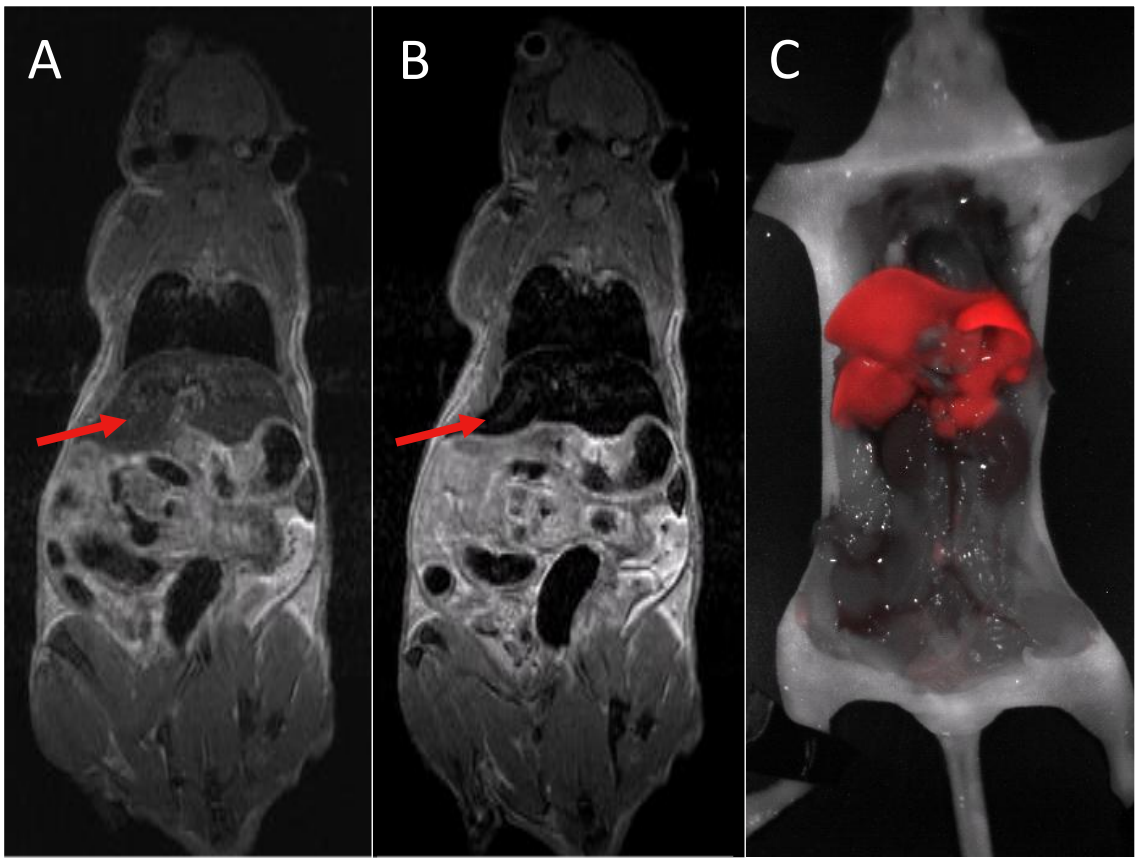

Figure 5-62: Liver and spleen uptake of SCION particle in an athymic mouse given i.v. injection of untargeted and non-radiolabeled SCION. (A) T_2-weighted MR image of mouse pre-injection and (B) at 1 hr post-injection. (C) Optical image (composite of spectrally unmixed white light and NIR light) of mouse at 24 hour post-injection.

5.2.3 MR Signal Intensity in Liver and Blood

To compare SCION versus Feridex clearance from circulation when administered intravenously, a dynamic T_1-weighted MR scan was used to record T_1 signal in the heart

and carotid artery. The same 3T scanner (Intera, Philips Medical Systems) was equipped with a multiple mouse coil comprised of 38 mm diameter by 77 mm length conventional series saddle coils spaced 48.3 mm apart in a square array for a 4-mouse design (Figure 5-63). Mice were anesthetized using gas mixtures of 1.5-2.5% isofluorane in O_2 to maintain a respiration rate of ~ 30 bpm during the acquisition of all images. A one hour dynamic T_1-weighted spoiled gradient (SPGR) echo scan (repetition time of 15 ms, echo time of 2.3 ms, 24° flip angle, voxel size of 0.16 x 0.16 x 0.6 mm, resolution of 6.4 pixels per mm) was started as the animals were simultaneously injected with either SCION or Feridex particles after one initial pre-injection image had been taken. For each agent, the dose of 50 µL of 50 mM Fe in saline solution followed by 100 µL of saline was administered through tail intravenous injections at a rate of 150 µL/sec simultaneously to four female athymic mice.

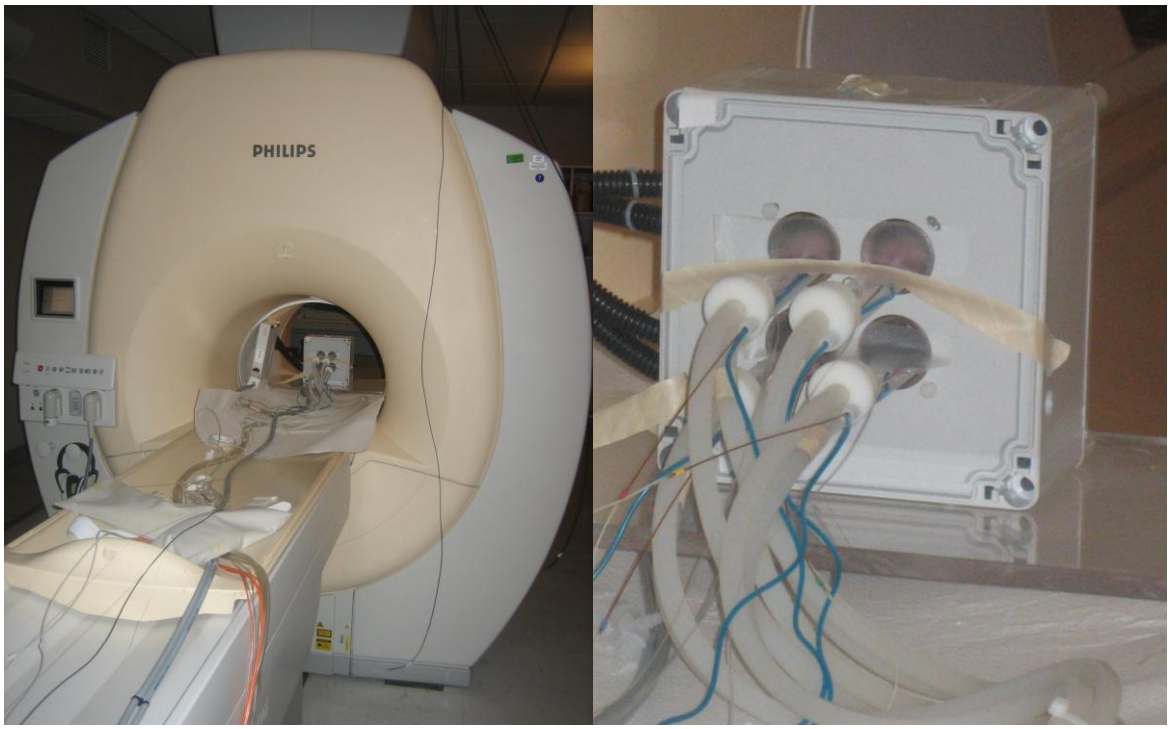

Figure 5-63: Four-mouse coil used in 3T Philips MR scanner. Anesthesia and oxygen provided to each mouse, as well as thermal heating.

In ImageJ, image analysis software, regions of interest (ROIs) were drawn on the heart and carotid artery of each mouse and signal intensity over time was recorded. Signal from the liver was also examined. Comparing to the initial T_1 signal (S_0), the signal intensity over the one hour period is shown in Figure 5-64.

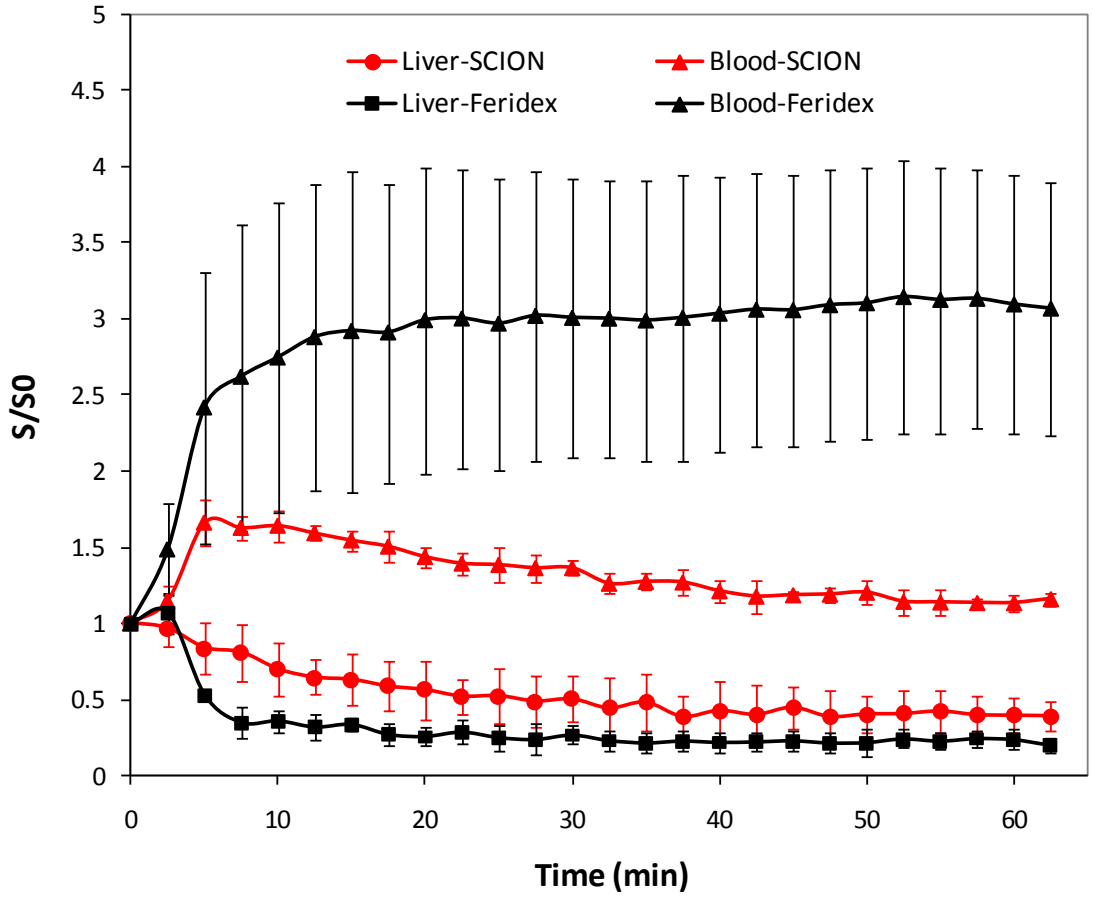

Figure 5-64: One hour plot of mean T_1 signal from blood (heart and carotid artery) and liver of mice with either SCION or Feridex intravenous injection at ~2nd time-point (n = 4, error bars = 1 standard deviation).

When evaluating this figure, the T_2 effect of USPIO on T_1 signal intensity must also be considered. Unlike radiographic contrast agents, signal intensity is not proportionally or even monotonically related to MR contrast agent concentration. Paramagnetic species and USPIOs reduce both T_1, which increases signal intensity, and

T_2, which results in the loss of signal. At lower concentrations the effects of T_1 shortening predominate, while at higher concentrations, T_2 shortening is substantial enough to cause signal loss, overcoming T_1 shortening. In other words, beyond a certain concentration (depending on the pulse sequence), the signal intensity starts to decrease with increased USPIO concentration, as shown in Figure 5-65.

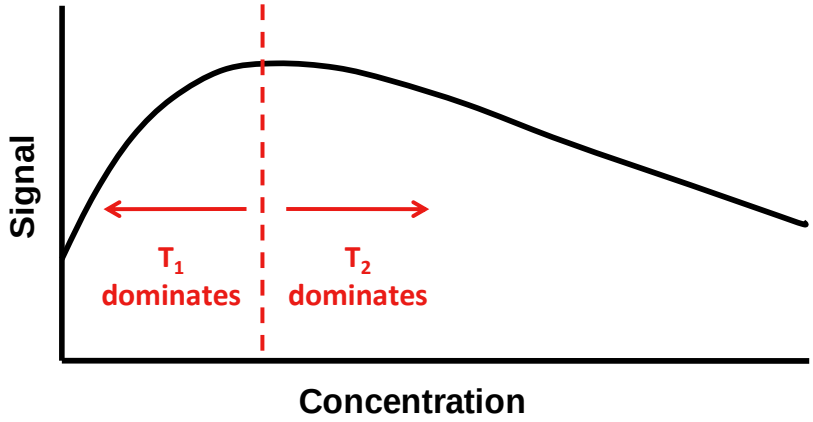

Figure 5-65: Schematic relationship between MR signal intensity (T_1-weighted sequence) and contrast agent concentration. At low doses, T_1 effects dominate and the signal intensity increases nonlinearly with concentration. Above a certain concentration, depending on the characteristics of the pulse sequence, T_2 effects lead to signal loss.

Signal observed from a given tissue arises as a consequence of differences in the intrinsic tissue properties of spin density, relaxation times, resonant frequency (chemical shift and magnetic susceptibility), and motion (macroscopic and microscopic). The relative contribution of these properties is influenced by the acquisition parameters specified: pulse sequence, repetition time (TR), echo delay time (TE), inversion recovery time (TI), flip angle (FA), and magnetic field strength [200]. For spoiled gradient echo sequences, the signal intensity (S) is

$$S = S_0 \frac{\sin(FA)[1\text{-}e^{-TR/T_1}]e^{-TE/T_2}}{1-\cos(FA)e^{-TR/T_1}} \quad (15)$$

where T_1 and T_2 are a function of concentration c_{agent}:

$$\frac{1}{T_{1,2(observed)}} = \frac{1}{T_{1,2(intrinsic)}} + R_{1,2(agent)} c_{agent} \quad (16)$$

The complex relationship between USPIO concentration and image signal intensity has an important consequence for the analysis of SCION and Feridex in Figure 5-66. Where highly concentrated, the T_1 signal intensity may be paradoxically low, and so signal intensity cannot be used to directly quantify the amount of USPIO without more sophisticated tools. What can be analyzed are general trends. In the case of liver accumulation, both agents show a drop in liver signal within minutes after injection. Here, signal loss is an indication that the agent concentration is high enough to have T_2 effects dominate. The Feridex signal drop was larger than the SCION signal drop, and this may be because Feridex is sequestered faster and/or because it has greater relaxivity than SCION, as was noted in Chapter 3. This higher relaxivity is also playing a role in blood signal intensity.

The typical blood volume for the mice used is 2 mL and so the peak concentration of injected agent in the blood would be ~1 mM Fe. As demonstrated in Figure 5-66, the injected dose for both in is in the T_1 dominant region and below the highlighted concentration range where Feridex and SCION would have different T_1 and T_2 dominant effects. SCION blood signal intensity is decreasing over time and seems to be cleared fairly quickly with significant signal loss within the first hour. For Feridex, the slow rise in blood enhancement is a result of the clearance of large particles of Feridex from circulation while a small fraction of smaller particles (around 30 nm or less) that were contained in the injection solution remains with a long blood retention time, similar to ferumoxtran-10. It was later learned that Feridex solutions actually contain a distribution

of sizes and many groups perform fractionation procedures to collect controlled samples [201]. The clearance rate of SCION is probably somewhere between the small and large Feridex particles. Since the SCION solution is more monodisperse, the loss of blood signal enhancement roughly occurs proportionally to the rate of loss of liver signal as the agent is taken up by the liver.

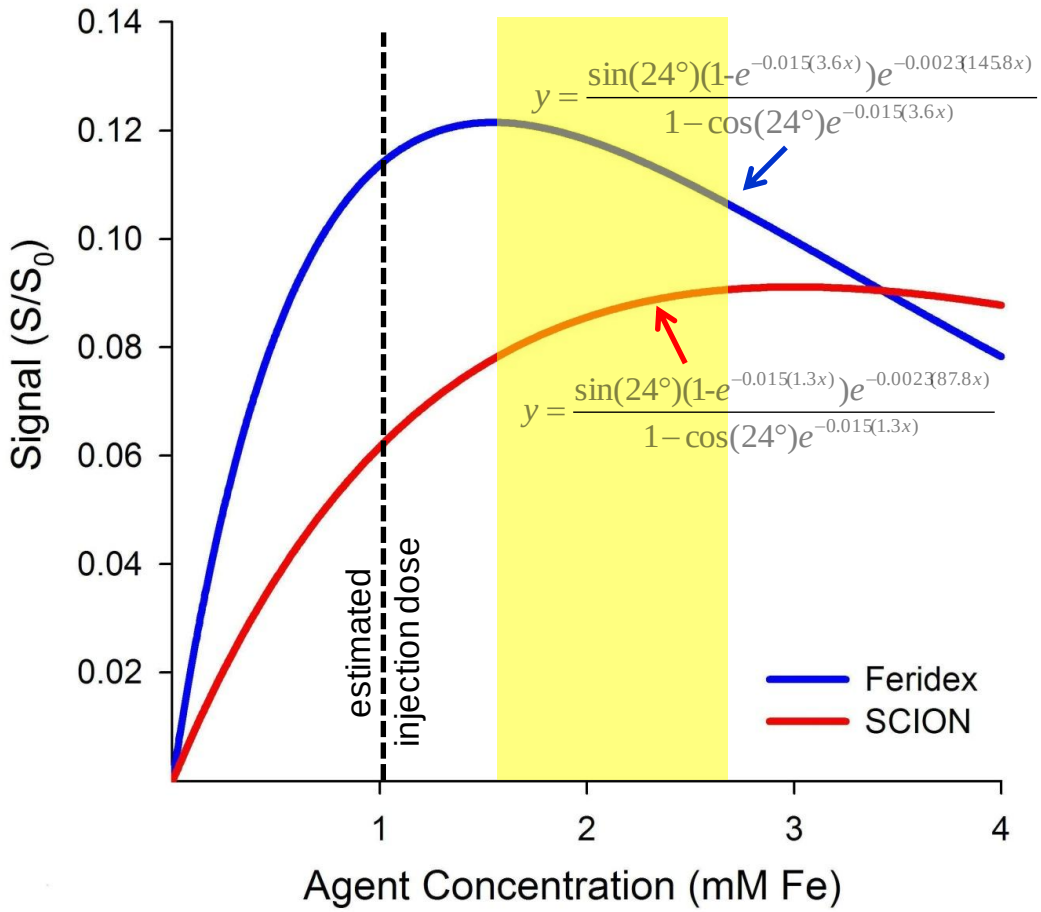

Figure 5-66: Signal versus concentration curves (intrinsic terms excluded) of Feridex and SCION. The highlighted region is an area where Feridex is in its T_2 effect region while SCION is in the T_1 dominant region even though both are of equal concentration in terms of iron. The injected dose in the blood falls below this range in the T_1 dominant rage for both agents. Liver signal is in the T_2 dominant region for both particles; however this effect begins at different concentrations for each.

5.3 Biodistribution and Pharmacokinetics of Antibody-Conjugated SCION

A second goal of this project is targeted delivery of SCION to, for instance, tumor. As shown in the previous section, untargeted SCION accumulates in the liver fairly quickly. This could potentially prove negative for targeted delivery if the particles are not allowed to circulate long enough to permit localization to the target versus liver uptake. Therefore, initially, to simplify the situation and determine the targeting effectiveness of the antibody, biodistribution studies in athymic mice with interperitoneal rather than subcutaneous tumor were performed. The clearance rate was analyzed with pharmacokinetics studies. Xenograft human colon carcinoma LS-174T tumors were targeted by the EGFR1 mAb Cetuximab (Erbitux; ImClone Systems, New York, NY) [179], with a negative control of humanized mAb HuM195 that is similar in every respect except its variable region.

5.3.1 Biodistribution of Antibody-Targeted SCION in Interperitoneal Tumor Model

Female athymic mice (*nu/nu*) at 4–6 weeks of age were injected with LS-174T cells (1×10^8 in 1 mL DMEM) into the peritoneal cavity. After 8 days of growth, the mice were co-injected with the paired ^{125}I- and ^{111}In-labeled preparations. One set of mice were given injections of ^{125}I-Cetuximab and ^{111}In-Cetuximab-SCION and a second group of ^{125}I-HuM195 and ^{111}In-HuM195-SCION. The preparations (5 μCi of each in 0.5mL conjugate buffer, ~pH8.5) were injected into the peritoneal cavity. The mice (n=5) were sacrificed at 24, 48, 72, 96 and 168 hr post-injection of radioactivity. Blood, tumor and

major organs were collected (assisted by Mark Williams), wet weighed and counted in a γ-scintillation counter with a three inch crystal (Wizard, 1480 Autogamma counter, EG&G WALLAC, Turku, Finland). Counts were corrected for decay and spillover. Under our counting conditions, ^{125}I and ^{111}In had 0.00% and 3.1% spillovers, respectively, into each other's windows. The percent injected dose per gram (%ID/g) and tissue:blood ratios were determined. Means, standard deviations, one-tail unequal variance t-test significance, and ANOVA (two-factor with replication) significance were calculated using Microsoft Excel.

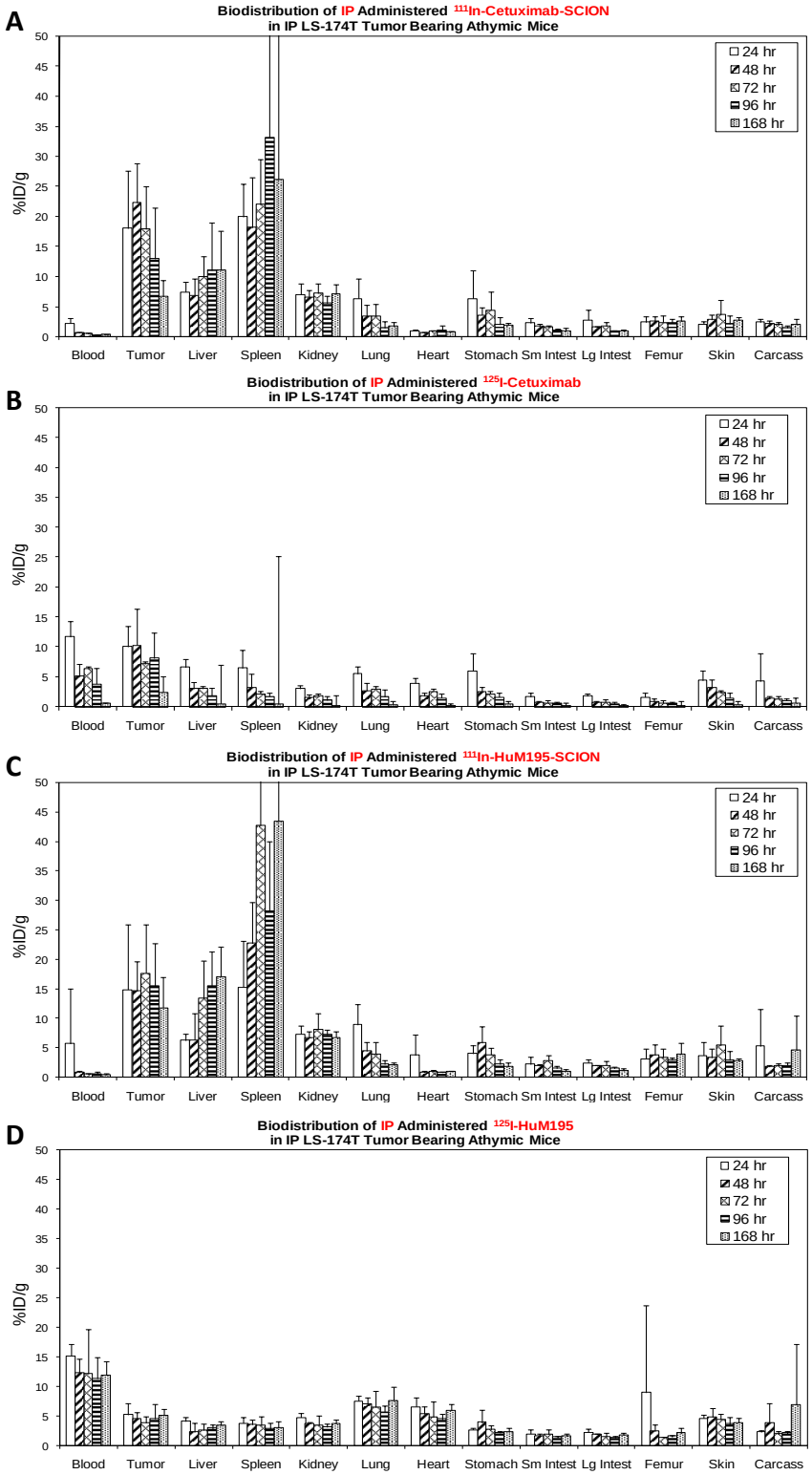

Figure 5-67: Biodistribution interperitoneally administered (A) ^{111}In-Cetuximab-SCION, (B) ^{125}I-Cetuximab, (C) ^{111}In-HuM195-SCION, and (D) ^{125}I-HuM195 in interperitoneal LS-174T tumor-bearing mice. Animals were sacrificed in groups of five at 24, 48, 72, 96 and 168 hr post-injection of agent. For all major organs and blood, the mean and standard deviation (error bars) of %ID/g are presented.

Table 5-12: Biodistribution in %ID/g of agents in i.p. LS-174T tumor model.

^{111}In-Cetuximab-SCION Biodistribution: %ID/gm

Tissue	Timpoints (hr)				
	24	48	72	96	168
Blood	2.19 ± 0.85	0.55 ± 0.16	0.45 ± 0.10	0.21 ± 0.04	0.29 ± 0.05
Tumor	18.04 ± 9.52	22.27 ± 6.57	17.82 ± 7.18	12.88 ± 8.60	6.69 ± 2.63
Liver	7.37 ± 1.69	6.79 ± 2.88	9.88 ± 3.40	10.94 ± 8.00	10.99 ± 6.55
Spleen	19.95 ± 5.48	18.07 ± 8.41	21.98 ± 7.57	33.05 ± 28.28	26.02 ± 24.71
Kidney	6.98 ± 1.87	6.51 ± 1.18	7.18 ± 1.59	5.58 ± 1.23	7.03 ± 1.64
Lung	6.28 ± 3.39	3.38 ± 1.88	3.38 ± 1.98	1.41 ± 1.05	1.73 ± 0.60
Heart	0.92 ± 0.13	0.61 ± 0.13	0.86 ± 0.18	1.00 ± 0.84	0.68 ± 0.23
Stomach	6.35 ± 4.71	3.53 ± 1.31	4.36 ± 3.12	1.97 ± 1.18	1.80 ± 0.37
Sm Intest	2.28 ± 0.79	1.68 ± 0.40	1.52 ± 0.32	1.01 ± 0.21	0.82 ± 0.52
Lg Intest	2.80 ± 1.60	1.48 ± 0.23	1.66 ± 0.65	0.86 ± 0.16	0.83 ± 0.28
Femur	2.41 ± 0.96	2.54 ± 0.83	2.30 ± 1.18	2.18 ± 0.68	2.50 ± 0.83
Skin	2.02 ± 0.54	2.80 ± 0.82	3.67 ± 2.41	2.12 ± 1.35	2.59 ± 0.59
Carcass	2.42 ± 0.51	2.13 ± 0.48	1.98 ± 0.35	1.45 ± 0.40	1.99 ± 0.88

^{125}I-Cetuximab Biodistribution: %ID/gm

Tissue	Timpoints (hr)				
	24	48	72	96	168
Blood	11.69 ± 2.56	5.08 ± 2.08	6.37 ± 3.88	3.82 ± 2.54	0.56 ± 0.58
Tumor	10.02 ± 3.41	10.27 ± 6.12	7.15 ± 4.16	8.12 ± 4.26	2.41 ± 2.00
Liver	6.56 ± 1.36	3.03 ± 1.08	3.05 ± 1.50	1.89 ± 1.27	0.48 ± 0.25
Spleen	6.49 ± 3.04	3.24 ± 2.27	2.15 ± 0.63	1.69 ± 0.64	0.42 ± 0.14
Kidney	3.01 ± 0.60	1.50 ± 0.52	1.80 ± 0.93	1.10 ± 0.68	0.23 ± 0.14
Lung	5.49 ± 1.17	2.71 ± 1.29	2.98 ± 1.70	1.63 ± 1.16	0.34 ± 0.30
Heart	3.91 ± 0.89	1.77 ± 0.57	2.54 ± 1.54	1.48 ± 0.66	0.21 ± 0.18
Stomach	5.97 ± 2.90	2.54 ± 0.74	2.13 ± 1.17	1.59 ± 0.69	0.51 ± 0.15
Sm Intest	1.61 ± 0.75	0.69 ± 0.23	0.62 ± 0.27	0.53 ± 0.28	0.17 ± 0.07
Lg Intest	1.79 ± 0.37	0.68 ± 0.20	0.77 ± 0.47	0.49 ± 0.25	0.11 ± 0.06
Femur	1.57 ± 0.72	0.84 ± 0.48	0.64 ± 0.51	0.52 ± 0.24	0.11 ± 0.09
Skin	4.34 ± 1.66	3.15 ± 1.33	2.34 ± 1.04	1.45 ± 0.88	0.35 ± 0.29
Carcass	4.24 ± 4.60	1.41 ± 0.36	1.30 ± 0.32	1.05 ± 0.32	0.58 ± 0.12

^{111}In-HuM195-SCION Biodistribution: %ID/gm

Tissue	Timpoints (hr)				
	24	48	72	96	168
Blood	5.69 ± 9.24	0.73 ± 0.25	0.45 ± 0.09	0.55 ± 0.27	0.31 ± 0.22
Tumor	14.79 ± 11.14	14.54 ± 5.08	17.57 ± 8.37	15.43 ± 7.23	11.71 ± 5.22
Liver	6.22 ± 1.08	6.27 ± 4.58	13.37 ± 6.31	15.39 ± 5.90	17.02 ± 5.09
Spleen	15.28 ± 7.76	22.65 ± 7.06	42.63 ± 26.39	28.21 ± 11.73	43.34 ± 22.08
Kidney	7.32 ± 1.34	6.60 ± 1.12	8.06 ± 2.77	7.17 ± 0.90	6.67 ± 1.09
Lung	8.88 ± 3.44	4.38 ± 1.53	3.87 ± 1.97	2.12 ± 0.67	1.97 ± 0.42
Heart	3.73 ± 3.47	0.78 ± 0.19	0.93 ± 0.20	0.79 ± 0.11	0.85 ± 0.15
Stomach	4.00 ± 1.28	5.81 ± 2.72	3.76 ± 1.22	2.13 ± 0.82	1.76 ± 0.59
Sm Intest	2.20 ± 1.22	1.87 ± 0.32	2.78 ± 0.86	1.49 ± 0.32	0.96 ± 0.31
Lg Intest	2.35 ± 0.64	1.86 ± 0.18	1.94 ± 0.81	1.43 ± 0.29	1.01 ± 0.37
Femur	3.08 ± 1.67	3.73 ± 1.80	3.22 ± 1.53	2.88 ± 0.39	3.77 ± 1.99
Skin	3.61 ± 2.33	3.21 ± 1.55	5.36 ± 3.34	2.85 ± 1.45	2.72 ± 0.41
Carcass	5.25 ± 6.28	1.73 ± 0.22	1.86 ± 0.40	1.92 ± 0.53	4.54 ± 5.86

^{125}I-HuM195 Biodistribution: %ID/gm

Tissue	Timpoints (hr)				
	24	48	72	96	168
Blood	15.19 ± 2.01	12.26 ± 2.37	12.09 ± 7.57	11.24 ± 3.68	11.84 ± 2.36
Tumor	5.21 ± 1.91	4.40 ± 1.23	3.75 ± 1.20	4.47 ± 2.56	5.04 ± 1.05
Liver	4.10 ± 0.70	2.18 ± 1.65	2.53 ± 1.13	2.87 ± 0.61	3.37 ± 0.75
Spleen	3.81 ± 0.88	3.51 ± 0.80	3.31 ± 1.52	2.76 ± 0.99	2.94 ± 1.05
Kidney	4.76 ± 0.68	3.58 ± 0.38	3.29 ± 1.76	3.02 ± 0.64	3.62 ± 0.71
Lung	7.55 ± 0.88	6.92 ± 1.19	6.35 ± 2.88	5.54 ± 1.19	7.48 ± 2.36
Heart	6.56 ± 1.50	5.25 ± 1.36	4.70 ± 2.74	4.39 ± 0.90	5.82 ± 1.11
Stomach	2.62 ± 0.38	3.84 ± 2.10	2.59 ± 0.83	2.11 ± 0.32	2.24 ± 0.65
Sm Intest	2.01 ± 0.65	1.48 ± 0.50	1.83 ± 0.83	1.33 ± 0.26	1.57 ± 0.42
Lg Intest	2.28 ± 0.56	1.80 ± 0.24	1.44 ± 0.73	1.25 ± 0.25	1.67 ± 0.46
Femur	8.96 ± 14.68	2.38 ± 1.18	1.30 ± 0.14	1.46 ± 0.24	2.01 ± 0.93
Skin	4.55 ± 0.64	4.73 ± 1.52	4.29 ± 1.00	3.56 ± 1.14	3.74 ± 0.89
Carcass	2.31 ± 0.25	3.71 ± 3.41	1.87 ± 0.53	2.01 ± 0.41	6.82 ± 10.31

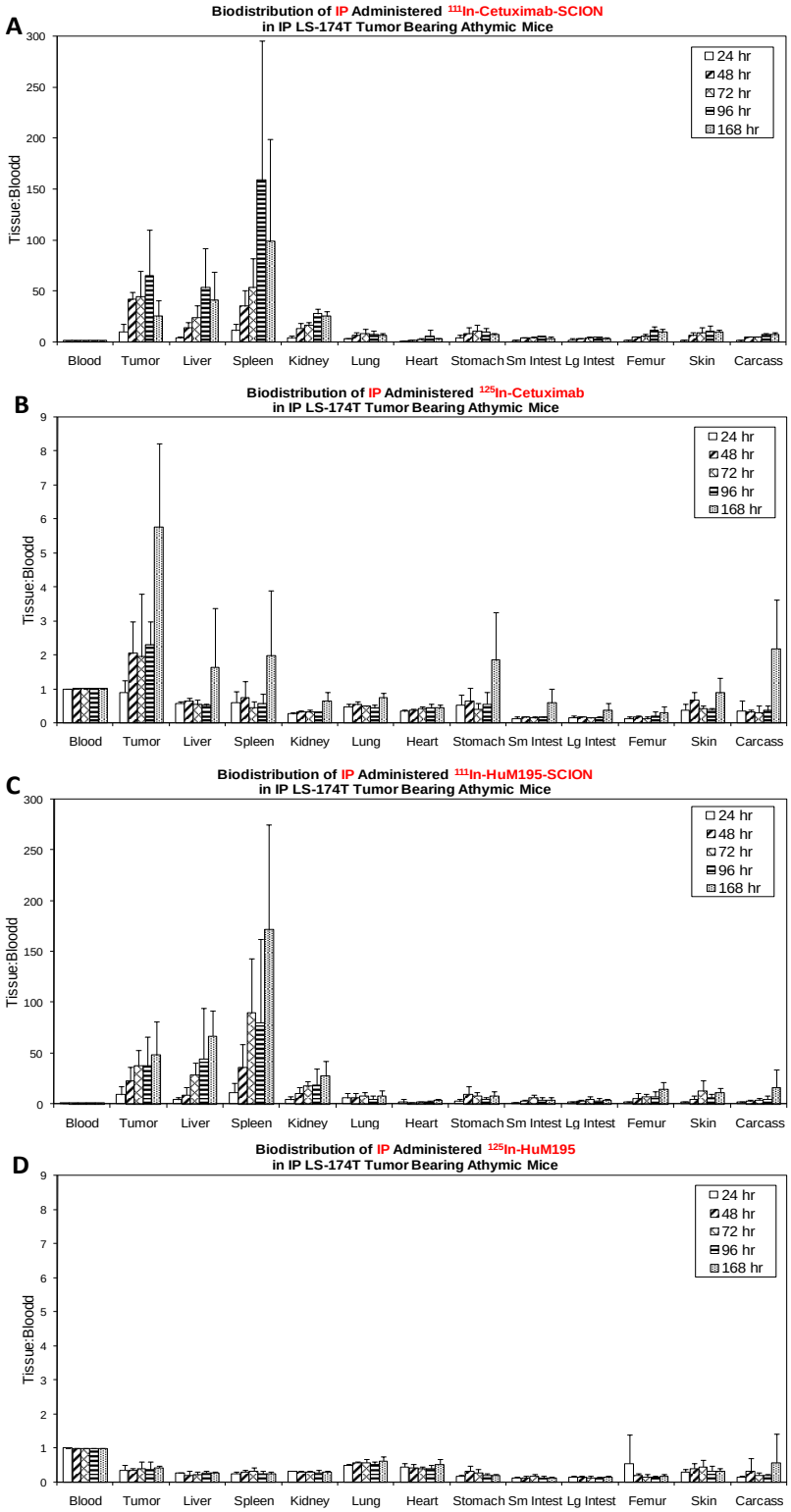

Figure 5-68: Biodistribution interperitoneally administered (A) ^{111}In-Cetuximab-SCION, (B) ^{125}I-Cetuximab, (C) ^{111}In-HuM195-SCION, and (D) ^{125}I-HuM195 in interperitoneal LS-174T tumor-bearing mice. Animals were sacrificed in groups of five at 24, 48, 72, 96 and 168 hr post-injection of agent. For all major organs and blood, the mean and standard deviation (error bars) of tissue:blood ratios are presented.

Table 5-13: Biodistribution as tissue:blood ratios of agents in i.p. LS-174T tumor model.

^{111}In-Cetuximab-SCION Biodistribution: Tissue:Blood Ratio

Tissue	Timpoints (hr)				
	24	48	72	96	168
Blood	1 ± 0	1 ± 0	1 ± 0	1 ± 0	1 ± 0
Tumor	9.90 ± 7.57	41.16 ± 7.24	43.69 ± 25.67	64.42 ± 45.70	25.23 ± 15.19
Liver	3.70 ± 1.16	13.09 ± 6.20	23.65 ± 12.22	52.83 ± 38.45	40.54 ± 28.06
Spleen	10.86 ± 6.85	34.90 ± 15.23	52.90 ± 28.67	158.29 ± 136.92	98.59 ± 100.32
Kidney	3.78 ± 2.30	12.89 ± 5.29	16.28 ± 3.16	27.10 ± 5.33	24.67 ± 4.84
Lung	2.75 ± 1.05	6.08 ± 3.18	7.88 ± 4.64	6.52 ± 4.34	6.10 ± 1.93
Heart	0.47 ± 0.18	1.15 ± 0.26	2.10 ± 1.10	5.42 ± 5.85	2.36 ± 0.72
Stomach	3.57 ± 3.36	7.76 ± 6.12	9.84 ± 6.69	9.16 ± 3.90	6.47 ± 2.01
Sm Intest	1.10 ± 0.31	3.18 ± 0.82	3.57 ± 1.33	4.86 ± 0.30	3.00 ± 1.86
Lg Intest	1.68 ± 1.68	2.87 ± 0.84	3.80 ± 1.48	4.16 ± 0.18	2.94 ± 0.98
Femur	1.22 ± 0.52	4.57 ± 0.40	5.30 ± 2.62	11.06 ± 4.22	9.03 ± 3.71
Skin	1.07 ± 0.57	5.79 ± 3.52	8.63 ± 5.66	10.25 ± 5.79	9.25 ± 2.71
Carcass	1.26 ± 0.56	4.04 ± 1.02	4.46 ± 0.55	7.02 ± 1.66	6.87 ± 2.33

^{125}I-Cetuximab Biodistribution: Tissue:Blood Ratio

Tissue	Timpoints (hr)				
	24	48	72	96	168
Blood	1 ± 0	1 ± 0	1 ± 0	1 ± 0	1 ± 0
Tumor	0.89 ± 0.35	2.03 ± 0.95	1.94 ± 1.85	2.27 ± 0.70	5.74 ± 2.47
Liver	0.56 ± 0.05	0.62 ± 0.09	0.53 ± 0.13	0.49 ± 0.06	1.62 ± 1.75
Spleen	0.58 ± 0.32	0.73 ± 0.48	0.43 ± 0.18	0.54 ± 0.30	1.96 ± 1.94
Kidney	0.26 ± 0.05	0.30 ± 0.04	0.31 ± 0.08	0.30 ± 0.03	0.62 ± 0.28
Lung	0.47 ± 0.06	0.53 ± 0.09	0.48 ± 0.03	0.43 ± 0.08	0.72 ± 0.16
Heart	0.34 ± 0.03	0.36 ± 0.05	0.40 ± 0.06	0.42 ± 0.11	0.43 ± 0.08
Stomach	0.53 ± 0.28	0.62 ± 0.39	0.39 ± 0.18	0.54 ± 0.36	1.83 ± 1.42
Sm Intest	0.13 ± 0.03	0.15 ± 0.04	0.12 ± 0.06	0.15 ± 0.03	0.57 ± 0.44
Lg Intest	0.16 ± 0.05	0.14 ± 0.03	0.13 ± 0.02	0.14 ± 0.03	0.34 ± 0.22
Femur	0.13 ± 0.04	0.16 ± 0.04	0.11 ± 0.06	0.18 ± 0.15	0.28 ± 0.19
Skin	0.38 ± 0.16	0.66 ± 0.23	0.41 ± 0.10	0.38 ± 0.04	0.87 ± 0.45
Carcass	0.34 ± 0.32	0.30 ± 0.08	0.29 ± 0.20	0.34 ± 0.17	2.17 ± 1.45

^{111}In-HuM195-SCION Biodistribution: Tissue:Blood Ratio

Tissue	Timpoints (hr)				
	24	48	72	96	168
Blood	1 ± 0	1 ± 0	1 ± 0	1 ± 0	1 ± 0
Tumor	9.17 ± 8.36	22.99 ± 13.40	38.12 ± 14.99	38.14 ± 28.18	48.84 ± 32.26
Liver	3.94 ± 2.85	9.23 ± 6.90	28.73 ± 11.52	44.75 ± 49.91	67.20 ± 24.64
Spleen	11.16 ± 9.24	35.98 ± 23.02	90.26 ± 52.73	80.09 ± 82.49	171.80 ± 103.31
Kidney	4.30 ± 2.70	10.49 ± 5.54	17.81 ± 4.72	19.04 ± 15.89	28.00 ± 14.39
Lung	5.43 ± 4.84	6.73 ± 4.27	8.24 ± 3.51	5.02 ± 3.40	8.23 ± 4.51
Heart	1.84 ± 2.56	1.22 ± 0.65	2.09 ± 0.45	1.99 ± 1.50	3.49 ± 1.38
Stomach	2.65 ± 2.32	9.88 ± 7.60	8.41 ± 2.98	4.63 ± 2.13	7.63 ± 4.77
Sm Intest	1.05 ± 0.63	2.77 ± 0.90	6.43 ± 2.74	3.64 ± 2.66	4.07 ± 2.73
Lg Intest	1.36 ± 0.96	2.77 ± 0.85	4.59 ± 2.40	3.41 ± 2.30	3.77 ± 1.19
Femur	1.47 ± 1.02	5.87 ± 4.84	7.05 ± 2.52	7.15 ± 5.05	14.31 ± 7.07
Skin	1.50 ± 0.76	4.77 ± 3.41	12.77 ± 10.10	6.40 ± 3.71	11.03 ± 4.52
Carcass	1.62 ± 0.76	2.67 ± 1.20	4.23 ± 1.20	4.76 ± 3.26	16.26 ± 17.84

^{125}I-HuM195 Biodistribution: Tissue:Blood Ratio

Tissue	Timpoints (hr)				
	24	48	72	96	168
Blood	1 ± 0	1 ± 0	1 ± 0	1 ± 0	1 ± 0
Tumor	0.34 ± 0.14	0.36 ± 0.05	0.38 ± 0.20	0.38 ± 0.21	0.43 ± 0.05
Liver	0.27 ± 0.02	0.19 ± 0.14	0.23 ± 0.06	0.26 ± 0.05	0.28 ± 0.02
Spleen	0.25 ± 0.05	0.29 ± 0.07	0.31 ± 0.11	0.25 ± 0.07	0.24 ± 0.05
Kidney	0.31 ± 0.01	0.30 ± 0.03	0.29 ± 0.03	0.28 ± 0.06	0.31 ± 0.02
Lung	0.50 ± 0.03	0.57 ± 0.03	0.57 ± 0.11	0.51 ± 0.09	0.62 ± 0.13
Heart	0.44 ± 0.11	0.43 ± 0.08	0.40 ± 0.04	0.41 ± 0.09	0.51 ± 0.15
Stomach	0.17 ± 0.03	0.31 ± 0.16	0.26 ± 0.11	0.20 ± 0.05	0.19 ± 0.05
Sm Intest	0.13 ± 0.03	0.12 ± 0.04	0.17 ± 0.05	0.13 ± 0.04	0.13 ± 0.03
Lg Intest	0.15 ± 0.03	0.15 ± 0.03	0.13 ± 0.05	0.12 ± 0.03	0.14 ± 0.02
Femur	0.54 ± 0.85	0.19 ± 0.06	0.14 ± 0.08	0.14 ± 0.03	0.17 ± 0.07
Skin	0.30 ± 0.06	0.40 ± 0.15	0.44 ± 0.21	0.33 ± 0.14	0.32 ± 0.08
Carcass	0.15 ± 0.01	0.33 ± 0.36	0.19 ± 0.08	0.19 ± 0.04	0.57 ± 0.84

Table 5-14: Statistical analysis of tumor targeting with SCION. Highlighted values are significant at $p < 0.05$.

Tumor %ID/gm					
	24 hr	48 hr	72 hr	96 hr	168 hr
Cetuximab-SCION	18.04	22.27	17.82	12.88	6.69
HuM195-SCION	14.79	14.54	17.57	15.43	11.71
t-test p-value (1-tail, uneq var)	0.317	0.037	0.480	0.270	0.052
ANOVA p-value (2-factor, replication)	Source of Variance	Antibodies		0.733	
		Antibodies & Timepoints		0.370	
Cetuximab	10.02	10.27	7.15	8.12	2.41
HuM195	5.21	4.40	3.75	4.47	5.04
t-test p-value (1-tail, uneq var)	0.016	0.049	0.072	0.074	0.020
ANOVA p-value (2-factor, replication)	Source of Variance	Antibodies		0.002	
		Antibodies & Timepoints		0.046	

Tumor:Blood					
	24 hr	48 hr	72 hr	96 hr	168 hr
Cetuximab-SCION	9.90	41.16	43.69	64.42	25.23
HuM195-SCION	9.17	22.99	38.12	38.14	48.84
t-test p-value (1-tail, uneq var)	0.4444	0.0181	0.3445	0.1559	0.0959
ANOVA p-value (2-factor, replication)	Source of Variance	Antibodies		0.414	
		Antibodies & Timepoints		0.170	
Cetuximab	0.89	2.03	1.94	2.27	5.74
HuM195	0.34	0.36	0.38	0.38	0.43
t-test p-value (1-tail, uneq var)	0.0229	0.0762	0.0070	0.0124	0.0887
ANOVA p-value (2-factor, replication)	Source of Variance	Antibodies		5.8E-09	
		Antibodies & Timepoints		1.4E-04	

The graphs in Figure 5-67 and Figure 5-68 show that antibody-SCION conjugates were distributed differently from free antibody, with high uptake by the spleen and liver. This action was most likely a result of SCION uptake by RES cells, whereas free antibody was normally cleared through the blood. In terms of tumor uptake, there was a difference in free Cetuximab versus free HuM195, both in the figures as well as in the

statistical analysis (Table 5-14) where $p<0.05$ was considered significant. Targeted-SCION results are not as clear. Based on Figure 5-68, there was a general increasing trend of uptake of HuM195-SCION over time, while Cetuximab-SCION peaked at 96 hr. The significant time point (Table 5-14) was at 48 hr where Cetuximab-SCION showed 22.27 %ID/g tumor presence and 41.16 tumor:blood ratio, and HuM195-SCION had 14.54 %ID/g in tumor and 22.99 tumor:blood ratio. This time point may prove to be a useful one for imaging. However, as the ANOVA test demonstrates, there was no significant difference between the targeted SCION particles when taking into consideration all the timepoints, while there was for the control antibodies. This biodistribution suggests that targeting may be possible, but it needs to be repeated after a better understanding of the effect of SCION conjugation on antibody immunoreactivity. If the antibody is in fact unaffected by the particle attachment, then a challenge with these particles will be how to avoid nonspecific uptake as a result of the SCION particles.

5.3.2 Pharmacokinetics

Pharmacokinetics is a quantitative description of drug concentration within the body. The organism is regarded as an open system in a state of equilibrium which it tries to regain after any disturbance, including drug administration. This behavior can be elucidated by dose-time curves that permit calculation of parameters of distribution and elimination, which in turn supply the basis for dosage regimes and can also disclose the functional performance of different organs. In first order kinetics, a constant fraction of drug from the body is eliminated per unit time and the rate of elimination is proportional to the amount of drug in the body. Figure 5-69 demonstrates the profile of first-order kinetics clearance.

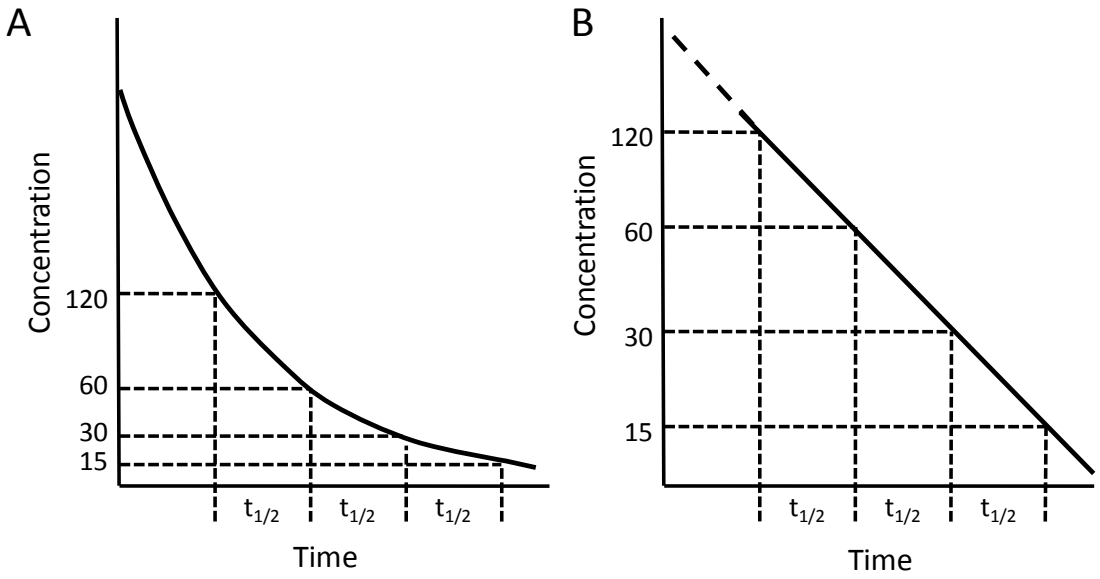

Figure 5-69: First order kinetic of elimination (A) in a linear plot and (B) in a semi-logarithmic plot.

The apparent volume of distribution (V_d) is the volume in which the amount of drug would need to be uniformly distributed to produce the observed blood concentration. It is calculated as the total amount of drug in the body divided by the blood drug concentration and is reported in mL/kg body weight. Highly lipid soluble drugs have a high volume of distribution, whereas those that are lipid insoluble, i.e. neuromuscular blockers, remain in the blood with a low V_d. The clearance (Cl) of a drug is the volume of blood from which the drug is completely removed per unit of time. The clearance half-life ($t_{1/2}$) is the time required for concentration in the plasma to reduce by 50%. After 4 half-lives of time, elimination is 94% complete. This description only applies in the single compartment model where the assumption is that the bloodstream is the only compartment in the body (or if the V_d = the blood volume). However, the human body is composed of many compartments, including muscle, fat, and brain tissue.

Multi-compartment models describe a complex clearance profile that incorporates the redistribution between various compartments. The biggest hazard of using half-life to describe drug elimination is that most drugs do not have a single half-life, but have multiple half-lives because drug elimination rate often changes as a function of time after administration. Figure 5-70 represents a two-compartment clearance profile with an initial rapid fall in blood concentration, a plateau, and then a slower gradual fall. The rapid redistribution phase is characterized by the α half-life. The plateau is the equilibrium phase where blood concentration is equal to tissue concentration, and the slower elimination phase, characterized by β half-life, is where blood and tissue concentrations fall in tandem. After a drug is administered, it is absorbed and reaches a peak concentration (C_{max}) at time T_{max}.

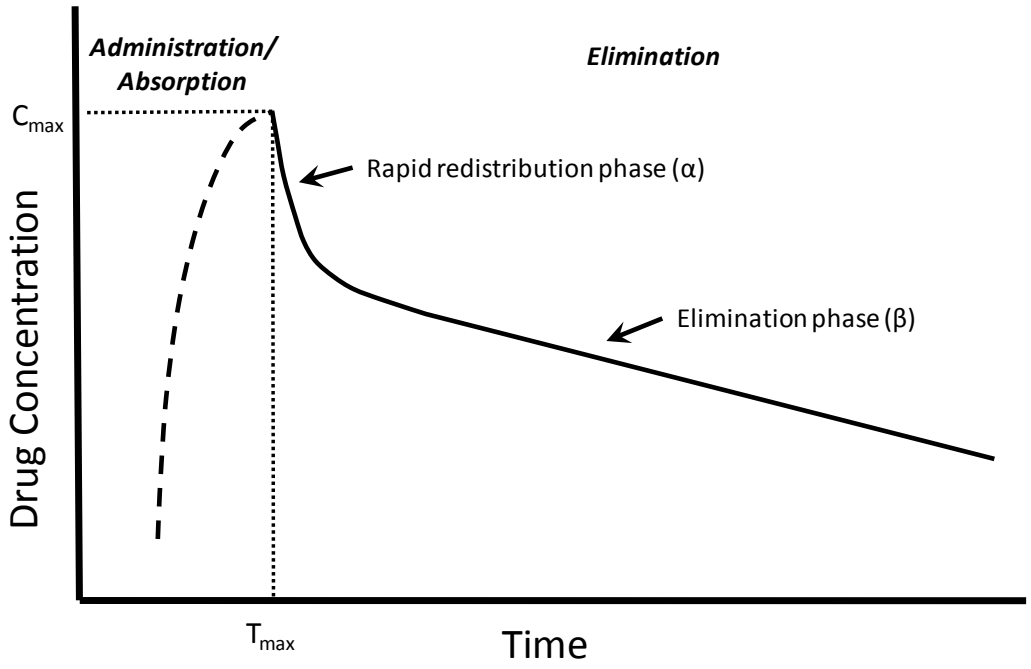

Figure 5-70: Two-compartment pharmacokinetic clearance profile. Once reaching the maximum concentration after administration, the agent first undergoes a rapid re-distribution phase characterized by half-life α, followed by the slow elimination phase with half-life β.

5.3.3 Pharmacokinetics of Antibody-Targeted SCION in Interperitoneal Tumor Model

The pharmacokinetics of the radiolabeled antibody and particles were also determined for each matched pair described in 5.3.1. An additional set of tumor-bearing and non-tumor bearing mice (n=5 each) was injected intraperitoneally with either a preparation of ^{125}I-Cetuximab and ^{111}In-Cetuximab-SCION or of ^{125}I-HuM195 and ^{111}In-HuM195-SCION (5 μCi of each in 0.5 mL conjugate buffer, ~pH 8.5). Blood samples at time points up to 216 hr post-injection of agent were collected, via a tail vein nick, using 10-μL heparinized capillary tubes (Drummond Scientific, Broomall, PA). The blood samples were ejected onto harvesting filters (Molecular Devices Corp., Sunnyvale, CA), and the radioactivity was measured in a γ-counter. The percent injected dose per milliliter (%ID/ml) and standard deviations were calculated and plotted. The α and β half-lives in the blood compartment were calculated using a two-compartment model in SigmaPlot version 9 software (Systat Software, Point Richmond, CA).

As the graphs in Figure 5-71 show, a greater percentage of injected dose of labeled-antibody was found in the blood than labeled-particle. The half-lives (Table 5-15) demonstrate that in each case, the particle cleared slower than free antibody. The free antibody HuM195 was cleared fairly similarly in both animal models, while labeled-Cetuximab demonstrated faster clearance in the tumor-bearing model. Though it was expected that in the non-tumor bearing model, both antibody-SCION constructs would have similar half-lives, a difference was seen where Cetuximab-SCION was cleared slower. There was slow clearance of HuM195-SCION in tumor bearing animals, indicating some nonspecific uptake facilitated by the SCION particle as was also seen in the biodistribution in Section 5.3.1. The slowest clearance was by Cetuximab-SCION in tumor-bearing animals, which is the most desirable outcome.

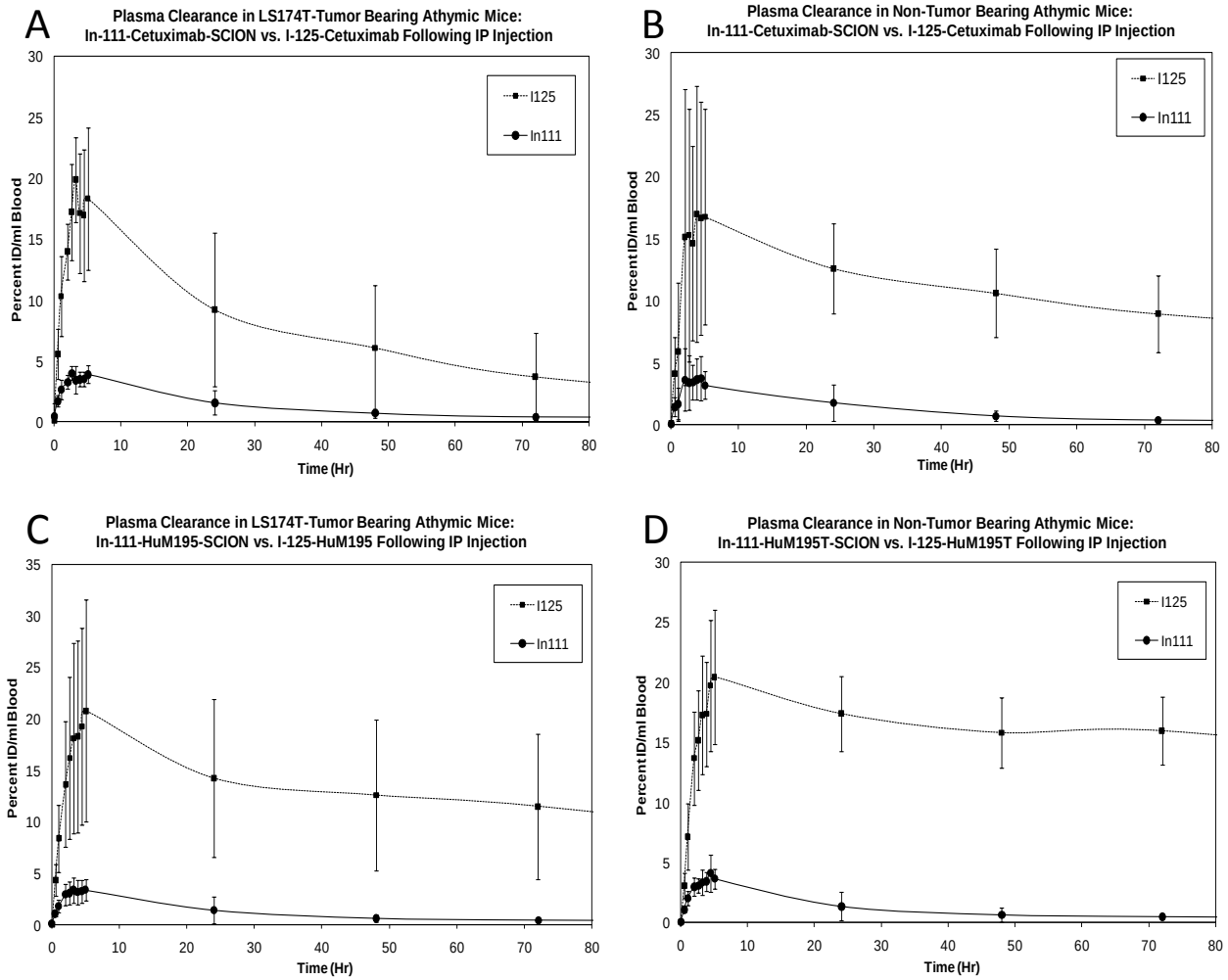

Figure 5-71: Pharmacokinetics of (A) ^{111}In-Cetuximab-SCION and ^{125}I-Cetuximab in LS-174T tumor bearing mice, (B) ^{111}In-Cetuximab-SCION and ^{125}I-Cetuximab in non-tumor bearing mice, (C) ^{111}In-HuM195-SCION and ^{125}I-HuM195 in LS-174T tumor bearing mice, and (D) ^{111}In-HuM195-SCION and ^{125}I-HuM195 in non-tumor bearing mice.

Table 5-15: Plasma half-lives of labeled and targeted SCION and labeled antibody.

Antibody (Ab)	$t_{½}$ (hr)	Non-Tumor		Tumor	
		^{111}In-Ab-SCION	^{125}I-Ab	^{111}In-Ab-SCION	^{125}I-Ab
Cetuximab	α	17.1	8.4	15.4	3.8
	β	4589	135.4	indefinite	34.7
	R^2	0.993	0.998	0.986	0.993
HuM195	α	6.3	1.4	12.8	1.2
	β	185.1	249.7	490.1	116.9
	R^2	0.998	0.924	0.999	0.995

5.4 Sentinel Lymph Node Imaging with Untargeted SCION

5.4.1 Sentinel Node Imaging

Breast cancer is the most common malignancy amongst women in the United States. Annually, 45,000 deaths are reported [202]. More than 180,000 new diagnoses are made [203] each year and a rising rate of 3% has been reported [204]. Statistics show that approximately one in nine women will develop breast cancer during her lifetime [205]. The presence of regional lymph node metastases has become cornerstone information on which both prognosis and therapy of the tumors is based, particularly in melanoma and breast cancer. It is used as a major criterion for determining the need for adjuvant chemotherapy [206]. Separate from blood circulation, the lymphatic system is a network of vessels, organs, and nodes for transporting immune system cells that maintain fluid homeostasis and immunocompetence. Surgical axillary lymph node dissection has been the reference standard for establishing lymph node involvement [207, 208], although 40%–70% of patients with breast cancer have histopathologically negative axillary lymph nodes [209-211]. The procedure is also highly demanding on the patient. The surgeon removes a pad of fat in which 10 to 20 lymph nodes are embedded, and often a drain is left in place for the first 2-3 weeks after the operation to collect leaking lymph fluid. Morbidity reports include seroma formation, numbness, limitation of shoulder movement, and lymphedema [212]. Recently, to spare patients the more extensive and traumatic axillary lymph node dissection, a less invasive surgical sentinel node biopsy technique has been become more common as an alternative. The sentinel lymph node (SLN) is the first node into which the primary tumor drains, making it the most likely to contain metastatic cells [213] (Figure 5-72). SLN accurately reflects the status of more distant

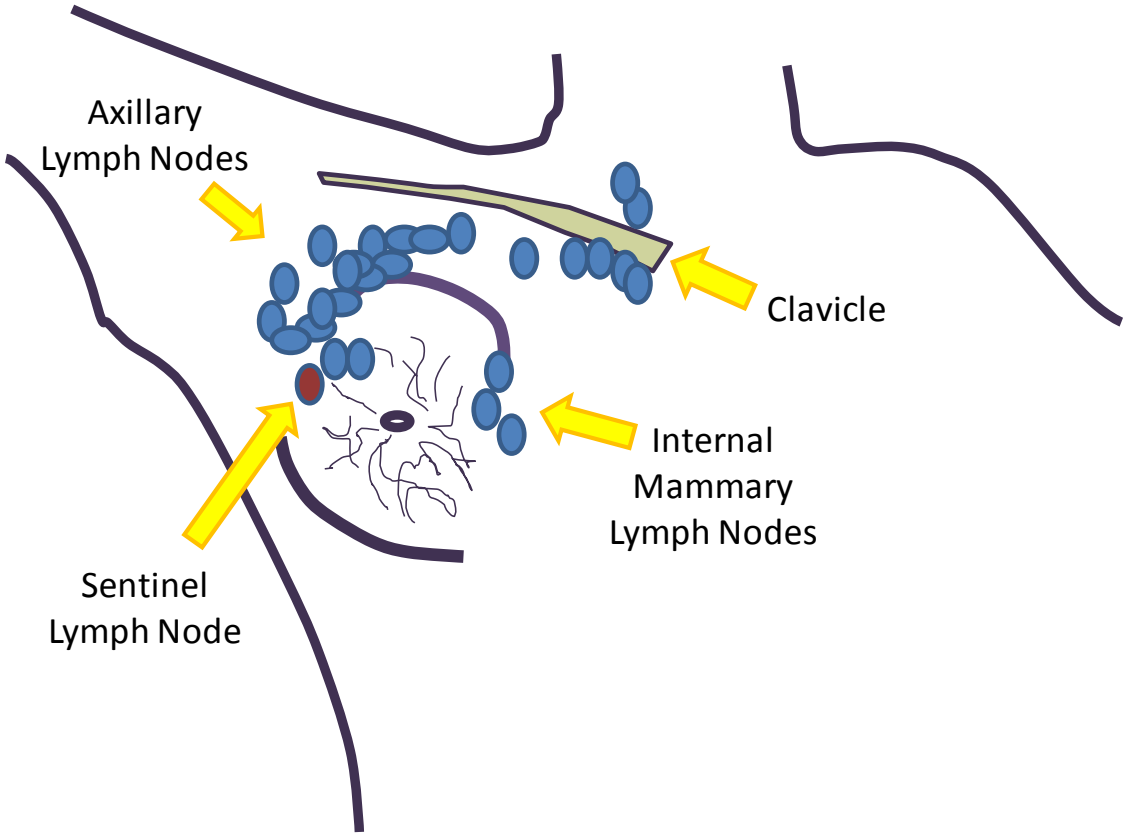

Figure 5-72: Representation of breast lymphatic drainage into internal mammary and axillary lymph nodes. The first draining node from, for instance, a tumor is identified as the sentinel lymph node.

axillary lymph nodes, where a negative biopsy indicates a >95% chance that the remaining nodes are also cancer free [214].

To locate SLNs, peritumoral injections of isosulfan blue dye and/or a radionuclide-labeled sulfur or albumin colloid are used. The local accumulation of the radioisotope is detected using a handheld gamma ray counter. SLNs are identified as any blue node or any node with greater than or equal to three times *in vivo* background counts per minute (*ex vivo*, ten times the counts per minute of a non-sentinel node). After excision, a pathologist critically evaluates the nodes by histology and immunohistochemistry for the presence of a metastatic tumor. If tumor is present, a complete dissection of the nodal basin is performed [215]. Nevertheless, sentinel node

biopsy is an invasive technique and is associated with radiation exposure to patients and physicians. Thus, a non-invasive technique that assists in the accurate identification of lymph node metastases would be ideal for patients. While the radionuclide can be imaged through lymphoscintigraphy (LS), the method has low temporal and spatial resolution where detailed anatomy cannot be visualized. Despite its limitation, LS is the only licensed method of imaging sentinel nodes that is widely available in clinical practice.

Many different imaging techniques, including magnetic resonance, computed tomography, and ultrasonography, allow visualization of lymph nodes that may not be palpable at physical examination [216, 217]. However, important criteria, such as thickened lobular cortex, displacement or absence of fatty hilus, enhancement patterns, and nodal grouping are parameters that are not easily evaluated and standardized [218]. Lymph nodes are tightly regulated in size, and so these imaging techniques currently differentiate benign from metastatic lymph nodes by measuring nodal enlargement, i.e. a maximum short axis diameter greater than 1 cm is considered malignant [219]. Nevertheless, micro-metastases are often found in 'normal' sized and shaped lymph nodes [220]. Enlarged nodes may not be malignant and simply be the result of hyperplasia, while small nodes may contain microfoci of disease and not be abnormal in shape or size. Studies indicate a decrease in disease-free survival of patients harboring micro-metastases compared to those with tumor-negative lymph nodes [221, 222].

USPIOs have been used to provide better resolution of nodal anatomy and to differentiate absolute signal intensities of benign and malignant nodes. Ferumoxtran-10, or Combidex is a 20-40nm dextran-coated USPIO which has been used for magnetic resonance lymphangiography (MRL) when administered intravenously. Its small

diameter allows for endothelial transcytosis from the systemic circulation into the interstitium where it is directly drained into or picked up by macrophages to be taken to the lymphatic system (Figure 5-73). The ferumoxtran-10 accumulated in lymph nodes markedly reduces T_2 signal intensity in normal nodes and is readily detectable by MRI [223]. Cells that lack reticulo-endothelial activity, such as malignant cells, do not uptake USPIO. Thus, in USPIO-contrast enhanced MRI, malignant lymph nodes retain signal and are relatively bright as compared to darkened benign nodes. A single intravenous injection of USPIO enables detection of multiple nodes allowing for multiple sites of disease to be evaluated. Since 1994, ferumoxtran-10 has been used to detect lymph node metastases in patients with head and neck [53], urological and pelvic [224], gastric [225], and breast cancers [226].

Figure 5-74 and Figure 5-75 demonstrate the application of USPIO enhanced detection of metastasis. A Phase III clinical study has been conducted [227], and when injected slowly, the USPIO was well-tolerated, with no adverse side-effects. Metastatic lymph nodes were detected with a sensitivity of 100% and specificity of`80%, catching normal-looking metastatic nodes that would not have been considered pathological based on size criteria. Sensitivity, specificity, and accuracy of detection increased from 54, 82 and 68%, respectively, in pre-contrast MRI to 85, 85 and 85% with USPIO-enhanced MRI [227]. Other MR agents used for lymphatic imaging are Gd-DTPA and Gd-containing macromolecular agents such as liposomes and dendrimers.

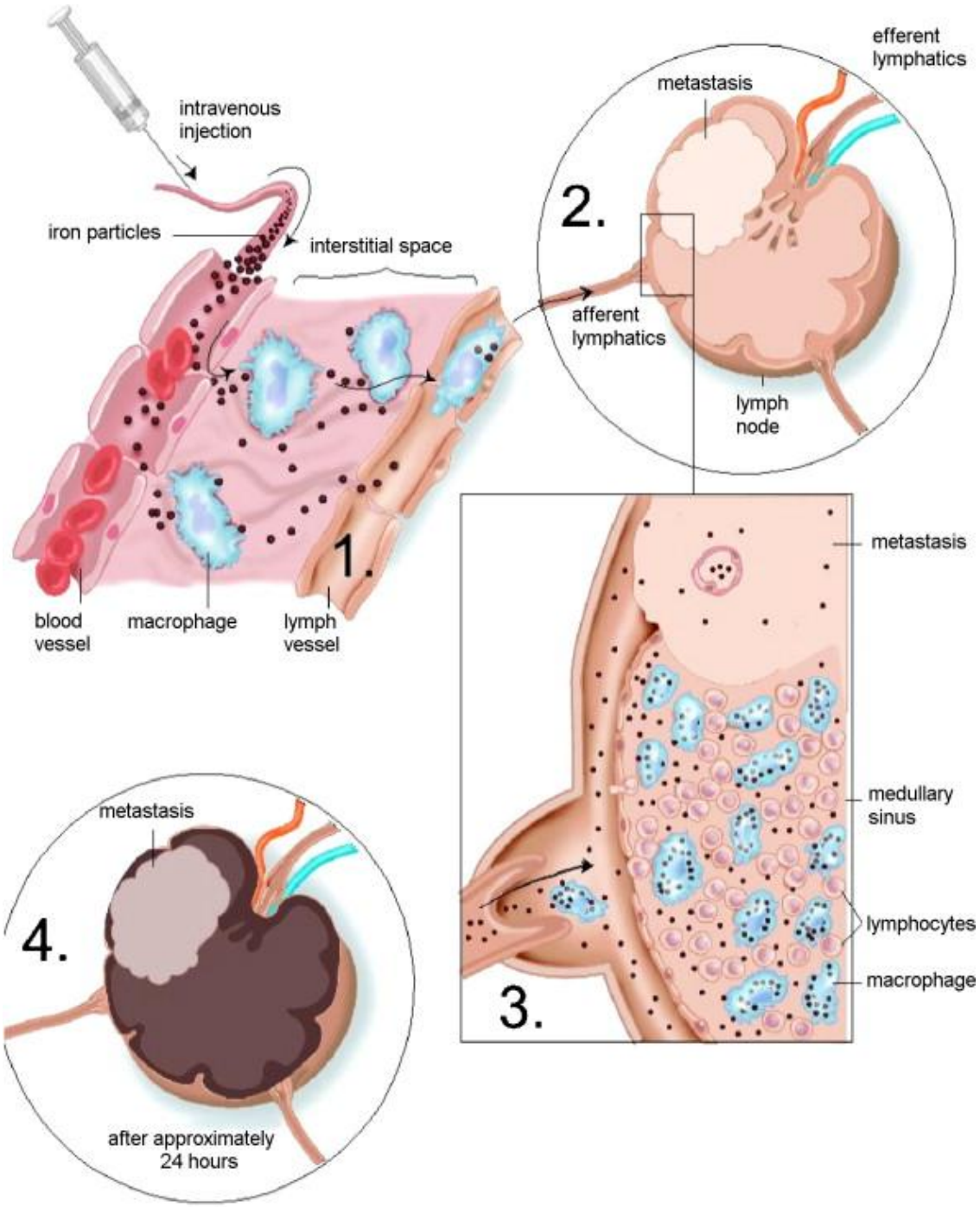

Figure 5-73: Uptake mechanism of ferumoxtran-10 (Combidex). (1) IV injected particles slowly extravasate from vascular to interstitial space and (2) are then transported to lymph nodes via lymphatic vessels. In lymph nodes, (3) particles are internalized by macrophages, and these intracellular iron-containing particles cause normal nodal tissue to have low signal intensity. (4) Disturbances of lymph flow or nodal architecture by metastases lead to abnormal accumulation patterns depicted by the lack of decreased signal intensity. [69]

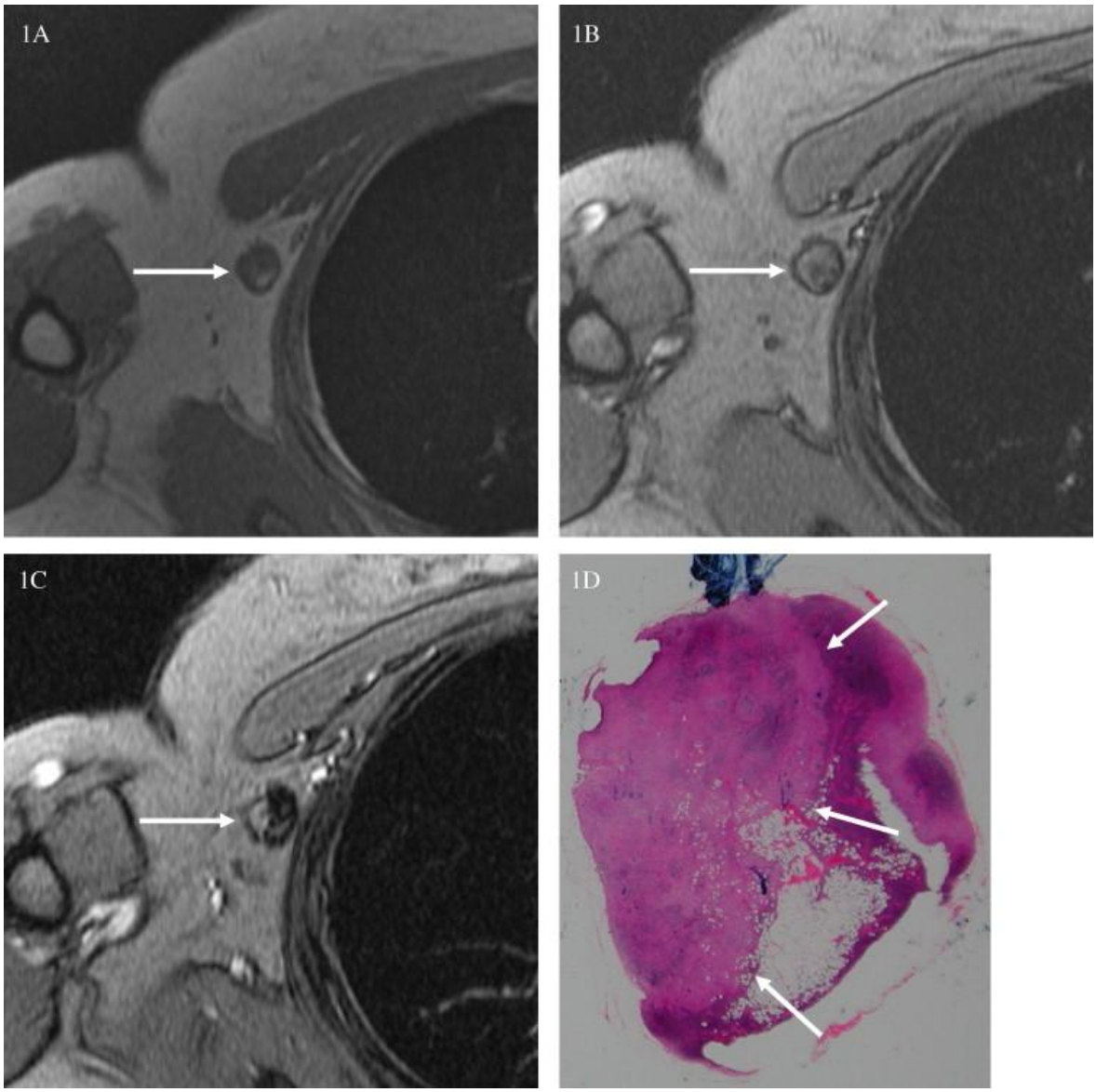

Figure 5-74: Metastatic lymph nodes on T_1- and T_2*-weighted USPIO images. (1A) T_1-weighted image where the short axis diameter of the lymph node (arrow) was 10.5 mm and was diagnosed correctly as metastatic; (1B) the lymph node (arrow) shows high signal intensity before the administration of USPIO, and (1C) after the administration of USPIO, the lymph node (arrow) showed an irregular darkening pattern. (1D) This diagnosis was histologically confirmed as a metastatic lymph node. The arrows represent the metastatic areas of the lymph node. [226]

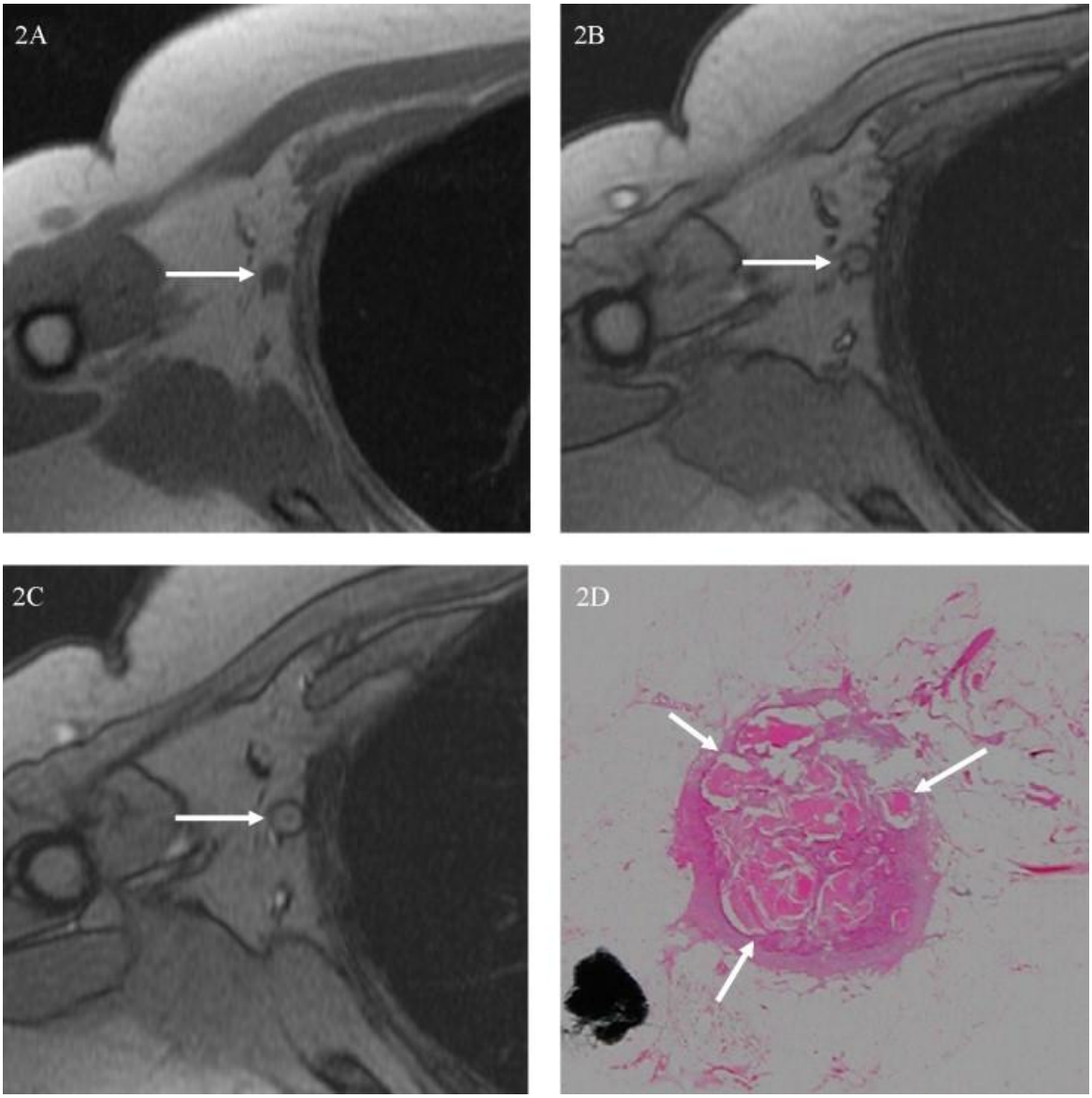

Figure 5-75: Error of T_1-weighted image. (2A) T_1-weighted image where the short axis diameter of the lymph node (arrow) was 4.8 mm and was incorrectly diagnosed as nonmetastatic. (2B) The lymph node (arrow) showed high signal intensity before the administration of USPIO, and (2C) after administration, there was an overall high signal pattern. (2D) Histologically, metastatic lymph node disease was confirmed. [226]

The described body of work with USPIOs for lymphatic imaging has been primarily focused on intravenous injection of an agent, rather than intradermal or subcutaneous injection for sentinel node detection. While MRI does not involve radiation exposure and offers good spatial resolution and functional information for preoperative

analysis, its limitation is that it does not provide real-time feedback to the surgeon and so would not be ideal for identifying SLN, if the need be, for a biopsy. Optical or fluorescence imaging provides a potential solution. Not only does this imaging modality not require radiation exposure, it has high temporal and spatial resolution with the ability to image at a molecular level. A NIR fluorescence imaging system that simultaneously displays color video and NIR images has been developed for real-time surgical applications. This technique's main disadvantage, even while using NIR probes, is poor depth sensitivity of a few centimeters. Therefore, optical probes would only be applicable for animal studies or superficial human imaging. Sentinel node imaging with a dual modality MR/optical agent, however, would allow for detailed anatomical information from MRI and functional and real-time information from optical imaging.

5.4.2 Dual-Modality Sentinel Lymph Node Imaging with SCION

A mouse model was used to test if the sentinel lymph node could be elucidated by SCION particles in both MR and fluorescence imaging. Similar to humans, mice also have a lymphatic system, as shown in Figure 5-76. Lymphatic ducts in the upper feet pads drain into the axillary nodes.

An untargeted (no antibody) SCION solution (10 μL of a 40 mM [Fe]) in saline was intracutaneously injected into the feet pad of normal *nu/nu* mice. Approximately 24 hr post-injection, the agent was observed in draining axillary lymph node, termed the "sentinel node". For MRI (assisted by Marcelino Bernardo), the same setup as described in 5.2.2 was used. With fat suppression by spectral attenuated inversion recovery (SPAIR) sequence, respiratory triggered T_2-weighted multi-slice spin-echo images (repetition time of 4000 ms, echo time of 30 ms, 90° flip angle, voxel size of 0.15 x 0.15

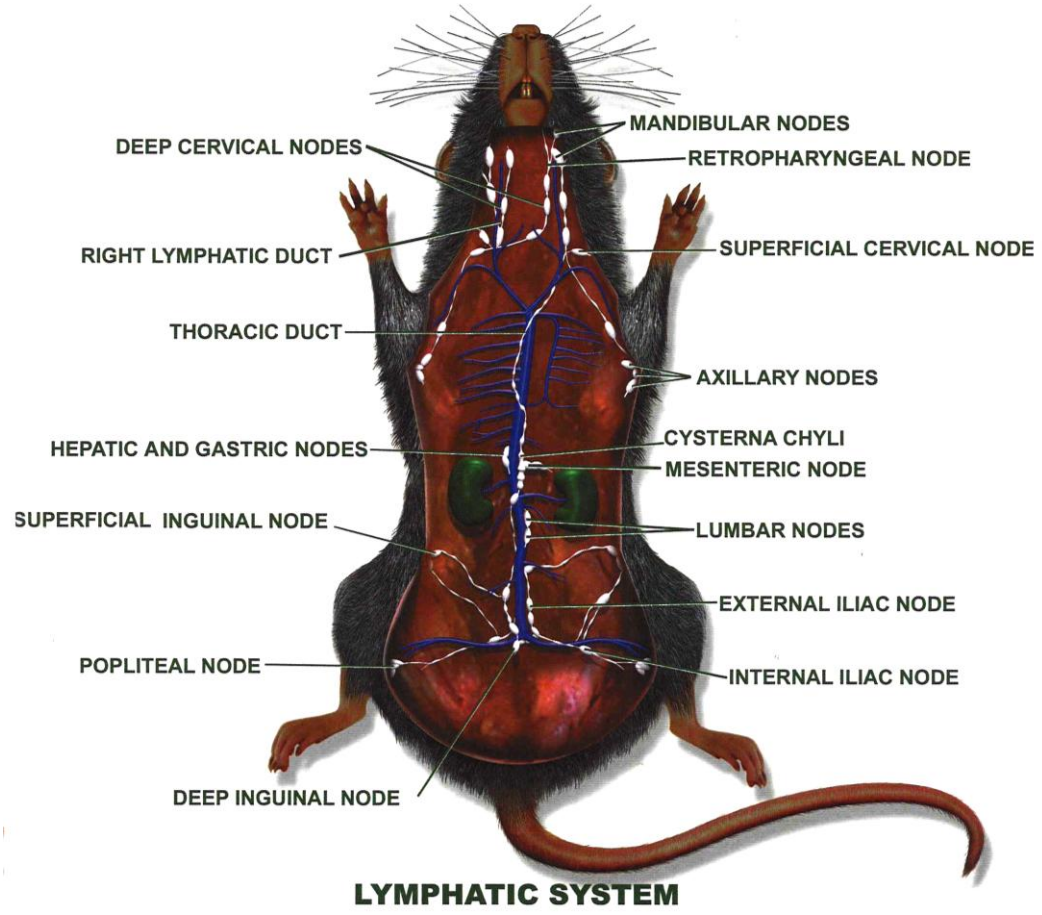

Figure 5-76: Mouse lymphatic system. [228]

x 0.6 mm, resolution of 6.6 pixels per mm) were obtained prior to injection of the agent (t = 0 hr) and post-injection at 24 hr. After acquisition of MRI data, optical imaging of the same mice was performed to generate matched sets of dual modality imaging data of the sentinel nodes. Visualization of the sentinel lymph node(s) in the both magnetic resonance and fluorescence images was clearly achieved (Figure 5-77), where the white arrows point to control nodes on the side with no SCION injection and the red arrows point to the nodes that have been darkened after particle injection. In optical imaging, the

lateral thoracic node, which drains from the axillary lymph node, was also illuminated. When dissected and removed from the body, the nodes continued to fluoresce.

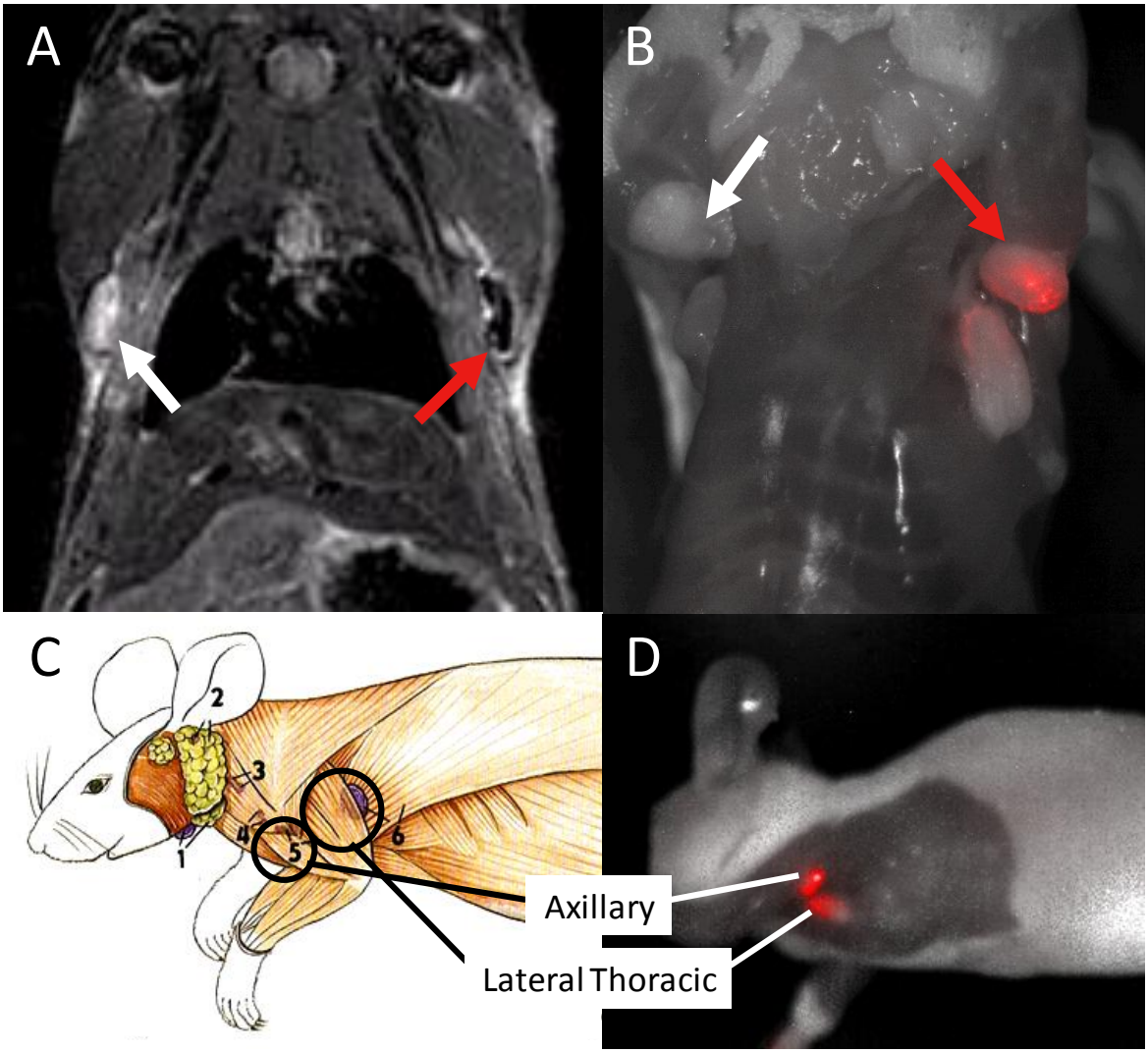

Figure 5-77: Sentinel lymph node imaging with SCION. The white arrows in (A) T_2-weighted MR and (B) optical imaging point to control nodes on which side no injection of SCION was give to the foot pad. The red arrows indicate nodes that were clearly visualized after SCION footpad injection, where in MR the node darkened and in spectrally unmixed optical imaging the NIR fluorescence was captured. The illuminated nodes are the axillary and lateral thoracic lymph nodes, as pointed out in (C) and (D).

Though nodes were invisible to the naked eye, they had intense NIR enhancement. Figure 5-78 demonstrates the location of a sentinel node through the skin of the mouse.

A limitation of the optical image, however, is that the margins of the node are somewhat blurry due to light diffusion. The MR image has a much higher spatial resolution that is allowing for some nodal anatomy to be deciphered. On the other hand, while an injection of 10 μL of a 40 mM [Fe] solution was necessary to consistently identify the lymph nodes using a 3-Tesla MRI instrument, nodes were detectable by the more sensitive optical imaging with as little as 2 mM [Fe] SCION solution. Thus, the combination of MR and optical imaging within one agent could potentially allow sentinel nodes to be examined and mapped with MRI prior to surgical resection, and during surgery, optical imaging could be employed to guide the surgeon to the appropriate sentinel node(s). Real-time fluorescence imaging could be accomplished with commercial-grade video cameras with suitable filtering.

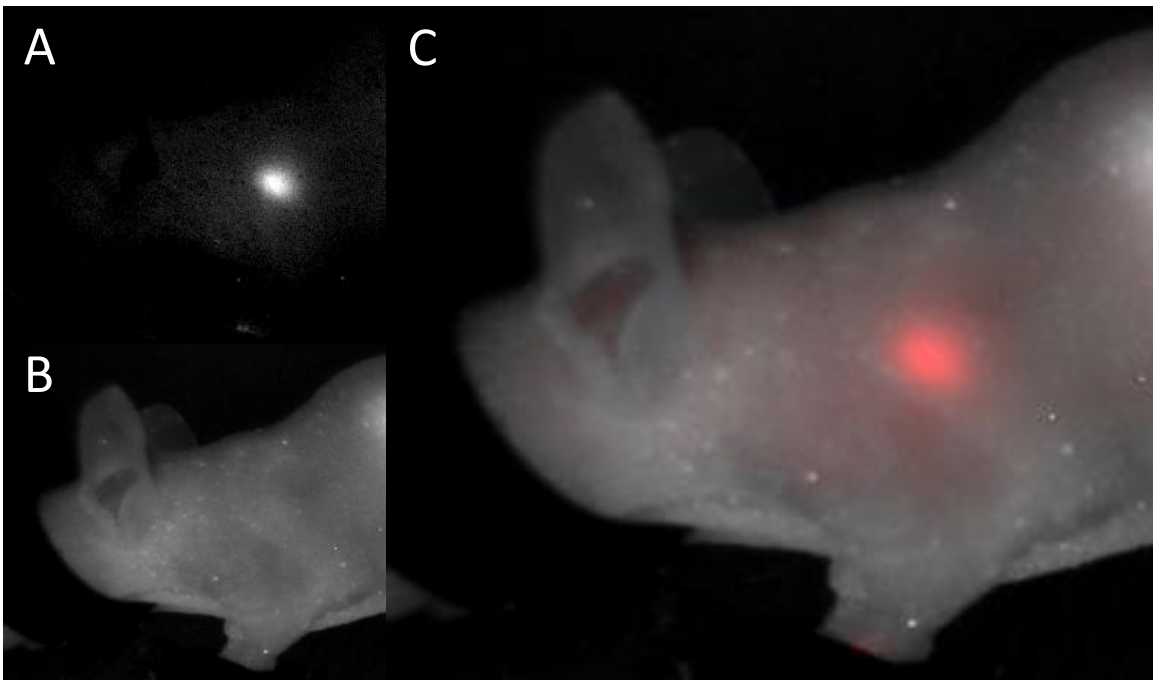

Figure 5-78: Spectral unmixing for optical imaging of sentinel lymph node with SCION. In (C), the composite of (A) separated NIR light and (B) white light, the node is clearly visible through the skin.

Talanov and co-workers [229] have taken a similar approach and shown dual-modality SLN imaging with a Cy5.5-Gd-PAMAM G6 dendrimer that was injected into the mammary fat pad of mice. As far as we are aware of, these are the only two dual-modality agents that have demonstrated MR and optical imaging of sentinel nodes. Though there is promise for dendrimer and other macromolecular agent use in MRL, USPIOs are the only agents that have been tried in humans.

5.4.3 Tumor Detection in Sentinel Lymph Node with SCION

To examine the ability to use SCION to detect tumor in the SLN, *nu/nu* mice were given intravenous injections of human colon carcinoma LS-174T cells (50,000 cells in 200 μL media) with the hopes that some tumors would form in the axillary LNs. Precedence for this model exists in work presented by Shah and co-workers [230], but whereas they pretreated the animals with β-estradiol to suppress natural killer cell activity, we did not. Similar to a clinical case, it was not certain that cells would in fact migrate and grow into tumor at the axillary LN. Sets of mice (3-10 per group) were analyzed with SCION injections and viewed in MR and optical imaging (as described in 5.4.2) at 1, 2, 3, and 4 weeks post-inoculation. Mice with no injection of LS-174T were used as controls. Excised lymph nodes were fixed in formalin and a selection (based on their MR scans) was sent to Mass Histology (Worcester, Massachusetts) where they were evaluated with immunohistochemistry and histology. There were three analyses per lymph node: 1) hematoxylin and eosin stain, 2) Prussian blue iron stain for SCION, and 3) human mitochondria stain with Abcam. The only human cells that should be in the animals are the injected LS-174T cells.

Figure 5-79 is a representation of the results obtained. Control animals with no LS-174T cell injection had LNs that completely darkened in MR when using SCION for SLN imaging. Of the experimental group, an animal whose axillary LN remained bright was suspected to have tumor "metastasis". With both sets of animals, the SLN was clearly visible in optical imaging because of its greater sensitivity than MR. In histology, the control mice demonstrated significant iron and no human mitochondria staining, indicating the presence of SCION and absence of tumor cells. The animals that possibly had tumors based on their MR, stained positive for tumor and negative for SCION in the areas with tumor. This initial study has demonstrated proof-of-concept in diagnosing tumor presence in the SLN with MR and illuminating it in optical imaging. Further statistical work to characterize the animal model and efficacy of using SCION for tumor detection must be performed.

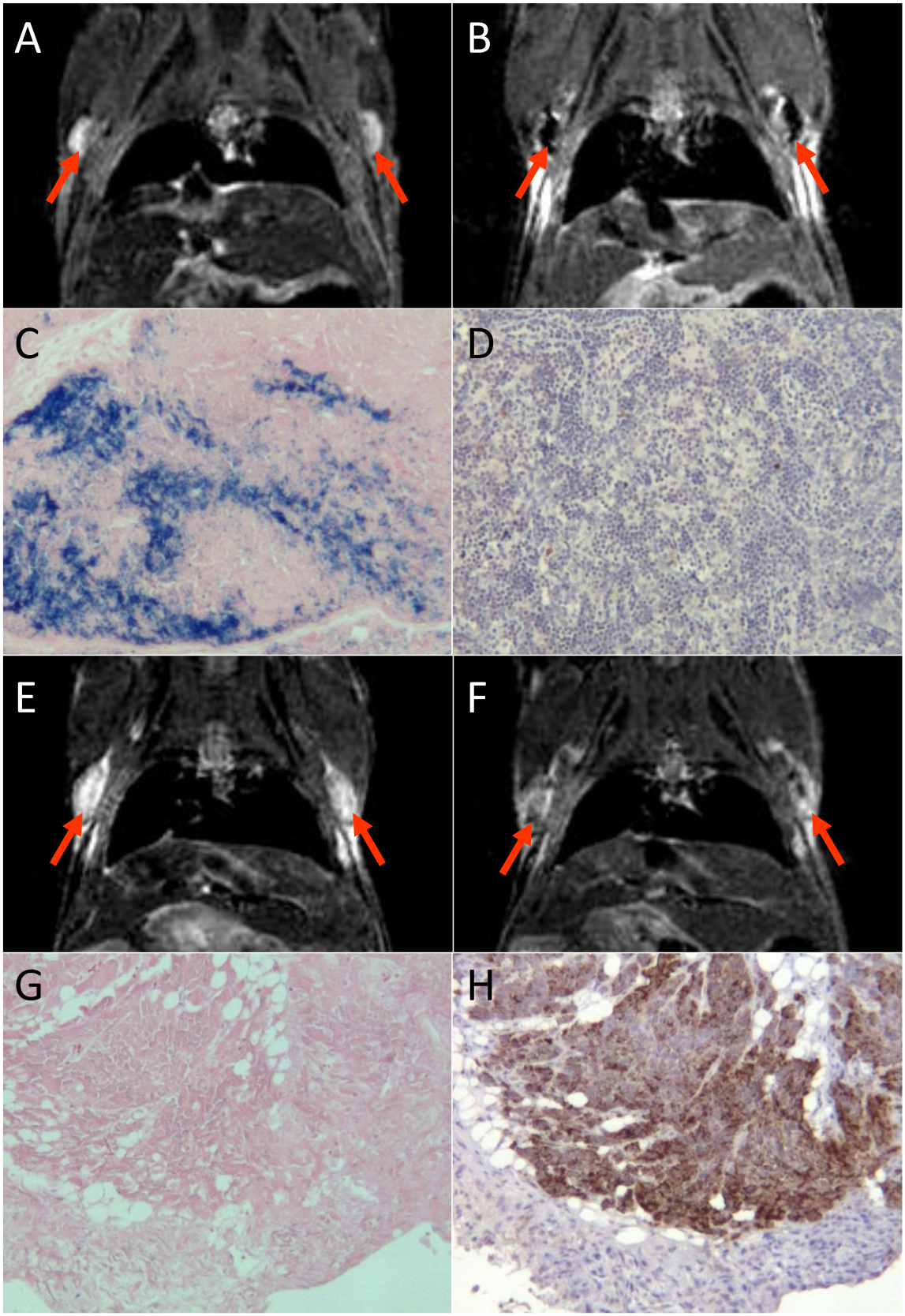
A
B
C
D
E
F
G
H

Figure 5-79: Sentinel lymph node tumor detection by SCION. (A) Pre-contrast and (B) post-contrast study of control animal with no cancer cell injection showed darkening of and clear lymph nodes. (E) Pre-contrast and (F) post-contrast study of animal injected with LS-174T cells demonstrated significant signal from the nodes with abnormal anatomy and was classified as having LN tumor. Histology confirmed this diagnosis. Control LN stained (C) positive for SCION with the Prussian blue stain and (D) negative for carcinoma with a human mitochondrial (Abcam) stain, while experimental LN stained (G) negative for SCION and (H) positive for cancer.

Contrast-enhanced imaging offers the ability to diagnose lymphatic disease and dual-labeled agents that permit imaging with MRI and optical cameras are at the forefront of this science. In addition, agents such as SCION have the potential to incorporate or attach drugs to their structure, which may enable targeted therapy at the same time as diagnostic imaging.

Chapter 6

Future Applications & Conclusions

Herein, a rapid and economical method of synthesizing USPIOs with controlled thin coatings of silica has been reported. Though such SCION particles have industrial applications, including use in power transformers, magnetic recording heads, and microwave applications [231], this work has focused on optimizing particles for medical applications. USPIOs have been widely reported as strong MRI contrast agents with high T_2 relaxivity; however they need a stabilizing outer functionality. Silica improves biocompatibility and also provides a negative surface charge under physiological pH conditions, imitating most biological species. Furthermore, silica inhibits self-aggregation of USPIOs that could lead to ferromagnetic behavior and conserves the superparamagnetic properties of the iron oxide cores. By coupling the magnetic properties of the iron oxide core with the optical contrast agent Cy5.5, that has emissions in the infrared range, and an antibody that is labeled with the radioisotope ^{111}In, the developed nanoparticle allows for not only triple verification of location through sensitive and high resolution techniques, but also quantification of the delivered structure. These SCION particles have a diameter advantageous for prolonged blood circulation and can

further be directed to a specific target via conjugation of antibodies or their fragments to the large particle surface area.

While the work presented is a significant beginning to having a new imaging and drug delivery agent for patients, there are some unknowns that were identified in the previous chapters. While these particles are clearly superparamagnetic, their relaxivity is not as high as larger Feridex particles. Doping the iron core with zinc [146] or manganese [147] might enhance the relaxivity, and upon doing so, it would be necessary to re-characterize particle properties, i.e. surface charge, effect on cell viability, etc. Furthermore, while SCION particles at 20 nm diameter fall in the range that literature shows has prolonged blood circulation [62], the surface coating will most likely result in different *in vivo* properties than those by the typical dextran coating. Though a particle suspension might be monodisperse during synthesis, there is very little in the literature analyzing if aggregation occurs *in vivo*. Given that size is considered to be an advantage of nanotechnology, this issue is one that needs to be studied. Attached antibody immunoreactivity and the targeted and specific uptake of such particles were not analyzed in as much detail as we wished, and one of the major impediments to doing so was SCION solubility once conjugated to antibody. Published work on *in vivo* studies with antibody-conjugated USPIO does not typically mention solubility. It is less likely that the silica coating is the reason for this because the same aggregation was not seen in un-conjugated solutions. The conjugation chemistry is a well established and often used one, so perhaps it is the combination of the two components that results in a conjugate with not enough charge to remain stable, as was observed with the rise in PZC. Strategies to enhance the surface charge without affecting antibody immunoreactivity need to be explored. Two components that were not quantified with regards to SCION synthesis

were the number of dye molecules and number of antibodies per particle because, in both cases, standard techniques were unable to control for the iron oxide core's inherent optical absorption or chemical properties. Working through the synthesis, characterization, and application of the SCION particle clearly identified unanswered questions that those in the field of medical nanotechnology must continue to study.

Despite the above concerns, studies with untargeted SCION demonstrate great promise for their use in liver and sentinel lymph node imaging, two of the most common sites for cancer metastasis. However, there are other areas that have not yet been explored where these particles can also be applied, namely cell tracking and thermotherapy.

6.1 Magnetic Particles for Cell Tracking

In recent years, there has been increased interest in cell-tracking strategies in order to apply cell-based therapies such as monitoring antigen-specific cytotoxic leukocytes in cancer patients [232, 233], inflammatory cells in autoimmune diseases, and stem cells for tissue repair of myocardial infarction [234], ischemic stroke, and neurodegenerative disorders [235, 236]. Cell-tagging agents should ideally allow for single-cell detection and quantification of cell number while not interfering with the target cell function. Furthermore, signal should persist in the target cell with minimum label dilution after cell division and with minimal transfer to non-target cells. Finally, such agents should be biocompatible and non-toxic.

Cells have been labeled by SPIOs through a number of techniques. A variety of cells can naturally internalize large particles through phagocytosis and small particles through pinocytosis. Cell lines that have been shown take up SPIOs without facilitation include blood cells, fibroblasts, immortalized rat progenitor cells, human hepatocellular liver carcinoma cells, and human hematopoietic progenitor cells [237]. The majority of nonspecific cellular labeling has been performed with macrophages, key players in the innate immune response and important markers of local inflammation. A method of *ex vivo* labeling has been successfully used to track the migration of SPIO-labeled macrophages for seven days from the injection site in the basal ganglia of the brain left hemisphere through the corpus callosum to the ventricular system [91].

For cells that lack substantial phagocytic capacity, methods have been developed to encourage penetration of the particle through cell membrane either non-specifically or by involving cell surface receptors. Walczak et al [238] recently demonstrated the use of magnetoelectroporation, a technique that induces reversible electromechanical permeability changes in cell membranes to rapidly label cells. Another approach has been the application of anionic maghemite nanoparticles as a class of surface modified particles that have strong negative surface charges and interact strongly but non-specifically with the cell plasma membrane [239]. These magnetite particles are surface adsorbed and then efficiently internalized by a wide range of cell lines. Riviere et al [240] used such particles to label and monitor smooth-muscle cell engraftment in a rat model of myocardial ischemic injury. After particle internalization, cell proliferation was unaffected but the iron load per cell did dilute in subsequent daughter cells.

A popular and effective technique for *ex vivo* cell labeling is by using permeation agents such as proteins, lipids, dextrans, phosphonates, and dendrimers. Matuszewski et

al [241] successfully tagged human lung and breast cancer, fibrosarcoma, and leukocytes with carboxydextran-coated SPIOs (17–65 nm) and a dextran-coated iron oxide (150 nm). They observed greater labeling in the presence of transfectant media and spontaneous fluid-phase endocytosis in all dividing cell types with no effect on viability, growth rate, and apoptotic index after endosomal SPIO incorporation. Studies where poly-L-lysine was used as the transfectant to load encephalitogenic T cells with SPIO have demonstrated the ability to detect T cell migration into the central nervous system of an experimental autoimmune encephalomyelitis (EAE) mouse model for relapsing-remitting multiple sclerosis [88]. Multiple sclerosis is a T cell–mediated autoimmune disease with early lesions characterized by mononuclear cellular infiltrate, edema, demyelination, and axonal loss. SPIO–labeled T cells were detected in the mouse spinal cord, both *in vivo*

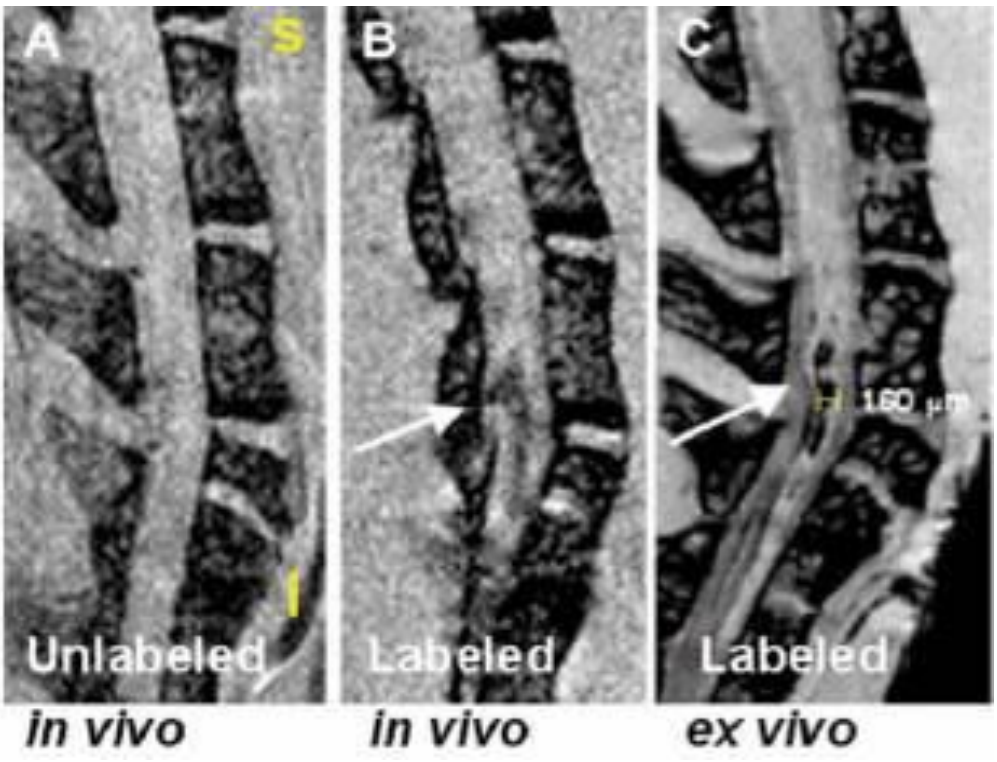

Figure 6-80: *In vivo* MRI from thoracic to lumbar cord of (A) labeled and (B) unlabeled experimental allergic encephalomyelitis mice with clinical score 3. (C) *Ex vivo* MR microscopy of labeled mouse (B). Images demonstrate clear visualization of lesion when T cells were labeled with SPIO. [88]

and *ex vivo* (Figure 6-80)

Protamine sulfate has also been used to improve cell permeation. Feridex and protamine sulfate are a promising combination because they are both FDA approved. Cells, including mesenchymal stem cells, hematopoietic ($CD34^+$) stem cells, macrophages, lymphoblast cells and splenocytes treated in this manner were viable for 4 weeks, [83]. Arbab and colleagues showed that mesenchymal and hematopoietic stem cells labeled with these agents preserved their expression of surface phenotypic markers and chondrogenic differentiation capacity [242]. Other transfection agents used to label cells with SPIOs have been described by Rogers and co-workers [237].

A number of receptor-mediated approaches have been developed. Bulte and co-workers [235] used the mouse transferrin receptor, OX26, [243] to induce receptor-mediated endocytosis of attached nanoparticle in a rat oligodendrocyte progenitor cell line and then determine the immediate dispersion, migratory capacity and long-term survival of the cells when grafted into the spinal cord of myelin-deficient rats. They were successful in co-localizing areas of MR contrast with histopathologic staining for iron and newly formed myelin. Nanoparticle surfaces can also be modified with synthetic structures to aid in the permeation of cell membranes. Magnetodendrimers are iron oxide particles coated with highly branched carboxylated structure. Their highly charged nature results in cell membrane binding, induction of membrane bending, and eventual endocytosis [79, 244].

Some studies indicate that MRI cell tracking has the potential to detect even single cells both *in vitro* [245] and *in vivo* [246, 247]. Shapiro et al [247] showed that single SPIO-labeled primary mouse hepatocytes could be detected in the liver 1 month post-injection. However, tracking of individual cells for clinical application is not usually

achieved given the limitations on image resolution and the fundamental drawback of negative contrast techniques where void artifacts are not easily distinguished from the agent. Nuclear cell tracking techniques are considered more sensitive than MR cell-tracking techniques. Kraitchman and co-workers [248] directly compared the two modalities by tracking mesenchymal stem cells co-labeled with Feridex and ^{111}In-labeled oxine in a canine model of infarct reperfusion where SPECT/CT but not MR imaging was able to detect cells up to 8 days post-injection.

Methods for labeling cells with USPIOs have allowed the noninvasive tracking of stem cells[79], neural transplants[86], white blood cells[87], T-cells[88-90], and monocytes[91] in animal studies. SCION particles should be no different. Already in Chapters 3 and 4, a few cell lines have been labeled with particles *in vitro* with no effect on cell viability. Transfection agents and effective ligand binding will only enhance the uptake. Furthermore, because the particles are fluorescent, labeled cells can easily be separated by FACS for collection to use for *in vivo* studies.

6.2 Magnetic Particles as Mediators for Hyperthermia

The use of heat as a medical therapy is as old as written medicine itself. Probably the first medical textbook dating back more than 5000 years, the Edwin Smith Surgical papyrus contains a description of hyperthermia treatment of breast cancer [249]. Today, hyperthermia, particularly by use of magnetic particles, remains a promising form of cancer therapy for 1) mild hyperthermia (41 to 46 °C) to stimulate an immune response for non-specific immunotherapy of cancers and 2) thermoablation (46 °C to 56 °C) for

tumor destruction by direct cell necrosis, coagulation or carbonization [250]. Compared to traditional techniques, hyperthermia treatment can be locally applied with no systemic effects and reduced side effects. Chemotherapy drugs have severe side effects on healthy organs and radiotherapy adversely affects nearby tissues. The limitation, however, is that for tumor thermoablation to be successful an almost unrealistic level of temperature control is required, and so hyperthermia is typically used in combination with chemotherapy or irradiation. In fact, this combined therapy approach has been found to be quite effective. Normoxic, or well oxygenated, cancer cells are more sensitive to radiation than hypoxic, or poorly oxygenated, cancer cells, while hypoxic cells are more heat-sensitive than normoxic cells [251].

Table 6-16: Comparison of the three main techniques of magnetic hyperthermia using magnetic particles as mediators [252]

	Arterial Embolization Hyperthermia (AEH)	Direct Injection Hyperthermia (DIH)	Intracellular Hyperthermia (IH)
Magnetic Particle Administration	Through the arterial supply of the tumour	Directly injected in the tumour	Arterial embolization or direct injection or ideally *i.v.* injection of targeted particles
Heat Origin	Intravascular (within the blood vessels)	Extracellular	Intracellular
Expected Advantages	• A more effective tissue temperature distribution due to the concentration gradient of particles through the tumour and the surrounding tissues, with the highest concentration in the tumour (no sharp drop in temperature at the tumour edge)	• Not dependent on an arterial pathway to the tumour: could be applicable to a wide range of tumour types • No consequent risk from arterial catheterisation	• Probable improvement of the treatment efficacy • Treatment of scattered tumours and metastases • Lower and therefore safer required magnetic field
Probable Drawbacks	• Not applicable to tumours without a good arterial supply (*e.g.* micrometastases) and tumours outside the liver • Risk of embolization and subsequent ischemic necrosis of normal tissues	• Restricted to tumours which would be accurately visualized and accessible under radiological guidance • Necessity of repeated injections for large or irregularly shaped tumours • Increased risk of needle track implantation or local tumour spread	• non-specific uptake of the particle • low concetrations of agent at target

Injectable colloidal dispersions of magnetic particles are used for arterial embolization hyperthermia (AEH), direct injection hyperthermia (DIH), and intracellular hyperthermia (IH) (Table 6-16) [252]. Their use in combination with hyperthermia is advantageous because of the ability to image their distribution and because of better temperature homogeneity [250]. Additionally, these particles have the potential to be designed for selective uptake by tumor cells, permitting therapy for even metastases.

Particle heating is a function of size and magnetic properties. Ferro- and ferrimagnetic materials generate heat through hysteresis losses. However, superparamagnetic materials have no hysteresis losses. In this case, when an applied external AC magnetic field supplies energy, this energy is dissipated through Néel and rotational Brown relaxation [253, 250]. Neel relaxation is dependent on the reorientation of internal magnetic dipoles, while rotational Brown relaxation is based on the rotation of the particles themselves due to torque exerted on the magnetic moment (Figure 6-81) [254]. The frequency dependent imaginary part of magnetic susceptibility is used to

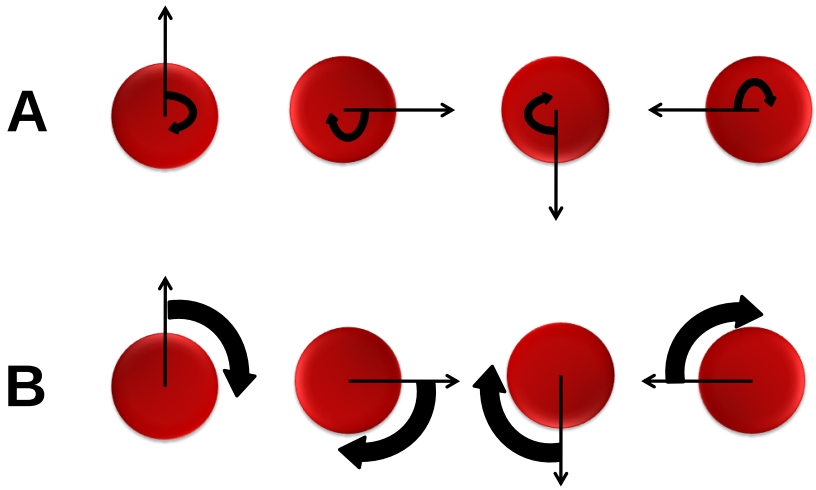

Figure 6-81: (A) Néel rotation of magnetization in a magnetic particle (the particle does not rotate) as it overcomes the magnetic moment anisotropic energy barrier. (B) Brown rotation of a magnetic particle (the particle rotates as a whole) as it overcomes rotational friction energy barrier.

analyze both Neel and Brown relaxation. There is also a second type of Brownian motion, previously described in Chapter 3, involving the random movement of particles due to thermal energy and the bombardment of surrounding solvent molecules. However, this Brownian motion has minimal contribution to hyperthermia heating.

Localized thermotherapy utilizing magnetic materials in an alternating magnetic field has been used in a number of *in vitro* and *in vivo* studies since the pioneering work of Gilchrist and co-workers in 1957 [255]. Because macroscopic liver tumors derive their blood supply primarily from the hepatic arterial system and normal liver tissue primarily from the portal venous system [256], AEH experiments were performed in rabbits [257] and in pigs [258] by hepatic arterial infusion of 32 μm microspheres of magnetite and a polyester of valeric and butyric acids. The results demonstrated a higher efficacy of AEH than DIH with iron concentration in liver tumors five times as high as iron concentration in liver normal tissues. *In vivo* experiments of magnetic fluid hyperthermia with intralesional injection of dextran-coated magnetite particles into a mouse mammary carcinoma model showed some local tumor growth control [259]. Phospholipid-coated magnetite particles (~80nm) targeted to glioma cell lines demonstrated 60% tumor uptake of total injection. When exposed to AC magnetic field, the temperature of the tumor tissue increased to 43°C in 30 min and tumor growth was completely suppressed for over two weeks [260].

Factors that are important to consider when using magnetic particles for hyperthermia treatment include the technical parameters of the external AC magnetic field and the particle specific absorption rate, or the power of heating of a magnetic material per gram. Appropriate control of these factors allow for even very small amounts of USPIO, on the order of a 10^{-4} grams, to be used for hyperthermia in biological

tissue. A well-defined agent distribution within tumor tissue is one of the main tasks to be addressed for magnetic hyperthermia to be a useful therapy, and USPIO characteristics make them all the more promising for this purpose. In future work, the imaginary part of the magnetic susceptibility of USPIO, which determines electromagnetic losses and hence heating, needs to be measured and quantified.

6.3 Concluding Remarks

Magnetic nanoparticles are used as contrast agents for the liver and spleen and the work presented herein demonstrates proof-of-principle for multi-modal imaging with SCION in other areas such as sentinel lymph node imaging. Future developments will be continue to be in the direction of active targeting through molecular imaging and cell tracking, as well as for thermotherapy.

An imaging agent such as SCION is also uniquely suited for targeted drug delivery applications, because it can function as a vehicle for the therapeutic, as well as be confirmed and quantified by noninvasive medical imaging techniques. Present-day non-invasive drug delivery techniques, such as pills, aerosols, and patches, deliver therapeutics systemically and rely on a certain proportion of the pharmaceutical reaching the intended target. But a significant number of drug molecules never arrive at their target, which is both inefficient and can have negative side effects. For example, chemotherapy has notoriously unpleasant side effects because the highly toxic agents used to kill cancerous tumors also damage healthy cells. Hence, targeted delivery of therapeutics is a major goal of pharmaceutical development. Accurate imaging of

targeted drugs permits confirmation that the drug is "hitting" the target and in some cases can be used to convert a pro-drug from its inactive to active form by local application of energy. Though many drug delivery techniques exist, few allow *in vivo* imaging and control of drug release at the cellular level. The use of a particle such as SCION holds great potential of providing new opportunities for both diagnostics and targeted therapies. Next generation platforms that incorporate drugs onto the SCION particle are drawn in Figure 6-82.

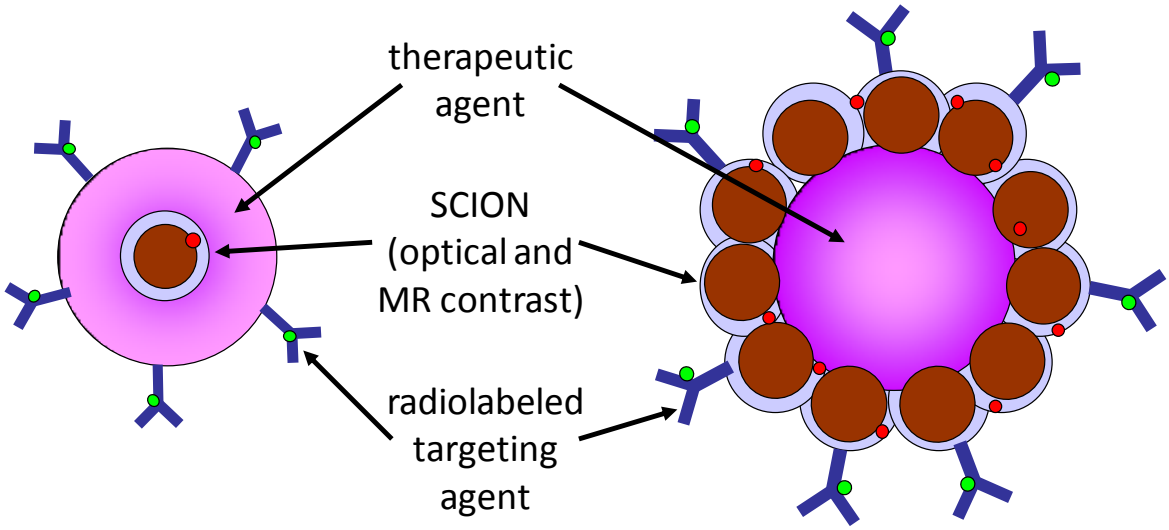

Figure 6-82: Possible drug delivery vehicles with SCION.

One way to control drug delivery could be to store the therapeutic agent in a porous or biodegradable material on the iron oxide core which could slowly release and sustain a desired drug level at the target over time for treating a range of conditions such as inflammation, cancer, diabetes etc. There are also thermosensitive polymers [261], e.g. poly(acry1amide-cobutylmethyacrylate) and poly(acry1ic acid), whose chemical structure, such as with hydrogen bonding, can change by increasing temperature, causing polymer swelling and potential release of drugs. Temperature increase could be

generated by manipulating the superparamagnetic properties of the SCION core. A second design with a hollow core containing the therapeutic surrounded by a shell of functionalized SCIONs could be heated to rupture or release its payload also using the local application of AC magnetic field. In both cases, intracellular drug release could be triggered by the temperature increase during the hyperthermia treatment sequence under MRI monitoring and followed up by examination with SPECT/CT. If a surgery or biopsy was still required for further characterization, the optical tagging would assist in guiding these procedures as well as help document the lesion during histologic analysis. Such drug delivery technologies could incorporate very efficient drugs that are already known, but too toxic for systemic administration. Furthermore, rational drug delivery strategies allow target tissue concentrations to be estimated on the day of treatment rather than be presumed from clinical outcomes assessed during follow-up several weeks later.

In order to reach patients, certainly, the safety profile of these particles must also be studied. Although the field of nanomedicine may be new, the submission of applications for nanomaterials and nanoparticlized drugs is not particularly new to the Food and Drug Administration (FDA). Liposomal encapsulated doxorubicin (Doxil), Magnevist, and Feridex are just a few of such agents that are approved. Both the FDA and the European Science Foundation on Nanomedicine define nanotechnology devices and materials as within the size range of 1-100 nm, and most nanomaterials are presented to the FDA as an Investigational New Drug (IND). The preclinical requirements for approval include both short-term and long-term toxicity testing in rodent and non-rodent species. Prior to New Drug Application (NDA), studies typically include pharmacology (mechanism of action), safety pharmacology (functional studies in various organ systems, most notably in the cardiovascular system), ADME (absorption, distribution, metabolism,

and excretion), genotoxicity (potential to cause mutations in both *in vivo* and *in vitro* assays), developmental toxicity (effects on reproduction, fertility, and lactation), immunotoxicology (effects on the immune system), and carcinogenicity [262]. Others may be requested on a case-by-case basis. Before these studies begin, however, proper characterization is crucial, i.e. of size, surface charge, stability, etc. The early particle characterization of SCION has been presented. To take it through to the FDA, both the safety and efficacy of the particle would need to be extensively characterized. This would include understanding the fate and toxicity of each individual component, as well as the full conjugate. A silica-coated USPIO used by MagForce, presented in Section 5.1, has reached its Phase II trials with success, offering a positive outlook for SCION. However, the additional dye incorporation would need to be compared *in vivo*. Furthermore, the efficacy of the agent for a different application would also need to be studied, particularly if it is being targeted.

This technology has great potential to be a sensitive, minimally invasive, and highly specific method to trace biomolecules and deliver therapy. The healing and diagnostic power of magnetism which can be traced back to Egyptian scripts has a promising future and particles such as those described here will play a prominent role in the field of nanomedicine.

References

[1] Andrä W and Nowak H 2006 *Magnetism in medicine: A handbook* (Berlin: Wiley-VCH)

[2] Gupta A K and Gupta M 2005 Synthesis and surface engineering of iron oxide nanoparticles for biomedical applications *Biomaterials* **26** 3995-4021

[3] Shinkai M 2002 Functional magnetic particles for medical application *J Bioscience Bioengineering* **94** 606-13

[4] Shellock F G and Kanal E 1999 Safety of magnetic resonance imaging contrast agents *J Magn Reson Imaging* **10** 477-84

[5] GEHealthcare 2008 Physics, techniques and procedures: Mr contrast medium. In: *Medcyclopaedia*,

[6] Caravan P, Ellison J, McMurry T and Lauffer R 1999 Gadolinium(iii) chelates as mri contrast agents: Structure, dynamics, and applications *Chem. Rev.* **99** 2293-352

[7] Aime S, Chiaussa M, Digilio G, Gianolio E and Terreno E 1999 Contrast agents for magnetic resonance angiographic applications: 1h and 17o nmr relaxometric investigations on two gadolinium(iii) dtpa-like chelates endowed with high binding affinity to human serum albumin *J. Biol. Inorg. Chem.* **4** 766-74

[8] Zhang Z, S.A. N and T.J. M 2005 Gadolinium meets medicinal chemistry: Mri contrast agent development *Cur. Med. Chem.* **12** 751-78

[9] Grobner T 2006 Gadolinium - a specific trigger for the development of nephrogenic fibrosing dermopathy and nephrogenic systemic fibrosis? *Nephrol. Dial. Transplant.* **21** 1104-8

[10] High W A, Ayers R A, Chandler J, Zito G and Cowper S E 2007 Gadolinium is detectable within the tissue of patients with nephrogenic systemic fibrosis *J. Am. Ac. Derm.* **56** 21-6

[11] Wiener E and Narayanan V V 2002 Magnetic resonance imaging contrast agents: Theory and the role of dendrimers *Adv. Dend. Macro.* **5** 129-247

[12] Wiener E, Brechbiel M W, Brothers H, Magin R L, Gansow O A, Tomalia D A and Lauterbur P C 1994 Dendrimer-based metal chelates: A new class of magnetic resonance imaging contrast agents *Magnetic Resonance in Medicine* **31** 1-8

[13] Bloembergen N and Morgen L O 1961 Proton relaxation times in paramagnetic solutions: Effects of electron spin relaxation *J. Chem. Phys.* **34** 842-50

[14] Bloembergen N, Purcell E M and Pound R V 1948 Relaxation effects in nmr absorption *Phys. Rev.* **73** 679-712

[15] Solomon I 1955 Relaxation processes in a system of two spins *Phys. Rev.* **99** 559-65

[16] Burton D R, Forsen S, Karlstrom G and Dwek R A 1979 Proton relaxation enhancement (pre) in biochemistry: A critical survey *Pro. Nuc. Magn. Res. Spectr.* **13** 1-45

[17] Lauffer R B 1987 Paramagnetic metal complexes as water proton relaxation agents for nmr imaging: Theory and design *Chem. Rev.* **87** 901-27

[18] Venditto V J, Regino C A S and Brechbiel M W 2005 Pamam dendrimer based macromolecules as improved contrast agents *Mol. Pharmaceutics* **2** 302-11

[19] Ogan M D, Schmiedl U, Moseley M E, Grodd W, Paajanen H and Brasch R C 1987 Albumin labeled with gd-dtpa. An intravascular contrast-enhancing agent for magnetic resonance blood pool imaging: Preparation and characterization *Invest. Radiol.* **22** 665-71

[20] Weinmann H H J, Brasch R R C, Press W W R and Wesbey G G E 1984 Characteristics of gadolinium-dtpa complex: A potential nmr contrast agent *Am. J. Roentgen.* **142** 619-24

[21] Peters T 1975 *Serum albumin* vol 1 (New York: Academic Press)

[22] Lauffer R B, Parmelee D J, Ouellet H S, Dolan R P, Sajiki H, Scott D M, Bernard P J, Buchanan E M, Ong K Y, Tyeklár Z, Midelfort K S, McMurry T J and Walovitch R C 1996 Ms-325: A small-molecule vascular imaging agent for magnetic resonance imaging *Acad Radiol.* **3** S356–8

[23] Parmelee D J, Walovitch R C, Ouellet H S and Lauffer R B 1997 Preclinical evaluation of the pharmacokinetics, biodistribution, and elimination of ms-325, a blood pool agent for magnetic resonance imaging *Invest Radiol* **3** 741-7

[24] Wang S C, Wikstrom M G and White D L 1990 Evaluation of gd-dtpa-labeled dextran as an intravascular mr contrast agent: Imaging characteristics in normal rat tissues *Radiology* **175** 483–8

[25] Ladd D L, Hollister R, Peng X, Wei D, Wu G, Delecki D, Snow R A, Toner J L, Kellar K, Eck J, Desai V C, Raymond G, Kinter L B, Desser T S and Rubin M D D L 1999 Polymeric gadolinium chelate magnetic resonance imaging contrast agents: Design, synthesis, and properties *Bioconjugate Chem.* **10** 361-70

[26] Lebduskova P, Kotek J, Hermann P, VanderElst L, Muller R N, Lukes I and Peters J A 2004 A gadolinium(iii) complex of a carboxylic-phosphorus acid derivative of diethylenetriamine covalently bound to insulin, a potential macromolecular mri contrast agent *Bioconjugate Chem.* **15** 881-9

[27] Schuhmann-Giampieri G, Schmitt-Willich H, Frenzel T, Press W R and Weinmann H J 1991 In vivo and in vitro evaluation of gd-dtpa-polylysine as a macromolecular contrast agent for magnetic resonance imaging *Invest. Radiol.* **26** 969-74

[28] Helbich T H, Gossman A, Mareski P A, Radüchel B, Roberts T P L, Shames D M, Mühler M, Turetschek K and Brasch R C 2000 A new polysaccharide macromolecular contrast agent for mr imaging: Biodistribution and imaging characteristics *J. Magn. Res. Im.* **11** 694-701

[29] Majoral J P and Caminade A M 1999 Dendrimers containing heteroatoms (si, p, b, ge, or bi) *Chemical Reviews* **99** 845-80

[30] Bryant L H, Brechbiel M W, Wu C, Bulte J W, Herynek V and Frank J A 1999 Synthesis and relaxometry of high generation (g)5,7,9,10) pamam dendrimer-dota-gadolinium chelates *J. Magn. Reson. Imag.* **9** 348-52

[31] Wu C, Brechbiel M W, Kozak R W and Gansow O A 1994 Metal-chelate-dendrimer-antibody constructs for use in radioimmunotherapy and imaging *Bioorg. Med. Chem. Lett.* **4** 449-54

[32] Stark D D, Weissleder R, Elizondo G, Hahn P F, Saini S, Todd L E, Wittenberg J and Ferrucci J T 1988 Superparamagnetic iron oxide: Clinical application as a contrast agent for mr imaging of the liver *Radiology* **168** 297-301

[33] Blakemore R P and Frankel R 1981 Magnetic navigation in bacteria *Sci Am* **246** 58-65

[34] Coroiu I 1999 Relaxivities of different superparamagnetic particles for application in nmr tomography *Journal of Magnetism and Magnetic Materials* **201** 449-52

[35] Jung C W and P. J 1995 Physical and chemical properties of superparamagnetic iron oxide mr contrast agents: Ferumoxides, ferumoxtran, ferumoxsil *Magn Reson Imaging* **13** 661-74

[36] Bean C P 1995 Hysteresis loops of mixture of ferromagnetic micropowders *J Appl Physiol* **26** 1381

[37] Bean C P and Livingston J D 1959 Superparamagnetism *J Appl Physiol* **30** 120S

[38] Schneider S and Rusconi S 1996 Magnetic selection of transiently transfected cells *Biotechniques* **21** 876-80

[39] Yanase M, Shinkai M, Honda H, Wakabayashi T, Yoshida J and Kobayashi T 1997 Intracellular hyperthermia for cancer using magnetite cationic liposomes: Ex vivo study *Jpn.J.Cancer Res.* **88** 630-2

[40] Yanase M, Shinkai M, Honda H, Wakabayashi T, Yoshida J and Kobayashi T 1998 Intracellular hyperthermia for cancer using magnetite cationic liposomes: An in vivo study *Jpn.J.Cancer Res.* **89** 463-9

[41] Jordan A, Scholz R, Maier-Hauff K, van Landeghem F, Waldoefner N, Teichgraeber U, Pinkernelle J, Bruhn H, Neumann F, Thiesen B, von Deimling A and Felix R 2006 The effect of thermotherapy using magnetic nanoparticles on rat malignant glioma *Journal of Neuro-Oncology* **78** 7-14

[42] Chan D C F, Kirpotin D B and Bunn P A 1993 Synthesis and evaluation of colloidal magnetic iron-oxides for the site specific radiofrequency-induced hyperthermia of cancer *J.Magn.Magn.Mater.* **122** 374-8

[43] Bach-Gansmo T 1993 Ferrimagnetic susceptibility contrast agents *Acta Radiol* **387** 1-30S

[44] Hahn P F, Stark D D, Lewis J M, Saini S, Elizondo G, Weissleder R, Fretz C J and Ferrucci J T 1990 First clinical trial of a new superparamagnetic iron oxide for use as an oral gastrointestinal contrast agent in mr imaging *Radiology* **175** 695-700

[45] Weissleder R, Stark D D, Engelstad B L, Bacon B R, Compton C C, White D L, Jacobs P and Lewis J 1989 Superparamagnetic iron oxide: Pharmacokinetics and toxicity *Am. J. Roentgenol.* **152** 167-73

[46] Reimer P, Rummeny E J, Daldrup H E, Balzer T, Tombach B, Berns T and Peters P E 1995 Clinical results with resovist: A phase 2 clinical trial *Radiology* **195** 489-96

[47] Reimer P and Tombach B 1998 Hepatic mri with spio: Detection and characterization of focal liver lesions *Eur Radiol* **8** 1198-204

[48] McLachlan S J, Morris M R, Lucas M A, Fisco R A, Eakins M N, Fowler D R, Scheetz R B and Olukotun A Y 1994 Phase i clinical evaluation of a new iron oxide mr contrast agent *J Magn Reson Imaging* **4** 301-7

[49] Stillman A E, Wilke N, Li D, Haacke M and McLachlan S 1996 Ultrasmall superparamagnetic iron oxide to enhance mra of the renal and coronary arteries: Studies in human patients *J Comput Assist Tomogr* **20** 51-5

[50] Stillman A E, Wilke N and Jerosch-Herold M 1997 Use of an intravascular t1 contrast agent to improve mr cine myocardial-blood pool definition in man *J Magn Reson Imaging* **7** 765-7

[51] Mayo-Smith W W, Saini S, Slater G, Kaufman J A, Sharma P and Hahn P F 1996 Mr contrast material for vascular enhancement: Value of superparamagnetic iron oxide. *Am J Roentgenol* **166** 73-7

[52] Anzai Y, Brunberg J A and Lufkin R B 1997 Imaging of nodal metastases in the head and neck *J Magn Reson Imaging* **7** 774-83

[53] Anzai Y, Blackwell K E, Hirschowitz S L, Rogers J W, Sato Y, Yuh W T, Runge V M, Morris M R, McLachlan S J and Lufkin et a 1994 Initial clinical experience with dextran-coated superparamagnetic iron oxide for detection of lymph node metastases in patients with head and neck cancer *Radiology* **192** 709-15

[54] Saeed M, Wendland M F, Engelbrecht M, Sakuma H and Higgins C B 1998 Value of blood pool contrast agents in magnetic resonance angiography of the pelvis and lower extremities *Eur Radiol* **8** 1047-53

[55] Tombach B, Reimer P, Bremer C, Allkemper T, Engehardt M, Mahler M and Heindel W L 2000 Mra with a new blood pool contrast agent: Phase i clinical trial *ECR 2000 abstract book* 279

[56] Simonsen C Z, Ostergaard L, Vestergaard-Poulsen P, Rohl L, Bjornerud A and Gyldensted C 1999 Cbf and cbv measurements by uspio bolus tracking: Reproducibility and comparison with gd-based values *J Magn Reson Imaging* **9** 342-7

[57] Weissleder R, Lee A S, Khaw B A, Shen T and Brady T J 1992 Antimyosin-labeled monocrystalline iron oxide allows detection of myocardial infarct: Mr antibody imaging *Radiology* **182** 381-5

[58] Weissleder R, Lee A S, Fischman A J, Reimer P, Shen T, Wilkinson R, Callahan R J and Brady T J 1991 Polyclonal human immunoglobulin g labeled with polymeric iron oxide: Antibody mr imaging *Radiology* **181** 245-9

[59] Wang Y X, Hussain S M and Krestin G P 2001 Superparamagnetic iron oxide contrast agents: Physicochemical characteristics and applications in mr imaging *European Radiology* **11** 2319-31

[60] Softways 2003 Magnetic resonance - technology information portal.

[61] Andrews N C 1999 Disorders of iron metabolism *New England Journal of Medicine* **341** 1986-95

[62] LaConte L, Nitin N and Bao G 2005 Magnetic nanoparticle probes *Materials Today* **8** 32-8

[63] Bacon B R, Stark D D, Park C H, Saini S, Groman E V, Hahn P F, Compton C C and Ferrucci J T 1987 Ferrite particles: A new magnetic resonance imaging contrast agent. Lack of acute or chronic hepatotoxicity after intravenous administration *The Journal of laboratory and clinical medicine* **110** 164-71

[64] Saini S, Stark D D, Hahn P F, Wittenberg J, Brady T J and Ferrucci J T 1987 Ferrite particles: A superparamagnetic mr contrast agent for the reticuloendothelial system *Radiology* **162** 211-6

[65] Weissleder R 1994 Liver mr imaging with iron oxides: Toward consensus and clinical practice *Radiology* **193** 593-5

[66] Pouliquen D. L I, Chouly C., Perdrisot R., Le Jeune J.J., Jallet P. 1993 Liver-directed superparamagnetic iron oxide: Quantitation of t2 relaxation effects *Magnetic Resonance Imaging* **11** 219-88

[67] Pouliquen D. P R, Ermias A., Akoka S., Jallet P., Le Jeune J.J. 1989 Superparamagnetic iron oxide nanoparticles as a liver mri contrast agent: Contribution of microencapsulation to improved biodistribution *Magnetic Resonance Imaging* **7** 619-27

[68] Anzai Y, McLachlan S, Morris M, Saxton R and Lufkin R B 1994 Dextran-coated superparamagnetic iron oxide, an mr contrast agent for assessing lymph nodes in the head and neck *AJNR. American Journal Of Neuroradiology* **15** 87-94

[69] Deserno W M L L G, Harisinghani M G, Taupitz M, Jager G J, Witjes J A, Mulders P F, Hulsbergen van de Kaa C A, Kaufmann D and Barentsz J O 2004 Urinary bladder cancer: Preoperative nodal staging with ferumoxtran-10-enhanced mr imaging *Radiology* **233** 449-56

[70] Vassallo P, Matei C, Heston W D, McLachlan S J, Koutcher J A and Castellino R A 1995 Characterization of reactive versus tumor-bearing lymph nodes with interstitial magnetic resonance lymphography in an animal model *Investigative Radiology* **30** 706-11

[71] Saleh A, Schroeter M, Jonkmanns C, Hartung H-P, Modder U and Jander S 2004 In vivo mri of brain inflammation in human ischaemic stroke *Brain: a Journal Of Neurology* **127** 1670-7

[72] Kool M E, Cappendijk V C, Cleutjens K B J M, Kessels A G H, Kitslaar P J E H M, Borgers M, Frederik P M, Daemen M J A P and Van Engelshoven J M A 2003 Accumulation of ultrasmall superparamagnetic particles of iron oxide in human atherosclerotic plaques can be detected by in vivo magnetic resonance imaging *Circulation* **107** 2453-8

[73] Ruehm S G, Corot C, Vogt P, Cristina H and Debatin J F 2002 Ultrasmall superparamagnetic iron oxide-enhanced mr imaging of atherosclerotic plaque in hyperlipidemic rabbits *Academic Radiology* **9**

[74] Schmitz S A, Taupitz M, Wagner S, Wolf K J, Beyersdorff D and Hamm B 2001 Magnetic resonance imaging of atherosclerotic plaques using superparamagnetic iron oxide particles *Journal of Magnetic Resonance Imaging* **14** 355-61

[75] Beckmann N, Cannet C, Fringeli-Tanner M, Baumann D, Pally C, Bruns C, Zerwes H G, Andriambeloson E and Bigaud M 2003 Macrophage labeling by spio as an early marker of allograft chronic rejection in a rat model of kidney transplantation *Magnetic Resonance in Medicine* **49** 459-67

[76] Kanno S, Lee P C, Dodd S J, Williams M, Griffith B P, Ho C, Mentzer S J, Egan T M and DeCamp M M 2000 A novel approach with magnetic resonance imaging used for the detection of lung allograft rejection *Journal of Thoracic and Cardiovascular Surgery* **120** 923-34

[77] Kanno S, Yi-Jen Lin W, Lee P C, Dodd S J, Williams M, Griffith B P and Ho C 2001 Macrophage accumulation associated with rat cardiac allograft rejection detected by magnetic resonance imaging with ultrasmall superparamagnetic iron oxide particles *Circulation* **104** 934-8

[78] Zhang Y, Dodd S J, Hendrich K S, Williams M and Ho C 2000 Magnetic resonance imaging detection of rat renal transplant rejection by monitoring macrophage infiltration *Kidney International* **58** 1300-10

[79] Bulte J W M, Douglas T, Witwer B, Zhang S C, Strable E, Lewis B K, Zywicke H, Miller B, Van Gelderen P, Moskowitz B M, Duncan I D and Frank J A 2001 Magnetodendrimers allow endosomal magnetic labeling and in vivo tracking of stem cells *Nature Biotechnology* **19** 1141-7

[80] Josephson L, Tung C H, Moore A and Weissleder R High-efficiency intracellular magnetic labeling with novel superparamagnetic-tat peptide conjugates *Bioconjugate Chemistry* **10** 186-91

[81] Lewin M, Carlesso N, Tung C H, Tang X W, Cory D, Scadden D T and Weissleder R 2000 Tat peptide-derivatized magnetic nanoparticles allow in vivo tracking and recovery of progenitor cells *Nature Biotechnology* **18** 410-4

[82] Arbab A S, Bashaw L A, Miller B R, Jordan E K, Lewis B K, Kalish H and Frank J A 2003 Characterization of biophysical and metabolic properties of cells labeled with superparamagnetic iron oxide nanoparticles and transfection agent for cellular mr imaging *Radiology* **229** 838-46

[83] Arbab A S, Yocum G T, Kalish H, Jordan E K, Anderson S A, Khakoo A Y, Read E J and Frank J A 2004 Efficient magnetic cell labeling with protamine sulfate complexed to ferumoxides for cellular mri *Blood* **104** 1217-23

[84] Frank J A, Miller B R, Arbab A S, Zywicke H A, Jordan E K, Lewis B K, Bryant Jr L H and Bulte J W M 2003 Clinically applicable labeling of mammalian and

stem cells by combining superparamagnetic iron oxides and transfection agents *Radiology* **228** 480-7

[85] Kalish H, Arbab A S, Miller B R, Lewis B K, Zywicke H A, Bulte J W M, Bryant Jr L H and Frank J A 2003 Combination of transfection agents and magnetic resonance contrast agents for cellular imaging: Relationship between relaxivities, electrostatic forces, and chemical composition *Magnetic Resonance in Medicine* **50** 275-82

[86] Hawrylak N, Ghosh P, Broadus J, Schlueter C, Greenough W T and Lauterbur P C 1993 Nuclear magnetic resonance (nmr) imaging of iron oxide-labeled neural transplants *Experimental Neurology* **121** 181-92

[87] Bulte J W M, Ma L D, Magin R L, Kamman R L, Hulstaert C E, Go K G, The T H and De Leij L 1993 Selective mr imaging of labeled human peripheral blood mononuclear cells by liposome mediated incorporation of dextran-magnetite particles *Magnetic Resonance in Medicine* **29** 32-7

[88] Anderson S A, Shukaliak-Quandt J, Jordan E K, Arbab A S, Martin R, McFarland H and Frank J A 2004 Magnetic resonance imaging of labeled t-cells in a mouse model of multiple sclerosis *Annals of Neurology* **55** 654-9

[89] Sundstrom J B, Mao H, Santoianni R, Villinger F, Little D M, Huynh T T, Mayne A E, Hao E and Ansari A A 2004 Magnetic resonance imaging of activated proliferating rhesus macaque t cells labeled with superparamagnetic monocrystalline iron oxide nanoparticles *Journal of Acquired Immune Deficiency Syndromes* **35** 9-21

[90] Yeh T C, Zhang W, Ildstad S T and Ho C 1993 Intracellular labeling of t-cells with superparamagnetic contrast agents *Magnetic Resonance in Medicine* **30** 617-25

[91] Zelivyanskaya M L, Nelson J A, Poluektova L, Uberti M, Mellon M, Gendelman H E and Boskal M D 2003 Tracking superparamagnetic iron oxide labeled monocytes in brain by high-field magnetic resonance imaging *Journal of Neuroscience Research* **73** 284-95

[92] Shapiro E M, Skrtic S and Koretsky A P 2005 Sizing it up: Cellular mri using micron-sized iron oxide particles *Magn Reson.Med.* **53** 329-38

[93] Koyama Y, Barrett T, Hama Y, Ravizzini G, Choyke P and Kobayashi H 2007 In vivo molecular imaging to diagnose and subtype tumors through receptor-targeted optically labeled monoclonal antibodies *Neoplasia* **9** 1021-9

[94] Milenic D E, Brady E D and Brechbiel M W 2004 Antibody-targeted radiation cancer therapy *Nat Rev Drug Discov* **3** 488-99

[95] Blankenberg F G and Strauss H W 2002 Nuclear medicine applications in molecular imaging *Journal of Magnetic Resonance Imaging* **16** 352-61

[96] Nitin N, LaConte L E W, Zurkiya O, Hu X and Bao G 2004 Functionalization and peptide-based delivery of magnetic nanoparticles as an intracellular mri contrast agent *Journal of Biological Inorganic Chemistry* **9** 706-12

[97] Kim D K, Mikhaylova M, Wang F H, Kehr J, Bjelke B, Zhang Y, Tsakalakos T and Muhammed M 2003 Starch-coated superparamagnetic nanoparticles as mr contrast agents *Chemistry of Materials* **15** 4343-51

[98] Shen T, Weissleder R, Papisov M, Bogdanov Jr A and Brady T J 1993 Monocrystalline iron oxide nanocompounds (mion): Physicochemical properties *Magnetic Resonance in Medicine* **29** 599-604

[99] Pileni M P 2003 The role of soft colloidal templates in controlling the size and shape of inorganic nanocrystals *Nature Materials* **2** 145-50

[100] Seip C T and O'Connor C J 1999 Fabrication and organization of self-assembled metallic nanoparticles formed in reverse micelles *Nanostructured Materials* **12** 183-6

[101] Park J, An K, Hwang Y, Park J E G, Noh H J, Kim J Y, Park J H, Hwang N M and Hyeon T 2004 Ultra-large-scale syntheses of monodisperse nanocrystals *Nature Materials* **3** 891-5

[102] LaMer V and Dinegar R 1950 Theory, production, and mechanism of formation of monodispersed hydrosols *Journal of American Chemical Society* **72** 4847-54

[103] Vayssieres L, Chaneac C, Tronc E and Jolivet J P 1998 Size tailoring of magnetite particles formed by aqueous precipitation: An example of thermodynamic stability of nanometric oxide particles *Journal of Colloid and Interface Science* **205** 205-12

[104] Massart R 1981 Preparation of aqueous magnetic liquids in alkaline and acidic media *Ieee Transactions on Magnetics* **17** 1247-8

[105] Jolivet J P and Tronc E 1988 Interfacial electron-transfer in colloidal spinel iron-oxide - conversion of fe3o4-gamma-fe2o3 in aqueous-medium *Journal of Colloid and Interface Science* **125** 688-701

[106] Bee A, Massart R and Neveu S 1995 Synthesis of very fine maghemite particles *Journal of Magnetism and Magnetic Materials* **149** 6-9

[107] Sickafus K E 1992 *Encyclopedia of materials characterization: Surfaces, interfaces, thin films,* ed C R Brundle, *et al.* (London: Butterworth-Heinemann) pp 99-115

[108] O'Grady K and Bradbury A 1983 Particle size analysis in ferrofluids *J Magn Magn Mater* **39** 91

[109] Ulman A 1996 Formation and structure of self-assembled monolayers *Chem.Rev.* **96** 1533-54

[110] Mulvaney P, Liz-Marzan L M, Giersig M and Ung T 2000 Silica encapsulation of quantum dots and metal clusters *J.Mater.Chem.* **10** 1259-70

[111] Liu D M and Chen I W 1999 Encapsulation of protein molecules in transparent porous silica matrices via an aqueous colloidal sol-gel process *Acta Materialia* **47** 4535-44

[112] Stober W and Fink A 1968 Controlled growth of monodisperse silica spheres in the micron size range *Journal of Colloid and Interface Science* **26** 62-9

[113] Bardosova M and Tredgold R H 2002 Ordered layers of monodispersive colloids *Journal of Materials Chemistry* **12** 2835-42

[114] Achilefu S 2004 Lighting up tumors with receptor-specific optical molecular probes *Technology in Cancer Research & Treatment* **3** 393-409

[115] Becker A, Hessenius C, Licha K, Ebert B, Sukowski U, Semmler W, Wiedenmann B and Grotzinger C 2001 Receptor-targeted optical imaging of tumors with near-infrared fluorescent ligands *Nature Biotechnology* **19** 327-31

[116] Licha K, Hessenius C, Becker A, Henklein P, Bauer M, Wisniewski S, Wiedenmann B and Semmler W 2001 Synthesis, characterization, and biological properties of cyanine-labeled somatostatin analogues as receptor-targeted fluorescent probes *Bioconjugate Chemistry* **12** 44-50

[117] Ntziachristos V, Bremer C and Weissleder R 2003 Fluorescence imaging with near-infrared light: New technological advances that enable in vivo molecular imaging *European Radiology* **13** 195-208

[118] Licha K 2002 *Topics in current chemistry,* (Berlin: Springer) pp 1-29

[119] Tromberg B J 2000 Non-invasive in vivo characterization of breast tumors using photon migration spectroscopy *Neoplasia* **2** 26

[120] Grosenick D, Wabnitz H, Rinneberg H, Moestra K T and Schlag P M 1999 Development of a time-domain optical mammograph and first in vivo applications *Appl. Optics.* **38** 2927-038

[121] Weissleder R 2001 A clearer vision for in vivo imaging *Nature Biotechnology* **19** 316-7

[122] Andersson-Engels S and Wilson B C 1992 In vivo fluorescence in clinical oncology: Fundamental and practical issues *J. Cell Pharmacol.* **3** 48-60

[123] Wagnières G A, Star W M and Wilson B C 1998 In vivo fluorescence spectroscopy and imaging for oncological applications *Photochem. Photobiol.* **68** 603-32

[124] Ziolo R F, Giannelis E P, Weinstein B A, Ohoro M P, Ganguly B N, Mehrotra V, Russell M W and Huffman D R 1992 Matrix-mediated synthesis of nanocrystalline gamma-fe2o3 - a new optically transparent magnetic material *Science* **257** 219-23

[125] Williams A T R, Winfield S A and Miller J N 1983 Relative fluorescence quantum yields using a computer controlled luminescence spectrometer *Analyst* **108** 1067

[126] Mujumdar S R, Mujumdar R B, C.M. G and Waggoner A S 1996 Cyanine-labeling reagents: Sulfobenzindocyanine succinimidyl esters *Bioconj. Chem.* **7** 356-62

[127] Storm A J, Chen J H, Ling X S, Zandbergen H W and Dekker C 2005 Electron-beam-induced deformations of sio[sub 2] nanostructures *Journal of Applied Physics* **98** 014307-8

[128] Pitts J R and Czanderna A W 1986 Reduction of silica surfaces with particle beams *Nuclear Instruments and Methods in Physics Research* **B13** 245-9

[129] de Broglie L 1924 *Recherches sur la théorie des quanta (researches on the quantum theory)* (Paris

[130] 1965 *Nobel lectures, physics 1922-1941* (Amsterdam: Elsevier Publishing Company)

[131] Thomson G P and Cochrane W 1939 *Theory and practice of electron diffraction* (London: Macmillan and Co., Limited)

[132] Vainshtein B K 1964 *Structure analysis by electron diffraction* (Oxford: Pergamon Press)

[133] Bendersky L A and Gayle F W 2001 Electron diffraction using transmission electron microscopy *J. Res. Natl. Inst. Stand. Technol.* **106** 997-1012

[134] Ma H, Shieh K J and Qiao T X 2006 Study of transmission electron microscopy (tem) and scanning electron microscopy (sem) *Nature and Science* **4** 14-22

[135] 1960 Xray powder data file ed J V Smith (Philadelphia: ASTM Special Technical Publication 48-J)

[136] 1963 Fink inorganic index to the powder diffraction file. ed J V Smith and A S Beward (Philadelphia: ASTM Special Technical Publications 48-M3) pp 68, 328

[137] Plaza R C, Arias J L, Espin M, Jimenez M L and Delgado A V 2002 Aging effects in the electrokinetics of colloidal iron oxides *Journal of Colloid and Interface Science* **245** 86-90

[138] Gomez-Lopera S A, Plaza R C and Delgado A V 2001 Synthesis and characterization of spherical magnetite/biodegradable polymer composite particles *Journal of Colloid and Interface Science* **240** 40-7

[139] Vroman L 1974 Surface charge, protein adsorption, and thrombosis *Science* **184** 585-6

[140] Neel L 1949 *Ann. Grophys. (C.N.S.R.)* **5** 99

[141] Kumar D, Narayan J, Kvit A V, Sharma A K and Sankar J 2001 High coercivity and superparamagnetic behavior of nanocrystalline iron particles in alumina matrix *Journal of Magnetism and Magnetic Materials* **232** 161-7

[142] Martinez B, Roig A, Obradors X, Molins E, Rouanet A and Monty C 1996 Magnetic properties of gamma-fe2o3 nanoparticles obtained by vaporization condensation in a solar furnace *Journal of Applied Physics* **79** 2580-6

[143] Vejpravova J P, Sechovsky V, Niznansky D, Plocek J, Hutlova A and Rehspringer J L 2005 Superparamagnetism of co-ferrite nanoparticles *WDS'05 Proced. Contr. Pap.* **3** 518–23

[144] Kim D K, Zhang Y, Voit W, Rao K V and Muhammed M 2001 Synthesis and characterization of surfactant-coated superparamagnetic monodispersed iron oxide nanoparticles *Journal of Magnetism and Magnetic Materials* **225** 30-6

[145] Tartaj S, Gonzalez-Carreno T and Serna C J 2003 Magnetic behavior of γ-fe[2]o[3] nanocrystals dispersed in colloidal silica particles *J Phys Chem B* **107** 20-4

[146] Bárcenaa C, Sraa A K, Chaubeyb G S, Khemtonga C, Liub J P and Gao J 208 Zinc ferrite nanoparticles as mri contrast agents *Chem. Commun.* 2224-6

[147] Lee J-H, Huh Y-M, Jun Y-w, Seo J-w, Jang J-t, Song H-T, Kim S, Cho E-J, Yoon H-G, Suh J-S and Cheon J 2007 Artificially engineered magnetic nanoparticles for ultra-sensitive molecular imaging *Nat Med* **13** 95-9

[148] Robinson J P and Gregori G 2007 *Flow cytometry with plant cells,* ed J Dolezel, *et al.* (Weinheim: WILEY-VCH Verlag GmbhH &Co)

[149] 2000 *Flow cytometry - a practical approach. 3rd edition.* (Oxford, UK: Oxford University Press)

[150] Givan A L 1992 *Flow cytometry: First principles* (New York: Wiley-Liss)

[151] Fulcher D A and Basten A 1997 B cell life span: A review *Immunology and Cell Biology* **75** 446–55

[152] Tsouchnikas I, Tsilipakou M, Daniilidis M, Kyriazis G, Pasadakis P, Parapanissiou E, Vargemezis V and Tsakiris D 2007 Effect of iron loading on

peripheral blood lymphocyte subsets and on circulating cytokine levels in iron-depleted hemodialysis patients receiving erythropoietin *Nephron Clinical Practice* **107** c97-c102

[153] Okuhata Y 1999 Delivery of diagnostic agents for magnetic resonance imaging *Advanced Drug Delivery Reviews* **37** 121-37

[154] Weinmann H, Ebert W, Misselwitz B and Schmitt-Willich H 2003 Tissue-specific mr contrast agents *Eur J Radiol* **46** 33

[155] Cerdan S, Lotscher H R, Kunnecke B and Seelig J 1989 Monoclonal antibody-coated magnetite particles as contrast agents in magnetic resonance imaging of tumors *Magn Reson Imaging* **12** 151

[156] Remsen L G, McCormick C I, Roman-Goldstein S, Nilaver G, Weissleder R, Hellstrom I, Kroll R A and Neuwelt E A 1996 Mr of carcinoma-specific monoclonal antibody conjugated to monocrystalline iron oxide nanoparticles: The potential for noninvasive diagnosis *Am J Neuroradiol* **17** 411-8

[157] Wolcott A, Gerion D, Visconte M, Sun J, Schwartzberg A, Chen S W and Zhang J Z 2006 Silica-coated cdte quantum dots functionalized with thiols for bioconjugation to igg proteins *Journal of Physical Chemistry B* **110** 5779-89

[158] Lu B, Xie J M, Lu C L, Wu C G and Wei Y 1995 Oriented immobilization of fab' fragments on silica surfaces *Analytical Chemistry* **67** 83-7

[159] Zhao X J, Hilliard L R, Mechery S J, Wang Y P, Bagwe R P, Jin S G and Tan W H 2004 A rapid bioassay for single bacterial cell quantitation using bioconjugated nanoparticles *Proceedings of the National Academy of Sciences of the United States of America* **101** 15027-32

[160] Santra S, Zhang P, Wang K M, Tapec R and Tan W H 2001 Conjugation of biomolecules with luminophore-doped silica nanoparticles for photostable biomarkers *Analytical Chemistry* **73** 4988-93

[161] Yang H H, Qu H Y, Lin P, Li S H, Ding M T and Xu J G 2003 Nanometer fluorescent hybrid silica particle as ultrasensitive and photostable biological labels *Analyst* **128** 462-6

[162] Wang L, Yang C Y and Tan W H 2005 Dual-luminophore-doped silica nanoparticles for multiplexed signaling *Nano Letters* **5** 37-43

[163] Jonsson U, Malmqvist M and Ronnberg I 1985 Immobilization of immunoglobulins on silica surfaces - stability *Biochemical Journal* **227** 363-71

[164] Smith E A, Wanat M J, Cheng Y, Barreira S V P, Frutos A G and Corn R M 2001 Formation, spectroscopic characterization, and application of sulfhydryl-terminated alkanethiol monolayers for the chemical attachment of DNA onto gold surfaces *Langmuir* **17** 2502-7

[165] Falk K 2002 Ligand exchange of major histocompatibility complex class ii proteins is triggered by h-bond donor groups of small molecules *The Journal of biological chemistry* **277** 2709-15

[166] Krogsgaard M, Wucherpfennig K W, Cannella B, Hansen B E, Svejgaard A, Pyrdol J, Ditzel H, Raine C, Engberg J and Fugger L 2000 Visualization of myelin basic protein (mbp) t cell epitopes in multiple sclerosis lesions using a monoclonal antibody specific for the human histocompatibility leukocyte antigen (hla)-dr2-mbp 85-99 complex *The Journal of experimental medicine* **191** 1395-412

[167] Lang H L, Jacobsen H, Ikemizu S, Andersson C, Harlos K, Madsen L, Hjorth P, Sondergaard L, Svejgaard A, Wucherpfennig K, Stuart D I, Bell J I, Jones E Y and Fugger L 2002 A functional and structural basis for tcr cross-reactivity in multiple sclerosis *Nat Immunol* **3** 940-3

[168] Madsen L S, Andersson E C, Jansson L, krogsgaard M, Andersen C B, Engberg J, Strominger J L, Svejgaard A, Hjorth J P, Holmdahl R, Wucherpfennig K W and Fugger L 1999 A humanized model for multiple sclerosis using hla-dr2 and a human t-cell receptor *Nat Genet* **23** 343-7

[169] Klenerman P, Cerundolo V and Dunbar P R 2002 Tracking t cells with tetramers: New tales from new tools *Nature Reviews Immunology* **2** 263-72

[170] Dornmair K, Goebels N, Weltzien H U, Wekerle H and Hohlfeld R 2003 T-cell-mediated autoimmunity: Novel techniques to characterize autoreactive t-cell receptors *American Journal of Pathology* **163** 1215-26

[171] Ding Y H, Baker B M, Garboczi D N, Biddison W E and Wiley D C 1999 Four a6-tcr/peptide/hla-a2 structures that generate very different t cell signals are nearly identical *Immuniity* **11** 45-56

[172] Ellman G 1959 Tissue sulfhydryl groups. *Arch.Biochem. Biophys* **82** 70-7

[173] Huneke R B, Pippin C G, Squire R A, Brechbiel M W, Gansow O A and Strand M 1992 Effective alpha-particle-mediated radioimmunotherapy of murine leukemia *Cancer Research* **52** 5818-20

[174] McDevitt M R, Barendswaard E, Ma D, Lai L, Curcio M J, Sgouros G, Ballangrud A M, Yang W H, Finn R D, Pellegrini V, Geerlings M W, Lee M, Brechbiel M W, Bander N H, Cordon-Cardo C and Scheinberg D A 2000 An alpha-particle emitting antibody ([bi-213]j591) for radioimmunotherapy of prostate cancer *Cancer Research* **60** 6095-100

[175] Roselli M M D, Brechbiel MW, Mirzadeh S, Pippin CG, Gansow OA, Colcher D, Schlom J. 1999 In vivo comparison of chx-dtpa ligand isomers in athymic mice bearing carcinoma xenografts. *Cancer Biother Radiopharm* **14** 209-20

[176] Wu C, Kobayashi H, Sun B, Yoo T M, Paik C H, Gansow O A, Carrasquillo J A, Pastan I and Brechbiel M W 1997 Stereochemical influence on the stability of

radio-metal complexes in vivo. Synthesis and evaluation of the four stereoisomers of 2-(p-nitrobenzyl)-trans-cydtpa *Bioorganic & Medicinal Chemistry* **5** 1925-34

[177] Pippin C G, Parker T A, McMurry T J and Brechbiel M W 1992 Spectrophotometric method for the determination of a bifunctional dtpa ligand in dtpa monoclonal-antibody conjugates *Bioconjugate Chemistry* **3** 342-5

[178] Lowry OH R N, Farr AL, Randall RJ 1951 Protein measurement with the folin phenol reagent. *J Biol Chem* **193** 265-75

[179] Saltz L B, Meropol N J, Loehrer P J, Sr., Needle M N, Kopit J and Mayer R J 2004 Phase ii trial of cetuximab in patients with refractory colorectal cancer that expresses the epidermal growth factor receptor *Journal of Clinical Oncology* **22** 1201-8

[180] Jurcic J G, Larson S M, Sgouros G, McDevitt M R, Finn R D, Divgi C R, Ballangrud A M, Hamacher K A, Ma D, Humm J L, Brechbiel M W, Molinet R and Scheinberg D A 2002 Targeted alpha particle immunotherapy for myeloid leukemia *Blood* **100** 1233-9

[181] Ghosh S S, Kao P M, McCue A W and Chappelle H L 1990 Use of maleimide-thiol coupling chemistry for efficient syntheses of oligonucleotide-enzyme conjugate hybridization probes *Bioconj. Chem.* **1** 71-6

[182] Kircher M F, Mahmood U, King R S, Weissleder R and Josephson L 2003 A multimodal nanoparticle for preoperative magnetic resonance imaging and intraoperative optical brain tumor delineation *Cancer Res* **63** 8122-5

[183] Huber M M, Staubli A B, Kustedjo K, Gray M H B, Shih J, Fraser S E, Jacobs R E and Meade T J 1998 Fluorescently detectable magnetic resonance imaging agents *Bioconj. Chem.* **9** 242-9

[184] Cai W, Chen K, Li Z-B, Gambhir S S and Chen X 2007 Dual-function probe for pet and near-infrared fluorescence imaging of tumor vasculature *Journal of Nuclear Medicine* **48** 1862-70

[185] Lee H-Y, Li Z, Chen K, Hsu A R, Xu C, Xie J, Sun S and Chen X 2008 Pet/mri dual-modality tumor imaging using arginine-glycine-aspartic (rgd)-conjugated radiolabeled iron oxide nanoparticles *Journal of Nuclear Medicine* **49** 1371-9

[186] Williamson R, Aristizabal O, Turnbull D H, Ketterling J A, Zaim Y and Fahmy T M 2007 8b-1 polymer contrast particles for cellular imaging with ultrasound and mri. In: *Ultrasonics Symposium, 2007. IEEE,* pp 648-51

[187] Santra S, Bagwe R P, Dutta D, Stanley J T, Walter G, Tan W, Moudgil B M and Mericle R A 2005 Synthesis and characterization of fluorescent, radio-opaque, and paramagnetic silica nanoparticles for multimodal bioimaging applications *Advanced Materials* **17** 2165-9

[188] Jordan A, Scholz R, Wust P, Fahling H, Krause J, Wlodarczyk W, Sander B, Vogl T and Felix R 1999 Effects of magnetic fluid hyperthermia (mfh) on c3h mammary carcinoma in vivo *International Journal of Hyperthermia* **13** 587-605

[189] Johannsen M, Gneveckow U, Taymoorian K, Thiesen B, Waldöfner N, Scholz R, Jung K, Jordan A, Wust P and Loening S A 2007 Morbidity and quality of life during thermotherapy using magnetic nanoparticles in locally recurrent prostate cancer: Results of a prospective phase i trial *International Journal of Hyperthermia* **23** 315-23

[190] Kuan A K, Jackson F I and Hanson J 1988 Multimodality detection of metastatic melanoma *J R Soc Med* **81** 579-82

[191] Alderson P O, Adams D F, McNeil B J, Sanders R, Siegelman S S, Finberg H J, Hessel S J and Abrams H L 1983 Computed tomography, ultrasound, and scintigraphy of the liver in patients with colon or breast carcinoma: A prospective comparison *Radiology* **149** 225-30

[192] Semelka R C, Martin D R, Balci C and Lance T 2001 Focal liver lesions: Comparison of dual-phase ct and multisequence multiplanar mr imaging including dynamic gadolinium enhancement *J Magn Reson Imaging* **13** 397-401

[193] Stark D D, Wittenberg J, Butch R J and Ferrucci J T 1987 Hepatic metastases: Controlled comparison of detection with mr imaging and ct *Radiology* **165** 399-406

[194] Chezmar J L, Rumancik W M, Megibow A J, Hulnick D H, Nelson R C and Bernardino M E 1988 Liver and abdominal screening in patients with cancer: Ct versus mr imaging *Radiology* **168** 43-7

[195] Weissleder A, Stark D D, Rummeny E J, Compton C C and Ferrucci J T 1988 Splenic lymphoma: Ferrite-enhanced mr imaging in rats *Radiology* **166** 423-30

[196] Saini S, Stark D D, Hahn P F, Bousquet J C, Introscasso J, Wittenberg J, Brady T J and Ferrucci J T 1987 Ferrite particles: A superparamagnetic mr contrast agent for enhanced detection of liver carcinoma *Radiology* **167** 217-22

[197] Tsang Y M, Stark D D, Chen M C M, Weissleder R, Wittenberg J and Ferrucci J T 1988 Hepatic micrometastases in the rat: Ferrite-enhanced mr imaging *Radiology* **167** 21-4

[198] Kawamura Y, Endo Y, Watanabe Y, Saga T, Nakai T, Hikiat H, Kagawa K and Konishi J 1990 Use of magnetite particles as a contrast agent for mr imaging of the liver *Radiology* **174** 357-60

[199] Fretz C, J., Stark D D, Metz C E, Elizondo G, Weissleder R, Shen J H, Wittenberg J, Simeone J and Ferrucci J T 1990 Detection of hepatic metastases: Comparison of contrast-enhanced ct, unenhanced mr imaging, and iron oxide-enhanced mr imaging *AJR* **155** 763-70

[200] Bernstein M A, King K F and Zhou X J 2004 *Handbook of mri pulse sequences* (Amsterdam: Elsevier)

[201] Briley-Saebo K C, Mani V, Hyafil F, Cornily J C and Fayad Z A 2008 Fractionated feridex and positive contrast: In vivo mr imaging of atherosclerosis *Magnetic resonance in medicine* **59** 721-30

[202] Landis S H, Murray T, Bolden S and Wingo P A 1999 Cancer statistics, 1999. pp 8-31

[203] Wingo P A, Tong T and Bolden S 1995 Cancer statistics, 1995. pp 8-30

[204] Rice S, Khalkhali I and Diggles L 1998 The role of radionuclide breast imaging in the evaluation of suspected breast abnormalities. *Breast Disease* **10** 177-87

[205] Taillefer R 1999 The role of 99mtc-sestamibi and other conventional radiopharmaceuticals in breast cancer diagnosis. *Semin Nucl Med.* **29** 16-40

[206] Goldhirsch A, Glick J H, Gelber R D, Coates A S and Senn H-J 2001 Meeting highlights: International consensus panel on the treatment of primary breast cancer. pp 3817-27

[207] Orel S G and Schnall M D 2001 Mr imaging of the breast for the detection, diagnosis, and staging of breast cancer *Radiology* **220** 13-30

[208] Morrow M 1996 Role of axillary dissection in breast cancer management *Ann Surg Oncol* **3** 233-4

[209] Dauway E L, Giuliano R, Pendas S, Haddad F, Costello D, Cox C E, Berman C, Ku N N and Reintgen D S 1999 Lymphatic mapping: A technique providing accurate staging for breast cancer *Breast Cancer* **6** 145–54

[210] Kinne D W 1998 Axillary clearance in operable breast cancer: Still a necessity? *Recent Results Cancer Res* **152** 161-9

[211] Silverstein M J, Skinner K A and Lomis T J 201 Predicting axillary nodal positivity in 2282 patients with breast carcinoma *World J Surg* **25** 767-72

[212] Yeoh E K, Denham J W, Davies S A and Spittle M F 1986 Primary breast cancer: Complications of axillary management *Acta Radiol Oncol* **25** 105-8

[213] Morton D and Chan A 2000 The concept of sentinel node localization: How it started *Seminars in Nucl Med* **30** 4-10

[214] Bass S S, Cox C E, Ku N N, Berman C and Reintgen D S 1999 The role of sentinel lymph node biopsy in breast cancer *J Am Coll Surg* **189** 183-94

[215] Cochran A J 2000 The pathologist's role in sentinel lymph node evaluation *Seminars in Nucl Med* **XXX** 11-7

[216] Dooms G C, Hricak H, Crooks L E and Higgins C B 1984 Magnetic resonance imaging of the lymph nodes: Comparison with ct *Radiology* **153** 719-28

[217] Krishnamurthy S, Sneige N, Bedi D G, Edieken B S, Fornage B D, Kuerer H M, Singletary S E and Hunt K K 2002 Role of ultrasound-guided fine-needle aspiration of indeterminate and suspicious axillary lymph nodes in the initial staging of breast carcinoma *Cancer* **95** 982-8

[218] Memarsadeghi M, Riedl C C, Kaneider A, Galid A, Rudas M, Matzek W and Helbich T H 2006 Axillary lymph node metastases in patients with breast carcinomas: Assessment with nonenhanced versus uspio-enhanced mr imaging **241** 367-77

[219] Barrett T, Choyke P L and Kobayashi H 2006 Imaging of the lymphatic system: New horizons **1** 230-45

[220] Cserni G 1999 Metastases in axillary sentinel lymph nodes in breast cancer as detected by intensive histopathological work up *J. Clin. Pathol.* **52** 922-4

[221] Trojani M, De Mascareli I, Bonichon F, Coindre J M and Delsol G 1987 Micrometastases to axillary lymph nodes from carcinoma of breast: Detection by immunohistochemistry and prognostic significance *British Journal of Cancer* **55** 303-6

[222] Sedmak D D, Meineke T A, Knechtges D S and Anderson J 1989 Prognostic significance of cytokeratin-positive breast cancer metastases *Mod Pathol* **2** 516-20

[223] Barentsz J O, Fütterer J J and Takahashi S 2007 Use of ultrasmall superparamagnetic iron oxide in lymph node mr imaging in prostate cancer patients *European Journal of Radiology* **63** 369-72

[224] Bellin M F R, C., Kinkel K, Thoumas D, Zaim S, Vanel D, Tuchmann C, Richard F, Jacqmin D, Delcourt A, Challier E, Lebret T and Cluzel P 1998 Lymph node metastases: Safety and effectiveness of mr imaging with ultrasmall superparamagnetic iron oxide particles - initial clinical experience *Radiology* **207** 799-808

[225] Tatsumi Y, Tanigawa N, Nishimura H, Nomura E, Mabuchi H, Matsuki M and Narabayashi I 2006 Preoperative diagnosis of lymph node metastases in gastric cancer by magnetic resonance imaging with ferumoxtran-10 *Gastric Cancer* **9** 120-8

[226] Harada T, Tanigawa N, Matsuki M, Nohara T and Narabayashi I 2007 Evaluation of lymph node metastases of breast cancer using ultrasmall superparamagnetic iron oxide-enhanced magnetic resonance imaging *Eur J Radiol* **63** 410-07

[227] Anzai Y, Piccoli C W, Outwater E K, Stanford W, Bluemke D A, Nurenberg P, Saini S, Maravilla K R, Feldman D E, Schmiedl U P, Brunberg J A, Francis I R, Harms S E, Som P M and Tempany C M 2003 Evaluation of neck and body

metastases to nodes with ferumoxtran 10-enhanced mr imaging: Phase iii safety and efficacy study *Radiology* **228** 777-88

[228] 2005 (Memphis, Tennessee: American Association for Labratory Animal Science)

[229] Talanov V S, Regino C A S, Kobayashi H, Bernardo M, Choyke P L and Brechbiel M W 2006 Dendrimer-based nanoprobe for dual modality magnetic resonance and fluorescence imaging *Nano Lett.* **6** 1459-63

[230] Shah S A, Gallagher B M and DSands H 1987 Lymphoscintigraphy of human colorectral carcinoma in athymic by use of radioiodinated b72.3 monoclonal antibody *J NCI* **78** 1069-77

[231] Bumb A, Brechbiel M W, Choyke P L, Fugger L, Eggeman A, Prabhakaran D, Hutchinson J and Dobson P J 2008 Synthesis and characterization of ultra-small superparamagnetic iron oxide nanoparticles thinly coated with silica *Nanotechnology* **19** 335601

[232] Weissleder R 2002 Scaling down imaging: Molecular mapping of cancer in mice *Nat Rev Cancer* **2** 11-8

[233] Kircher M F, Allport J R, Graves E E, Love V, Josephson L, Lichtman A H and Weissleder R 2003 In vivo high resolution three-dimensional imaging of antigen-specific cytotoxic t-lymphocyte trafficking to tumors *Can. Res.* **63** 6838-46

[234] Kraitchman D L, Heldman A W, Atalar E, Amado L C, Martin B J, Pittenger M F, Hare J M and Bulte J W M 2003 In vivo magnetic resonance imaging of mesenchymal stem cells in myocardial infarction *Circulation* **107** 2290-3

[235] Bulte J W M, Zhang S C, van Gelderen P, Herynek V, Jordan E K, Duncan I D and Frank J A 1999 Neurotransplantation of magnetically labeled oligodendrocyte progenitors: Magnetic resonance tracking of cell migration and myelination *PNAS* **96** 15256-61

[236] Fleige G, Nolte C, Synowitz M, Seeberger F, Kettenmann H and Zimmer C 2001 Magnetic labeling of activated microglia in experimental gliomas *Neoplasia* **3** 489-99

[237] Rogers W J, Meyer C H and Kramer C M 2006 Technology insight: In vivo cell tracking by use of mri *Nature Clinical Practice Cardiovascular Medicine* **3** 554-62

[238] Walczak P, Kedziorek D A, Gilad A A, Lin S and Bulte J W M 2005 Instant mr labeling of stem cells using magnetoelectroporation *Magn Reson Imaging* **54** 769-74

[239] Wilhelm C, Billotey C, Roger J, Pons J N, Bacri J C and Gazeau F 2003 Intracellular uptake of anionic superparamagnetic nanoparticles as a function of their surface coating *Biomaterials* **24** 1001-11

[240] Riviere C, Boudghene F P, Gazeau F, Roger J, Pons J N, Laissy J P, Allaire E, Michel J B, Letourneur D and Deux J F 205 Iron oxide nanoparticle-labeled rat smooth muscle cells: Cardiac mr imaging for cell graft monitoring and quantitation *Radiology* **235** 959-67

[241] Matuszewski L, Persigehl T, Wall A, Schwindt W, Tombach B, Fobker M, Poremba C, Ebert W, Heindel W and Bremer C 2005 Cell tagging with clinically approved iron oxides: Feasibility and effect of lipofection, particle size, and surface coating on labeling efficiency *Radiology* **235** 155-61

[242] Arbab A S, Yocum G T, Rad A, Khakoo A Y, Fellowes V, Read E J and Frank J A 2005 Labeling of cells with ferumoxides-protamine sulfate complexes does not inhibit function or differentiation capacity of hematopoietic or mesenchymal stem cells *NMR Biomed.* **18** 553-9

[243] Jefferies W A, Brandon M R, Hunt S V, Williams A F, Gatter K C and Mason D Y 1984 Transferrin receptor on endothelium of brain capillaries *Nature* **312** 162-3

[244] Zhang Z Y and Smith B D 2000 High-generation polycationic dendrimers are unusually effective at disrupting anionic vesicles: Membrane bending model *Bioconj. Chem.* **11** 805-14

[245] Zhang Z, van den Bos E J, Wielopolski P A, Jong-Popijus M, Bernsen M R, Duncker D J and Krestin G P 2005 In vitro imaging of single living human umbilical vein endothelial cells with a clinical 3.0-t mri scanner *Magnetic Resonance Materials in Physics, Biology and Medicine* **18** 175-85

[246] Heyn C, Bowen C V, Rutt B K and Foster P J 2005 Detection threshold of single spio-labeled cells with fiesta *Magn Reson Imaging* **53** 312-20

[247] Shapiro E M, Sharer K, Skrtic S and Koretsky A P 2006 In vivo detection of single cells by mri *Magn Reson Imaging* **55** 242-9

[248] Kraitchman D L, Tatsumi M, Gilson W D, Ishimori T, Kedziorek D, Walczak P, Segars W P, H. Chen H, Fritzges D, Izbudak I, Young R G, Marcelino M, Pittenger M F, Solaiyappan M, Boston R C, Tsui B M W, Wahl R L and Bulte J W M 2005 Dynamic imaging of allogeneic mesenchymal stem cells trafficking to myocardial infarction *Circulation* **112** 1451-61

[249] Overgaard J 1984 History and heritage - an introduction. In: *Hyperthermic Oncology*, ed J Overgaard (London and Philadelphia: Taylor & Francis) pp 3-8

[250] Jordan A, Scholz R, Wust P, Fähling H and Roland F 1999 Magnetic fluid hyperthermia (mfh): Cancer treatment with ac magnetic field induced excitation of

biocompatible superparamagnetic nanoparticles *Journal of Magnetism and Magnetic Materials* **201** 413-9

[251] Hofer K G 2002 *Eur. Cell Mater.* **3(suppl. 2)** 67-9

[252] Mornet S, Vasseur S, Grasset F and Duguet E 2004 Magnetic nanoparticle design for medical diagnosis and therapy *Journal of Materials Chemistry* **14** 2161-75

[253] Zhang J, Boyd C and Luo W 1996 Two mechanisms and a scaling relation for dynamics in ferrofluids *Physical Review Letters* **77** 390

[254] Hergt R, Andra W, d'Ambly C G, Hilger I, Kaiser W A, Richter U and Schmidt H G 1998 Physical limits of hyperthermia using magnetite fine particles *Magnetics, IEEE Transactions on* **34** 3745-54

[255] Gilchrist R, Medal R, Shorey W, Hanselman R, Parrott J and Taylor C 1957 Selective inductive heating of lymph nodes *Ann.Surg.* **146** 596-606

[256] Moroz P, Jones S K, Winter J and Gray B N 2001 Targeting liver tumors with hyperthermia: Ferromagnetic embolization in a rabbit liver tumor model *Journal of Surgical Oncology* **78** 22-9

[257] Moroz P, Jones S K and Gray B N 2002 Tumor response to arterial embolization hyperthermia and direct injection hyperthermia in a rabbit liver tumor model *Journal of Surgical Oncology* **80** 149-56

[258] Moroz P, Jones S K and Gray B N 2002 Arterial embolization hyperthermia in porcine renal tissue *Journal of Surgical Research* **105** 209-14

[259] Jordan A, Scholz R, Wust P, Fähling H, Krause J, Wlodarczyk W, Sander B, Vogl T and Felix R 1997 Effects of magnetic fluid hyperthermia (mfh) on c3h mammary carcinoma in vivo *International Journal of Hyperthermia* **13** 587-605

[260] Le B, Shinkai M, Kitade T, Honda H, Yoshida J, Wakabayashi T and Kobayashi T 2001 Preparation of tumor-specific magnetoliposomes and their application for hyperthermia *Journal of Chemical Engineering of Japan* **34** 66-72

[261] Gutowska A, Bae Y H, Jacobs H, Feijen J and Kim S W 1994 Thermosensitive interpenetratirig polymer networks: Synthesis, characterization, and macromolecular release *Macromolecules* **27** 4167-75

[262] Sadrieh N and Miller T J 2006 *Nanotechnology for cancer therapy* (Boca Raton, FL: CRC Press)

Declaration

I declare that this thesis is entirely my own work, and except where otherwise stated, describes my own research.

Ambika Bumb